BINDING SERVICES
Tel +44 (0)29 2087 4949
Fax +44 (0)29 20371921
e-mail bindery@cardiff.ac.uk

Alternative Fuels and Technology For Internal Combustion Engines

Thesis submitted for the
Degree of Doctor of Philosophy
of the University of Wales Cardiff

by
Anthony Peter Giles
(MEng)

May, 2006

ProQuest LLC
789 East Eisenhower Parkway
P.O. Box 1346
Ann Arbor, MI 48106-1346

Summary

Within this thesis is an investigation and appraisal of alternative automotive fuels, internal combustion engine technology and emission reduction techniques.

A review of the developments in engine technology, with specific focus on improvements in engine efficiency and emission reductions was undertaken. Tighter emission legislation imposed after the Kyoto agreement has resulted in technological advances in the field of internal combustion engines; improving the economy of modern motor vehicles while reducing their emissions of CO2 and particulate matter.

As part of an EU funded project entitled "Magnetic Movement Valve for Miller Cycle operation of engines", the application of a novel secondary valve apparatus to an internal combustion engine was investigated through the use of computer modelling. It was shown that the secondary valve concept is capable of controlling the output of an internal combustion engine, while increasing the operating efficiency and reducing the emission of NO_X through the use of Miller cycle operation and throttle free load control.

A development programme of the engine and the secondary valve apparatus, carried out in conjunction with EU project partners, resulted in a marketable engine incorporating the new technology which is now in production within Europe and the Far East.

An engine test-bed facility was commissioned to investigate the emissions and performance of a diesel engine fuelled by a variety of biodiesel / diesel fuel blends. It was found that incremental addition of biodiesel to a low sulphur diesel fuel resulted in a decrease in engine power and an increase in fuel consumption, CO_2 and NO_X emissions. The particulates levels of pure biodiesel emissions were found to be much lower (by mass and number concentration) than that of the low sulphur diesel fuel. From analysis of the exhaust gases it was found that the average size of the particulates is larger for biodiesel fuel than for the low sulphur diesel fuel.

Acknowledgements

I would like to take this opportunity to thank the following people who have helped me during my PhD studies at Cardiff University:

The academic, research and clerical staff from the Institute of Sustainability, Energy and Environmental Management for their help. Special thanks to my supervisors, Professor Philip Bowen and Professor Nick Syred, for their continual guidance and support throughout this study.

Also special thanks to the staff at NoNOx bv. and Aachan University for their assistance throughout the "MagMove" project.

The technical staff of the Mechanical Engineering workshop, in particular Mr A. Griffiths, Mr P. Malpas, Mr D. Hobbs, Mr L. Treherne and Mr M. Seabourne for their assistance in the construction and maintenance of the experimental facilities.

Finally, I would like to express a deep gratitude to my family and friends for their constant support throughout the duration of this study.

Nomenclature

Symbol	*Unit*	*Definition*
A	m^2	cross sectional area
c	m/s	instantaneous speed of sound
C_D, C_d	-	discharge coefficient
F_i	Nm	body force
G	J/s	turbulent energy generation rate
H, h	J/kg	absolute enthalpy
K, k	m^2/s^2	turbulence kinetic energy
l	-	length scale
m	kg	mass
P	Nm	measured engine power
P_o	Nm	corrected engine power
p_s	Pa	dry atmospheric pressure
Pr	-	Prandtl number
Q	m^3/s	volumetric flow rate
q_{rad}	J	energy contribution from radiation
q_w	W/m^2	heat flux through the wall
r	-	expansion/compression coefficient
S_ϕ	-	source term
t	s	time
T	k	temperature
u	m/s	velocity
u'	-	velocity scale
U_i	m/s	local mass-averaged velocity
v	m/s	instantaneous gas velocity
x	m	sub volume length
Y	-	mass fraction of a given species

Symbol	*Unit*	*Definition*
ΔP	Pa	applied pressure difference
Δt	s	time step size,
$\Gamma_{\phi-L}$	m^2/s	molecular diffusivity
Φ	-	scalar variable
α_d	-	power correction factor
γ	-	heat capacity ratio
ε	J	turbulent energy dissipation rate
η	-	efficiency
μ_L	kg/ms	molecular dynamic viscosity
μ_t	kg/ms	turbulent viscosity
ν	m^2/s	kinematic viscosity
ρ	kg/m^3	density
σ_H	-	turbulent Schmidt number
$\tau_{\phi-t}$	m^2/s	effective diffusivity
ω	mol/s	species production rate / addition

Superscripts / Subscripts

Symbol	*Unit*	*Definition*
C	-	compression
CI	-	compression ignition
E	-	expansion
ext	-	external
H	J/kg	enthalpy
m	kg	mass
SI	-	spark ignition
U	kgm/s	momentum

Table of Contents

List of Figures and Tables

1 Introduction

For a broad variety of reasons, national (and global) energy consumption has been the focus of much recent political attention. A range of policy documents and energy consumption targets have been set, which have increasingly put under scrutiny the sectors of industry which rely either directly or indirectly upon high energy consumption. The transport sector is clearly one such example.

The introduction to the thesis describes the general background to the field of Internal Combustion (IC) engines, with emphasis on the technical areas pertinent to the focus of this thesis. A general review of international legislation that has affected and continues to affect engine research is summarised. Areas of particular interest are highlighted for further investigation throughout the course of this study.

1.1 Internal Combustion Engine

The IC engine is one of the few inventions that, since its inception, has affected virtually the entire population of the globe. An internal combustion engine is a heat engine, in which an exothermic reaction is made to occur by the controlled ignition of a fuel with an oxidizer, leading to the formation of gases of high temperature and pressure. In an internal combustion engine the gaseous combustion products are permitted to expand, and in doing so carry out useful work by acting directly to cause movement (usually the movement of a piston within an enclosed cylinder).

The majority of fuels used in internal combustion engines are basic hydrocarbons of the form C_XH_Y, and the formula for the complete combustion of a hydrocarbon fuel in oxygen is shown in equation 1-1.

$$C_XH_Y + (X + Y/4)\,O_2 \rightarrow XCO_2 + (Y/2)H_2O \qquad (1\text{-}1)$$

When there is precisely enough air in a fuel/air mixture for complete combustion to occur the mixture is said to be stoichiometric. If there is too much air the mixture is described as fuel "lean" and conversely if there is insufficient air the mixture is described as fuel "rich". In the case where there is insufficient oxygen for complete combustion of a hydrocarbon to occur, the gaseous products may include carbon monoxide (CO) and particulate matter (PM) such as soot. Other pollutants, such as nitrogen oxides (NO_X), can also be generated during the combustion process which are damaging to the environment.

1.1.1 Basic Engine Cycles

Internal combustion engines (or more specifically internal intermittent continuous combustion engines, excluding turbine machinery) can be broadly split up into two groups;

Spark Ignition (SI) — Engines in which a compressed air-fuel charge within the engine cylinder is ignited by a suitable energy source (typically a spark plug).

Compression Ignition (CI) — Engines in which the fuel ignites inside the engine cylinder due to the effects on the chemical kinetics of an increase in pressure and temperature caused by a tight fitting piston compressing the air-fuel charge within the cylinder.

The SI genre of engines almost entirely follows the four-stroke combustion cycle to convert the chemical energy contained in the fuel into kinetic energy. The basic four-stroke combustion cycle is known as the Otto cycle after Nikolaus Otto (1832-1891), who first described the cycles' operation in 1876. The patent held by Otto for the four-stroke cycle was invalidated in 1886 when it was discovered that another inventor, Alphonse Beau de Rochas, had already described the principle of the cycle in a privately published paper. The basic Otto cycle as well as an actual four-stroke SI

engine cycle is shown in Figure 1.1. As can be seen in Figure 1.1, the basic engine operation described by the Otto cycle is difficult to obtain in reality.

Each of the four-strokes of the SI combustion cycle can be described as follows. The induction stroke (points A-B in Figure 1.1) is the drawing in of the fresh air/fuel mixture into the engine cylinder; the compression stroke is the compression of the confined air/fuel mixture (points B-C), after which combustion is initiated in the cylinder by the spark plug; the expansion stroke (points C-D) is where the formation of the hot combustion gases carries out work on the piston; and finally the exhaust stroke (points D-A) is where the combustion products are evacuated from the engine cylinder.

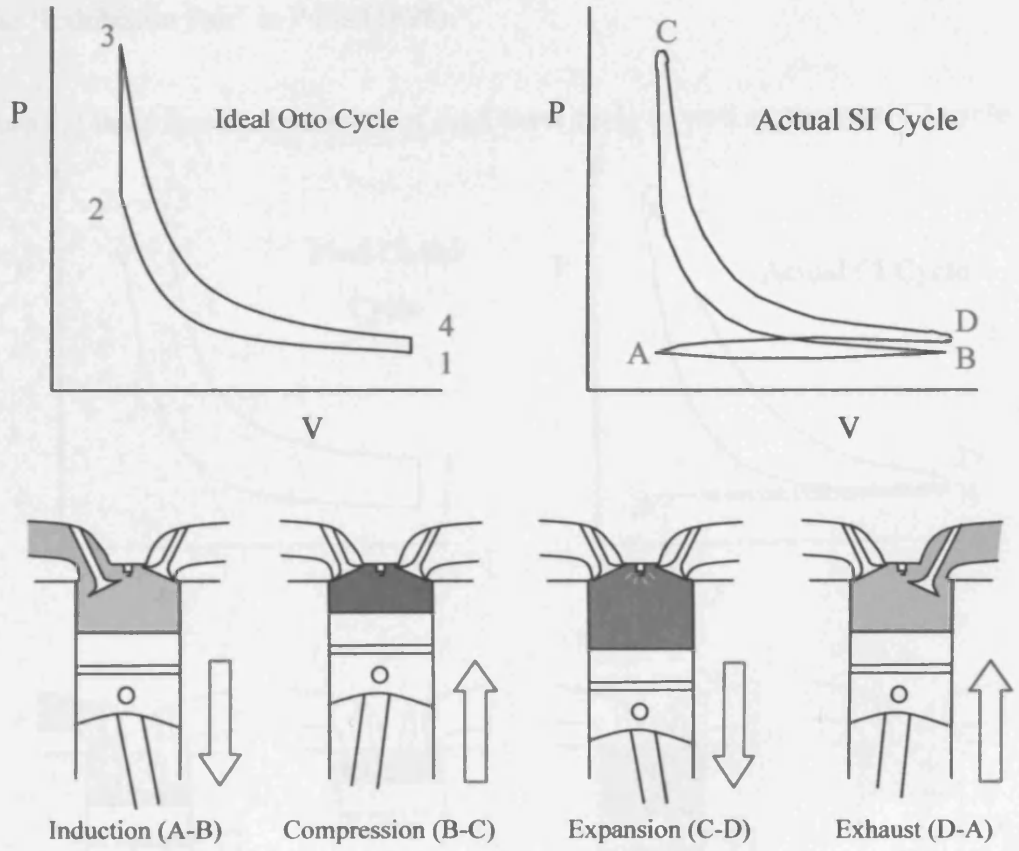

Figure 1.1 – Otto cycle and actual SI cycle comparison

engine cycle is shown in Figure 1.1. As can be seen in Figure 1.1, the basic engine operation described by the Otto cycle is difficult to obtain in reality.

Each of the four-strokes of the SI combustion cycle can be described as follows. The induction stroke (points A-B in Figure 1.1) is the drawing in of the fresh air/fuel mixture into the engine cylinder; the compression stroke is the compression of the confined air/fuel mixture (points B-C), after which combustion is initiated in the cylinder by the spark plug; the expansion stroke (points C-D) is where the formation of the hot combustion gases carries out work on the piston; and finally the exhaust stroke (points D-A) is where the combustion products are evacuated from the engine cylinder.

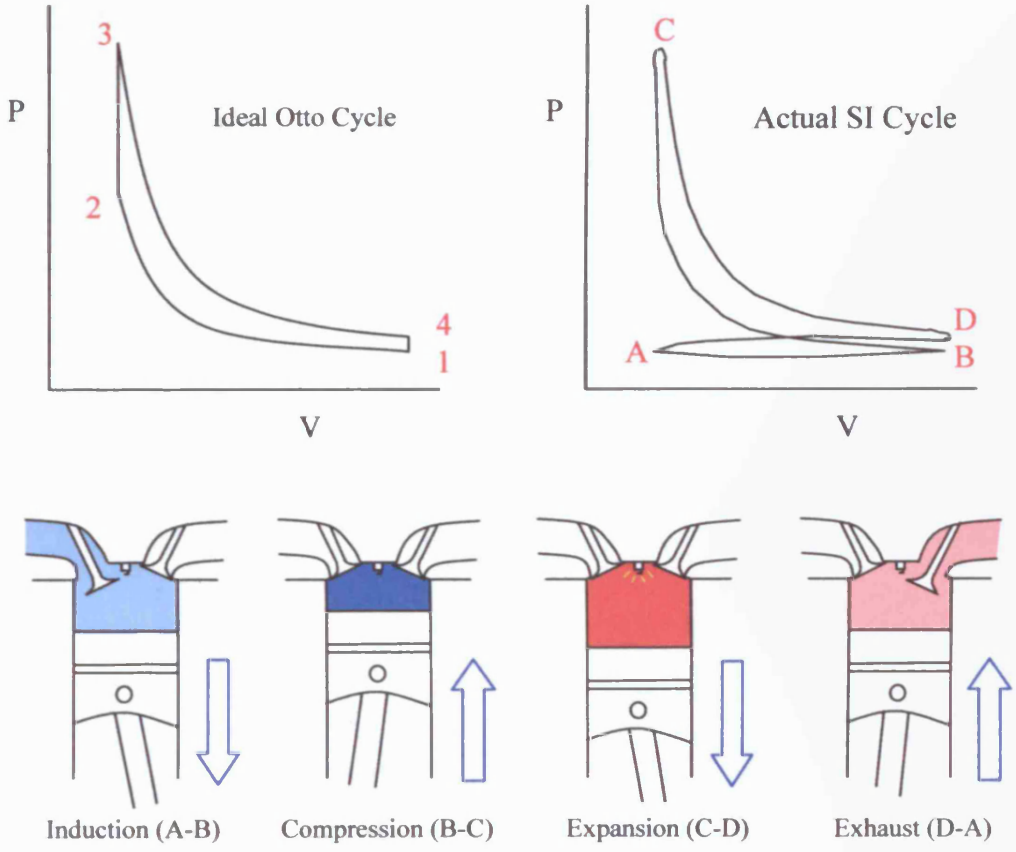

Figure 1.1 – Otto cycle and actual SI cycle comparison

The efficiency of the ideal Otto cycle is given by equation 1-2:

$$\eta_{SI} = 1 - r_{SI}^{(1-\gamma)} \qquad (1\text{-}2)$$

From equation 1-2 it can be seen that the efficiency of a spark ignition engine is therefore related to the compression ratio of the engine.

The CI genre of engines differs slightly in operation to their SI counterparts, in that typically a higher compression ratio is used to initiate combustion instead of using a spark plug to ignite the air-fuel charge. The basic principles behind the CI genre of engines are attributed to Rudolph Diesel (1858-1913) who first demonstrated his engine at the 'Exhibition Fair' in Paris (1898).

Figure 1.2 describes the operation of the Diesel cycle as well as an actual CI cycle.

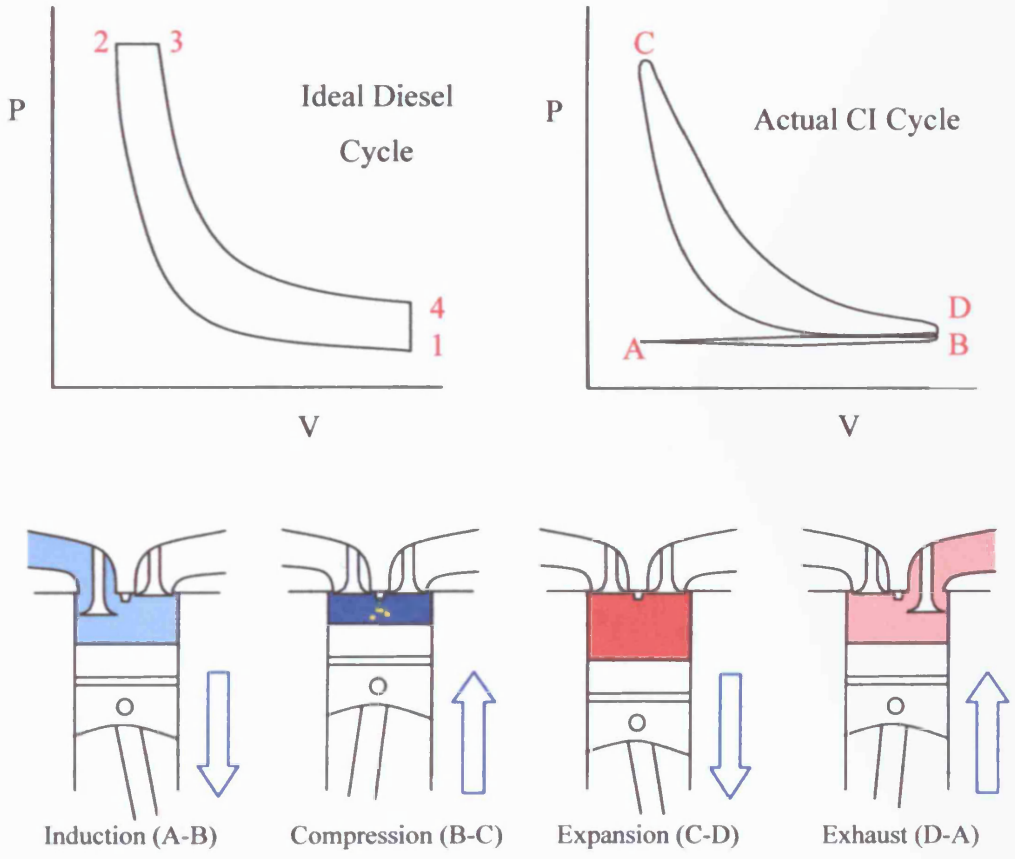

Figure 1.2 – Diesel cycle and actual CI cycle comparison

Each of the four-strokes of the diesel combustion cycle can be described as follows. The induction stroke (points A-B in Figure 1.2) is the drawing of the fresh air into the engine cylinder; the compression stroke is the compression of the confined air (points B-C), after which fuel is injected into the cylinder which then auto-ignites due to the high temperature and pressure caused by the compression; the expansion stroke (points C-D) is where the formation of the hot combustion gases carries out work on the piston; and finally the exhaust stroke (points D-A) is where the combustion products are evacuated from the engine cylinder.

The efficiency of the ideal diesel cycle is given by equation 1-3:

$$\eta_{CI} = 1 - \frac{1}{\gamma}\left(\frac{r_E^{-\gamma} - r_C^{-\gamma}}{r_E^{-1} - r_C^{-1}}\right) \tag{1-3}$$

It can be seen from equation 1-3 that the efficiency of a diesel engine is related to both the effective expansion ratio and compression ratio of the engine.

1.1.2 IC Engine Design

Figure 1.3 displays a schematic of a modern internal combustion engine, with labels pointing out components of interest.

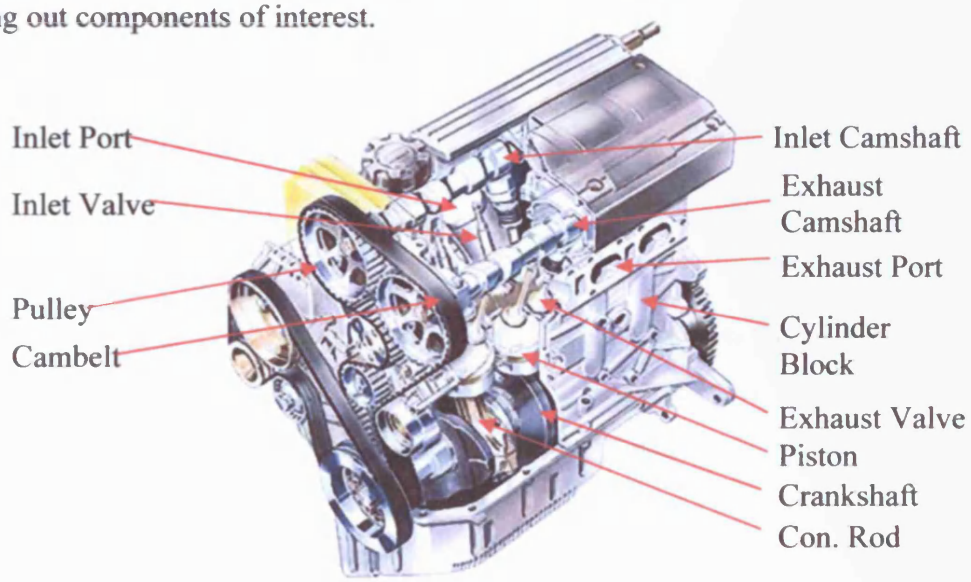

Figure 1.3 – Internal combustion engine schematic

1.2 Fuels

The abundance of crude oil reserves throughout the world, together with the suitable characteristics of some of its derivatives, led to it becoming the major fuel source for the Internal Combustion engine. The origin of crude oil is from the remains of plant life from 100 to 600 million years, with the hydrocarbons and other compounds present in the crude oil being linked to the fossil remains of the leaf waxes and other plant molecules (both marine and terrestrial) believed to exist throughout that era.

Early automotive fuels were the lighter fractions from the distillation of crude oil. It is now accepted that the natural products of crude oil distillation do not meet the required standards for modern engines, and because of this various chemicals are mixed with the crude oil distillates to improve their liquid and combustion properties. Four main types of automotive fuel are sold throughout the UK, these are:

- 95 octane unleaded petrol
- 97 octane unleaded petrol (known as super-unleaded)
- Lead replacement petrol (LRP, demand rapidly decreasing)
- Diesel fuel (DERV)

The three petrol (or gasoline) fuels are used in spark ignition engines, while the diesel fuel is used in compression ignition engines.

1.2.1 Petrol (Gasoline) Fuels

Petrol fuels typically consist of hydrocarbon molecules with between five and twelve carbon atoms. Modern petrol is predominantly a mixture of paraffins (alkanes), naphthenes (cycloalkanes), aromatics and olefins (alkenes). The exact ratio of the constituents of petrol depends on the location from which the raw crude is obtained, the refinery which processes the oil and the grade of the petrol (summer / winter grade and octane rating).

The most important characteristic of petrol fuels is the octane rating, which is the measure of how resistant a spark-ignition fuel is to premature detonation (known as knocking). Knocking is the premature ignition of the unburned air/fuel charge due to auto-ignition. The octane rating system was developed by the chemist Russel Marker and is measured relative to a mixture of 2,2,4-trimethylpentane (an octane isomer) and n-heptane. A fuel classed as '95 octane' has the same resistance to knock as a mixture of 95% iso-octane and 5% n-heptane. The most common octane rating system employed worldwide is the Research Octane Number (RON), which is determined by running the fuel through a specific test engine with a variable compression ratio under controlled conditions. The results are then compared with that of iso-octane and n-heptane.

Higher octane fuels allow for the use of higher compression ratios which results in higher peak cylinder pressures and greater efficiency, even though the higher octane fuels may contain less energy per litre. In practice however, the octane rating of the fuel has no relationship with its energy content.

The characteristics for petrol sold in the UK are stated in European directives 98/70/EC and 1999/32/EC and in UK law by the Motor Fuel (Composition and Content) regulations 1999 (The specifications for 95 and 97 octane unleaded petrol are also stated in British Standards BS EN 228:2004 and BS 7800:2004 respectively). From these rules the minimum Research Octane Number for UK petrol is 95, the maximum sulphur content is 50 ppm and the maximum aromatic content is 35% by volume.

1.2.2 Diesel Fuels

Diesel fuel typically consists of hydrocarbon molecules with between ten and fifteen carbon atoms and has a density typically 18% higher than petrol. Diesel fuel also has an energy content per unit volume about 18% greater than petrol, which along with the greater efficiency of diesel engines contributes to an increase in fuel economy. Standard diesel fuel contains much higher quantities of sulphur than the petrol equivalent, but through legislation and preferential taxation oil companies have been forced to lower the final sulphur content of their fuels.

The Cetane number of a diesel fuel is equivalent to the octane rating of a petrol fuel and is a measure of the quality of the fuel's combustion. Cetane is a hydrocarbon molecule that ignites very easy under compression, and was therefore assigned a Cetane number of 100. All the hydrocarbons in diesel fuel are indexed to Cetane by their ability to ignite under compression; therefore the Cetane number measures how quickly the fuel auto-ignites under diesel engine conditions. The overall Cetane number assigned to a fuel is thus the weighted average Cetane number of each of the hundreds of individual components that make up the diesel fuel. Fuels with high Cetane numbers will start to burn shortly after their injection into an engine cylinder (because of the high pressure and temperatures obtained during the compression stroke) due to their very short ignition delay. Fuels with low Cetane numbers resist auto-ignition and therefore have longer ignition delays. The Cetane number of most fuels is calculated using the density and distillation range of the constituent oils; the Cetane number can also be measured experimentally using a Cooperative Fuel Research engine under standard test conditions. In practice there is very little increase in performance or emissions once the Cetane number of a fuel is raised past 50.

The characteristics for diesel fuel sold in the UK are also covered by the European directives 98/70/EC and 1999/32/EC and in UK law by the Motor Fuel (Composition and Content) regulations 1999; and the British Standard for diesel fuel is BS EN 590:2004. The minimum Cetane number for UK diesel is 51, the maximum sulphur content is 50 ppm, and the maximum polycyclic aromatics content is 11% by volume. The maximum sulphur content of diesel fuel is set to change to 10 ppm by the 1st January 2008.

1.3 Emissions

Since the industrial revolution air pollution has been a concern for many countries; with airborne pollutants such as gases, chemicals and smoke particles reducing the ability for enjoyment or causing significant health and environmental problems.

1.3.1 Pollutants from Internal Combustion Engines

The combustion of petrol and diesel fuels is a known source of airborne pollutants such as:

- Carbon monoxide
- Carbon dioxide
- Nitrogen oxides
- Sulphur dioxide
- Particulate Matter
- Benzene
- Polycyclic Aromatic Hydrocarbons

Carbon monoxide (CO) is a colourless, odourless poisonous gas that is a product of the incomplete combustion of hydrocarbon based fuels. The method by which CO is formed is shown in equation 1-4.

$$C_XH_Y + \text{Insufficient } O_2 \rightarrow CO_2 + CO + H_2O \qquad (1\text{-}4)$$

CO binds to the haemoglobin contained in blood over two hundred times more avidly than oxygen; thus prevents the release of any remaining oxygen to the body tissues, effectively poisoning by suffocation. CO has also been observed to intensify cardiovascular disease in humans. Low levels of CO exposure cause headaches, disorientation and fatigue.

Carbon dioxide, although viewed as a product of perfect combustion, is now considered a pollutant due to its classification as a "greenhouse gas" and its contribution to global warming.

Nitrogen oxides (NO_X) is the generic term for a group of highly reactive colourless and odourless gases that contain varying amounts of nitrogen and oxygen. Many fossil fuels contain a small amount of nitrogen in their molecular structure, which on combustion is converted into NO_X. However, the main mechanism for the formation of NO_X involves the oxidation of atmospheric nitrogen under the high pressure and temperature conditions that occur in an internal combustion engine. NO_X as well as causing the formation of acid rain are linked to the formation of ground level ozone (O_3), which is known to be an eye irritant and cause breathing difficulties.

Sulphur dioxide is formed from the combustion of fossil fuels. Sulphur dioxide like NO_X leads to the formation of acid rain as well as contributing to ground level ozone. The sulphur content of fossil fuels is also known to increase the level of particulate matter in the exhaust gases.

Particulate Matter (PM) refers to a complex mixture of different small particles and liquid droplets and can be broadly split up into four distinct groups:

- Aqueous soluble
- Organic soluble
- Carbonaceous
- Inorganic insoluble

Of these groups the organic soluble and carbonaceous are the predominant forms of PM in automotive exhaust, with the organic soluble comprising mainly unburned hydrocarbons, the carbonaceous being mainly composed of soot/carbon black.

The particle size is the key characteristic that relates to the toxicity of airborne particulate matter, since it is particle size that determines the distance an airborne particle can be deposited within the respiratory tract. Coarse particles have little effect to health, whereas fine particles are deposited in the smallest passages (Bronchioles)

within the lungs. These fine particles cause inflammation within the lungs which impairs lung operation. There are many issues regarding the manner in which legislation controls the levels of PM by imposing mass limits, which do not take into account the size distribution of the PM. A new method of classifying PM is to state the total mass produced as well as that for PM_{10}, particles having an aerodynamic diameter less than ten micrometers (aerodynamic diameter is the diameter of a particle of unit density possessing the same aerodynamic properties). In this manner both the number and mass of the emitted PM can be assessed.

Benzene occurs naturally in small quantities in both petrol and diesel fuel and is emitted from vehicles as both unburned fuel in the exhaust as well as through evaporation within the fuel system. Benzene is both toxic and carcinogenic with long term exposure being linked with leukaemia. Benzene is classed as a volatile organic compound (VOC) and is also a product of decomposition of more complicated aromatic compounds during combustion.

Polycyclic Aromatic Hydrocarbons (PAHs) are a group of chemicals found naturally in crude oil as well as being formed during the incomplete combustion of hydrocarbon fuels. Many PAHs have been classified as possible carcinogens and have been linked to fertility and birth defects. PAHs are most easily absorbed into the body when they are present in oily mixtures or aerosols, and once absorbed into the body they are stored primarily within the kidneys, liver and fat tissue.

1.3.2 Emission Legislation

In the early 1990's the EU, the US government and Japan established separate emission targets for new vehicles. A comparison of these targets up to the year 2001 was made by Powers and Nicastri (2000) and is shown in Figure 1.4. It can be seen from Figure 1.4 that the emission targets set by the US were similar to that set for Europe, with the Japanese targets being less stringent.

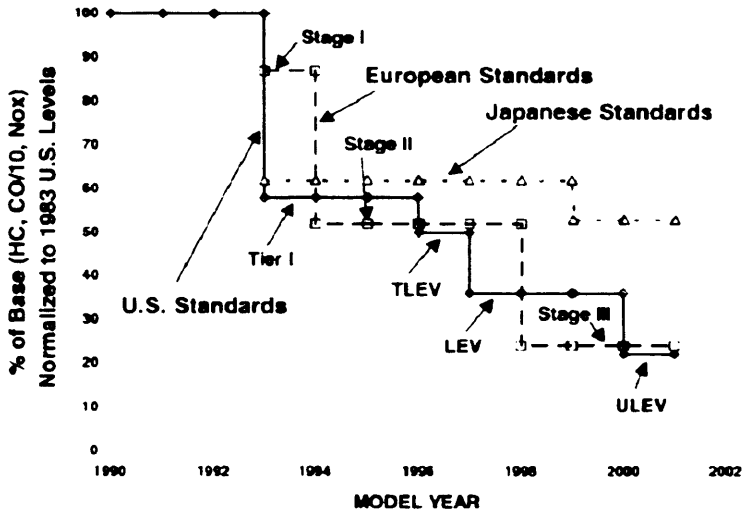

Figure 1.4 – US, Japanese and European emission targets for new vehicles

Tables 1.1 and 1.2 give the emission levels defined by the European Commission (Directive 70/220/EEC 2003) for passenger cars and heavy duty (HD) vehicles being currently produced, as well as the agreed levels which come into effect in 2008. The emission levels set by the standards are strictly enforced with severe penalties for any engine manufacturers that fail to attain these levels. The emission standard levels provide a series of goals that the vehicle manufacturers must meet in order for the vehicles to be given certificates of conformity to enable them to be sold throughout the European Union.

Table 1.2 also includes proposed HD diesel and gas engine levels for EURO VI (European Federation for Transport and Environment notes), the EURO VI levels have not been ratified as yet but are included for comparison.

Table 1.1 – European emission levels for passenger cars

Comparison of Standards	CO g/km	HC g/km	HC + NOx g/km	NOx g/km	PM g/km
Diesel					
EURO I (1992)	2.72	-	0.97	-	0.14
EURO II (1996)	1.0	-	0.7	-	0.08
EURO III (2000)	0.64	-	0.56	0.50	0.05
EURO IV (2005)	0.50	-	0.30	0.25	0.025
EURO V (2008)	0.50	-	0.25	0.20	0.005
Petrol					
EURO I (1992)	2.72	-	0.97	-	-
EURO II (1996)	2.20	-	0.5	-	-
EURO III (2000)	2.30	0.20	-	0.15	-
EURO IV (2005)	1.0	0.10	-	0.08	-
EURO V (2008)	1.0	0.075	-	0.06	0.005

Table 1.2 – European transient emission levels for HD diesel and gas engines

Comparison of Standards	CO g/kWh	THC g/kWh	CH4 g/kWh	NOx g/kWh	PM g/kWh
EURO III (2000)	5.45	0.78	1.6	5.00	0.16
EURO IV (2005)	4.0	0.55	1.1	3.5	0.03
EURO V (2008)	4.0	0.55	1.1	2.0	0.03
EURO VI (2010 proposed)	4.0	0.55	1.1	0.5	0.003
EEV - Enhanced environmentally friendly engine (2005)	3.00	0.40	0.65	2.00	0.02

The proposed emission levels for EURO VI, although largely similar to the currently enforced limits, have severely clamped down on particulate and NO_X emissions. The reasoning behind this is that the recent developments in particulate traps and catalytic converters have made such targets feasible, although costly. For heavy duty vehicles the estimated added production expense to meet the EURO VI targets could be as much as £2000 per vehicle, although it is expected that improvements in engine design would improve fuel consumption and allow the end-user to recover their added costs.

Based upon trends in legislated emission targets it can be expected that future emissions of CO, CO_2, NO_X and PM will have to continue to decline in the emissions of internal combustion engines. The implementation of emission targets will significantly affect the future emissions produced by road transport. New technologies will have to be developed and new fuels/fuel additives investigated. However, in addition to the reduction in emissions of each vehicle, other measures will continue to be used to alter people's driving habits.

1.4 Aims and Objectives

It is the aim of this thesis to investigate and develop scientific knowledge in the field of efficient internal combustion engine technology and emission reduction techniques.

The objectives that must be fulfilled in order to reach this aims are:-

- Thoroughly review previous work and developments in internal engine technology and trends. Discuss current and likely future trends and highlight areas open to further research.
- Appraise and analyse the claimed improvements in efficiency offered by Electro-Magnetically Operated load Control Valve technology through modelling techniques. Offer optimised designs for EOCV technology through modelling and analysis, comparing predictions with available measured data.
- Use modelling and engine test-bed facilities, analyse the performance of a heavy duty CI engine fuelled on biodiesel and diesel blends.

1.5 Structure of Thesis

The work required for the completion of this thesis is discussed throughout a number of different chapters. Chapter 1 is a general introduction to the thesis describing the background technology and international legislation that form the reasons for the undertaking of this research. Chapter 2, reviews the literature of relevant previous research and technological developments in the field of internal combustion engines, and highlights areas requiring further research and development; which are then pursued in the remainder of the thesis.

Chapter 3 details the work carried out at Cardiff University, in conjunction with its European project partners, in constructing a detailed computational model of a natural gas powered engine incorporating a novel secondary valve apparatus. Throughout Chapter 4 designs of the aforementioned secondary valve apparatus are evaluated using a commercially available 3-dimensional computational fluid dynamics code. The development work that was carried out by Cardiff University on the secondary valve apparatus and its associated engine is detailed and discussed in Chapter 5. The effect of the secondary valve apparatus on the engines operating cycle is examined in Chapter 6.

The development of the internal combustion engine testing facilities at Cardiff University, specifically in the area of diesel emission studies, is detailed in Chapter 7. In Chapter 8 the use of renewable fuels as an alternative to diesel fuel is examined; the effect of using fuels of this nature on engine operation is investigated and discussed.

Chapter 9 summarises and discusses all the conclusions from preceding chapters. The main findings and outcomes of the work are listed and areas of possible research discussed.

2 Literature Review

The aim of this chapter is to review the relevant published literature in the field of alternative automotive fuels, internal combustion engine technology and emission reduction techniques. It is hoped from this review that areas open for further research and development will be highlighted, which can then be pursued in the remainder of the thesis.

2.1 Emission Control

The development of the internal combustion engine has gone through several key stages since its inception. Initially reliability was the overriding concern in engine design, with power and then fuel economy being the next most important considerations. However in recent years due to legislation and customer perception, a major concern for engine designers has been the emissions generated by the engine's operation.

Both the SI and CI engine strategies have been constantly developed throughout the 20th century, with each engine gaining control over different market sectors. The CI engine strategy tended to be used in much larger vehicles, where its high torque and low relative speed characteristics were most suitable. The SI engine strategy tended to be used predominately in passenger vehicles, where their larger speed range and quieter operation were preferred.

2.1.1 Kyoto Protocol

For a long time environmental groups have expressed concerns over the effect of fossil fuel burning on the environment. Various claims have been made concerning the effect of burning fuel for power generation and transportation. The most popular and widely accepted theories are the greenhouse effect and global warming.

Figure 2.1 describes the so-called greenhouse effect and the role that "Greenhouse Gases" play in the global warming process.

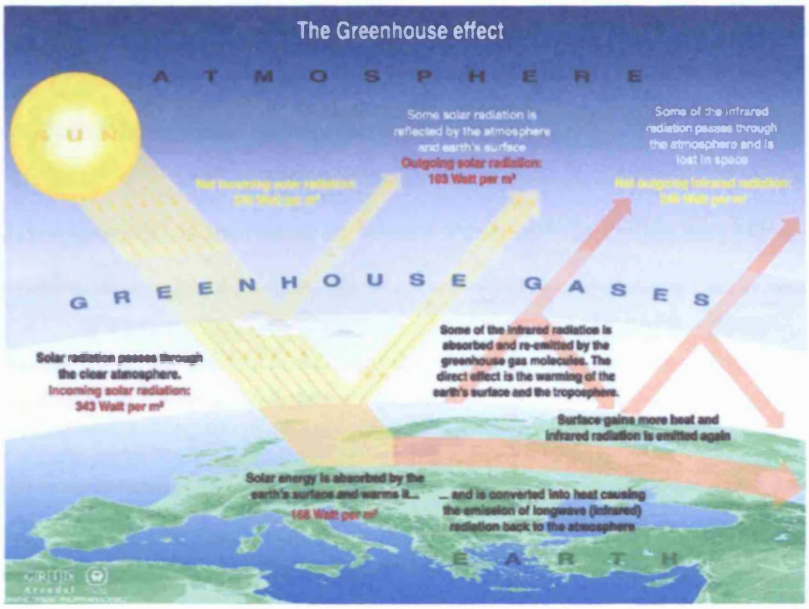

Figure 2.1 – The greenhouse effect

United Nations Framework Convention on Climate Change

Greenhouse Gases are a layer of gases in the upper atmosphere that delay the escape of reflected solar radiation from the earth's surface. Human activities are enhancing the greenhouse effect by increasing the thickness of the greenhouse gas layer; identified gases that supplement the greenhouse gas layer are Carbon Dioxide (CO_2), Methane (CH_4), Nitrous Oxide (N_2O), Hydrofluorocarbons, Perfluorocarbons, Sulphur Hexafluoride and to a certain extent Hydrogen.

In response to international concerns over such environmental issues as the greenhouse effect an international group was founded, the United Nations Framework Convention on Climate Change (UNFCCC). The UNFCCC acknowledged that a change in the Earth's climate and any adverse affects are a common concern of humankind. In addition to the UNFCCC agreement, a series of more detailed legally binding commitments for the reduction of greenhouse-gas emissions were established and are detailed in the 1997 Kyoto Protocol. The countries that have signed up to the Kyoto Protocol (adopted 11th December 1997) have pledged to reduce their greenhouse-gas emissions by at least 5% from their 1990 levels in the commitment period 2008-2012.

Table 2.1 details the emissions targets set out in Annex B of the Kyoto Protocol. The Kyoto Protocol entered into force on 16th February 2005. In an unpopular move the United States indicated its intention not to ratify the Kyoto Protocol. Together with rules brought in such as emissions trading, this has made the overall effectiveness of the agreement questionable to environmentalist groups.

Table 2.1 – Countries included in Kyoto Protocol and their emission targets

COUNTRY	TARGET (1990* - 2008-2012)
EU-15, Bulgaria, Czech Republic, Estonia, Latvia, Liechtenstein, Lithuania, Monaco, Romania, Slovakia, Slovenia, Switzerland	-8%
US	-7%
Canada, Hungary, Japan, Poland	-6%
Croatia	-5%
New Zealand, Russian federation, Ukraine	0
Norway	+1%
Australia	+8%
Iceland	+10%

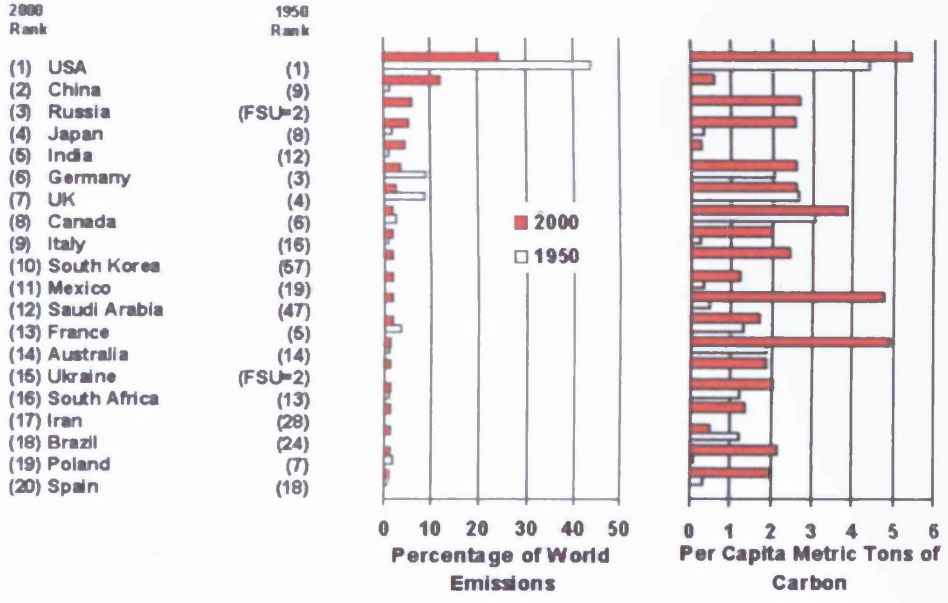

Figure 2.2 – Top 20 countries by total CO_2 emissions (2000)

Figure 2.2 displays the top 20 countries by CO_2 emissions as summarised by Marland and Boden (2001). It can be seen that the USA produces a significant proportion of the total CO_2 that is emitted worldwide.Countries that can be described as "developing" (such as China and India) are rapidly themselves becoming large scale polluters, and it is predicted that by the year 2010 that China will become the largest emitter of CO_2 (CDIAC 2006).

Figure 2.3 displays the growth in total CO_2 emissions, in thousands of tons of carbon, for the top twenty producing countries. It can be seen that the industrialised countries have been producing significant amounts of CO_2 since the early parts of the 20th century, with the USA being the major producer since 1880. It is also worthwhile noting that many European countries have substantially slowed the growth in their CO_2 production; whereas the developing countries and the USA are still rapidly increasing the amount of CO_2 they produce each year.

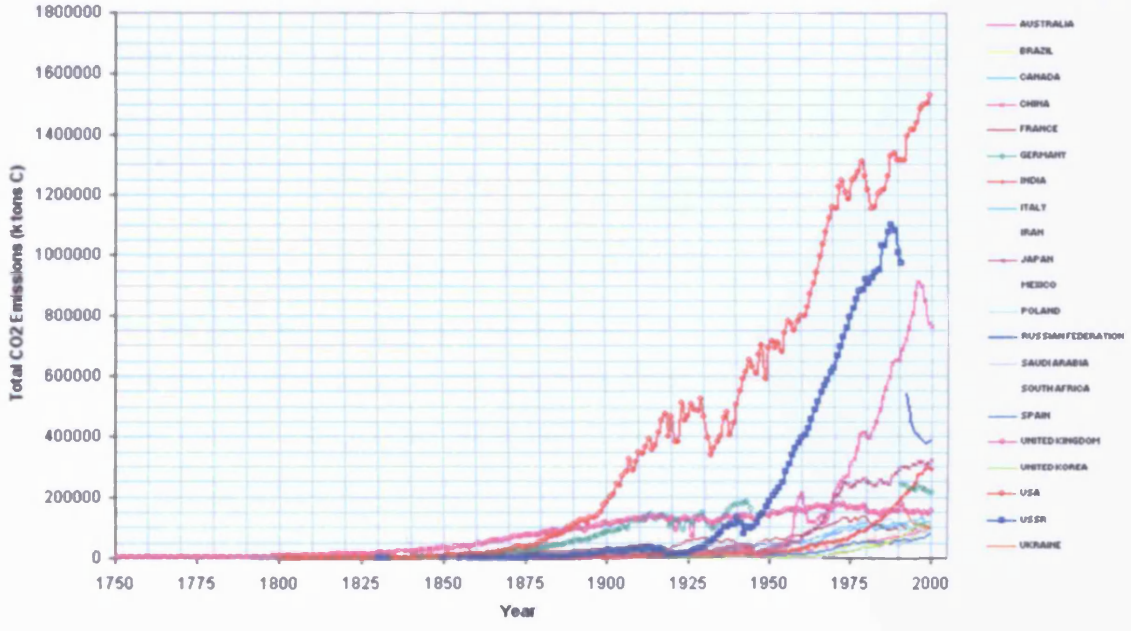

Figure 2.3 – Total CO_2 emissions for top 20 producing countries
[CDIAC, Marland et al (2005)]

A closer examination of the growth of CO_2 emissions in the UK by source is shown in Figure 2.4; with the CO_2 emissions being separated out into that produced by solid, liquid and gaseous fuels.

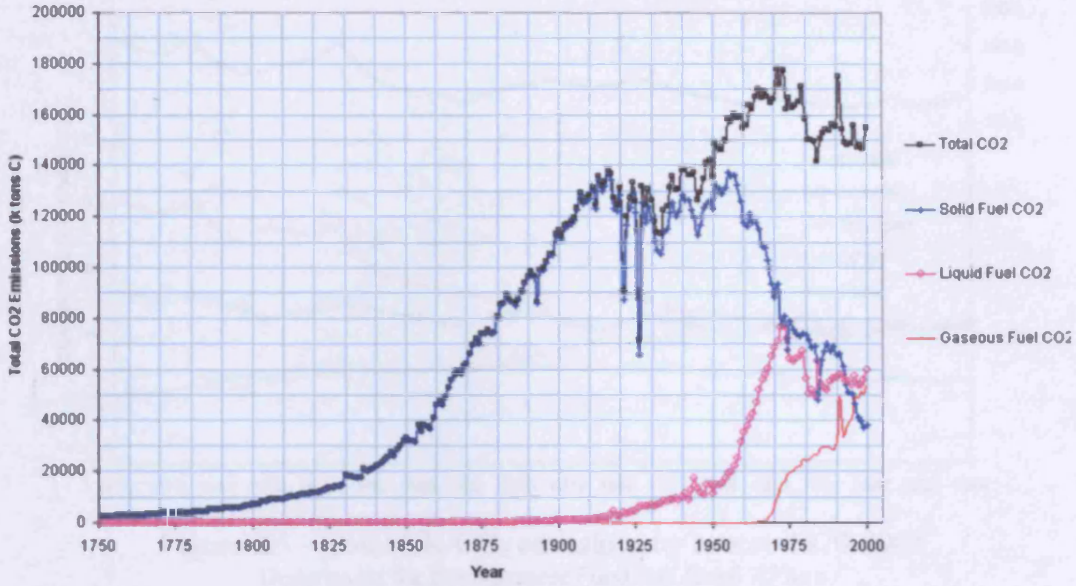

Figure 2.4 – Total UK CO_2 emissions by fuel type
[CDIAC, Marland et al (2005)]

It can be seen that up until the year 1900, the majority of the UK's CO_2 emissions were due to the combustion of solid fuels, primarily coal. After 1910 liquid fuels, mainly derived from crude oil, began to have an increasingly important contribution to the total CO_2 emission levels. From 1970 onwards it can be seen that solid fuels had been superseded by the combination of liquid and gaseous fuels.

The Kyoto Protocol defined key emission targets for the European Union as a whole, and in turn for each of its member states. In order to meet the levels specified by the Kyoto Protocol, the European Union specified emission targets for each of its member states. These emission targets are so stringent that widespread changes are required in all areas of energy utilization. Each of the countries that signed up to the Kyoto Protocol has had to decide upon their own legislation in order to achieve their specified emission levels. To achieve this each of the sources of the emissions must be separately controlled.

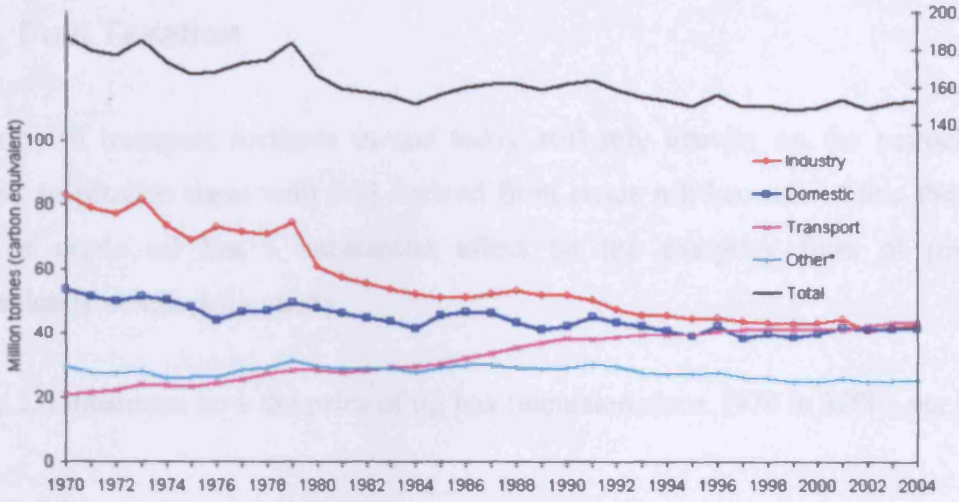

Figure 2.5 – Total UK CO_2 emissions by source 1970-2004
Department for Environment Food and Rural Affairs

It can be seen from Figure 2.5 that even though there has been a reduction in total CO_2 emissions since 1970, the proportion of the total CO_2 emissions caused by road transport has increased. This can easily be explained when it is considered that data on transport trends (Department of Transport 2005) state that between 1980 and 2004 the total traffic on British roads grew by 81% and in the same period the total number of licensed vehicles grew by 68%.

In order to reduce the CO_2 emissions from the European vehicle population several measures have been undertaken by both the European Union as a whole and by its member states. The most significant of these measures has been the imposition of emission targets for new vehicles.

As a result of the Kyoto protocol agreement the UK government pledged to reduce the emissions of greenhouse gases to 80% of the 1990 levels. This is an ambitious target, which is 12% lower than that required by the Kyoto protocol. In order to accomplish this reduction the UK governments strategy was to encourage both companies and individuals to "think greener" by adopting a policy of taxing the polluter.

2.1.2 Fuel Taxation

Virtually all transport methods in use today still rely heavily on the petrochemical industry to provide them with fuel derived from crude oil; because of this the trading price of crude oil has a substantial affect on the everyday lives of people in economically developed nations.

Figure 2.6 illustrates how the price of oil has fluctuated since 1970 in $2005 per barrel.

Figure 2.6 – Major events and real world oil prices 1970 – 2005

Energy Information Administration, DOE

It can be seen from Figure 2.6 that the price of oil is heavily dependent on world events. The high oil prices between 1974 and 1986 caused a substantial investment by engine manufacturers in order to improve the fuel economy of their product. The advent of technologies such as the electronic Engine Control Unit (ECU) and the replacement of carburettors with injectors as the means of delivering fuel were all driven by the goal of improving fuel economy.

The taxation of fuel has proven itself to be a controversial method of controlling the populations driving habits. Figures 2.7 and 2.8 show data published by Smith (2000)

and also by Leicester (2005), in which the average UK pump price of unleaded petrol and diesel fuel is broken-down into the pre-tax price, fuel duty and Value Added Tax (VAT). Current UK duties on road fuels are 48.32 pence per litre for low sulphur petrol and diesel, 20.0 pence per litre for biodiesel and bioethanol, 12.7 pence per litre for liquefied petroleum gas, 10.8 pence per litre for natural gas derived road fuels and 6.44 pence per litre for red diesel. In the 2006 UK budget (Her Majesty's Treasury 2006), the Chancellor of the Exchequer announced that the annual inline with inflation rises in fuel duty would be postponed to 1st September 2006 because of continuing volatility in worldwide oil prices.

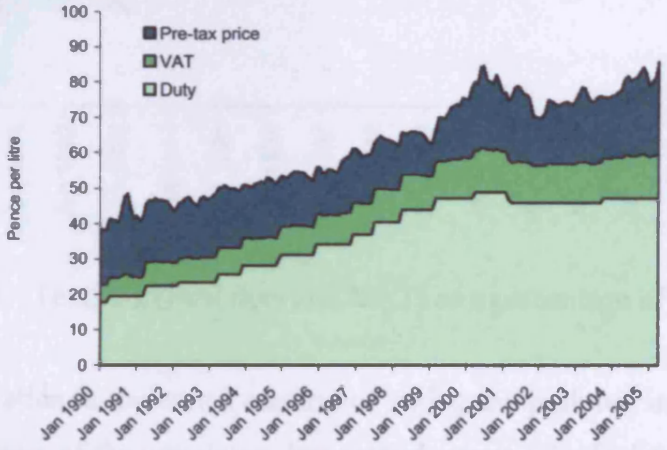

Figure 2.7 – Components of the pump price of unleaded petrol

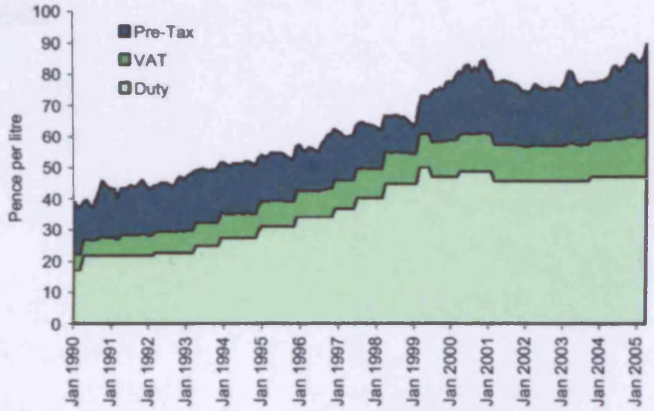

Figure 2.8 – Components of the pump price of diesel fuel

Reports from the Institute for Fiscal Studies (Smith 2000 and Leicester 2005) compared the combined tax rate of unleaded and diesel fuel to that of other EU member states. For unleaded petrol the UK has the highest combined tax rate of any EU member state. The

combined VAT and fuel duty for the period at the beginning of 2006 corresponds to about 70% of the total pump price; this is substantially lower than the period during 1999 when the VAT and fuel duty represented over 85% of the total pump price (See Figure 2.9 which shows the total tax as a percentage of fuel price).

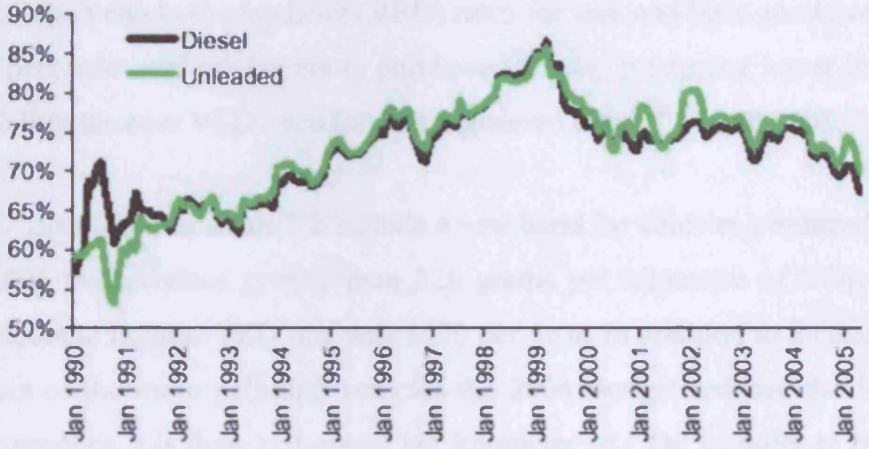

Figure 2.9 – Total tax (Fuel duty and VAT) as a percentage of pump prices

Whereas fuel taxation is the surest method of taxing the polluter, its increasing impact on the poorer sectors of the population has caused unrest. The fuel protests at the end of 2000 highlighted how increased taxation levels are an unpopular method of modifying peoples driving habits.

2.1.3 Other Methods of Controlling Vehicle Emissions

The British government has introduced several policies intended to alter the publics driving habits and persuade them to use alternate transport methods to their cars. Recent changes announced in the UK 2006 Budget (Her Majesty's Treasury 2006) have reassessed the Vehicle Excise Duty (VED) rates for cars and light goods vehicles, in an effort to persuade new car buyers to purchase vehicles producing lower levels of CO_2. Table 2.2 lists the new VED rates for cars registered after 1st March 2001.

The VED rates listed in Table 2.2 include a new band for vehicles produced after 23rd of March 2006 that produce greater than 226 grams per kilometre of CO_2. Prior to the 2006 budget the highest VED rate was £170 per year. In addition to increasing the cost for owners of the more polluting vehicles the 2006 Budget reduced the VED rate for cars that produce less than 120 grams per kilometre of CO_2, in order to persuade new car buyers to consider smaller, less polluting vehicles.

Table 2.2 – VED bands and rates for cars registered after 1st March 2001

VED Band	CO_2 Emissions (g/km)	VED Rate (£ per year)		
		Alternate Fuels	Petrol	Diesel
A	100 and below	0	0	0
B	101 to 120	30	40	50
C	121 to 150	90	100	110
D	151 to 165	115	125	135
E	166 to 185	140	150	160
F	186 and above[1]	180	190	195
G	226 and above[2]	200	210	215

[1] Cars registered before 23rd March 2006 [2] Cars registered after 23rd March 2006.

In addition to fuel taxation and vehicle taxation, various other schemes and initiatives have been introduced in order to reduce vehicle pollution in urban centres. One of the most controversial was the introduction of the London Congestion Charge in February of 2003 (Transport for London, 2004).

The London congestion charge zone is a large area of central London (see Figure 2.10) which prior to 2003 was a notorious area of traffic congestion and disruption. Throughout the area in which the congestion charges are enforced are number plate recognition cameras, which automatically record the registration number of any vehicle which enters the zone. Drivers of vehicles which are not exempt from the congestion charge can pay the £5 fee by a number of methods including telephone, the internet or over the counter at certain retailers within the zone. Drivers that have been proven to have entered the zone and have not paid the charge are issued with a fixed penalty notice and prosecuted.

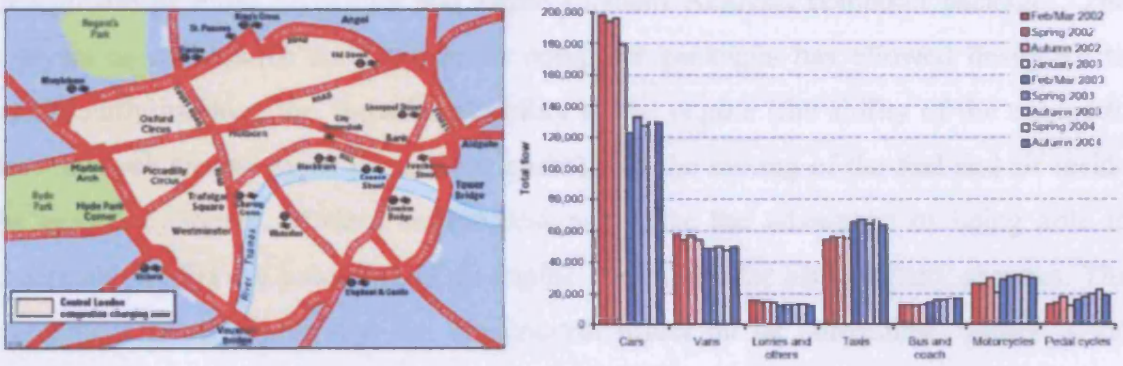

Figure 2.10 – London congestion charge area and effect on vehicle traffic

Although many opposed the implementation of the London congestion charge, data published by Transport for London (2005) has shown remarkable changes in commuter behaviour (see Figure 2.10). Car traffic into and out of the zone has seen a reduction of over 33%, while the amount of private hire vehicles and coach traffic has increased by 17% and 22% respectively. The introduction of the London congestion charge, has in a short period of time, reduced the pollution levels caused by vehicle traffic in the central London area while having no marked detrimental effect on local economy.

2.2 Engine Technology Development

There have been many advances made in the last century to the Internal Combustion engine. While the majority of these developments have been applicable to all engines, some are specific to either the SI petrol engines or the CI Diesel engines.

2.2.1 General Improvements

Many of the advances made in Internal Combustion engine design are through improvements in manufacturing techniques and the understanding of the basic principles in engine operation. In addition to this, the increased understanding of material technology and friction has also improved engine reliability.

Engine designers today have not only a greater understanding of the processes that occur within an engine, but also have access to advanced design tools such as Computational Fluid Dynamics and Finite Element Analysis computer packages. The analysis capabilities of fluid dynamics computer packages has allowed designers to significantly improve the "breathing" ability of the engine (the ability of the engine to draw in fresh air and expel the exhaust gases), and the mixing of the fuel and air inside the engine cylinders. Modern engine designers have the advantage of being able to accurately predict the behaviour of an engine and model the effect of any changes. The component of an engine that has the greatest effect on its "breathing" ability is the valve-train. The first multi-valve engine (more than one inlet and exhaust valve per cylinder) is believed to be that of a Peugeot GP racing car in 1912, however the earliest production car to use a multi-valve engine was the Honda s600 introduced in the 1960's. By the 1990's multi-valve engines had become mainstream.

Using basic CFD packages modern engines can be optimised for their operating conditions, this involves the "tuning" of the valves' opening and closing times as well as the choosing of optimum dimensions of inlet plenums, runners and exhaust manifolds. More complex CFD packages are used in the design of the combustion chamber; by precisely shaping the piston crown and the area around the valves a more

controlled and complete combustion process can be obtained, increasing the efficiency of the engine.

More advanced materials are now routinely used in modern engine manufacturing. Most modern engines utilise aluminium cylinder heads, mainly for its better cooling properties over steel/cast iron but also for its weight reduction. Many modern engines are now constructed with all aluminium cylinder blocks to reduce weight even further, helping to increase the fuel economy of the vehicle by weight reduction (also improving vehicle handling due to a more even weight distribution. Other more exotic materials such as titanium are now becoming popular for their high strength to weight ratio.

2.2.2. Petrol Specific Technology Advances

There are several key areas where technological advances have improved the efficiency and reduced the emissions of SI internal combustion engines.

Variable Valve Timing

Variable Valve Timing (VVT) in conjunction with Electronic Fuel Injection (EFI), all controlled by sophisticated Engine Control Units (ECUs) allows the accurate control and variation of engine fuelling and breathing at all engine speeds. To optimise the breathing, engines require different valve timings at different engine speeds and loads. There are several different VVT strategies employed by modern manufactures, ranging from the simple cam-changing VVT to the more complex Variable Valve Control system.

Honda was the first vehicle manufacturer to produce engines incorporating a VVT system in the late 1980's. The Honda VTEC (Valve Timing Electronic Control) first appeared in the Honda Civic and then became standard in most Honda vehicle models. The Honda VTEC system incorporates either two or three sets of cam lobes of different shapes, enabling different valve timings and lifts. Basic cam-changing VVT systems of this type that do not allow continuous adjustment of valve timings are said to be discrete

in nature. The changing over between cam profiles is noticeable to the driver and some perceive this as the weakness of discrete cam-changing VVT systems, although their simplicity compared to most other VVT systems provides a benefit of remarkable reliability.

The VVT system introduced by Rover in its MGF in 1995 is regarded by many as the most advanced form of variable valve control used in a production vehicle to date. The Rover Variable Valve Control (VVC) unlike most other VVT systems allows for continual variation in valve open/closure timing, as well as a continual variation in the duration of the time the valves are open. The VVC system drives the camshaft operating two adjacent cylinders by a pulley connected with a varying degree of eccentricity, allowing a controlled amount of non-linear rotation of the camshaft which changes its duration and phase. The VVC system is likely to eventually be taken up by other vehicle manufacturers as an alternative to cam-changing VVT systems.

VVT systems have a proven ability to improve fuel economy, increase peak torque and power while reducing NO_X emissions when compared to conventional engines. The development of VVT systems is continuing with much current research being in the area of electronic control such as that demonstrated by Nagaya et al (2006). The future of variable valve timing however is more likely to involve electromagnetic valve systems such as that developed by Lotus for the Hotfire project (Stansfield 2005).

Variable Intake / Exhaust Manifold

Many automotive vehicle manufacturers have developed variable intake or exhaust manifold systems in order to improve the performance of their engines at higher engine speeds; while also improving the fuel economy, the driveability and reducing the emissions at lower engine speeds. Variable intake and exhaust systems are likely to become more common in the medium to high end automotive market sectors, such as executive saloons and sports cars. It is unlikely that such systems will become common place in family cars due to cost issues, but there is some potential for variable intake and exhaust systems to be used in heavy duty diesel applications.

Variable Compression Ratio

Even though single cylinder Variable Compression Ratio engines are widely available for use in research from manufacturers such as Ricardo, there has been very little development work done to produce a suitable commercial engine for mass automotive use. The car manufacturer Saab presented details of its Saab Variable Compression (SVC) concept at the 2000 Geneva motor show.

The SVC concept uses a combined cylinder head and engine block which can be moved relative to the crank position by the use of a hydraulic actuator, thus altering the compressed volume of the combustion chamber and therefore compression ratio of the engine. The SVC engine utilises an ultra high boost supercharger (2.8 bar) and can vary its compression ratio between 8:1 and 14:1. Prototype SVC engines have returned powers of 150hp per litre while having 30% lower fuel consumptions when compared to conventional engine designs. The SVC series of engines are expected to meet all foreseeable emission regulations while also being suitable for many grades of fuel, with the engine management system always selecting the most appropriate compression ratio.

Variable Compression Ratio engines have huge potential, but like many new technologies the cost of such systems prohibits the extent to which they can penetrate the market.

Direct Injection Petrol Engines

Direct injection petrol engines have been developed by many modern engine manufacturers to take advantage of the increase in engine efficiency and the reduction in emissions that a lean burn engine provides. The current leader in direct injection engine technology is Mitsubishi, with their Gasoline Direct Injection (GDI) concept. Mitsubishi claim that their GDI engines develop 10% more power than conventional engines while consuming 20% less fuel and generating 20% less CO_2 emissions. Direct fuel injection is a recent development in petrol engines, but has been used in diesel

engines for many years. The main advantage of direct fuel injection ts that the injection of the fuel at high pressure directly into the combustion chamber moments before the spark plugs fire, allows the precise control of the stratified charge required for engines to operate with lean air / fuel mixtures. In addition to the utilisation of the lean-burn concept, direct injection engines do not require a throttle system and therefore benefit from a reduction in pumping losses.

Zhao et al (1999) contrasted the Mitsubishi GDI concept with that of other manufacturers; several problems were highlighted with the Mitsubishi concept, including that of reliability due to the increased complexity of GDI systems. One of the more significant factors affecting the performance of direct injection systems is the characteristics of the fuels. Unleaded petrol in Japan has a significantly lower sulphur content than that presently used in Europe, which allows for the use of a special catalyst to clean the excessive NO_X generated under ultra-lean combustion conditions. The direct injection petrol engine developed by Renault utilises high levels of Exhaust Gas Recirculation (EGR) instead of ultra lean air / fuel mixtures at part load conditions, which has been shown to reduce the particulate and NO_X emissions without the use of a special catalyst (Sasaki et al 1998).

The optimisation of the GDI concept is continuing, with much current research concerning the analysis and simulation (Lee et al. 2004 and Rotondi & Bella 2006) of the mixture preparation within the engine cylinder prior to combustion. Drake et al. (2005) have shown that even though a certain amount of air-flow swirl within the cylinder is required, too much swirl leads to undesirable mixture preparation and combustion characteristics, causing areas of localised rich combustion. Kano et al. (1999) also found that the control of swirl within the cylinder is important to ensure the air-fuel mixture is correctly directed towards the spark plug, with the interval between injection and ignition being a crucial parameter for controlled combustion. It has also been found by Stojkovic et al. (2005) that the actual act of injecting directly onto the piston surface is the principle cause of PM emissions from GDI engines, due to the thin fuel films developing into pool fires. The future use of GDI systems is expected to increase due to their many benefits for only a small additional cost.

Miller Cycle Engine

The Miller cycle is a concept patented by the American Ralph Miller in the 1940's and has been used in many different engines since its creation. The only engine in widespread production that employs the Miller cycle today is manufactured by Mazda. In the Mazda Miller cycle engine the inlet valves close 47 degrees after BDC, which means the inlet valves stay open for approximately 20% of the compression stroke. The late closure of the inlet valves effectively reduces the compression ratio of the engine, reducing the energy loss in compressing the air and reducing the peak cylinder temperature. The use of a supercharger compensates for the reduction in compression of the engine. Hatamura et al. (1997) proved that the use of a supercharger allows for an increase in power output of an engine operating under the Miller cycle without sacrificing reliability.

The Miller cycle engine developed by Mazda burns 13% less fuel than the 3 litre V6 engine it is based upon, while also generating slightly more power. However, while the engine is marketed as a 2.3 litre it effectively costs more and is larger than the 3 litre engine, due to the added costs of superchargers and intercoolers. A study into Miller cycle operation carried out by Wu et al. (2003) concluded that the Miller cycle has no inherent potential for improving efficiency, but its use in conjunction with a supercharger can be used to increase the power output of an engine while reducing the risk of pre-ignition, and reducing emissions. By contrast a numerical study carried out by Ge et al. (2005) concluded that the Miller cycle effect allowed for the use of a higher compression ratio while providing an increase in efficiency and power.

The use of advanced engine cycles such as the Miller cycle is an area with huge potential for future engine development. Current Miller cycle engine systems have suffered from additional weight penalties and inflexibility. If these drawbacks can be overcome whilst minimising cost, the use of advanced engine cycles could be exploited across all automotive market sectors, particularly in heavy duty applications.

Exhaust Gas Treatment

The treatment of an engines exhaust gases to reduce the emission content is an increasingly important method used by engine manufacturers to meet the stringent legislation. The recirculation of exhaust gas back into the combustion chamber is a proven method of reducing an engine's fuel consumption and emission's. EGR works by recirculating up to 10% of the exhaust gas back into the cylinder via a recirculation valve controlled by the ECU; which effectively reduces the engine's displacement and pumping losses.

The focus of current emission legislation is the reduction in the Non-Methane Volatile Organic Compounds (NMVOCs) content of exhaust gases, which include organic compounds such as aldehydes, alcohols, alkanes, aromatics and esters. Honda is leading the way in the reduction of NMVOC by developing multi-catalyst arrangements which include a high temperature high-efficiency catalyst close to the exhaust port as well as an electrically pre-heated hydro-carbon absorbing catalyst further along the exhaust system.

Heck and Farrauto (2001) reviewed the development of exhaust catalyst systems; highlighting the developments that have been made in the 30 years since their introduction. The main problems encountered in developing advanced catalyst systems are coping with the many diverse operating regimes that modern engines encounter in day-to-day operation. Modern developments in exhaust gas treatment are concerned with multiple catalytic converters systems with three-way honeycomb catalysts being used in conjunction with NO_X reduction techniques and regenerative particulate traps. A major problem in exhaust gas treatment development is improving the tolerance of the catalyst metals to the sulphur content of the exhaust gases. This has been shown by Matsumoto et al. (2000) to be relatively straightforward to control for the ultra low sulphur fuels used in Japan, but more difficult for the fuels of other countries. The use of catalytic converters in modern vehicle design is no longer an option but a necessity, and the continued development of such systems is a priority in order to attain future emission targets.

2.2.3 Diesel Specific Technology Advances

Within Europe the share of the new car market taken up by diesels has been increasing, as consumers take advantage of the improvement in fuel economy diesel vehicles offer over petrol. One possible reason why even more diesel vehicles are not sold is the perception of diesel vehicles being "dirty" due to the excessive amount of particulate matter in their exhausts.

Diesel Fuel Systems

As Diesel engines operate under compression ignition, with combustion occurring under a certain pressure and temperature combination during the compression stoke, Diesel engines inherently use much higher compression ratios than spark ignition petrol engines (in the region of 22:1 if naturally aspirated). The absence of any ignition system in addition to the absence of a throttle system means that a Diesel engine is controlled only by the amount of fuel injected, therefore the design of the injection system is critical to the efficient operation of a Diesel engine.

Indirect injection fuel systems refer to that where the fuel is not injected into the cylinder of the engine. Instead fuel in an indirect injection diesel engine is injected into a small chamber (known as a pre-chamber), which is separate from the main combustion chamber. Combustion begins in the pre-chamber and spreads into the main chamber assisted by turbulence. Nearly all indirect injection diesel engines require the use of a glow plug to act as a cold start device. Indirect injection engines are cheap and comparatively easy to build, providing smooth quiet running. Indirect injection diesel engines are still common in applications with less stringent emission controls and are still also used in some road-going vehicles.

In direct injection fuel systems the fuel is injected directly into the cylinder of the engine at a relatively high pressure when compared to indirect injection systems.

European car manufacturers have invested heavily in the development of diesel injection technology. Common rail fuel systems are the latest innovation in diesel fuel injection systems and were developed during the 1990's, improving both the fuel economy and the emissions of diesel powered vehicles. Common rail direct injection fuel systems involve the use of a high pressure fuel pump to pressurize a common rigid pipe connected to the injector of each engine cylinder; with the diesel fuel being pressurized to over 1800 bar within the fuel rail. Solenoid or piezo type valve injectors are used then to inject the fuel into the cylinder, with the high fuel pressure guaranteeing good atomisation and mixing.

The benefit of the ultra high injection pressures used in common rail diesel engines is that the injection durations are much lower, and the atomisation of the diesel fuel is significantly improved. Common rail diesel engines utilise ECU's to control the injectors, monitoring the injection duration and injection timing precisely. In order to reduce engine noise, common rail engines often utilise a small pilot injection prior to the main injection to reduce the severity of the main combustion event. Some of the more advanced common rail fuel systems can perform as many as five injections per stroke.

Nearly all European and many Japanese manufacturers now utilise common rail direct injection techniques in their diesel engines. The injection technology used in common rail systems is continuing to develop, with injection pressures being increased further to improve fuel atomisation, producing finer fuel sprays allowing for more complete combustion and a reduction in PM generation.

Diesel Particulate Filters

If the recent trends in emission legislation carry-on at their present rate, Particulate Filters will become a necessity in all new diesel vehicles to reduce the emission of particulates to satisfactory levels.

Durán et al. (2004) investigated the simulation of diesel particulate matter while Figler et al. (1996), Kim et al. (2005) and Harris et al. (2001) have all carried out experimental analysis of diesel particulates. The researchers found that diesel particulates are mainly composed of volatile and non-volatile particles, and that the formation of the volatile particulates (generally less than 50nm in size) is attributed to the cooling of hydrocarbon and sulphur compounds in the exhaust, while the non-volatile particulates (normally between 50nm and 100nm in size) are formed during the early stages of combustion. The sizes of the particulates depend on the processes involved in the particulate formation and the location from which they are sampled.

Particulate traps have been successfully applied to a number of diesel engine equipped applications such as city buses and fork lift trucks, but due to large size and power requirements no system has as yet been applied to light commercial vehicles or cars. Particulate traps work by collecting the particulate matter in the exhaust gases and then regenerating by oxidizing (burning off) the collected particulate. The most common problems with particulate trap systems are:

- The increase in exhaust back pressure as the trap becomes clogged, prior to the regeneration cycle, reduces the efficiency of the engine.
- During the particulate trap regeneration the fuel consumption of the engine increases, this is due to most particulate traps requiring exhaust gas temperatures in excess of 500°C (normally only achieved at higher engine loads) to oxidize the soot.

Stamatelos (1997) predicted that the installation of a particulate trap increases the fuel consumption of the vehicle by up to 5%. However, Durbin et al. (2003) showed that the

use of a particulate trap in conjunction with an ultra low sulphur diesel can reduce the PM generated by up to 98%. Currently, more advanced particulate filters are being developed which include internal heater systems. The benefit of such systems is that fuel consumption would not increase as the special regeneration cycles would not be required. Such self-regenerative systems have shown trapping efficiencies greater than 80% (Kojima et al. 1999).

Diesel Oxidation Catalysts

Oxidation catalytic converters work by oxidizing the hydrocarbons (both the soluble organic fraction {SOF} due to unburned fuel and lubricating oil and the carbon/soot {HC} combustion products) and the carbon monoxide content of the exhaust gases. Oxidation catalysts normally consist of a ceramic monolith covered in a precious metal catalyst material. As the exhaust gases pass by the catalyst the following reactions take place:

$$SOF + O_2 \rightarrow CO_2 + H_2O \quad (2\text{-}1)$$

$$HC + O_2 \rightarrow CO_2 + H_2O \quad (2\text{-}2)$$

$$CO + O_2 \rightarrow CO_2 \quad (2\text{-}3)$$

Diesel engines operate under lean combustion conditions and therefore have a much lower exhaust gas temperature than modern gasoline engines. Hence the catalyst material chosen must operate at lower temperatures than its gasoline equivalent, and be capable of oxidizing condensed hydrocarbon liquids as well as gaseous combustion products. The traditionally high sulphur content of diesel fuels throughout Europe has caused problems with selecting suitable catalyst materials due to the reaction shown in equation 2-4, which leads to the formation of sulphuric acid which poisons traditional catalyst materials.

$$SO_2 + O_2 \rightarrow SO_3 \quad (2\text{-}4)$$

A review of the effectiveness of oxidation catalysts as well as their effect on engine operation was carried out by the Cummins engine company (Clerc 1996); the conclusions of which highlighted the difficultly in catalyst selection and sizing for the wide range of operating conditions required.

2.3 Fuel Technology

The fuels used in internal combustion engines continue to change and develop as new legislation is announced, and new fuel treatments are discovered. Although some alternative fuels can be used without any modifications to the standard petrol or diesel engine, other alternative fuels do require modifications to both a vehicle's engine and fuel system, and this can prove to be costly.

When considering alternative fuels for internal combustion engines, many factors must be considered including the actual fuel cost, the extra costs involved in equipping the vehicles for use of that fuel and the costs to the environment through pollution (e.g. CO_2, VOCs, PM and NO_X). Johansson (1999) found that alternative fuels can be competitive with petrol and diesel when the impact on the environment of emissions is considered. In cities with an established natural gas network for example, natural gas has cost benefits over both diesel and petrol as a fuel. Masumoto et al. (1997) carried out a study of alternative fuels for passenger cars by CO_2 fixation, which involved the appraisal of vehicles powered by methanol, compressed natural gas, electricity, hydrogen, and hybrid technology. This study concluded that compressed natural gas offered the potential for lowest CO_2 emissions.

2.3.1 Petrol and Diesel Fuels

Section 1.2 describes the current specifications of diesel and petrol fuels available in the UK. Both petrol and diesel fuels are obtained by the fractional distillation of crude oil and can differ substantially batch-to-batch due to changes in the source of the crude oil, the refinery equipment used and the grade of fuel that is being made.

Fossil fuel derived fuels such as petrol and diesel are seen as one of the largest contributors to the increase in atmospheric CO_2, as the combustion of such fuels releases into the atmosphere carbon that has been "locked away" for millions of years. It is likely that to reduce this effect the use of "carbon neutral" substitutes such as bio-ethanol and biodiesel will increase over time.

For diesel fuel the use of higher pressure multiple injection techniques as well as the addition of oxygenates such as long chain esters and ethers, has shown to substantially reduce soot emissions with little effect on NO_X formation at high engine loads (Ali et al. 1995, Choi and Reitz 1999). Lin and Wang (2004) investigated the use of two and three stage diesel emulsions as an alternative to regular diesel fuel. Diesel emulsions were shown to have significantly lower NO_X and smoke emissions, but had the drawback in increasing the emissions of CO and CO_2. Many other fuel additives have been developed which can substantially reduce the PM emissions of diesel powered vehicles. Burtscher et al. (1999) investigated the effect of Cerium compound additives in diesel fuel, showing that only a small concentration were required to substantially reduce the PM emissions.

Common petrol additives used today include ethanol and methyl tert-butyl ether (MTBE). Song et al. (2006) compared the effects of both additives on the exhaust emissions, showing that the use of the MTBE additive reduces the emission of benzene and improves the efficiency of an exhaust catalyst. The effects of the addition of ethanol to petrol are well documented; with Hsieh et al. (2002) and Topgül et al. (in press, 2006) both demonstrating the reduction in CO and hydrocarbon emissions induced by the blending of ethanol with petrol.

Both petrol and diesel fuel will carry on being the main transport fuels in the short to medium term. However, future emission legislation will force the petrochemical companies to improve the fuels; this is likely to be done by using more complex refining techniques (such as that used to lower the concentration of sulphur) as well as the use of fuel additives.

2.3.2 Bioethanol

Bioethanol is ethanol obtained from the fermentation of carbohydrates in the form of starches, sugars and cellulose derived from harvested plant material. Ethanol (C_2H_5OH) is a proven fuel for spark ignition engines; even before the oil crises of the 1970's, many vehicles were being manufactured that could be configured to run on alcohols (the Ford model T was designed by Henry Ford so that it could be fuelled by petrol, ethanol or any mixture of the two). However, after the rapid price rises of crude petroleum throughout the 1970's many countries began to take more seriously the possibilities of biomass derived fuels as an alternative. The most publicised biomass project is the "Proalcohol" project of Brazil, which now produces billions of gallons of ethanol annually for use as a transport fuel (Lee 1996).

Ethanol has been heavily researched as an additive to petrol with Jia et al. (2005), Wu et al. (2004), and Ceviz et al. (2005), all presenting the benefits of ethanol and petrol blends. The use of ethanol-petrol blends as a fuel leads to significant reductions in both hydrocarbon and CO emissions, but at the same time an increase in CO_2 has been reported. The increase in the volume of CO_2 emissions however is counteracted by the fact that the CO_2 per unit horsepower is less for the ethanol-petrol blends than for the pure petrol fuel. However it was shown that there is little difference in the emissions of NO_X and aromatics between the ethanol-petrol blends and 100% petrol. It was also shown that a 10% ethanol blend with 90% unleaded petrol had the optimum overall performance and emission characteristics.

As well as biomass-derived oils and their derivatives showing improvements in emissions when used in compression emission engines, the addition of ethanol to standard diesel fuel has been shown (Lu et al. 2005) to have beneficial effects on NO_X, CO and smoke emissions. Hansen et al. (2005) reviewed the blend properties of ethanol-diesel mixtures, showing that with increasing concentrations of ethanol in diesel, the specific fuel consumption increases due to a reduction in energy content. Substantial reductions in particulate matter have been observed with ethanol-diesel blends, but potential safety and durability concerns were also noted due to the changes

in fuel properties associated with the addition of ethanol. A reduction in particulate matter emissions was also observed in experiments carried out by Shi et al. (2006) in which a blend of ethanol, diesel and biodiesel was tested, although in this case no similar reduction in CO emissions were observed.

The use of biomass-derived ethanol as an additive for both traditional petrol and diesel is expected to increase in the future. The increased CO_2 associated with the addition of ethanol is offset by its "carbon neutral" properties; while the reduction in other pollutants will help future vehicles meet ever new stringent emission targets.

2.3.3 Biodiesel

Rudolph Diesel saw biomass derived fuels as the future of his engine and as such chose to run his demonstration engine on peanut oil. He was also quoted between 1911 and 1912 as saying "The use of vegetable oils for engine fuels may seem insignificant today. But such oils may become in course of time as important as petroleum and the coal tar products of the present time", and "The diesel engine can be fed with vegetable oils and would help considerably in the development of the agriculture of the countries which use it."

Vegetable oil based fuels have been shown to have very promising benefits as an alternative to crude oil-derived diesel fuels. Vegetable oils such as sunflower, cottonseed, soybean and rapeseed oil have all shown reductions in power output, CO_2 and NO_X emissions compared to diesel fuel, whilst also showing an increase in CO, smoke and fuel consumption. The high fuel density and viscosity, as well as factors such as chemical stability and lower cetane numbers currently make raw vegetable oils unsuitable for widespread use in internal combustion engines, although with some modifications to the engine and optimization of fuel delivery systems their performance can be substantially improved. However, it has been shown by Kumar et al. (2003) that the performance of a compression ignition engine can be improved and its emissions of hydrocarbons and carbon monoxide reduced when the vegetable oil fuel is supplemented with a small proportion of hydrogen. The reported improvements were

attributed to an enhanced combustion rate with the presence of hydrogen, but due to the increased cylinder temperatures an increase in NO_X emissions was recorded. Labeckas and Slavinskas (2006a) also demonstrated that the pre-heating of the vegetable oil to 60°C substantially improved the liquid properties of the fuel, reducing the specific fuel consumption when compared to tests with unheated oil.

A proven alternative to the use of raw vegetable oils themselves is the processing of the oils into more suitable fuels. Currently the most suitable vegetable oil derived fuel for use in compression ignition engines is biodiesel. Biodiesels are the methyl esters of vegetable oils, the two most commonly available being rapeseed methyl ester and sunflower seed methyl ester. Biodiesel has significantly better fuel properties than the raw vegetable oils due to reductions in viscosity and density, and improved fuel stability.

Williamson and Badr (1998) carried out an in-depth study into the feasibility of using the Rapeseed Methyl Ester (RME) biodiesel as a major transportation fuel in the UK; with their findings concluding that a 5% replacement of mineral diesel with biodiesel is a feasible short term target. Labeckas and Slavinskas (2006b) also found that using RME biodiesel reduced the CO, hydrocarbon and smoke content of the exhaust, but increased the specific fuel consumption and emissions of CO_2 and NO_X.

Lin and Lin (2006) carried out comparative tests between a selection of biodiesels and a conventional ASTM No. 2D diesel fuel. Their findings indicated that the use of biodiesel increases the fuel consumption and thermal efficiency of the engine whilst lowering the emissions of CO and CO_2 compared to the diesel fuel.

Carraretto et al. (2004) investigated the combustion of biodiesel in internal combustion engines with varying injection timing. It was found that the comparative performance of biodiesel to normal diesel fuel was reduced along with the CO_2 emissions, while the specific fuel consumption and emissions of NO_X increased. It was also found that the optimization of the injection timing when using biodiesel improves performance without affecting emission levels. Lapuerta et al. (2005) investigated the use of

sunflower methyl ester as an alternate to diesel fuel. From their studies a reduction in PM was recorded for all engine operating conditions, although no corresponding increase in NO_X was recorded.

It is anticipated that biodiesel will become an increasingly important fuel resource throughout Europe in the next decade. At present biodiesel is only available as a 5% blend with diesel in a limited number of filling stations throughout the UK, but this number is expected to grow over time as the tax incentives for biomass derived fuels continue.

2.3.4 Natural Gas

Natural gas is a combustible mixture of hydrocarbon gases, and in its purest form is colourless and odourless. Natural gas is primarily composed of methane, but does also usually contain some ethane and small trace amounts of propane and butane. Compressed Natural Gas (CNG) is a suitable fuel for use in spark ignition engines, with only fairly simple modifications required to the engine and fuelling system.

Hekkert et al. (2005) carried out an analysis of utilising natural gas as an automotive fuel as a transition strategy between the current petrol/diesel infrastructure and that of the potential future hydrogen infrastructure. The findings of the investigation concluded that a natural gas engine allows for the development of a gaseous automotive fuel supply network while also providing a significant reduction in CO_2 emissions in the short term. This corresponds to several manufacturers such as Nissan (Kato et al. 2001) developing CNG powered vehicles based upon standard petrol equivalents. Aslam et al. (2006) demonstrated that the retrofitting of a petrol engine to run on CNG can reduce the emissions of CO, CO_2 and hydrocarbons while reducing the specific fuel consumption, although overall power was reduced and NO_X emissions increased.

Zeng et al. (2006) investigated the combustion characteristics of natural gas in a direct-injection compression ignition internal combustion engine. It was found that the fuel injection timing had a significant effect on engine performance and emissions due to the

effect of air fuel mixing on combustion speed. Ristovski et al. (2000) studied the PM and gaseous emissions from spark ignition heavy duty natural gas engines. Their investigation found that even though the CO and NO_X emissions of the natural gas engines were very low (below the standards for low emission vehicles), the PM emissions from the natural gas engines were comparable to that for heavy duty diesel engines, with similar size distributions and number concentrations.

The future of CNG vehicles depends not only on the market price of natural gas, but also on the taxation applied to CNG, which is at present 10.8 pence per litre in the UK. Hekkert et al. (2005) compared the vehicle efficiency and fuel chain well-to-wheel efficiency of a number of different internal combustion fuels. From this study the quoted average vehicle efficiency of diesel was 22%, CNG 19% and petrol 18%. The average well-to-wheel fuel chain efficiency of diesel was 19.4%, CNG 16.5% and petrol 14.8%. CNG has much better anti-knocking characteristics than petrol due to its comparatively high octane rating, and therefore could be perfectly suited for use in either engines with a high compression ratio or engines operating with high inlet pressures, such as that found with Miller cycle operation. For CNG to be competitive with both diesel and petrol fuels, further investigation is required into improving the operating efficiency of CNG engines.

2.3.5 Hydrogen

Investigations into the development of the hydrogen infrastructure for widespread deployment of fuel cell powered vehicles have been continuing for sometime. However, for the most part, the use of hydrogen as a fuel for automotive applications is seen as the medium to long term solution for energy and environmental problems. Hydrogen has huge potential for use as a transport fuel, with the possibility of eliminating most of the hazardous emissions from automotive applications. It must also be considered that the development of a completely new infrastructure may also have unforeseen negative consequences, as discussed by Cherry (2004). Some potential drawbacks of future hydrogen usage include the reliance on exotic metals in fuel cell catalysts causing an

increase in vehicle costs, and the effect of the reshaping of the petrochemical industry causing unknown employment shifts.

Within Europe it is expected that the use of renewable energy resources will have to significantly increase in the long term to provide the required energy for hydrogen to have even a small impact on the automotive market. In the short term natural gas is regarded as an important raw material for hydrogen usage to be feasible, and for hydrogen to be competitive with conventional internal combustion fuels the cost of fuel cells needs to substantially decrease (Wietschel et al. 2006). However with the price of natural gas continuing to rise, renewable energy resources such as wind energy become more attractive, and the use of wind power to produce hydrogen via electrolysis generates the lowest greenhouse gas emissions of all hydrogen manufacturing methods (Granovskii et al. 2006).

Hydrogen fuel cells are seen as the long term goal for the use of hydrogen in vehicle applications, and a project testing the feasibility of hydrogen fuel cells in buses in Stockholm (Haraldsson et al.2005) has shown that fuel cells vehicles even in prototype stages are remarkably reliable. Höhlein et al. (2000) concluded that the use of hydrogen as the principle fuel in fuel cell vehicles has many intrinsic benefits, including zero emissions, but at best they are a long term option. It can therefore be concluded that in the short-to-medium term the hydrogen infrastructure should be allowed to develop, but the use of hydrogen in spark ignition engines must be encouraged until the production costs of fuel cells make them economically viable.

The benefits as well as the drawbacks of using hydrogen as a spark ignition fuel have been discussed by Karim (2003) and White et al. (in press, 2006) The benefits of using hydrogen in internal combustions engines include its only emissions being water and a small amount of NO_X, its high combustion rates over wide pressure and temperature ranges, its ability to combust at very lean mixtures with air facilitating high compression ratios, excellent cold starting ability and its fast burning characteristics allowing for stable operation at high engine speeds. Some detrimental properties of hydrogen for its use as a spark ignition fuel include its low energy density, it's very low

heating value means engines develop less power, its high burning rates produce high cylinder pressures and temperatures which lead to the formation of NO_X and its low ignition energy can lead to the onset of knock.

There has been a great deal of research into the practical use of hydrogen as a fuel in a spark ignition internal combustion engine. Vandenborre and Sierens (1996) demonstrated the low emission potential of hydrogen using a converted diesel engine bus; with the emissions of CO_2, CO, PM and H_2 from the vehicle being below the resolution of their measuring devices. The effect of compression and equivalence ratio on the performance and the emissions of a hydrogen fuelled spark ignition engine were investigated by Maher et al. (2003) and Maher and Sadiq (2004), whose results showed that supercharging or high compression ratios and lean fuel air mixtures can be used to increase engine efficiency. Verhelst and Sierens (2001) found in their investigation that injection and ignition timing had strong influence on the efficiency of a hydrogen fuelled engine; similar results were found in a numerical study carried out by Yamin et al. (2000). From the results of published research it can be seen that a great deal of further work is required to optimise hydrogen IC engine technology.

2.3.6 Hybrid Systems

Hybrid vehicles are vehicles with more than one power source; usually a combination of an electrochemical battery and an internal combustion engine. The internal combustion engine and an electric motor provide the propulsion, with the battery being continuously charged during braking and low load driving conditions. There are many hybrid vehicles currently available on the market with Toyota pioneering the technology.

The main drawbacks with hybrid vehicles include the added weight of additional power train components limiting the potential increase in fuel economy, and the limited driving cycle over which the hybrid vehicle concept is effective. The chosen engine and battery size of a hybrid vehicle is a compromise, usually best suited for mixed driving cycles. When driving though an urban environment in a rush hour situation; the repetitive acceleration events will discharge the battery of the vehicle, with the driver

usually then having to rely on an undersized internal combustion engine. The development of more powerful battery systems continues, with the management of the battery resources being an important area for research (Corson 2002).

2.4 Summary

This chapter provides a review of the various drivers currently influencing developments in engine technology, with specific focus on improvements in engine efficiency and emission reductions. This covers fiscal-influence, electro-mechanical engine developments and fuel technology.

The signing of the Kyoto Protocol by many countries has proven to be a watershed moment in the global technological development of the internal combustion engine, with all major motor manufacturers investing in the development of cleaner transportation. To this end, advances in the understanding of the concepts behind internal combustion engines together with developments such as variable valve timing, direct injection and exhaust gas treatment have improved the economy of modern motor vehicles while reducing their emissions of CO_2 and particulate matter.

Alternative internal combustion engine fuels are expected in the short to medium term future to partially replace petrol and diesel, and together with developments in technology will further reduce the pollutants emitted by the transport sector. It is expected that the use of biomass derived fuels, which are already being used to supplement both petrol and diesel, will increase. Both CNG and hydrogen will become increasingly important as transportation fuels, but do require developments in engine technology and global infrastructure before use on a significant scale becomes possible.

The following chapters will utilise this background knowledge to advance understanding in several contemporary areas of research, and contribute towards the continued development of efficient 'cleaner' engines of the future.

3 Miller Cycle Engine Simulation

The investigation undertaken in Chapter 2 showed that advanced engine cycles, such as the Miller cycle, have considerable potential for future engine development. The realisation of this potential is explored in the context of natural gas powered IC engines, through an EU funded project under the "Competitive and Sustainable Growth" Programme (1998-2002) entitled "Magnetic Movement Valve for Miller Cycle operation of engines – reducing NO_X, CO2 and particulate emission" (Acronym: MagMove, project No. G3RD-CT-2002-00845).

3.1 The MagMove Miller Cycle

The MagMove project involved Cardiff University, in conjunction with its European project partners, working on the development of a natural gas powered engine incorporating a novel secondary valve apparatus. The project partners for the MagMove project are:

Project Leader	- NoNOx bv.	(Netherlands)
Modelling / CFD	- Cardiff University	(United Kingdom)
Materials	- Aachen University	(Germany)
European Coordinator	- Europus Ltd	(United Kingdom)

Cardiff University's responsibilities within the MagMove project included the development of computer models of the Electronically Operated load Control Valve (EOCV), and the integration of this valve into a computer model of the engine.

The EOCV technology allows an engine to operate under Miller cycle conditions, whilst also utilizing throttle free load control. This is achieved through the use of an electro-magnetically actuated secondary inlet valve, which operates independently of the crankshaft rotation. This valve replaces the continuously variable throttle plate, which is a primary cause of pumping losses.

The EOCV apparatus allows accurate metering of the charge allowed into each engine cylinder by effectively advancing the inlet valve closing time. If a turbocharger is used in conjunction with the EOCV apparatus, early EOCV closure allows the use of higher compression ratios / boost pressures.

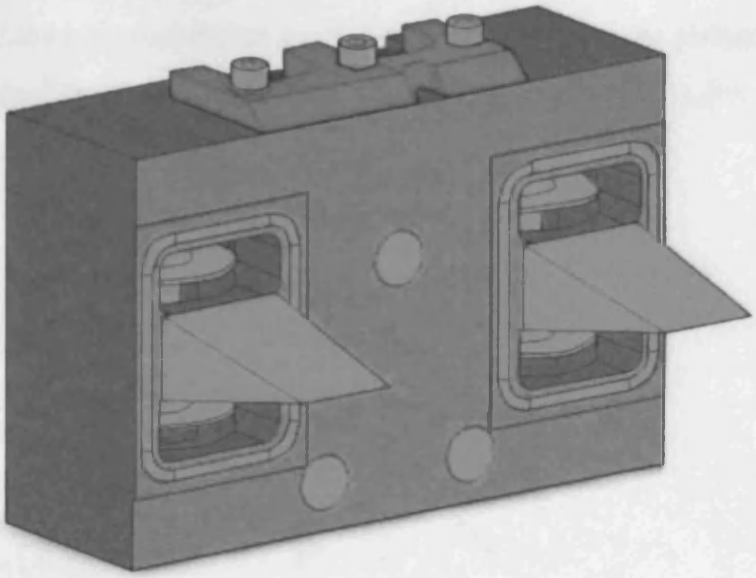

Figure 3.1 - EOCV apparatus

Currently the EOCV valve apparatus (pictured in Figure 3.1) is in its third incarnation. The work represented here forms part of a program of development for the EOCV concept, with the ultimate aim being a technology suitable for mass production. The role of Cardiff University involved the modelling and development of the valve design and the validation / development of the engine operation. The mark 3 version of the EOCV technology had been proven at low engine operating speeds (<2000 rpm) on a natural gas test engine, meeting emission standards set by EURO V with specific fuel consumption comparable to that of heavy duty Diesel engines.

The principles by which the EOCV apparatus operates is essentially that proposed by Ralph Miller; early closing of the inlet valves reducing the compression stroke of the engine, while still retaining a full length expansion stroke. Essentially adding a fifth stage to the standard four-stroke Otto cycle.

The five stages of the EOCV induced Miller cycle are as follows: The shortened induction stroke (points A-B in Figure 3.2) is the drawing in of the fresh air/fuel

mixture into the engine cylinder; the Miller effect then occurs with the expansion and compression of the confined charge (points B-B*-B); the compression stroke is the compression of the confined air/fuel mixture (points B-C), after which combustion is initiated in the cylinder by the spark plug; the expansion stroke (points C-D) is where the formation of the hot combustion gases carries out work on the piston; and finally the exhaust stroke (points D-A) is the where the combustion products are evacuated from the engine cylinder.

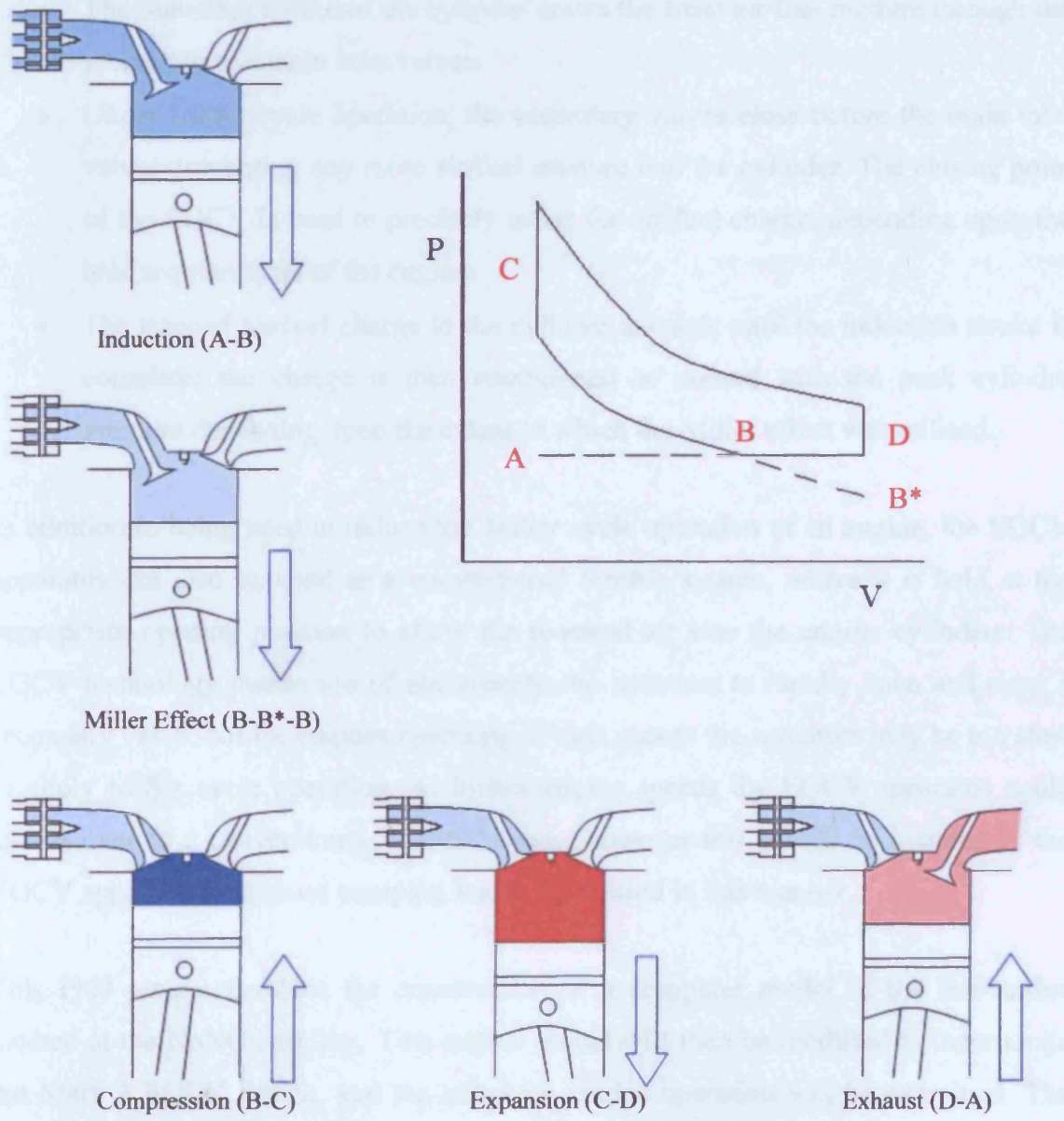

Figure 3.2 – EOCV Miller cycle principles

The EOCV apparatus operates completely independently to the main inlet and exhaust valves of the engine; with completely variable opening and closing times. The standard procedure by which the EOCV system operated is as follows:

- The individual secondary valves for each cylinder open shortly before the main inlet valves. The precise duration between the opening of the secondary and main inlet valves can be varied depending upon engine speed and other conditions.
- The induction stroke of the cylinder draws the fresh air/fuel mixture through the secondary and main inlet valves.
- Under Miller cycle operation, the secondary valves close before the main inlet valves preventing any more air/fuel mixture into the cylinder. The closing point of the EOCV is used to precisely meter the air/fuel charge, depending upon the load requirements of the engine.
- The trapped air/fuel charge in the cylinder expands until the induction stroke is complete; the charge is then compressed as normal with the peak cylinder pressure depending upon the extent to which the Miller effect was utilized.

In addition to being used to induce the Miller cycle operation of an engine, the EOCV apparatus can also be used as a conventional throttle system, where it is held at the appropriate opening position to allow the required air into the engine cylinders. The EOCV technology makes use of electromagnetic actuators to rapidly open and close a secondary valve, but for engines operating at high speeds the actuators may be too slow to apply Miller cycle operation. At higher engine speeds the EOCV apparatus could switch over to a conventional 'throttle' mode, however this should be avoided as the EOCV apparatus will cause pumping losses when used in this manner.

This PhD project involves the construction of a computer model of the test-engine located at the NoNOx facility. This engine model will then be modified to incorporate the Mark 3 EOCV design, and the effect on engine operation will be examined. The completed EOCV equipped engine model will then be tested using a series of validation cases taken from the actual test engine, providing an indication of the models suitability for investigative studies.

3.2 Ricardo Wave

Wave is an engineering code developed by Ricardo Software to analyse and predict the pressure waves, mass flows and energy losses associated with flow through pipes, plenums, and components of inlet and exhaust systems. Wave provides a fully integrated treatment of time-dependent fluid dynamics and thermodynamics by means of a one-dimensional finite-difference formulation, incorporating a general thermodynamic treatment of working fluids such as air, air-hydrocarbon mixtures, liquid fuels and combustion products. An additional property of Wave is that it can be coupled to "higher-level" CFD codes enabling more detailed studies of individual system components.

Wave models a network of pipes, volumes and junctions in terms of a set of building blocks, which include:

- Constant area or conical pipes / ducts.
- Passages with abrupt changes of area.
- Junctions of multiple ducts.
- Elbows, orifices and plenums.
- Terminations such as infinite plenums (ambients) and anechoic (no reverberation, absorbs all pressure waves) boundaries.

The Wave software also includes a library of machinery components such as engine cylinders, fuel injectors, piston compressors, turbocharger compressors and turbines, pumps and catalytic converters. These components can be attached to a pipe network to serve as sources or absorbers of pulsating flows.

The basic methodology incorporated in Wave has been extensively tested against a set of reference test cases, including shock wave propagation in a duct, pressure wave reflection from closed and open ends of a duct, steady state flow through a duct with an abrupt change in cross-sectional area, flow through an orifice, pipe flow with friction, pipe flow with heat transfer, and flow through a junction of three ducts.

The method by which Wave produces a simulation of the flow through a duct system is to solve the compressible flow equations governing the conservation of mass, momentum and energy. The duct system is subdivided, or discretized, into a series of smaller volumes. The quasi-one dimensional governing equations are then produced for each of these elementary volumes in a finite difference form. The equations for mass and energy are solved for each volume, and the momentum equation is solved for each boundary between volumes.

The main governing equations, written in an explicitly conservative form, are as follows:

$$Mass = \frac{dm}{dt} = \sum \dot{m} \tag{3-1}$$

$$Energy = \frac{dme}{dt} = \sum \dot{m}h + sources \tag{3-2}$$

$$Momentum = \frac{dmu}{dt} = A\frac{dp}{dx}dx + \sum \dot{m}u - losses \tag{3-3}$$

The thermodynamic properties of the fluids used are based on the appropriate governing relationships, for the thermo-chemistry of hydrocarbon/air mixtures (i.e. general C, H, O, N type fuels) the perfect gas equations are utilised.

The application of a finite-volume technique is used in order to solve the governing partial differential equations. The explicit technique is used for time differencing with the time-step being governed by the Courant condition. This condition can be written as:

$$\Delta t = \frac{CFL\Delta x}{C + |V|} \tag{3-4}$$

3.2.1 Wave Build

In order to create a Wave simulation of a duct network, it is first necessary to obtain all available data detailing the geometry, and all physical parameters and operating conditions. A model of the network can then be built up from a collection of junctions using the Wave Build Graphical User Interface (GUI). The Wave Build GUI allows a user to simplify the complex geometry of engines and pipe-networks into a series of ducts and junctions. The Wave Build GUI is shown in Figure 3.3.

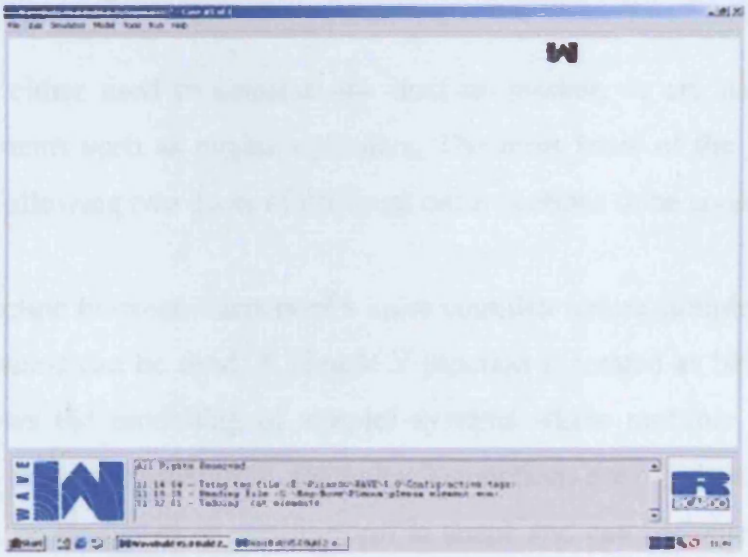

Figure 3.3 - The Wave Build environment.

The Wave Build GUI uses the standardized Window format, incorporating a series of pull-down menu options to define the model parameters and operating conditions. A model is constructed from a network of ducts connected together by suitable junction types chosen from the junction palette (see Figure 3.4), such as engine cylinders, duct junctions and turbocharger machinery. The junctions are positioned onto the work canvas first and are connected together by simple dragging a duct from one junction to another.

Figure 3.4 - The Wave Build junction palette

"Junctions" are either used to connect one duct to another, or are used to represent physical sub-systems such as engine cylinders. The most basic of the junctions is the orifice junction, allowing two ducts of different cross-sections to be connected together.

When the connection between ducts is of a more complex nature, simple Y-junctions or complex Y-junctions can be used. A simple Y-junction is treated as being spherical in nature, and allows the modelling of simpler systems where multiple pipes join at a single point, i.e. an exhaust manifold. Complex Y-junctions are of a much more flexible nature; they can be elongated or non-uniform in shape and can be joined together with "mass-less" ducts to model inlet plenums, filters, silencers, heat exchangers and catalysts.

An example of a completed Wave model is shown in Figure 3.5. This particular model is of a heavy-duty diesel engine. Once a model has been completed it is necessary to carry out an "input check". This feature checks the form of the input file, ensuring continuity between ducts and checking that all the necessary modules are present. Once the input check has been completed the solver component of the Wave software can then be run.

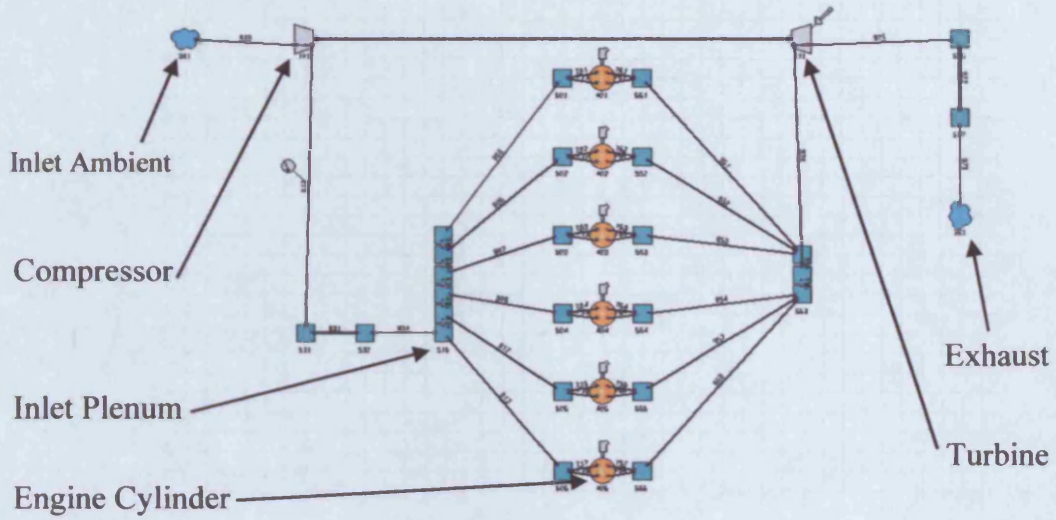

Figure 3.5 - Example Wave model

Upon completion of the simulation, several output files are generated. The results of the simulation can either be imported into standard spreadsheet type packages; or be viewed using Ricardo's own post-processing software Wave Post and RPlot.

3.2.2 Supporting Codes

There are several different support codes embedded into the Wave software. The two that are of most use are PROPTY and TCMAP.

PROPTY - PROPTY is used by Wave to calculate the thermodynamic properties of the mixture of air, fuel and combustion products as a function of temperature, pressure and composition. PROPTY generates property maps for each specific fuel from which accurate values can be interpolated. PROPTY calculates the properties over a wide range of parameters using a comprehensive equilibrium program, which is applicable to any general CCHHOONN fuel. The information is passed to Wave in the form of an auxiliary input file created by the PROPTY code.

TCMAP produces a model of a turbocharger that may be linked with a Wave engine model to simulate turbocharged engines. The TCMAP code produces performance maps for turbine and compressor components at the pre-processing stage, and then rates the efficiency of the system in post-processing.

3.2.3 Wave Mesher

Wave Mesher is a new addition to the Wave software package allowing the imputation of 3D geometry in a CAD file format. This greatly improves the practicality of the Wave package, as prior to the inclusion of Wave Mesher the production of a Wave model relied heavily upon the modeller's interpretation of the system geometry.

A CAD file in the .stl (stereo lithography) format can be imported directly into the Wave Mesher program. The contents of the CAD file cannot be a 3D solid model of the component, but must represent the inner surface of the component. Figure 3.6 illustrates the form of an imported file.

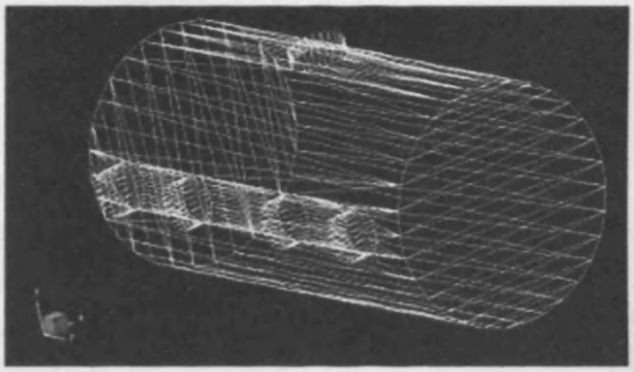

Figure 3.6 - Imported geometry in .stl format

The first stage of Wave Mesher is to ensure that the model geometry is fully stitched (has no holes other than the inlets and outlets) and to manually remove any geometry imperfections using the options available for geometry manipulation.

The next stage of the Wave Mesher program is to upgrade the model by entering the body mode. This part of the process controls the division of the geometry into sub-volumes. Once the geometry has been split up as required by the 'modeller', the model is then transferred to the element mode where the properties of the volumes are decided. The user decides which of the Wave junctions/ducts would best represent the geometry; at this stage the dimensions that have been calculated by Wave Mesher for the individual volumes can be viewed and altered if required. The geometry created by the Wave Mesher program can then be imported directly into wave through the component browser option panel.

3.3 Deutz V6 Engine Model

This section describes the model building process used to construct the simulation of the engine that will incorporate the EOCV technology. In order to construct a computer simulation of an engine a great deal of information is required. Like all computer simulations, the accuracy of the results is dependent upon detailed information.

3.3.1 Wave Engine Model

3.3.1.1 Engine Specifications

An overview of the engine specifications that are required by the Wave software to produce an engine model is now outlined. The engine to be modelled in the early stages of this project is the EOCV test engine; which is based upon a Deutz 1015, 12.0 litre V6 marine diesel engine, shown in Figure 3.7 (for further engine details see Appendix A).

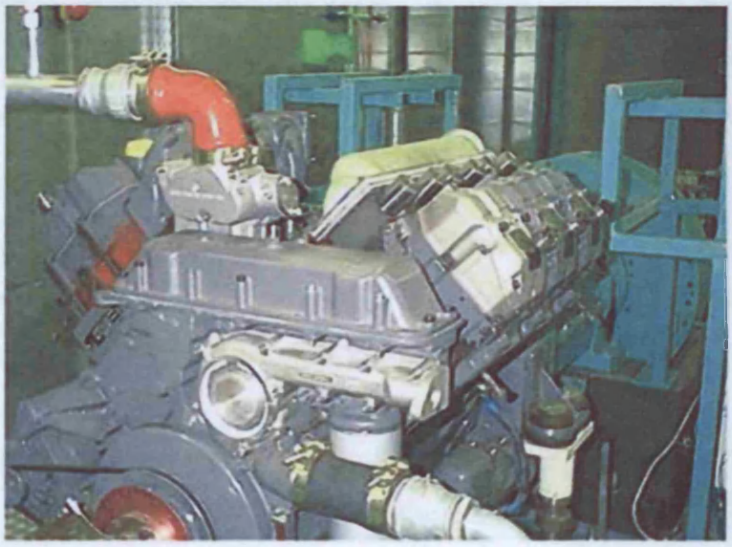

Figure 3.7 - The EOCV test engine

The Deutz 1015 marine diesel engine to be used for the EOCV work is a modern water-cooled four stroke 6 cylinder turbocharged engine. The main characteristics of the Deutz engine are listed in Table 3.1.

Table 3.1 – Deutz 1015 engine specifications

VARIABLE	TEST ENGINE
Cylinder Bore (mm)	132.0
Piston Stroke (mm)	145.0
Total Displacement (litres)	11.91
Connecting Rod Length, centre to centre (mm)	261.733
Piston Pin Offset {+ve towards major thrust side} (mm)	0
TDC Combustion Chamber Volume (cm^3)	158.74
Compression Ratio	17.0
Number of Cylinders	6
Firing Order	1-6-3-5-2-4
Firing Interval	120°
Power Rating for continuous operation at 1800 rpm at 1900 rpm at 2100 rpm	272 kW 287 kW 287 kW

The basic engine operating details are entered into the Wave engine panel (shown in Figure 3.8). The details entered into the engine panel are used by Wave to control the combustion process. Some of the parameters entered here must be customized for the engine being modelled; including friction, combustion and conduction parameters.

The information entered into the panel shown in Figure 3.9 allow the customisation of the combustion and emission aspects of the Wave simulation. The Wave simulation is then able to predict hydrocarbon formation and other pollutant emissions.

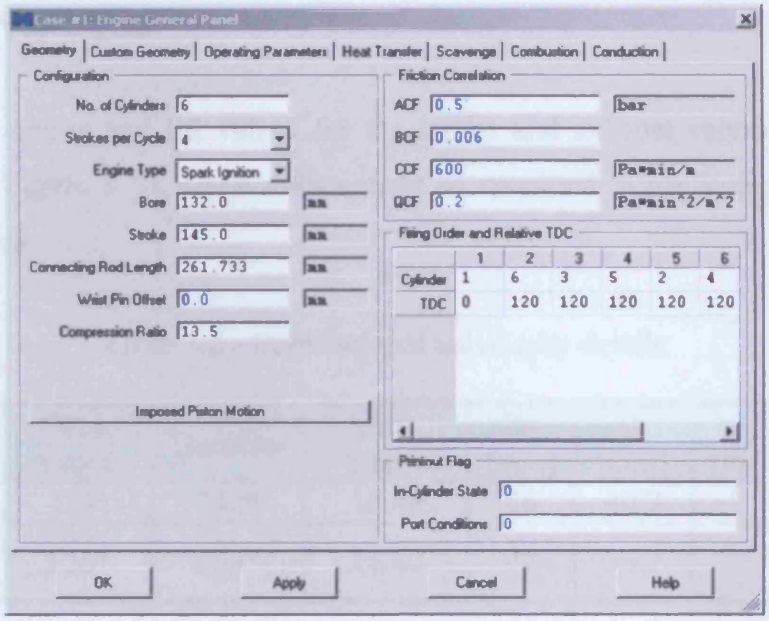

Figure 3.8 - Wave engine panel

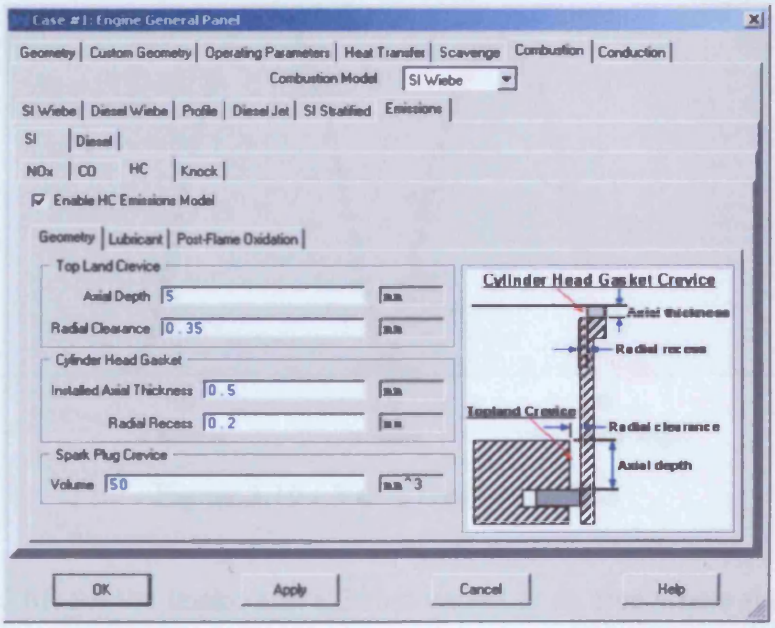

Figure 3.9 - Combustion and emission modelling

The combustion modelling process used in Wave is another set of variables that must be configured and validated. The heat release model used is time-based and must therefore be carefully configured for the engine and as it is RPM dependent will vary throughout the engine's speed range.

3.3.1.2 Valve-gear

Details of the timing and lift values for the intake and exhaust valves are shown in Table 3.2 and Figure 3.10. These values must be specified in the Valves panel of the Wave simulation.

Table 3.2 - Conventional valve-gear details

	Cycle Anchor	Duration	Max Lift [mm]	Dv [mm]	Di [mm]	b [mm] (valve seat length)
Intake Valve	338°	248°	10.48	46	40.7	2.3
Exhaust Valve	126°	259°	11.40	42	36.7	2.3

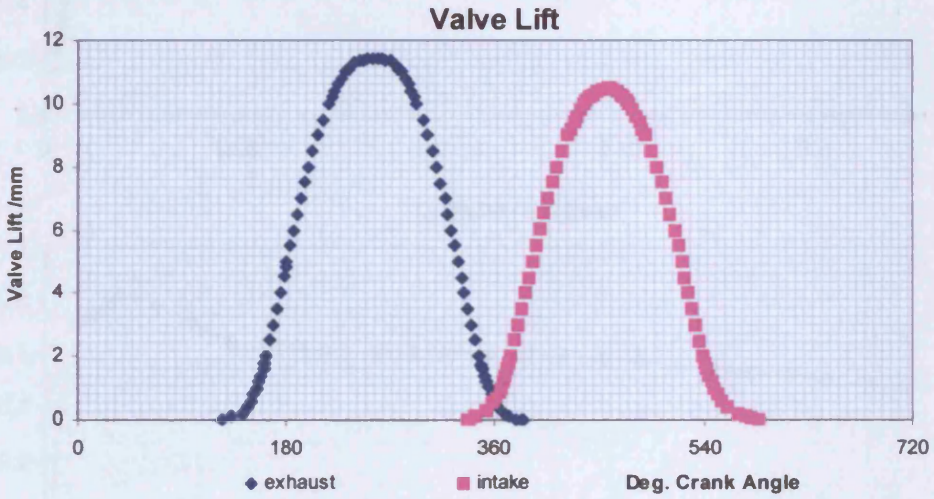

Figure 3.10 - Valve timing and lifts

The timing and lift for the intake and exhaust valves is an area where there is potential for improvements to be made to the engine. Detailed parametric studies can be used to find the optimum cam profiles. However, it is unlikely that the engines cams will be altered due to the added expense.

The discharge coefficients for the intake and exhaust side of the cylinder head were measured using a flow bench. The values obtained for all the flow directions are shown in Figure 3.11.

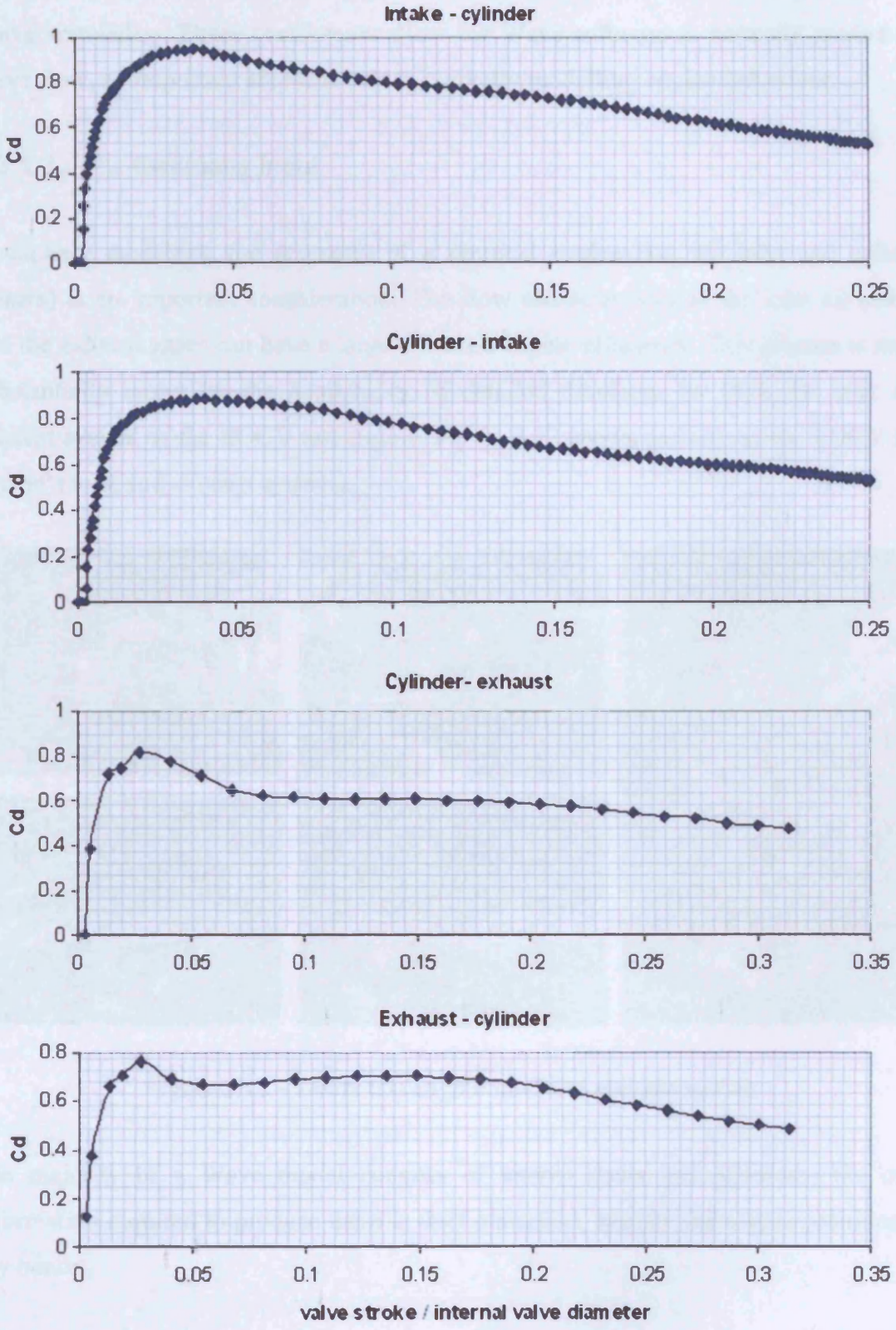

Figure 3.11 - Intake and exhaust discharge coefficients

The flow coefficients shown in Figure 3.11 are entered into the Valve panel of the Wave simulation. These coefficients allow the Wave software to correctly predict the valve flow, an important characteristic in correctly modelling engine behaviour.

3.3.1.3 Geometry Input

Accurately modelling the geometry of a physical engine (i.e. the inlet and exhaust system) is an important consideration. The flow characteristics of the inlet air stream and the exhaust gases can have a large effect on engine efficiency. This process is made substantially easier by the availability of detailed drawings for both the inlet and exhaust system of the EOCV test engine. Figure 3.12 shows pictures of the EOCV test engine's inlet and exhaust systems.

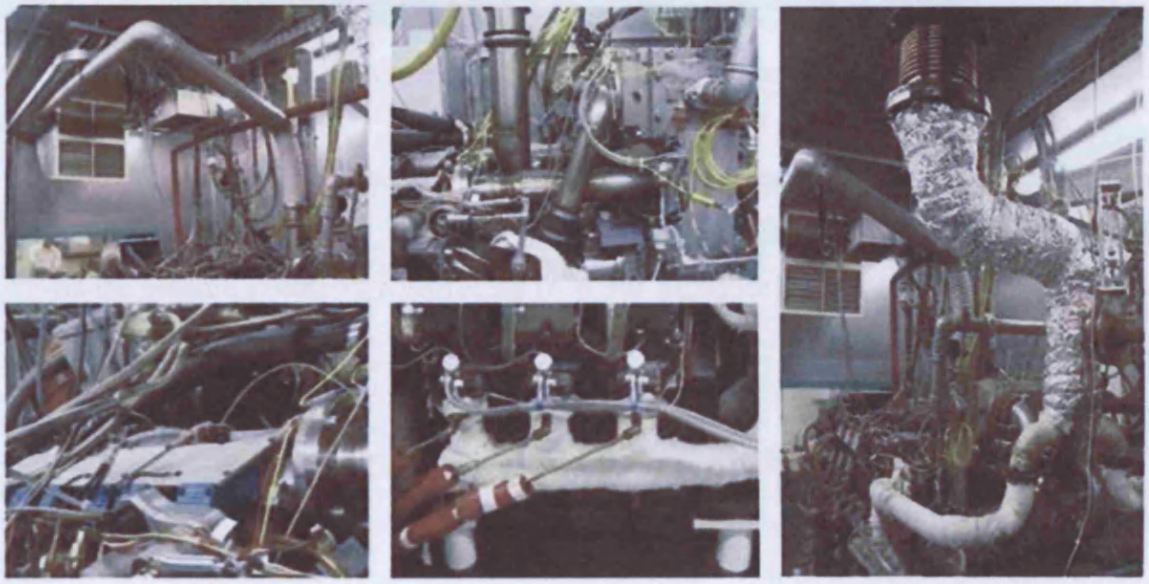

Figure 3.12 – Deutz test engine inlet and exhaust system

The majority of a Wave model consists of simple ducts and junctions; the only information required to produce these is duct diameters, lengths and angles/positions of any bends.

One component of the inlet system that can have a large effect on engine efficiency is the plenum. Because of the complex nature of plenum geometry it is necessary to use the Wave Mesher software to model the actual plenum design used on the test engine. Figure 3.13 shows the CAD file once it has been imported into the Wave Mesher software in the stereo-lithography format (*.stl).

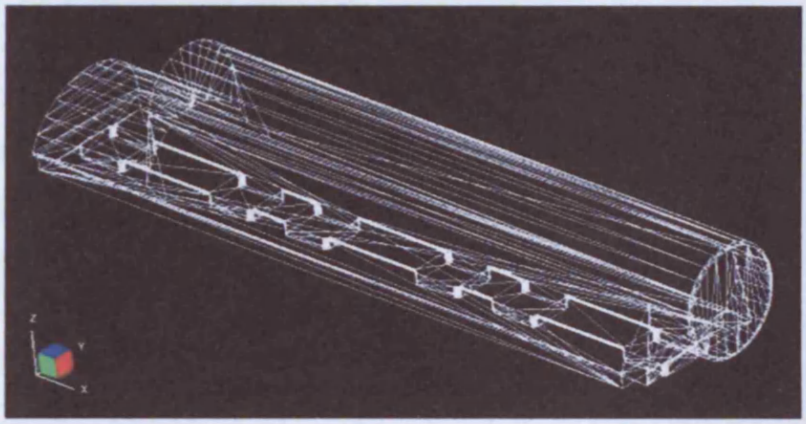

Figure 3.13 - Imported CAD geometry

The plenum geometry is interpreted by the Wave Mesher software, and is saved in a format that can be directly imported into the Wave Build environment. Figure 3.14 shows the plenum geometry constructed in Wave Build format.

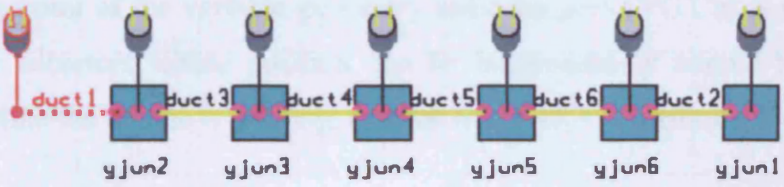

Figure 3.14 - Plenum model in Wave Build

The plenum model is directly imported into the Wave Build environment and incorporated in to the Deutz engine model.

3.3.1.4 Turbo Modelling

The modelling of the two variable geometry turbochargers used by the Deutz test engine is carried out using the TCMAP supporting code within the Wave Build environment. The turbochargers installed on the Deutz test engine at the $NoNO_X$ facility are manufactured by IHI; the data supplied by IHI detailing the turbochargers operating parameters is shown included in Appendix B.

The turbochargers used on the test engine incorporate both 'waste gate' and variable geometry systems. The waste gate allows the exhaust gases to bypass the turbine, reducing the speed at which the turbocharger operates thus reducing the 'boost' pressure provided by the compressor wheel. The variable geometry system also controls the speed of the turbine (and therefore compressor boost) by controlling the exhaust gas pressure entering the turbine housing. The exhaust gases that enter the turbine housing pass through a series of vanes, which can be closed to increase exhaust gas pressure and opened to reduce exhaust gas pressure. At low engine speeds when exhaust flow is low, the vanes are partially closed to increase the pressure in the exhaust before the turbine, increasing the turbochargers speed and providing more boost.

The operating point of the variable geometry turbochargers (VGT's) is controlled by a pair of linear actuators whose position can be independently altered by the test-bed technicians while the engine is running, as such the VGT's are infinitely variable.

Data obtained from the IHI supplied operating maps for the turbine and compressor is used to build up a simulation of the behaviour of these components. The information that is required is the relationship between volumetric flow rate, pressure ratio and operating efficiency for varying turbine and compressor speeds. The TCMAP code then produces its own behavioural maps for the compressor and turbine, which is accessed by the main Wave code during a simulation. The turbine modelling is a great deal more complex than that of the compressor because of its varying geometry, because of this a number of turbine maps are required for set actuator positions. The compressor map generated by the TCMAP code for the Deutz test engine is shown in Figure 3.15.

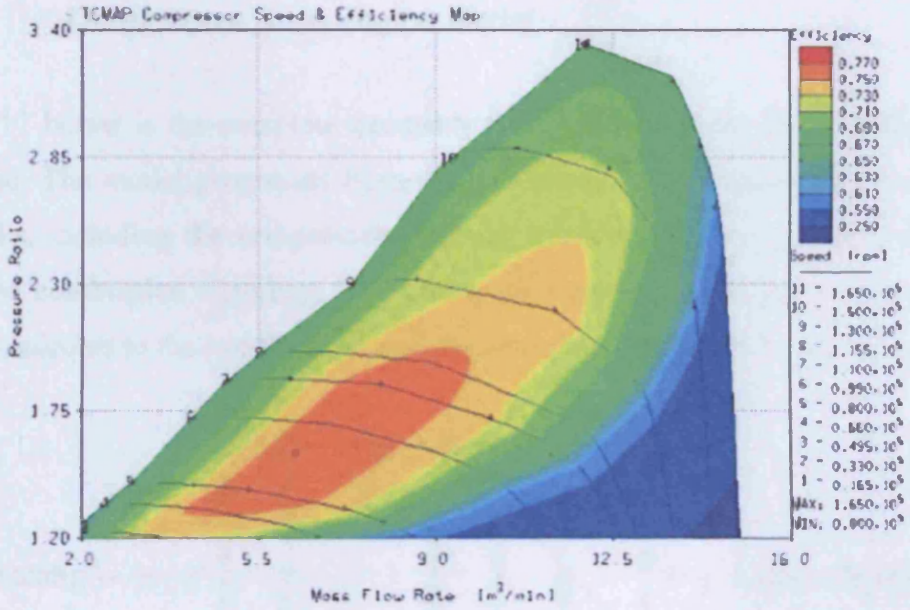

Figure 3.15 - TCMAP compressor data

From the turbocharger data provided by IHI, initial turbine maps were created and tested. A sample of a TCMAP generated turbine map is shown in Figure 3.16.

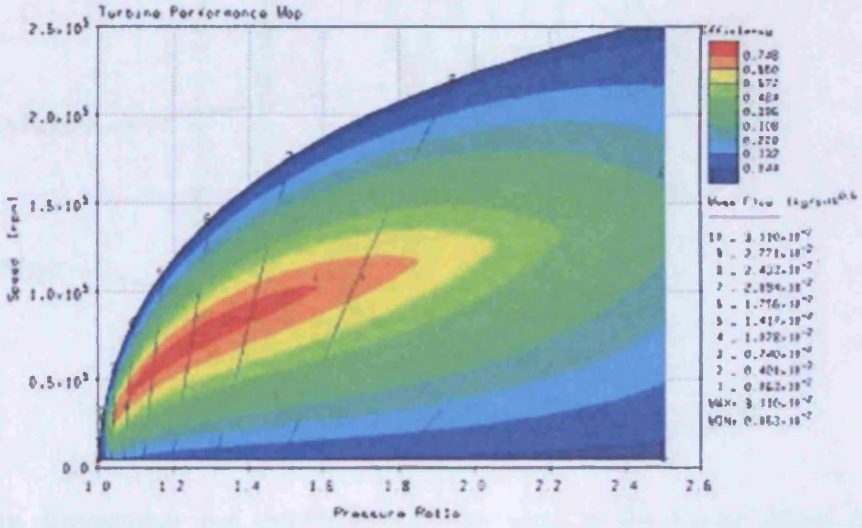

Figure 3.16 –TCMAP turbine data

The completed Turbocharger model is incorporated into the Wave Build model of the Deutz test engine. For the initial set of engine simulations only one of the turbine maps generated for the VGT is used. The map chosen for these simulations was that for the fully open VGT setting – corresponding to the zero setting on the VGT actuators.

3.3.1.5 Deutz Wave Build Engine Model

Figure 3.17 below is the complete geometry model for the basic diesel fuelled Deutz test engine. The model progresses from the two inlets (left), through the two separate inlet tracks, including the compressors and intercoolers, to the plenums (centre) and then to the combustion chambers. The combustion products then proceed through the exhaust manifolds to the two turbines, and then exit through the common exhaust pipe.

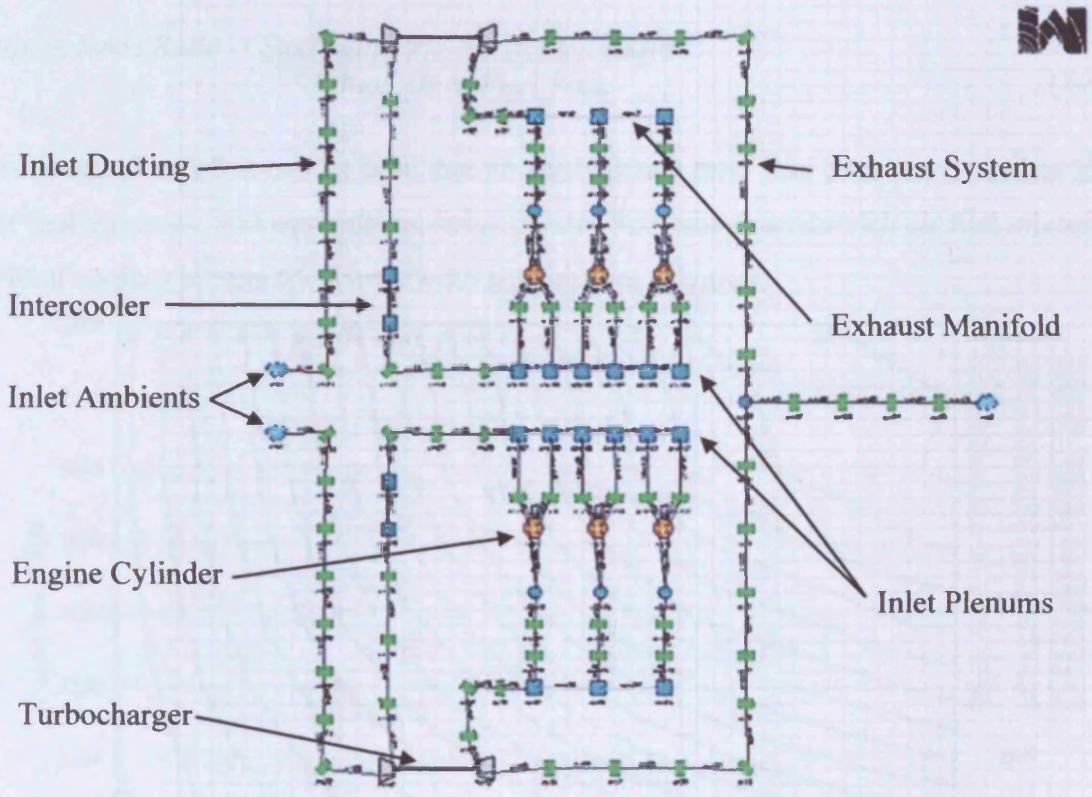

Figure 3.17 - Wave model of EOCV test engine

Many of the dimensions and model parameters used in the Deutz diesel model were obtained during the validation of the EOCV equipped engine model (reported in section 3.5) against experimental data. The refined model of the compressed natural gas EOCV test engine obtained from the validation process has been reverse engineered to model the standard diesel powered Deutz base engine; this will allow comparisons of power and operating efficiency to be made.

3.3.2 Deutz Simulation Results

The Wave computer model of the Deutz 1015 marine diesel engine shown in Figure 3.17 was used to simulate the behaviour of the engine throughout its operational speed range. An example of the results predicted by Wave is shown in the sample output file in Appendix C. Figure 3.18 shows the predicted variation of engine power with engine speed and equivalence ratio, where the equivalence ratio is defined by equation 3-5.

$$\textit{Equivalence Ratio} = \frac{\textit{Stoichiometric Air to Fuel Ratio}}{\textit{Actual Air to Fuel Ratio}} \qquad (3\text{-}5)$$

From equation 3-5 it can be seen that an equivalence ratio less than one describes lean air fuel mixtures, and equivalence ratios greater than one describe rich air fuel mixtures. Diesel engines inherently operate with lean air fuel mixtures.

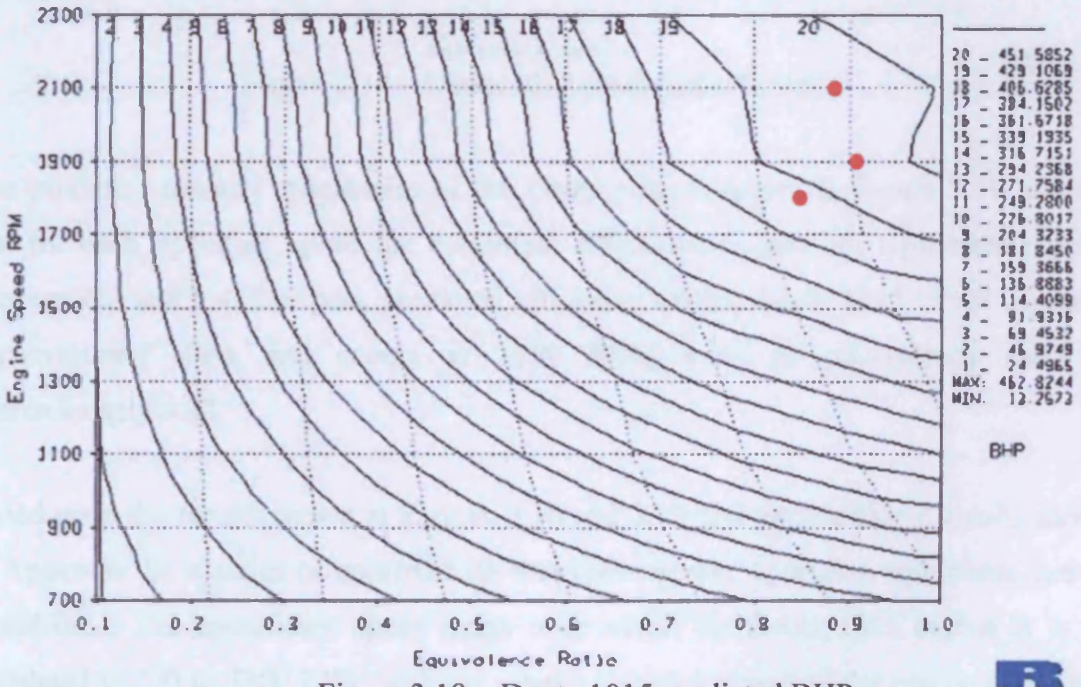

Figure 3.18 – Deutz 1015 predicted BHP

From an examination of Figure 3.18 it can be seen that, as expected, the predicted BHP of the Deutz 1015 diesel engine varies both with the operating speed of the engine and the equivalence ratio of the trapped charge. Also indicated in Figure 3.18 by the red dots are the maximum power ratings for the Deutz 1015 engine according to the specifications provided by the manufacturer (Appendix A).

Figure 3.19 illustrates the predicted Brake Efficiency of the Deutz 1015 diesel engine throughout its operating speed range and for varying equivalence ratios.

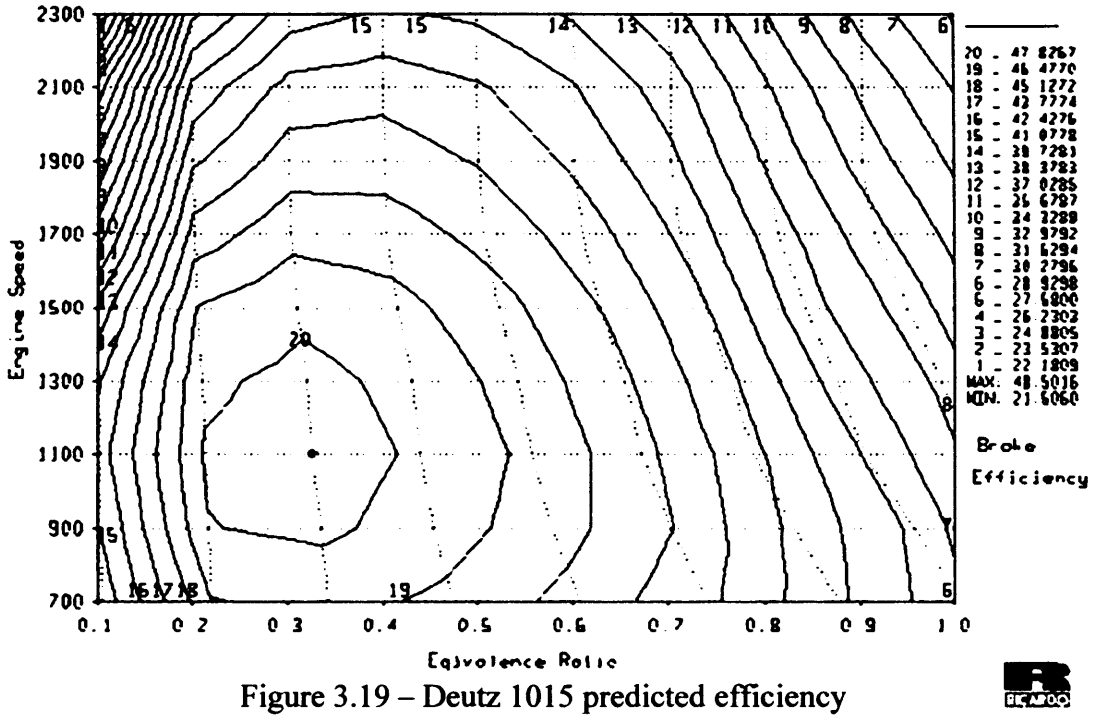

Figure 3.19 – Deutz 1015 predicted efficiency

The predicted thermal efficiencies of the Deutz engine shown in Figure 3.19 indicate that for each operating speed the maximum efficiencies occur for equivalence ratios between 0.3 and 0.4. The peak predicted efficiency for the Deutz 1015 diesel engine is approximately 49% and occurs at 1100 RPM with an equivalency ratio of approximately 0.33.

Based upon the results shown in Figures 3.18 and 3.19 and the additional results shown in Appendix D, a series of approximate maximum power operating conditions can be established. The operational speed range over which the Deutz 1015 engine is to be simulated is 700 to 2300 RPM with the rated maximum power of the engine being 442 BHP at 1900 to 2100 RPM. The results of the Wave simulations to determine the Deutz 1015 diesel engine's operating parameters are shown in Table 3.3.

Table 3.3 – Deutz 1015 predicted operating parameters

Speed RPM	Power BHP	Torque Nm	Brake Efficiency	BSFC Kg/KWhr	Equiv. Ratio	NOx ppm	HC g/hr
100% Load (Maximum Throttle)							
700	150	1527	43.07	0.1953	0.7926	956	11.14
900	210	1662	43.77	0.1922	0.7733	1005	15.27
1100	265	1715	43.90	0.1916	0.7534	1056	19.12
1300	320	1753	43.37	0.1940	0.7499	1041	23.27
1500	370	1757	42.74	0.1968	0.7456	1044	27.21
1700	410	1712	42.07	0.1999	0.7330	1087	30.29
1900	442	1657	40.85	0.2059	0.7394	1043	33.30
2100	442	1499	40.35	0.2084	0.7220	1051	32.83
2300	420	1300	40.81	0.2061	0.6290	1425	30.49
50% Load							
700	75	76	47.05	0.1788	0.4098	1720	5.13
900	105	831	48.68	0.1728	0.3971	1631	6.92
1100	133	861	49.32	0.1706	0.3794	1532	8.60
1300	160	876	49.17	0.1711	0.3670	1449	10.32
1500	185	878	48.59	0.1731	0.3604	1412	11.98
1700	205	859	47.35	0.1776	0.3572	1404	13.43
1900	211	828	46.03	0.1828	0.3547	1374	14.67
2100	211	749	44.73	0.1881	0.3468	1284	14.65
2300	210	650	42.21	0.1993	0.3168	1167	14.60

From an examination of the results shown in Table 3.3 it can be seen that while operating at the simulated 100% load conditions the predicted brake thermal efficiency of the Deutz engine is between 40 and 44 %, with an average brake specific fuel consumption of 0.199 kilogram per kilowatt hour.

Through the majority of the operational speed range the Wave computer software predicts that the Deutz engine operates at an equivalence ratio between 0.7 and 0.8 while under full load conditions, and between 0.3 and 0.4 while under half load conditions. The average predicted brake efficiency of the Deutz engine operating under half load conditions is 47 %. From the examination of the results it can be seen that the engine produces higher emissions of NO_X under part load conditions, but emits more unburned hydrocarbons under full load conditions.

3.4 EOCV Engine Model

For the application of the EOCV technology the Deutz test engine was converted to run on either LPG or CNG. There have been many other modifications made to the engine to accommodate the EOCV system including a change in compression ratio, the installation of sparkplugs, as well as the construction of new fuel, inlet and exhaust systems. Table 3.4 lists the main specifications of the EOCV test engine (standard engine specifications - Table 3.1).

Table 3.4 - Test engine specifications

VARIABLE	TEST ENGINE
Cylinder Bore (mm)	132.0
Piston Stroke (mm)	145.0
Connecting Rod Length, centre to centre (mm)	261.733
Piston Pin Offset {+ve towards major thrust side} (mm)	0
TDC Combustion Chamber Volume (cm^3)	158.74
Compression Ratio	13.5
Number of Cylinders	6
Firing Order	1-6-3-5-2-4
Firing Interval	120°
Clearance Height – Top of Piston and Top of Cylinder (mm)	3.0

Figure 3.20 shows the complete geometry model for the EOCV test engine. The model progresses from the two inlets (left), through the two separate inlet tracks, including the compressors and intercoolers, to the plenums (centre) and then through the EOCV's to the combustion chambers. The combustion products then proceed through the exhaust manifolds to the two turbines, and then exit through the common exhaust pipe.

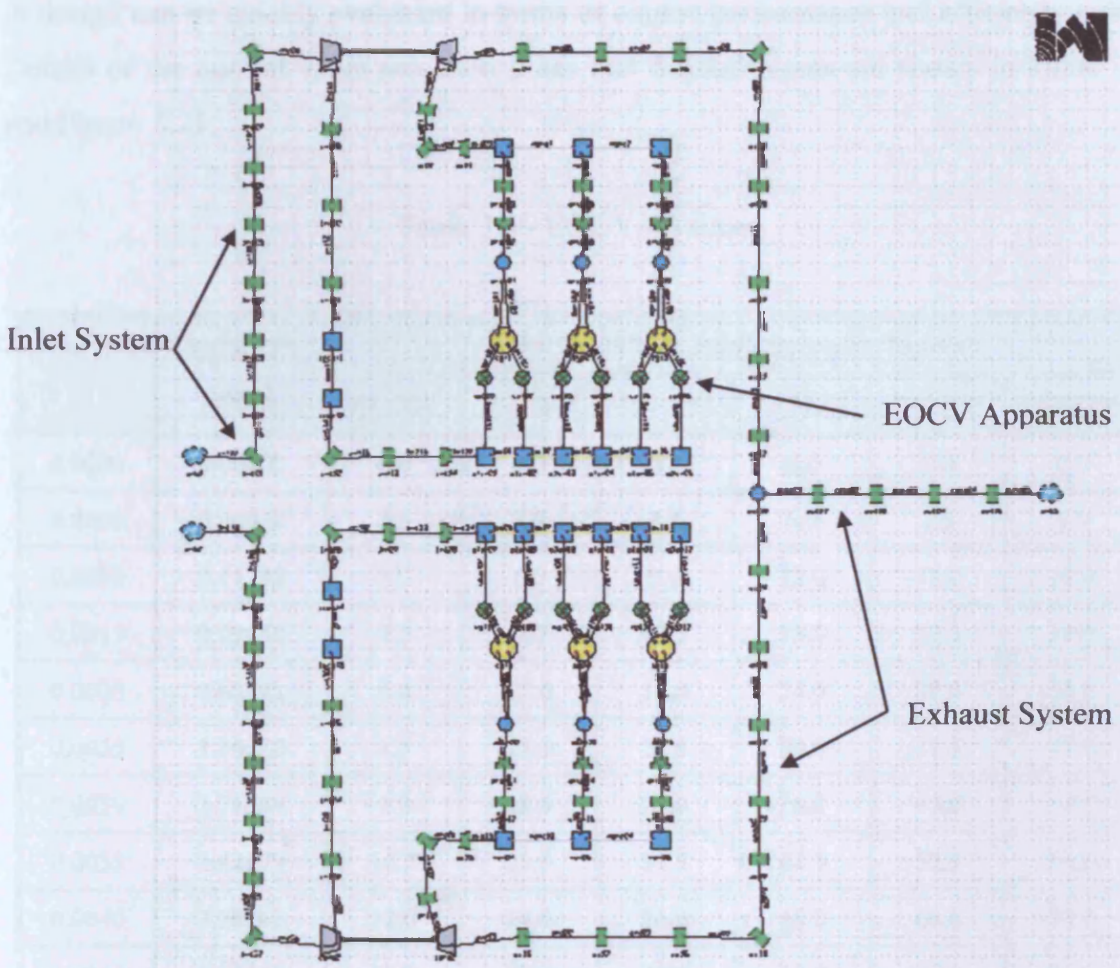

Figure 3.20 - Wave model of Deutz test engine incorporating EOCVs

The dimensions used in this initial model have been checked against the test engine set-up during the validation stage. All of the major components and ductwork are included.

3.4.1 EOCV Modelling

The modelling of the EOCV valve will form an important part of the engine model. In the early stages of the project the engine modelling will be based upon empirical data obtained from the test engine.

The next stage of the project involves the development of a 3-Dimensional computer model for the EOCV apparatus. Once this has been completed potential improvements

in design can be quickly evaluated in terms of engine performance and efficiency gains. Details of the current valve actuation times and displacements are shown in Table 3.5 and Figure 3.21.

Table 3.5 - EOCV lift times

Time (s)	Valve Lift (mm)	Associated Crank Angle Duration (Degrees)					
		500 RPM	1000 RPM	1500 RPM	2000 RPM	2500 RPM	3000 RPM
0.0000	0.00000	0.0	0.0	0.0	0.0	0.0	0.0
0.0005	0.04028	1.5	3.0	4.5	6.0	7.5	9.0
0.0010	0.11292	3.0	6.0	9.0	12.0	15.0	18.0
0.0015	0.29554	4.5	9.0	13.5	18.0	22.5	27.0
0.0020	0.62421	6.0	12.0	18.0	24.0	30.0	36.0
0.0025	1.10356	7.5	15.0	22.5	30.0	37.5	45.0
0.0030	1.71584	9.0	18.0	27.0	36.0	45.0	54.0
0.0035	2.42879	10.5	21.0	31.5	42.0	52.5	63.0
0.0040	3.20242	12.0	24.0	36.0	48.0	60.0	72.0
0.0045	3.99462	13.5	27.0	40.5	54.0	67.5	81.0
0.0050	4.76575	15.0	30.0	45.0	60.0	75.0	90.0
0.0055	5.48198	16.5	33.0	49.5	66.0	82.5	99.0
0.0060	6.11761	18.0	36.0	54.0	72.0	90.0	108.0
0.0065	6.65616	19.5	39.0	58.5	78.0	97.5	117.0
0.0070	7.09050	21.0	42.0	63.0	84.0	105.0	126.0
0.0075	7.42163	22.5	45.0	67.5	90.0	112.5	135.0
0.0080	7.65658	24.0	48.0	72.0	96.0	120.0	144.0
0.0085	7.80499	25.5	51.0	76.5	102.0	127.5	153.0
0.0090	7.87468	27.0	54.0	81.0	108.0	135.0	162.0
0.0095	7.86604	28.5	57.0	85.5	114.0	142.5	171.0
0.0100	7.76535	30.0	60.0	90.0	120.0	150.0	180.0

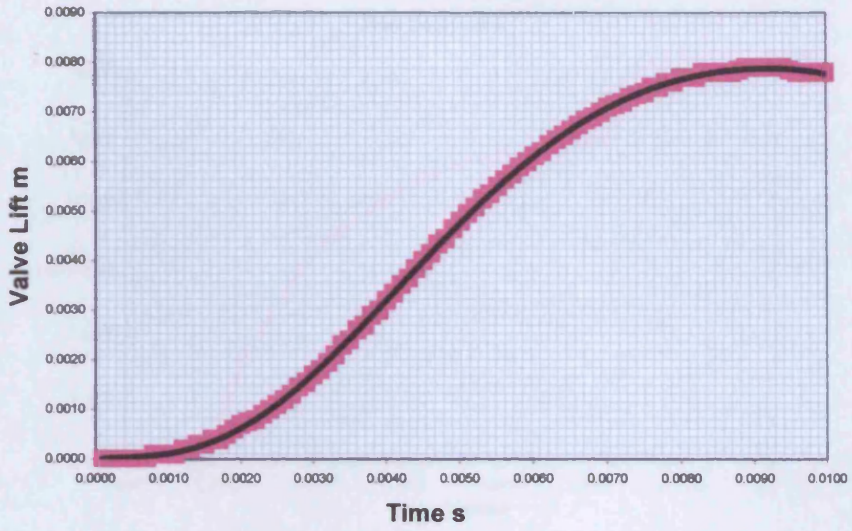

Figure 3.21 - Valve lift curve

The discharge coefficients for the EOCV apparatus were measured using a flow bench and are shown in Table 3.6 and Figure 3.22.

Table 3.6 - EOCV discharge coefficients

Measured Stroke (mm)	Actual Stroke (mm)	Flow (L/s)	Cd	Stroke / Diameter
-	0.0000	0.00	0.0000	0.0000
0.00	0.7653	0.40	0.0025	0.0001
0.25	1.0153	4.70	0.0288	0.0014
0.50	1.2653	15.60	0.0957	0.0048
0.75	1.5153	26.10	0.1601	0.0080
1.00	1.7653	34.00	0.2085	0.0104
1.25	2.0153	42.50	0.2606	0.0130
1.50	2.2653	49.10	0.3011	0.0150
2.00	2.7653	58.70	0.3600	0.0180
2.50	3.2653	65.10	0.3992	0.0200
3.00	3.7653	70.90	0.4348	0.0217
3.50	4.2653	75.00	0.4600	0.0230
4.00	4.7653	77.40	0.4747	0.0237
4.50	5.2653	79.00	0.4845	0.0242
5.00	5.7653	80.10	0.4912	0.0245
5.50	6.2653	80.70	0.4949	0.0247
6.00	6.7653	81.20	0.4980	0.0249
6.50	7.2653	81.30	0.4986	0.0249
7.00	7.7653	81.30	0.4986	0.0249

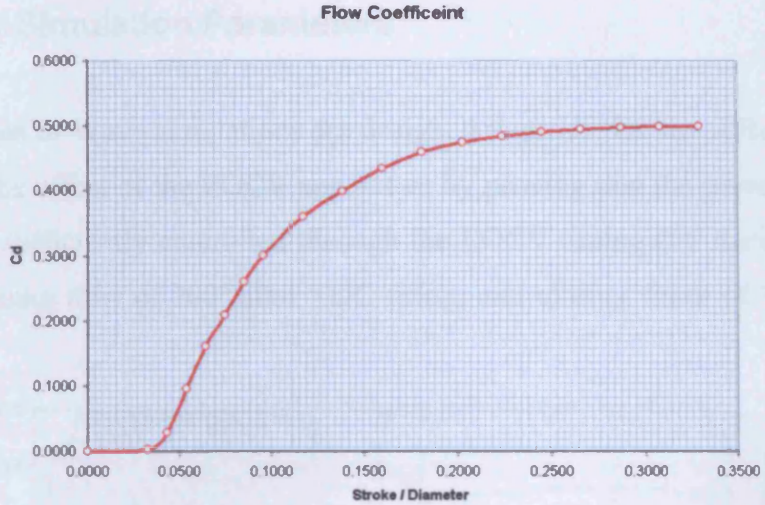

Figure 3.22 – Measured EOCV discharge coefficient

The flow bench data was then used to validate the 3-Dimensional CFD model of the EOCV apparatus in the next stage of the project. The limitation with the method in which the flow-bench has been used to measure the flow through the EOCV apparatus is that it required the EOCV to be fitted to a cylinder head. The values quoted in Table 3.5 are for flows through the EOCV apparatus at various lift positions, and through the normal inlet valves of the cylinder head; thus the discharge coefficients and flow values are lower because of the extra pressure losses incurred. The true values of discharge coefficient for the EOCV apparatus will be higher than that seen in Figure 3.22. The results of the CFD simulation of the EOCV apparatus described in Chapter 4 will be used for this purpose, and are shown in Figure 3.23.

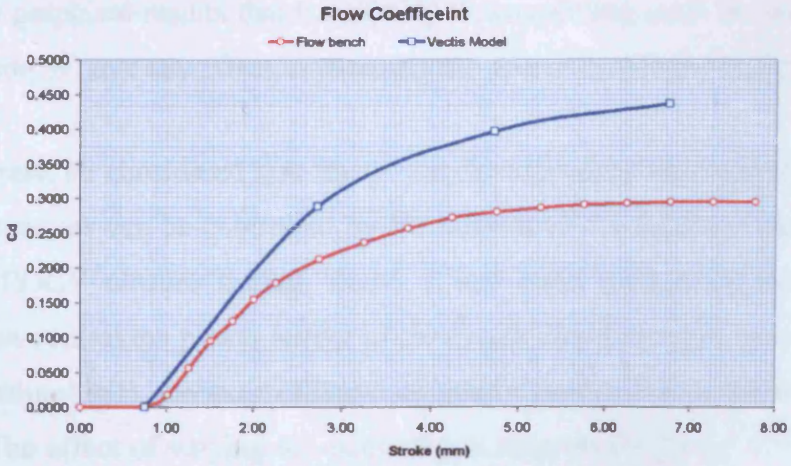

Figure 3.23 – Simulated EOCV discharge coefficient

3.4.2 EOCV Simulation Parameters

The initial series of Wave simulations are designed to prove that the software is capable of modelling the effect of the EOCV apparatus; by proving that the power output of the engine can be sufficiently controlled through the EOCV timing (for these initial results an EOCV opening time of 200° after TDC firing, and closing times of 300° - 580° are investigated).

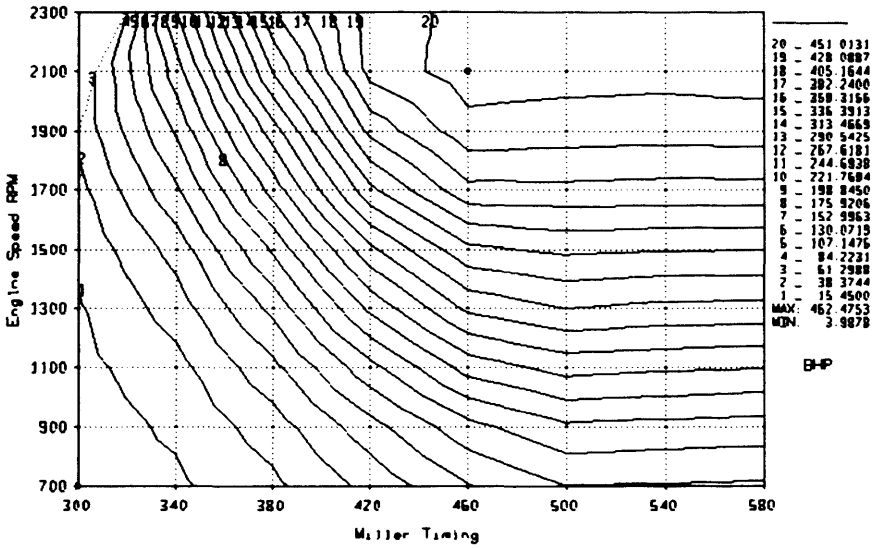

Figure 3.24 – Miller timing effect on predicted BHP

The results of the Wave simulation shown in Figure 3.24 show that through the use of the EOCV apparatus, the power output of an engine can be controlled. It can be also seen from the graphical results that the EOCV closure timing must be earlier than 500° after TDC firing to have any effect in reducing the power developed by the engine.

However, it must be considered that the power developed by an engine equipped with the EOCV apparatus can be controlled by the control of the fuelling characteristics, as well as the EOCV closure timing. Once it had been established that the EOCV technology can control the power output of the Deutz diesel engine (modified to run on compressed natural gas), the most efficient operating parameters for the engine must be established. The effect of varying the equivalence ratio on the power developed by the engine, for a fixed EOCV closure timing (580° after TDC firing), is shown in Figure 3.25.

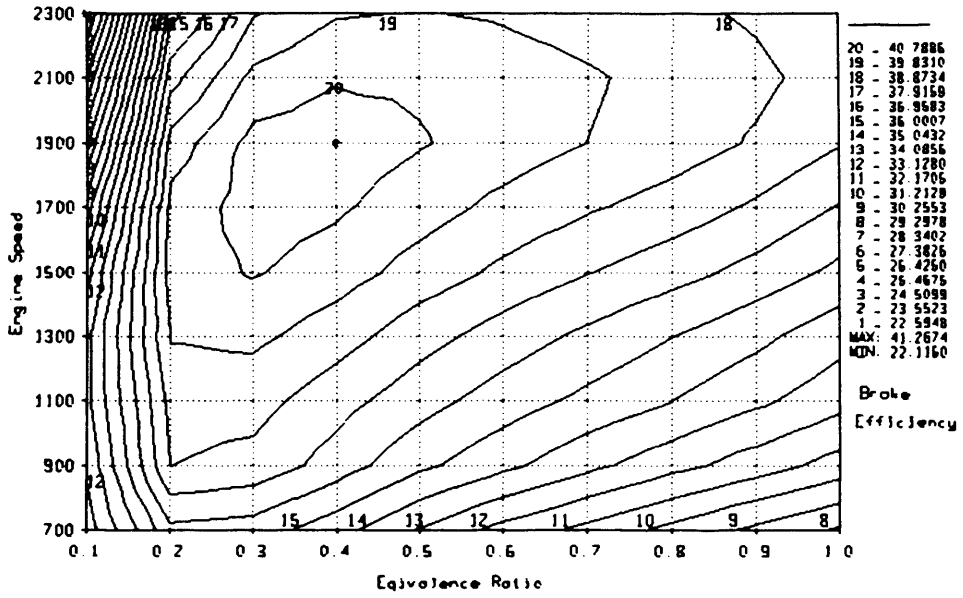

Figure 3.25 – Equivalence ratio effect on predicted engine efficiency

From the results shown in Figure 3.25 it can be seen that for each engine speed the predicted highest brake efficiency occurs at a different equivalence ratio; i.e. for low engine speeds (700-900 RPM) the highest brake efficiency occurs with an equivalence ratio of 0.2, at higher engine speeds an equivalence ratio of 0.45 to 0.5 is predicted to have the highest brake efficiency.

An important operating parameter of a spark ignition engine, such as the converted Deutz / EOCV engine, is the ignition timing. A variation in the ignition timing alters the point at which combustion of the compressed cylinder charge is initiated, which can affect the peak cylinder temperatures and pressures, which in turn affect the power and emissions of the engine.

In order for a complete engine model of the EOCV equipped engine to be constructed, an understanding of the effects of varying the ignition timing is required. It was decided that an investigation into ignition timing would be carried out for equivalence ratios of 0.4 and 0.8 for all operational engine speeds. The predicted variation of the brake efficiency and torque of the EOCV equipped engine for varying ignition timing is shown in Figure 3.26.

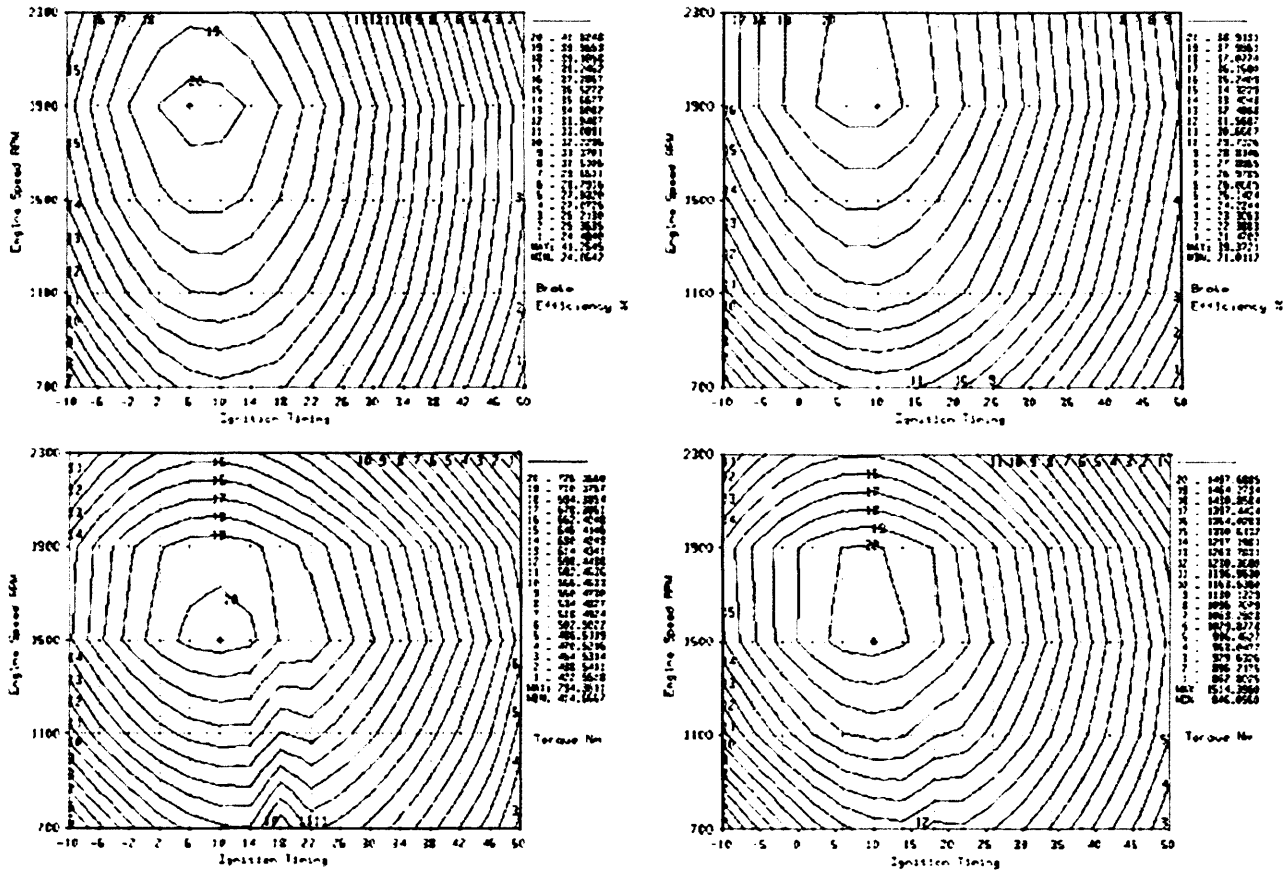

0.4 Equivalence Ratio

0.8 Equivalence Ratio

Figure 3.26 – The effect of ignition timing on engine torque and efficiency

From an examination of the results shown in Figure 3.26 it can be seen that different equivalence ratios require different ignition timings if peak efficiency and torque values are to be obtained. For an equivalence ratio of 0.4, an injection timing of +8° provides the highest torque and efficiency for all engine speeds; for an equivalence ratio of 0.8 an injection timing of +10° is the optimum.

It can also be seen from the results discussed here that there are several variables that must be controlled independently if the optimum setting for engine operating efficiency are to be obtained. For each required engine speed and load output there are many different combinations of EOCV closure timings, fuel equivalence ratios, ignition timings and turbocharger waste gate / variable geometry actuator settings that can be used. For these initial investigations the effect of different combinations of EOCV timing, equivalence ratios and ignition timings are explored.

3.4.3 EOCV Model Results

The model of the NoNOx test engine was used to simulate the maximum load conditions determined for the Deutz 1015 diesel engine. Table 3.7 displays the predicted efficiencies and emissions.

Table 3.7 – NoNOx predicted 100% load results

Speed RPM	Power BHP	Torque Nm	Brake Efficiency	BSFC kg/kWhr	Equiv. Ratio	NOx ppm	HC g/hr
100% Load (Maximum Throttle)							
700	150	1526	29.24	0.2462	0.9898	2927	7022
900	205.6	1627	31.57	0.2280	1.024	2496	7203
1100	265	1715	33.57	0.2144	0.9867	3408	7113
1300	320	1752	34.69	0.2075	0.9666	3907	7096
1500	370	1757	36.25	0.1986	0.9423	4475	5917
1700	410	1717	37.64	0.1912	0.9122	4968	4397
1900	442	1657	38.85	0.1853	0.8895	4957	2701
2100	442	1499	39.38	0.1828	0.8454	4023	1793
2300	420	1301	39.19	0.1837	0.7831	2974	1927

Comparing the results shown in Table 3.7 to that shown in Table 3.3, it can be seen that in order for the EOCV equipped NoNOx engine to develop the required torque for the 100% load conditions, much higher equivalence ratios are required (and even then the NoNOx engine fails to produce the required power at 900 RPM).

For all engine speeds at the 100% load operating conditions, the NoNOx engine produces higher emissions of NO_X and unburned hydrocarbons. The unburned hydrocarbons are likely to be composed entirely of methane, which is classified as a greenhouse gas. The higher emissions of NO_X however could be a problem if the NoNOx engine is to be considered as a replacement in heavy duty diesel engine applications (such as that of the Deutz 1015 base engine).

The inclusion of the EOCV technology in the NoNOx engine produces a secondary method of controlling the power output of the engine, with the primary method being the equivalence ratio.

Table 3.8 compares the predicted emissions and fuel consumption for three different 50% load operating criterion.

Table 3.8 – NoNOx predicted 50% load results comparison

Speed RPM	Power BHP	Torque Nm	EOCV Closure °	Brake Efficiency	BSFC kg/kWhr	Equiv. Ratio	NOx ppm	HC g/hr
50% Load (High Equivalence Ratio)								
700	75	763	457	26.15	0.2753	0.9922	2596	4928
900	105	831	466	29.44	0.2446	1.026	2434	4690
1100	133	861	468	31.67	0.2273	0.989	3049	4640
1300	160	876	471	32.38	0.2224	0.9673	3245	5169
1500	185	879	473	33.18	0.2170	0.9443	3386	5351
1700	205	859	478	34.03	0.2116	0.9140	3470	5155
1900	211	828	483	35.18	0.2046	0.8912	3322	4373
2100	211	749	484	35.60	0.2023	0.8467	2743	3850
2300	210	650	486	36.00	0.2000	0.7840	1950	3099
50% Load (Medium Equivalence Ratio)								
700	75	763	467	31.39	0.2293	0.6507	883	3260
900	105	831	504	34.33	0.2097	0.6506	887	3263
1100	133	861	502	35.60	0.2022	0.6507	843	3485
1300	160	877	502	36.17	0.1990	0.6508	788	3853
1500	185	878	504	37.01	0.1945	0.6508	759	3706
1700	205	859	505	37.64	0.1912	0.6508	703	3488
1900	211	828	507	38.11	0.1890	0.6510	678	3055
2100	211	749	503	38.11	0.1889	0.6512	585	2752
2300	210	650	499	37.59	0.1917	0.6512	585	2341
50% Load (Low Equivalence Ratio)								
700	75	763	540	34.22	0.2104	0.4999	93	2516
900	105	831	556	36.11	0.1993	0.5200	130	2761
1100	133	861	556	37.38	0.1926	0.5000	88	2958
1300	160	877	544	38.25	0.1881	0.5001	85	3021
1500	185	878	540	39.14	0.1839	0.5001	82	2791
1700	205	859	539	39.84	0.1807	0.5002	78	2381
1900	211	828	537	40.22	0.1790	0.5003	74	2000
2100	211	749	532	40.25	0.1789	0.5048	66	1617
2300	210	650	524	39.68	0.1814	0.5008	60	1411

The results shown in Table 3.8 show that the EOCV apparatus can have a large effect on overall engine efficiency. When a lower equivalence ratio is used in conjunction with a later EOCV closure time, the brake efficiency of the engine can increase by up to 8%.

It can also be seen from Table 3.8 that the use of a later EOCV closure time with a lower equivalence ratio has a large effect on the reduction in the emissions of unburned hydrocarbons. This is possibly because the use of a lower equivalence ratio reduces the mass of fuel contained in each charge, reducing the amount of fuel that can potentially remained unburned due to incomplete combustion.

The total emissions of NO_X are substantially reduced when the late EOCV closure, low equivalence ratio are used. If the NO_X emissions in Table 3.8 are compared to that of the Deutz 1015 engine shown in Table 3.3, it can be seen that the late EOCV closure, low equivalence ratio emissions of NO_X are substantially lower than that predicted for the diesel engine.

From the results shown in Table 3.8 it can be seen that a combination of varying the EOCV timing and equivalence ratio must be used to obtain the high efficiencies and low emissions that are desired throughout the speed and power range of the engine. Using this philosophy a potential predicted power distribution for the EOCV equipped engine (with the final design inlet geometry) is shown in Figure 3.27, additional results are shown in Appendix E.

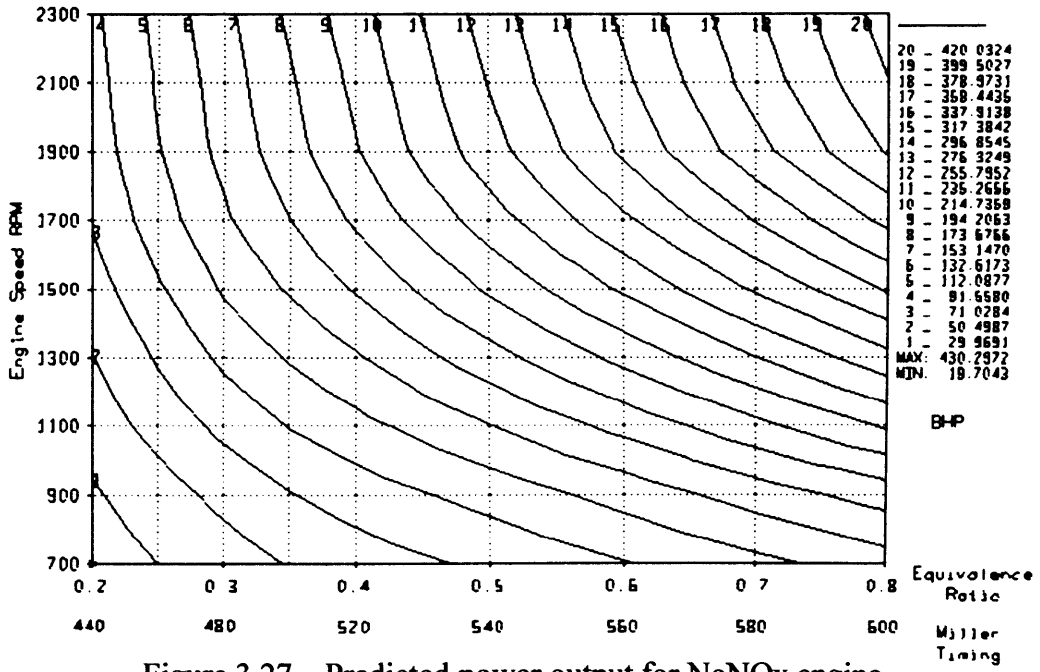

Figure 3.27 – Predicted power output for NoNOx engine.

3.5 EOCV Engine Model Validation

In order to evaluate the computer engine models performance, a series of validation cases were established. Details of the validation cases are shown in the following table.

Table 3.9 – Expanded validation case details

CASE NO	NONOX REF	ENGINE SPEED (RPM)	LAMBDA	EOCV SETTING[1]	VGT POSITION[2]	BMEP (BAR)	EFFICIENCY %	TURBINE SPEED (RPM)
1	12901	1800	1.85	200/580	285	14.6		141000
2	13506	1800	1.80	200/560	220	12.7		
3	12407	1800	1.72	200/560	50	10.4		120000
4	17601	1800	1.65	220/504	100	9.54		104000
5	14710	1800	1.59	200/489	0	6.38		78000
6	14701	1800	1.53	200/458	0	3.76		56000
7	12516	1200	1.59	200/580	635	16.0		135500
8	12001	1200	1.66	200/540	590	12.0		113000
9	12701	1200	1.59	200/481	0	6.0		57000
10	12402	1300	1.69	200/540	610	16.2		140000
11	12807	1500	1.74	200/580	590	16.3		152000
12	125_01	801	1.64	200/580	1000	10.53	0.390	92370
13	125_02	1004	1.61	200/580	875	14.00	0.389	120159
14	130_01	1605	1.44	200/496	350	10.13	0.390	99106
15	130_02	1605	1.55	200/503	350	9.97	0.390	100141
16	140_01	900	1.60	200/473	350	6.58	0.386	38631
17	152	799	1.545	200/458	0	4.79	0.360	27884
18	153	902	1.424	200/462	0	5.62	0.378	31720
19	154	1003	1.521	200/462	0	5.05	0.369	34443
20	155	1113	1.439	200/462	0	5.00	0.370	36626
21	156	1196	1.485	200/462	0	4.74	0.360	40543
22	157	1301	1.431	200/462	0	5.02	0.366	46247
23	158	808	1.531	200/475	0	5.96	0.380	33082
24	159	898	1.501	200/475	0	6.03	0.381	36043
25	160	1001	1.512	200/480	0	6.18	0.380	41202

[1] EOCV setting CA after TDC Open/Close [2] Estimated VGT actuator position (mV readout)

Figures 3.28 and 3.29 compare the actual pressures measured at locations in the inlet and exhaust system of the test engine with the predicted pressures of the Wave engine model for two of the test cases. There is good agreement between the simulated and measured pressures within the inlet system, with the simulated results being in phase with the measured values and having similar amplitudes. It can also be seen that the simulated and measured exhaust pressures display a very good agreement.

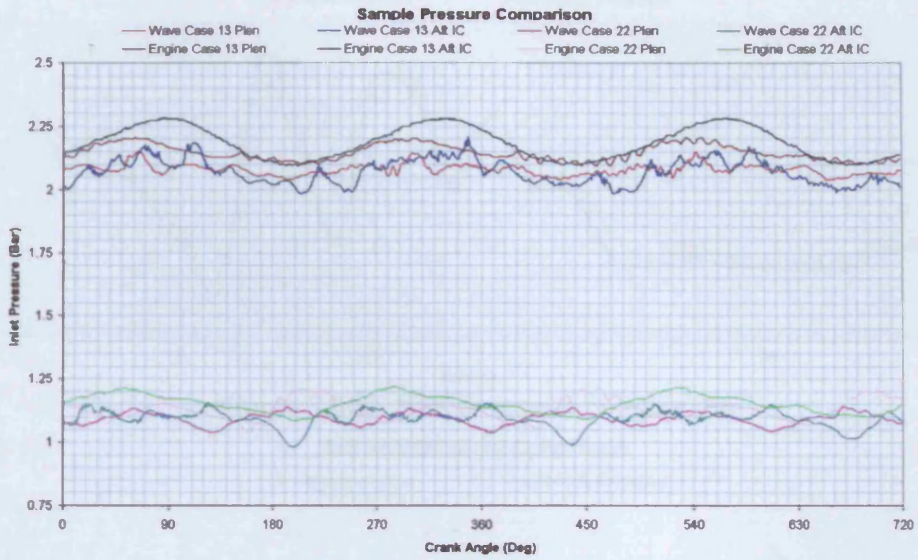

Figure 3.28 – Inlet system pressure comparison

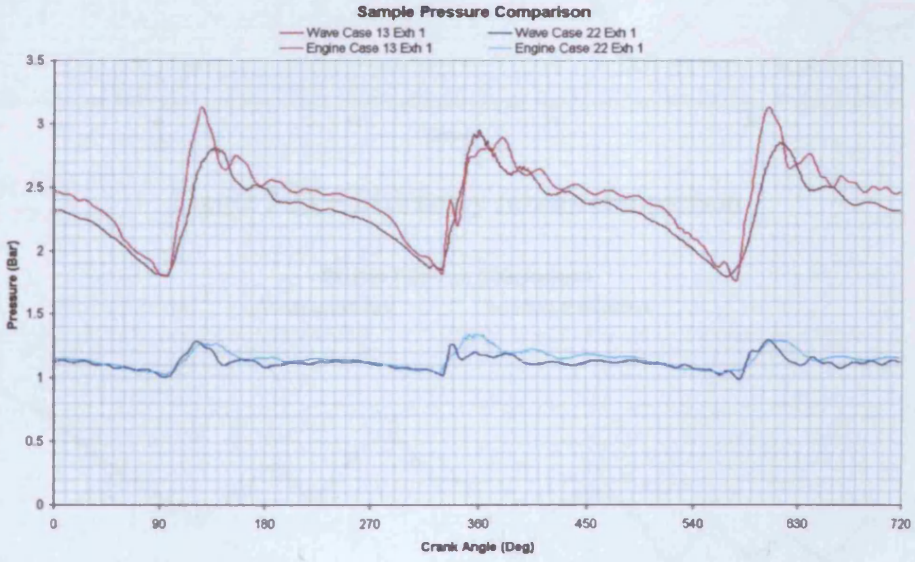

Figure 3.29 – Exhaust pressure comparisons

The results of the validation case simulations are shown in the following series of graphs; where the computer predictions are compared (where available) to empirical data obtained from the testing of the actual engine at the NoNOx facility.

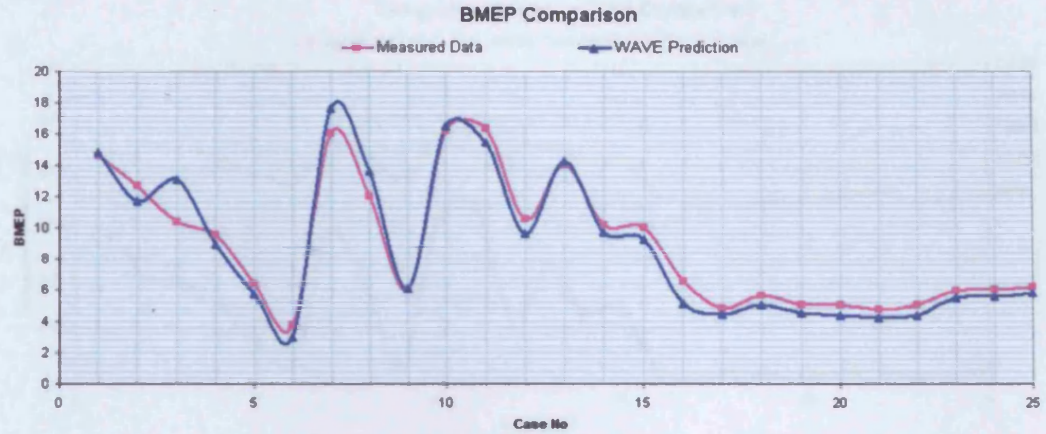

Figure 3.30 – BMEP results comparison

Figure 3.31 – Efficiency results comparison

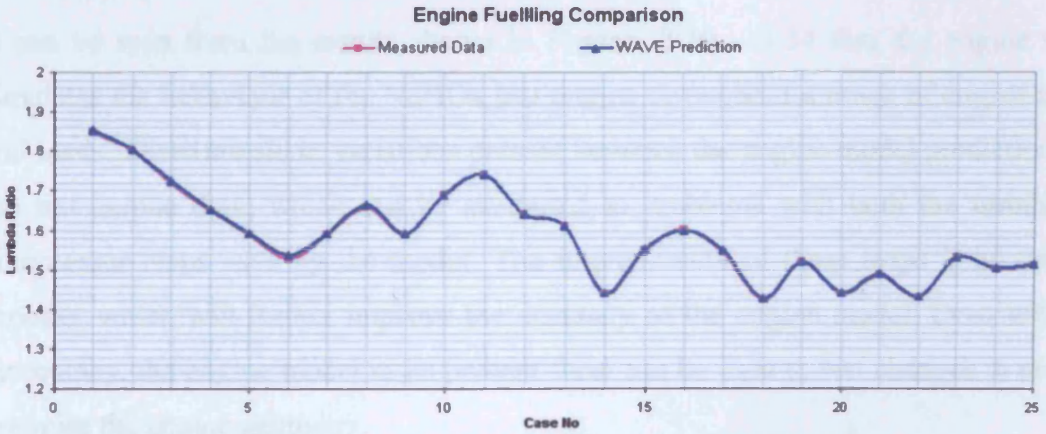

Figure 3.32 – Fuelling results comparison

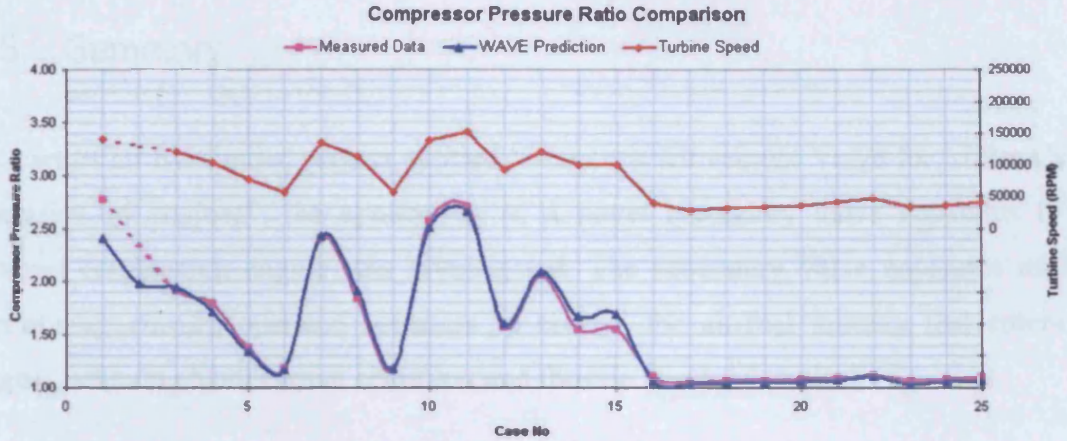

Figure 3.33 – Compressor results comparison

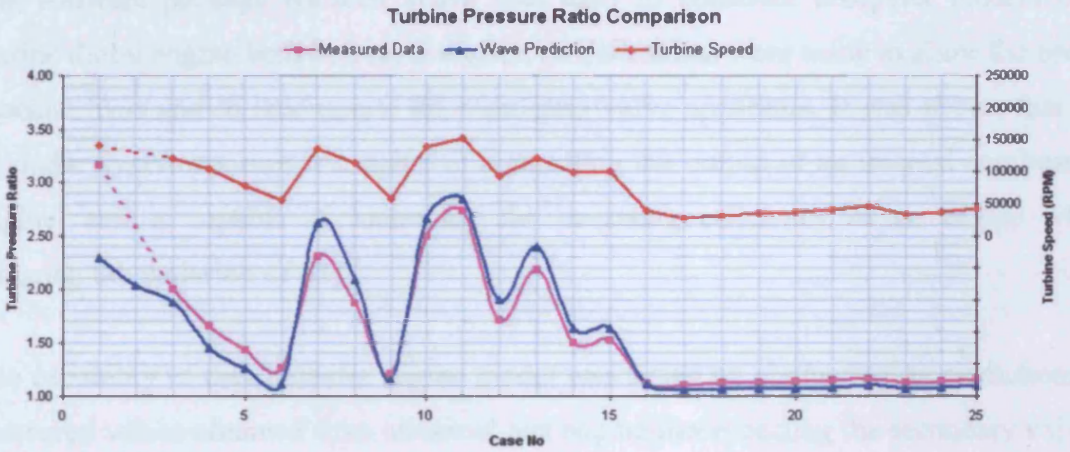

Figure 3.34 – Turbine results comparison

It can be seen from the results shown in Figures 3.30 – 3.34 that the engine model simulates the behaviour of the NoNOx test engine throughout a range of engine speeds and loads. There are slight variations present between the engine model predictions and the test engine data; which can be attributed to problems with both the turbine and compressor maps used by the model. The improvement of these maps is an ongoing process, which will further improve the accuracy of the engine model. Even with this inaccuracy, the engine model in its present form can be used to test changes in order to optimise the engine geometry.

3.5 Summary

As part of an EU funded project entitled "Magnetic Movement Valve for Miller Cycle operation of engines", the application of a novel secondary valve apparatus to an internal combustion engine was investigated. The secondary valve apparatus utilises electromagnetically operated actuators to control the air/fuel mixture that enters an engine, allowing Miller cycle operation and throttle free load control.

The software package Ricardo Wave was used to construct computer models of a marine diesel engine both before, and after, modifications were made to allow the use of gaseous fuels and to incorporate the secondary valve apparatus. It was shown that the secondary valve concept is capable of controlling the output of an internal combustion engine, and is capable of increasing the operating efficiency of an engine while reducing the emission of NO_X.

The capability of the computer engine model was tested by comparing its predictions to measured values obtained from an actual test engine incorporating the secondary valves. It was shown that the computer model closely simulated the behaviour of the physical test engine, and that the computer model was suitable for use in the further development of the secondary valve apparatus.

4 EOCV Simulation

In Chapter 2 of this report an investigation into the economic factors, the developments in engine technology and research into alternative fuels is described. This investigation reveals that there is considerable potential for the utilisation of natural gas derived fuels in conjunction with advanced engine cycles. An initial exploration of this potential, through an EU funded project under the entitled "Magnetic Movement Valve for Miller Cycle operation of engines – reducing NO_X, CO2 and particulate emission", is described in Chapter 3. The results of computer engine modelling described in Chapter 3 show that the Mag-Move secondary valve concept is capable of controlling the output of an internal combustion engine, while increasing the operating efficiency and reducing the emission of NO_X.

The work described in this section involves the construction of a Computational Fluid Dynamics (CFD) simulation of the Electromagnetically Operated-load Control Valve (EOCV) apparatus. Allowing the flow through the valve to be visualized for both steady-state conditions (flow through the valve at set opening positions) and for simulations of an actual opening event of the valve. The results for the Mark 3 EOCV simulation are compared to that of preliminary designs for the Mark 4 EOCV design.

4.1 Computational Fluid Dynamics

In recent years the widespread availability of sufficient computational power, together with the continuing development of the software codes has meant that CFD has become a cost effective alternative to practical testing.

Ricardo Vectis is a commercial three–dimensional CFD software package developed by Ricardo Software. The Vectis program solves the main flow equations (conservation of mass, momentum and energy) and is capable of solving problems involving incompressible and compressible flows using a laminar or turbulent modelling approach.

4.1.1 Ricardo Vectis

This section outlines the basic principles and equations used by the CFD software package Vectis; a more detailed analysis of the theory is explained in the Vectis Theory Manual available from Ricardo (2004).

In the following subsections the governing equations used by the Vectis software package are described, and the background theory behind the turbulence modelling is explained.

Conservation Equations

This section presents the basic conservation equations used by the Vectis software, governing turbulent flow, motion, energy and mass transfer. The standard field variables are replaced by the sum of mass mean values and a small fluctuation; the resulting equations are averaged:

$$\tilde{\Phi} = \Phi + \phi \tag{4-1}$$

The averaged equations for any general scalar variable Φ can be expressed as:

$$\frac{\delta \rho \Phi}{\delta t} + \frac{\delta}{\delta x_i}(\rho U_i \Phi) = \frac{\delta}{\delta x_i}\left(\tau_{\phi L-i} - \overline{\rho u_i \phi}\right) + S_\phi \tag{4-2}$$

where: ρ is the local density

U_i is the local mass-averaged velocity;

S_ϕ is the source term,

and $\tau_{\phi L-i} = \Gamma_{\phi-L} \nabla \Phi$ where $\Gamma_{\phi-L}$ is the molecular diffusivity.

During the averaging process, extra unknown terms appear in the equations, specifically $-\overline{\rho u_i \phi}$. Eddy viscosity turbulence models are used by Vectis to determine the variation of these terms (see later section on Turbulence Modelling). The use of these models allows equation 4-2 to be written as:

$$\frac{\partial \rho \phi}{\partial t} + \frac{\partial}{\partial x_i}(\rho U_i \Phi) = \frac{\partial \tau_{\phi-1}}{\partial x_i} + S_\phi \tag{4-3}$$

where $\tau_{\phi-i}$ represents the effective diffusivity (including molecular and turbulence contributions). The individual conservation equations solved in Vectis are as follows:

Continuity Equation

$$\frac{\partial \rho}{\partial t} + \frac{\partial}{\partial x_i}(\rho U_i) = S_d^m \tag{4-4}$$

where S_d^m represents the mass contribution due to evaporation from any liquid phase (not utilized in this programme of work (=0)).

Momentum Equation

$$\frac{\partial(\rho U_j)}{\partial t} + \frac{\partial}{\partial x_i}(\rho U_i U_j) = \frac{\partial}{\partial x_i}\left[(\mu_L + \mu_t)\left(\frac{\partial U_i}{\partial x_j} + \frac{\partial U_j}{\partial x_i} - \frac{2}{3}\frac{\partial U_k}{\partial x_k}\partial_{ij}\right)\right] - \frac{\partial(p + \rho k)}{\partial x_i} + F_i + S_d^U \tag{4-5}$$

where μ_L and μ_t are the molecular dynamic viscosity and turbulent viscosity respectively. F_i is the body force, such as buoyancy, giving $F_i = -\rho g_i$. k is the turbulence kinetic energy; S_d^U is the momentum contribution from the liquid phase.

Energy Equation

$$\frac{\partial \rho H}{\partial t}+\frac{\partial}{\partial x_i}(\rho U_i H)=\frac{\partial}{\partial x_i}\left[\left(\frac{\mu_L}{\Pr}+\frac{\mu_t}{\sigma_H}\right)\frac{\partial H}{\partial x_i}\right]+\frac{\partial p}{\partial t}+S_d^H+q_W+\omega_{ext}H_{ext}+q_{rad} \tag{4-6}$$

where H is the absolute enthalpy (including thermal enthalpy, kinetic energy and heat of formation), q_W and q_{rad} are the heat flux through the wall and energy contribution from radiation, Pr and σ_H are the Prandtl and turbulent Schmidt numbers, ω_{ext} is the species mass rate added from outside of the CFD domain and S_d^H is the energy contribution from the liquid phase.

Species Transport

Transport equations are solved for the different chemical species that make up the working fluid:

$$\frac{\partial \rho Y}{\partial t}+\frac{\partial}{\partial x_i}(\rho U_i Y)=\frac{\partial}{\partial x_i}\left[\left(\frac{\mu_L}{\sigma_Y}+\frac{\mu_t}{\sigma_{Y-t}}\right)\frac{\partial Y}{\partial x_i}\right]+\omega \tag{4-7}$$

where Y is the mass fraction of a given species, and ω is the rate of production of that species due to chemical reaction (and for the fuel mass fraction, also due to evaporation from the liquid phase).

Passive Scalar Transport

A transport equation can be solved for a passive scalar concentration (which effectively acts as a marker or "dye" in the flow):

$$\frac{\partial \rho Y_{PAS}}{\partial t}+\frac{\partial}{\partial x_i}(\rho U_i Y_{PAS})=\frac{\partial}{\partial x_i}\left[\left(\frac{\mu_L}{\sigma_Y}+\frac{\mu_t}{\sigma_{Y-t}}\right)\frac{\partial Y_{PAS}}{\partial x_i}\right] \tag{4-8}$$

The transport equations contain unknown Reynolds stresses $-\rho\overline{u_i u_j}$ and turbulent scalar fluxes $-\rho\overline{u_i\phi}$ after averaging. This necessitates the use of a turbulence model to provide a set of approximate equations that govern the distribution of the second order fluctuation within the flow.

Turbulence Modelling

The turbulent stresses and turbulent scalar fluxes physically represent the diffusive transport of momentum and scalar properties due to turbulence. Turbulent viscosity models are based on Boussinesq's assumption, which assumes that turbulent stresses are linearly related to the rate of mean flow strain, with a proportionality factor - the turbulent viscosity. This is the same stress-strain relation as a Newtonian fluid in laminar flow:

$$-\rho\overline{u_i u_j} = \mu_t\left(\frac{\partial U_i}{\partial x_j}+\frac{\partial U_j}{\partial x_i}\right)-\frac{2}{3}\partial_{ij}k \tag{4-9}$$

Similarly, the turbulent scalar fluxes are given through

$$-\rho\overline{u_i\Phi} = \frac{\mu_t}{\sigma_\Phi}\frac{\partial\Phi}{\partial x_i} \tag{4-10}$$

Thus, the turbulent viscosity μ_t is taken as an isotropic property of the flow, which changes with time and position. Different models provide different formulae for μ_t. Vectis uses the standard $k-\varepsilon$ turbulence model and the RNG (Renormalization Group) $k-\varepsilon$ turbulence model.

The turbulent viscosity is obtained from the velocity scale u' and a length scale l that is characteristic of the turbulent fluctuations.

$$\mu_t = c_\mu u' l \tag{4-11}$$

In the $k-\varepsilon$ model, the length scale is defined by

$$l = \frac{k^{\frac{3}{2}}}{\varepsilon} \tag{4-12}$$

where: $k = \frac{u_i u_j}{2}$ and $\varepsilon = \nu \frac{\partial u_i}{\partial x_j} \frac{\partial u_j}{\partial x_i}$ represent the turbulent kinetic energy and its dissipation rate.

The characteristic velocity u' is given by $u' = k^{1/2}$. Thus the turbulent viscosity is obtained from

$$\mu_t = \rho \nu_t = c_\mu \rho \frac{k^2}{\varepsilon} \tag{4-13}$$

where c_μ is nearly constant for high Reynolds number flows.

The transport equations for k and ε are as follows:

$$\frac{\partial \rho k}{\partial t} + \frac{\partial}{\partial x_i}(\rho U_i k) = \frac{\partial}{\partial x_i}\left[\left(\mu_L + \frac{\mu_t}{\sigma_{k-t}}\right)\frac{\partial k}{\partial x_i}\right] + G - \rho\varepsilon \tag{4-14}$$

$$\frac{\partial \rho \varepsilon}{\partial t} + \frac{\partial}{\partial x_i}(\rho U_i \varepsilon) = \frac{\partial}{\partial x_i}\left[\left(\mu_L + \frac{\mu_t}{\sigma_{\varepsilon-t}}\right)\frac{\partial \varepsilon}{\partial x_i}\right] + \frac{\varepsilon}{k}\left(c_1 G - c_2 \rho\varepsilon + c_3 \rho k \frac{\partial U_i}{\partial x_i}\right) \tag{4-15}$$

where $G = -\rho u_i u_j \frac{\partial U_i}{\partial x_j}$, the generation rate of turbulence energy. The coefficients appearing in the turbulence modelling equations take the standard values:

Table 4.1 – Vectis turbulence modelling coefficients (Vectis Theory Manual)

	σ_k	σ_ε	σ_H	σ_{Y-1}	c_μ	c_1	c_2	c_3
Standard	1.0	1.22	0.9	0.9	0.09	1.44	1.92	0.373
RNG	0.719	0.719	0.9	0.9	0.0845	1.42	c'_2	0.373

In the RNG model (Renormalization Group) the coefficient-of-dissipation term in the ε equation is not a constant as in the standard model. It is the sum of a constant and a term modified by the ratio of the turbulence time scale and the mean flow time scale:

$$c'_2 = 1.68 + \frac{C_\mu \eta^3 \left(1 - \frac{\eta}{\eta_0}\right)}{1 + \beta\eta^3} \tag{4-16}$$

where $\eta_0 \approx 4.38$, $\beta = 0.012$, $\eta = \frac{t_{turbulence}}{t_{mean-flow}}$, $t_{turbulencce} = \frac{k}{\varepsilon}$, $t_{mean-flow} = \left(2S_{ij}S_{ij}\right)^{0.5}$ and

$$S_{ij} = \frac{\partial U_i}{\partial x_j} + \frac{\partial U_j}{\partial x_i}.$$

The overall performance of the two $k-\varepsilon$ variants is quite similar. However, for flows with high strain rates, the RNG model tends to reduce the turbulence through increased dissipation.

4.1.2 A Vectis Simulation

A Vectis simulation is split up into stages (or Phases), each of which will now be explained (more detailed information is in the Vectis Users Manual).

Phase 1 – Geometry Input and Preparation

Phase 1 is the pre-processing stage of a Vectis simulation in which the geometry / boundaries are defined. The geometry is imported into the Phase 1 Graphical User Interface (GUI) using the Stereolithography (.STL) file format; this is a 3D file format that is compatible with the majority of engineering CAD systems.

The integrity of the geometry file must be checked and any 'holes' that may be present stitched. Boundaries can then be assigned to the geometry, whereby boundary numbers are created for each separate model surface which can be later defined as either a 'Wall' or an 'Inlet/Outlet'.

The global mesh parameters are specified for the entire geometry; areas of the geometry where a more detailed analysis is desired can be refined using 'IJK' blocks, whereby the mesh resolution is increased within the specified local volume.

Phase 2 – Mesh Generation

This stage is an automatic process that produces a locally refined Cartesian mesh suitable for a fluid flow analysis; the meshing process is non-interactive and is controlled by the mesh input file generated during Phase 1.

The mesh generation process automatically refines the mesh near the geometry boundaries; the refined cells are then truncated to conform to the geometry. The degree to which the mesh is refined close to the boundaries is specified during the mesh set-up procedure in Phase 1.

Phase 4 – Cell Connectivity

This process also occurs automatically, and forms the last stage of the geometry pre-processing. The cell data generated by the Phase 2 meshing process is examined, the connectivity information between adjacent cells is established and a geometry data file suitable for the solving stage is created.

Phase 5 – VECTIS Solver

Phase 5 is the solution stage of a Vectis simulation. The geometric and connectivity data contained in the Phase 4 output files is used together with a controlling input file (see Appendix F for sample Vectis input file) to carry out the fluid dynamics calculations.

The controlling input file is created using the Phase 5 GUI. Simulation parameters specified in this file include: the equations to be solved; numerical schemes to be used in solution; time step and global convergence criteria; mesh and boundary motion specifications; boundary conditions; initial conditions; fluid property data as well as data on combustion or spray simulations.

Phase 6 – Post-processing

The results produced by Phase 5, the main CFD solver, are displayed in the Phase 6 GUI. Output plots can be created from the results or flow data exported.

4.2 Model Building

This section describes the model building process used to construct the simulation of the EOCV technology. In order to construct a computer simulation of the EOCV apparatus, detailed geometrical and operational data is required.

4.2.1 EOCV Geometry

A 3D model of the EOCV apparatus fitted to the test-engine is shown below in Figure 4.1. This geometry was created using the Unigraphics solid modelling CAD package. This solid model of the EOCV apparatus is not suitable for direct importation into the Vectis pre-processor, as only the geometry of the surfaces to which the fluid flow is exposed is required.

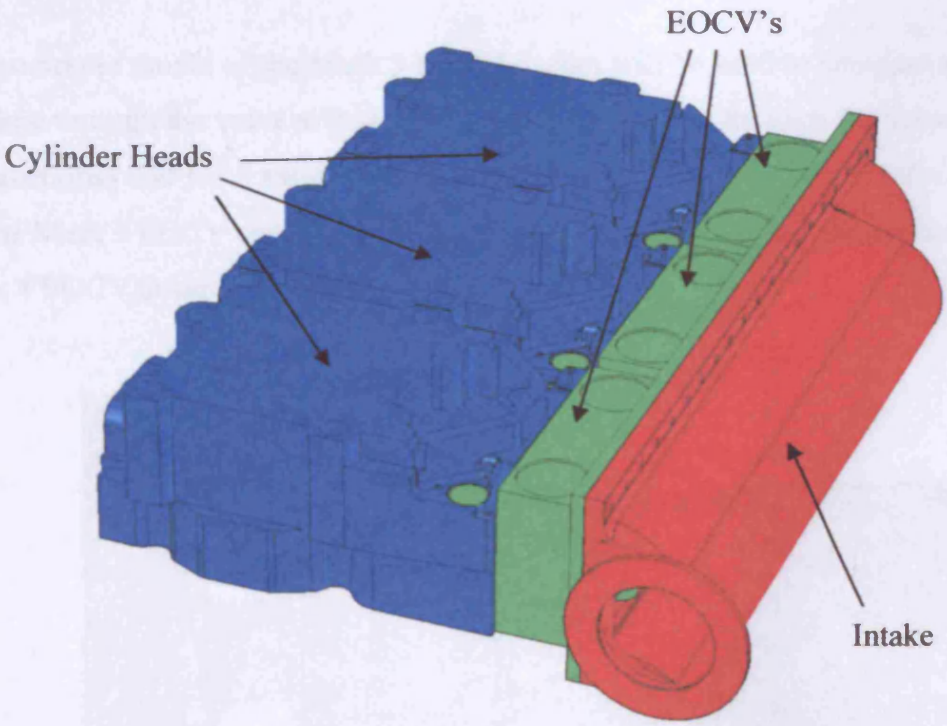

Figure 4.1 – EOCV CAD model.

A 'negative print' of the valve model must be created; this can then be exported to Vectis using the Stereolithography file format.

4.2.2 Geometry Creation

Using the CAD model of the EOCV apparatus, a solid model that represents the flow volume can be created. It is necessary to create a model of the flow volume for every valve lift that is to be simulated by Vectis; this can be done by creating a solid model representing the enclosed volume within the valve body, and then subtracting the volume representing the valve head for each valve lift position. Figure 4.2 shows an example of a solid model representing the flow boundaries created for the Mark 3 EOCV simulation. The air flows into the model through the inlet surface (left surface in Figure 4.2), through the three separate inlet paths into the main section of the valve where the 'valve spindle' is situated (with a valve lift of 6mm in this case), the air flows around the spindle though the two exits paths and into a volume representing the inlet port of the engine.

The computer model of the Mark 3 EOCV design will be used to simulate and visualize the flow through the valve at steady-state conditions (flow through the valve at set valve lift positions) and for a simulation of an actual opening event of the valve. The results for the Mark 3 EOCV simulation will be compared to that of preliminary designs for the Mark 4 EOCV design.

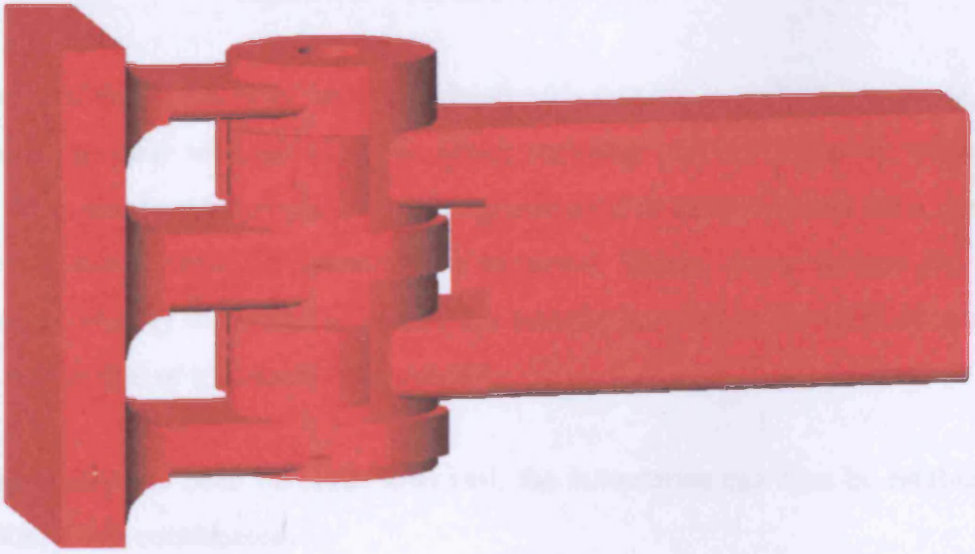

Figure 4.2 – Example flow volume geometry.

4.2.3 Vectis Phase 1

The Vectis Phase 1 GUI with the imported geometry of the EOCV apparatus for the 6mm lift case is shown in Figure 4.3. The main viewing window displays the geometry which can be modified using the various 'stitching', 'slicing' and 'marking' options, the valve spindle can also clearly be seen positioned within the main body of the valve.

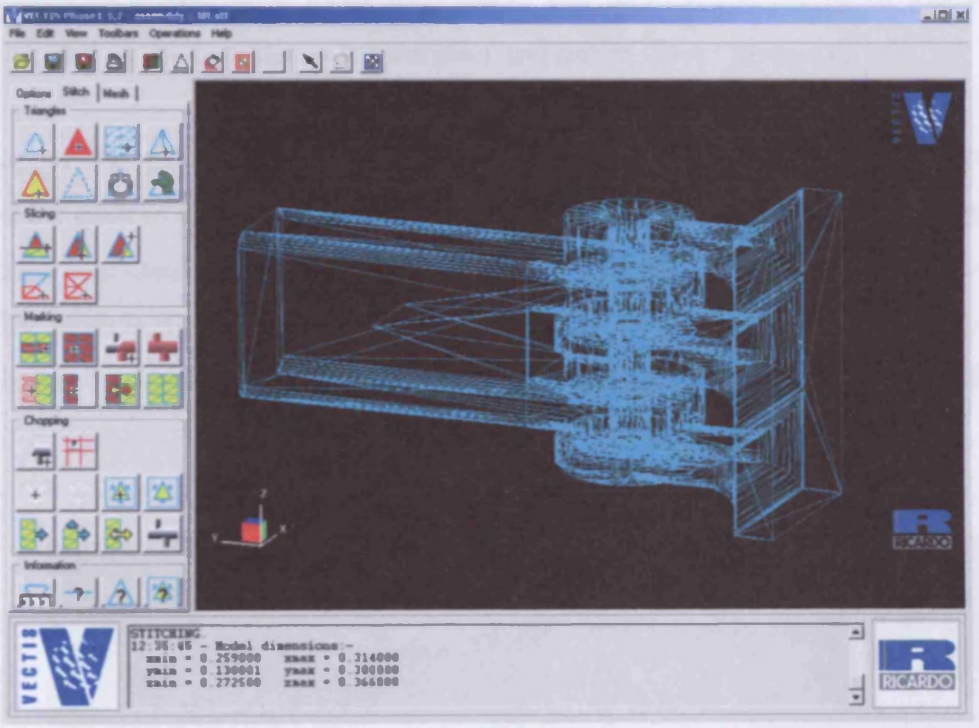

Figure 4.3 - Vectis Phase 1 GUI

The geometry of the valve-body and valve-head arrangement is quite complicated, and therefore a great deal of time must be spent carrying out the required 'stitching' operation. Also, due to the complexity of the geometry it is commonplace for a number of mistakes to occur when the geometry is imported. Hence, every surface that was created must be closely examined to ensure the boundaries used in the CFD simulation accurately reflect that of the actual components.

Once the geometry has been carefully checked, the boundaries can then be established and the global mesh constructed.

4.2.4 Boundary / Mesh Specification

The specification of the different boundaries for these simplified simulations is straightforward. The triangles that define the geometry must be grouped together, i.e. the triangles that represent the wall must be in one group, and the inlet and outlet triangles in additional separate groups. The boundary IDs assigned to these groups are then referred to in the main input file, where the surface conditions of the wall are defined as well as the conditions for the inlet and outlet flow / pressures.

The setup of the global mesh is also straightforward; the number of sub-divisions is specified for each of the Cartesian planes. Where necessary, IJK local refinement blocks can be used to increase the resolution of the mesh in areas of importance; in the case of the EOCV models the mesh should be more detailed in the area surrounding the valve-head. Figure 4.4 shows the 3-dimensional mesh spacing used for the 6mm lift valve model.

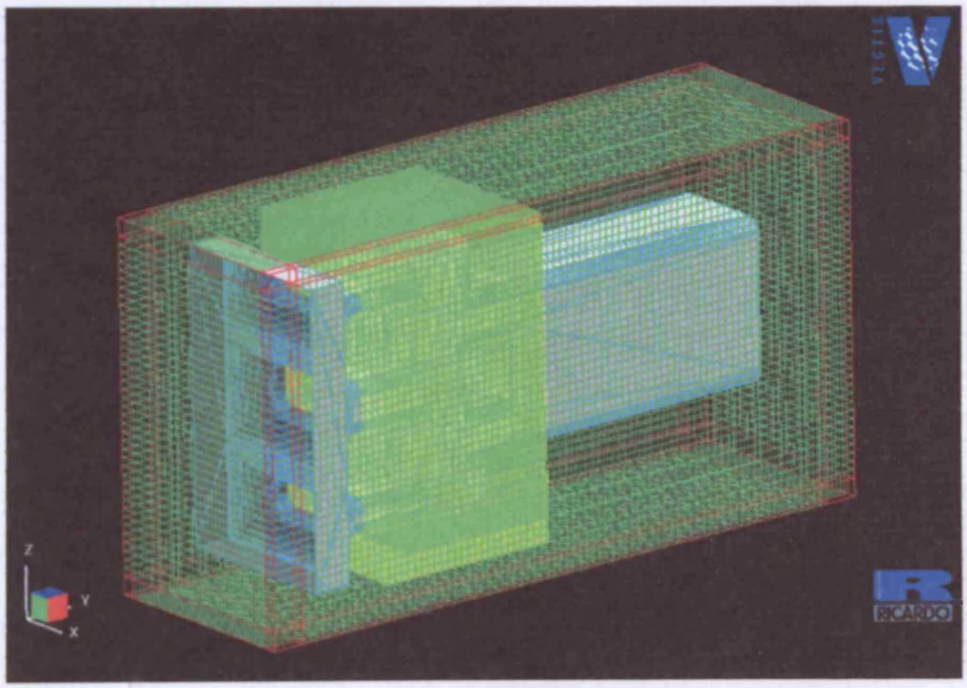

Figure 4.4 – Mesh set-up

4.2.5 EOCV Lift Parameters

Actual flow measurements for the EOCV apparatus have been obtained using a flow-bench - see Table 4.2. However, these values were obtained when the EOCV apparatus was attached to an engine cylinder head. In order for the results of the EOCV simulations to be compared with that of past and future flow-bench measurements, the actual pressure differential that is applied across the valve-head must be estimated.

Table 4.2 – Flow-bench data

MEASURED STROKE (mm)	ACTUAL STROKE (mm)	FLOW (L/s)	Cd	STROKE / DIAMETER
-	0.0000	0.00	0.0000	0.0000
0.00	0.7653	0.40	0.0014	0.0324
0.25	1.0153	4.70	0.0170	0.0430
0.50	1.2653	15.60	0.0564	0.0536
0.75	1.5153	26.10	0.0944	0.0642
1.00	1.7653	34.00	0.1230	0.0748
1.25	2.0153	42.50	0.1537	0.0854
1.50	2.2653	49.10	0.1776	0.0960
2.00	2.7653	58.70	0.2123	0.1172
2.50	3.2653	65.10	0.2354	0.1384
3.00	3.7653	70.90	0.2564	0.1595
3.50	4.2653	75.00	0.2712	0.1807
4.00	4.7653	77.40	0.2799	0.2019
4.50	5.2653	79.00	0.2857	0.2231
5.00	5.7653	80.10	0.2897	0.2443
5.50	6.2653	80.70	0.2919	0.2655
6.00	6.7653	81.20	0.2937	0.2867
6.50	7.2653	81.30	0.2940	0.3079
7.00	7.7653	81.30	0.2940	0.3290

4.2.6 Flow Bench Measurement Conditions

The flow bench apparatus, with the EOCV installed on the cylinder head, is shown in Figure 4.5. The flow data that was obtained for this setup (Table 4.2) together with the calculated discharge coefficients are actually measurements of the inlet flow into an engine cylinder. These measurements are the total flow through the two EOCV openings, the cylinder inlet ports and the two standard valves.

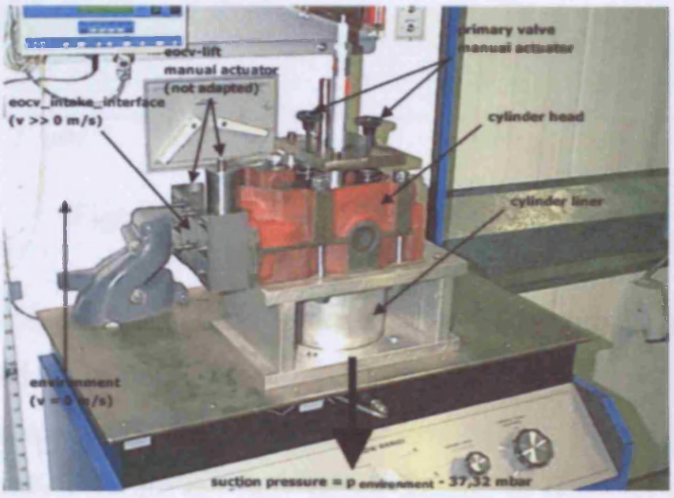

Figure 4.5 – Flow-bench set-up

A series of simulations were carried out to estimate the required pressure differential to be applied across the EOCV model, this value can then be used in the CFD simulations of the Mark 3 and subsequent EOCV designs. Figure 4.6 displays the flow convergence for a selection of pressure differentials that are applied across the 6mm open valve.

From the results displayed in Figure 4.6 it can be seen that for the 6mm open EOCV apparatus, the simulated flow through the valve matches the flow recorded using the flow bench when a pressure difference of approximately 18 mbar is applied. The pressure difference that was applied during the flow bench testing of the EOCV was 37.32 mbar.

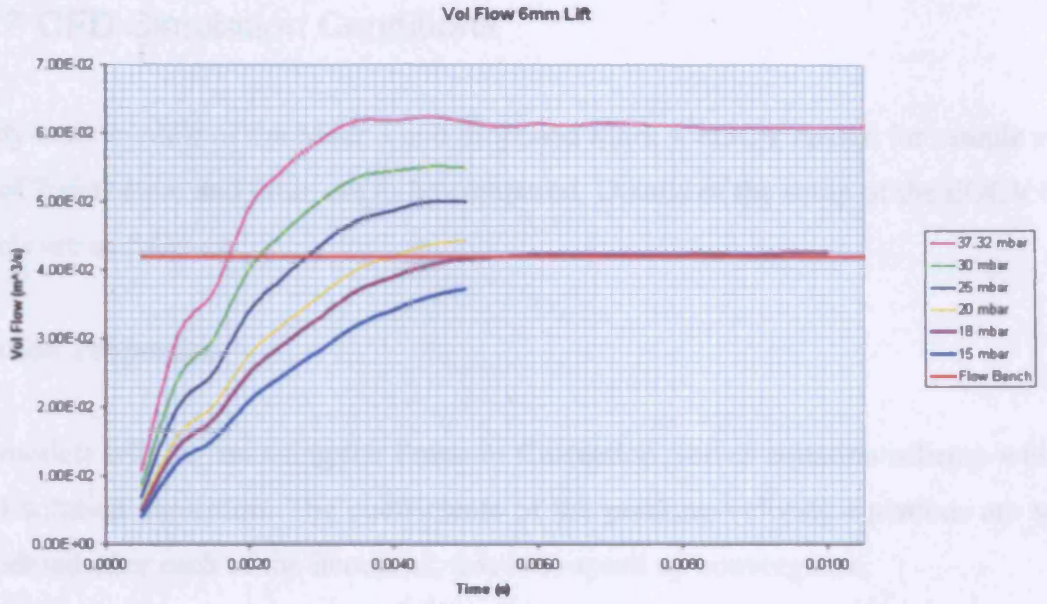

Figure 4.6 - Pressure differential results

During the flow bench testing, the pressure was applied across the EOCV apparatus while it was attached to the inlet side of a cylinder head from the NoNOx V6 engine. It can therefore be concluded that the applied pressure used in the CFD simulations must be less than that applied during the flow bench testing, as the inlet ports and valves of the engine (which are not modelled in this section) cause additional pressure losses which affect the flow.

For the simulation of the Mark 3 EOCV design the total pressure difference between the inlet and outlet boundaries is to be set to 18 mbar, which will allow a direct comparison to be made between the model predictions and the flow-bench results. The same pressure differential will be applied to the simulations of the proposed Mark 4 EOCV design and any further proposed designs. Once a final design for the Mark 4 EOCV has been decided upon, the results of the CFD simulations can then be validated by the flow-bench testing of a physical prototype.

4.2.7 CFD Simulation Conditions

Steady-state models of the Mark 3 and proposed Mark 4 EOCV design for sample valve lifts of 2mm, 4mm and 6mm are to be compared. Details of the setup of the EOCV CFD models are as follows:

Iteration Properties

The models will be run using the Pressure Correction Solver equation scheme with the PISO solution algorithm. The coefficients of the pressure-velocity equations are set to be updated after each of the iterations; this is to speed up convergence.

Global convergence criterion :	1e-008
Model start time:	0.0000s
Model end time:	0.0075s
Time step length:	5e-005s
Post-pro. Spacing:	0.0005s

Models

Only the species data and physical parameter models are needed, as the simulation does not require the complex modelling schemes for combustion, sprays etc. These initial EOCV models do not require any boundary, line or patch motion, as the valve head is stationary throughout each simulation.

Solving

All the momentum equations as well as pressure, turbulence and the passive scalar equations are to be solved in the EOCV simulations.

Boundary Conditions

The inlet boundary specification is to be set to 'Default Normal', and the inlet boundary conditions are to be as follows:

Pressure:	102237 Pa
Temperature:	293.5 K

The outlet boundary specification is to be set to 'Uniform', and the outlet boundary conditions are to be as follows:

Pressure:	100413 Pa
Temperature:	293.5 K

The wall roughness setting is: 0.00005 m.

Initial Conditions

The initial conditions of the EOCV model are specified as follows:

Pressure:	100415 Pa
Temperature:	293.5 K
Turbulence length scale:	0.0005m (Default setting)
Turbulence u':	0.1 m/s (Default setting)

Turbulence Modelling

Simulations were run to investigate the suitability of the two turbulence models used in the Vectis software (the standard $k-\varepsilon$ model and the RNG model); it was decided that as the numerical results from both models were nearly identical that the standard $k-\varepsilon$ model should be used for all subsequent simulations.

4.3 Steady-state EOCV Simulations

The results of a comparison between the flow-rates predicted by the CFD software and that measured using the flow bench for the Mark 3 EOCV design are shown in Figure 4.7. It can be seen that the two curves are very similar throughout the stroke of the valve.

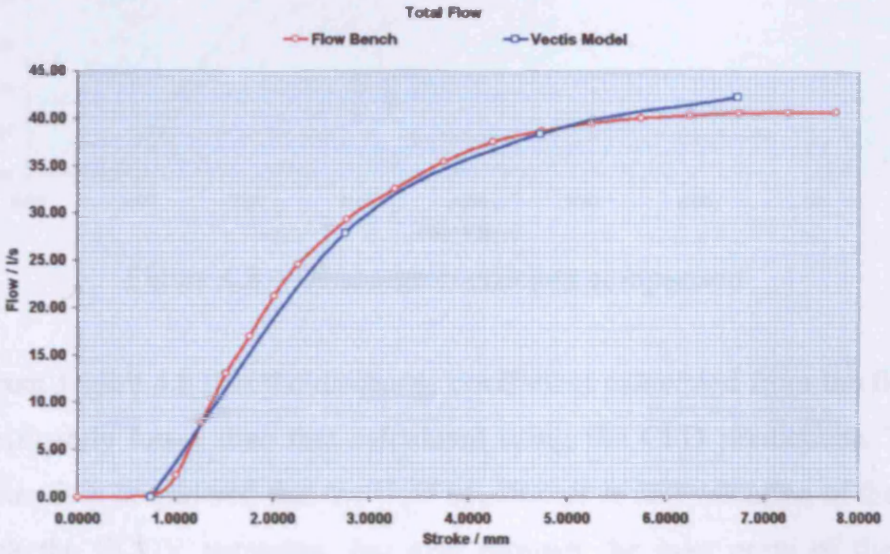

Figure 4.7 – Flow rate comparison

These results can be used to calculate the discharge coefficient (C_D) predicted by the CFD model. The equation relating the flow rate Q to the C_D value is as follows:

$$Q = C_D A \sqrt{\frac{2\Delta P}{\rho}} \tag{4-17}$$

where A is the cross sectional area (0.00177 m² for a single EOCV valve).

ΔP is the applied pressure difference (18 mbar, see Section 2.2.1)

ρ is the density of the fluid used.

A comparison can be made between the discharge-coefficient calculated using the flow bench results and that obtained from the CFD predictions; this is shown in Figure 4.8.

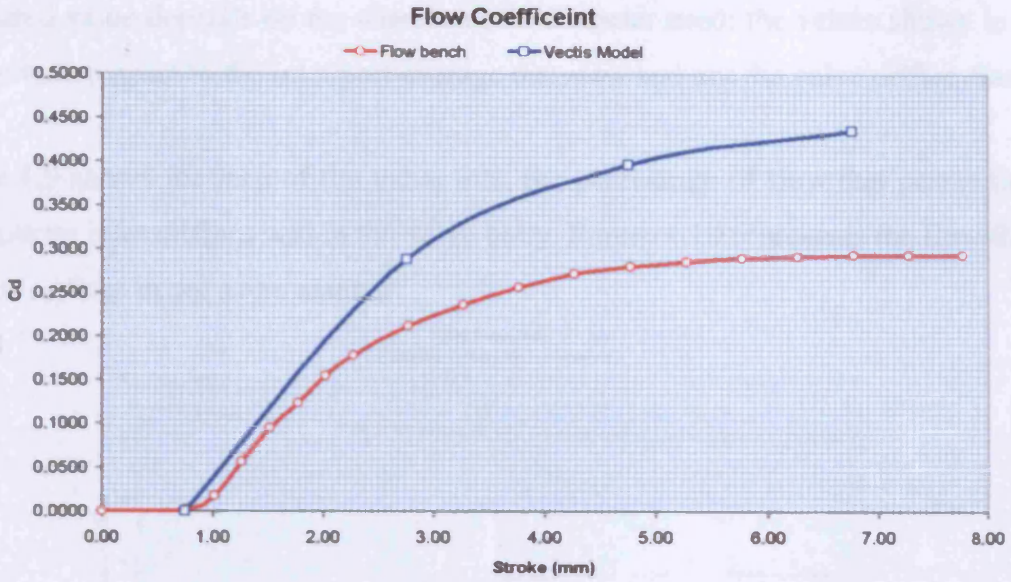

Figure 4.8 – Discharge coefficient comparison

It is clear from Figure 4.8 that the discharge coefficient calculated from the flow bench data is significantly lower than that calculated using the CFD predictions. This is as expected when it is considered that the flow bench data is an evaluation of the flow not only through the ECOV apparatus, but also through the inlet ports of the engine's cylinder head.

The values obtained for the discharge coefficient vary depending upon the stroke of the valve-head. From an examination of the graph it can be seen that when the EOCV is fully open (valve-head stroke ≈ 7.0mm) the discharge coefficient reaches its maximum value of approximately 0.45. The values for the discharge coefficient calculated from the CFD model reflect the degree of turbulence that is present within the flow through the valve.. During the evaluation / design of subsequent EOCV apparatus, a reduction in these losses should be sought in order to improve the overall valve performance.

The values of the discharge coefficients that are obtained from the CFD analysis of the Mark 3 and subsequent valve designs will be used for the modelling of the EOCV apparatus within a general engine model. This will allow any improvements in the EOCV technology to be instantly evaluated and any increase in engine efficiency predicted. Care must be taken when interpreting the discharge coefficient value, as the

calculated value depends on the characteristic diameter used; the values shown in Table 4.2 are with respect to the inlet port average diameter and not the valve orifice diameter.

Figure 4.9 shows for each of the valve lifts, the percentage of flow that passes through the separate inlet orifices within the valve body. Figure 4.10 represents the flow through the exit orifices in the same manner.

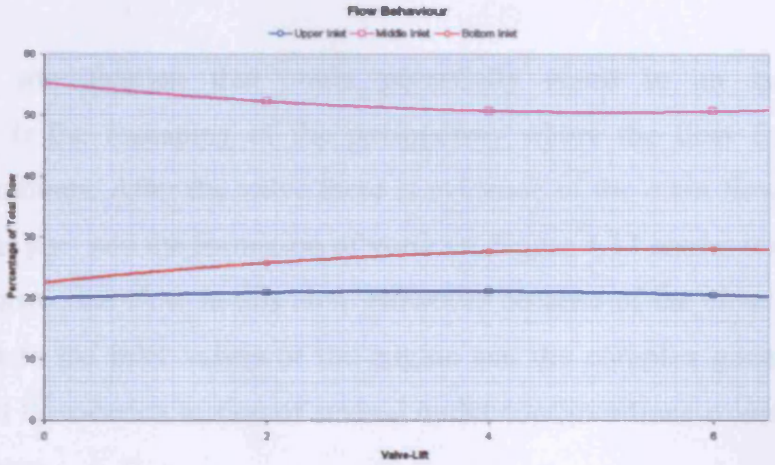

Figure 4.9 – Inlet flow behaviour.

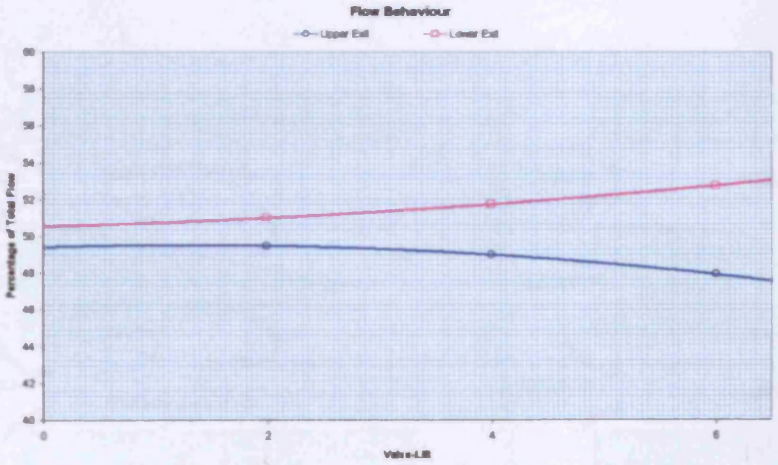

Figure 4.10 – Outlet flow behaviour.

It can be seen from Figure 4.10 that similar volumes of air flow through each valve exit orifice for all opening positions - the maximum flow difference between the two orifices is of the order of 8% of the total flow when the valve is wide open.

From Figure 4.9 it can be seen that the flow through the middle inlet orifice is approximately the sum of the flow through the other two inlet orifices. This is as

expected as the middle orifice is not only larger in size, but is located such that its flow can be shared between both exit orifices. The top inlet orifice has the lowest flow rate of the three inlet orifices, due to the fact that it is the smallest of the three. Subsequent valve designs with top and bottom orifices of equal size may result in an increase in the overall valve performance, as the flow into the valve and the pressures within the valve would be more evenly distributed.

One design modification that could potentially result in an increase in valve performance is the reshaping of the passageway where the flow from the two exit orifices recombines. After the valve there is evidence of the main flow separating from the wall of the port and the formation of vortices. Figure 4.11 shows one possible design that may improve the flow in this area. However because of the close proximity of the EOCV outlet to the inlet valves of the engine and the complex geometry of the inlet port, physical flow-bench testing of several outlet configurations would be simpler than CFD modelling.

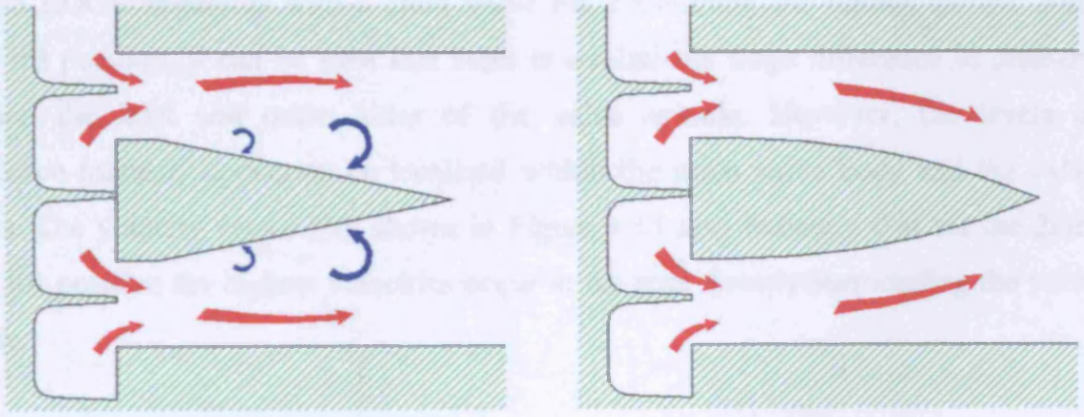

Figure 4.11 – Possible design improvement

4.3.1 Mark 3 EOCV Simulation Results

An example of a Mark 3 EOCV mesh constructed is shown in Figure 4.12 below. The local refinement in the area of the main valve body and spindle can be seen as well as the separate inlet boundary.

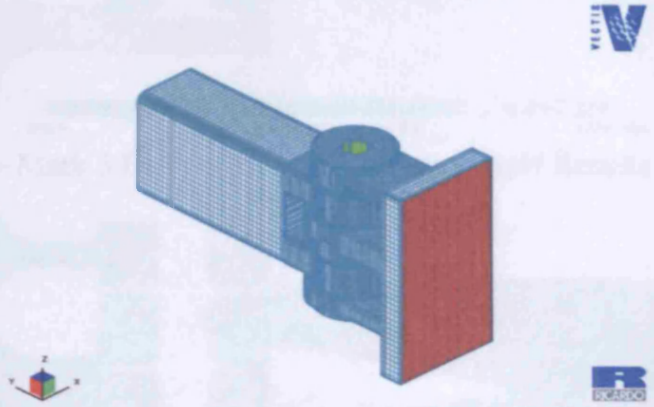

Figure 4.12 – Mark 3 CFD mesh.

Figures 4.13 – 4.15 show the pressure, turbulence intensity and velocity vectors for the Mark 3 EOCV apparatus with a 2mm valve lift. Examining the figures for the 2mm valve lift position, it can be seen that there is a relatively large difference in pressure between the inlet and outlet sides of the valve spindle. However, the levels of turbulence intensity appear to be localised within the main valve body and the valve outlets. The velocity vector plot shown in Figure 4.15 also indicates that for the 2mm valve lift position the highest velocities occur in the area directly surrounding the valve spindle.

Figures 4.16 – 4.18 show the pressure, turbulence intensity and velocity vectors for the Mark 3 EOCV apparatus with a 4mm valve lift. Comparing the results for the 4mm and the 2mm valve lifts it can be seen that the pressure difference across the valve spindle is smaller for the 4mm valve lift. With the 4mm lift there is also a much larger area with high levels of turbulence intensity within the outlets of the EOCV. It is also noticeable that the velocity vectors are distributed more evenly throughout the valve body than was seen with a 2mm lift.

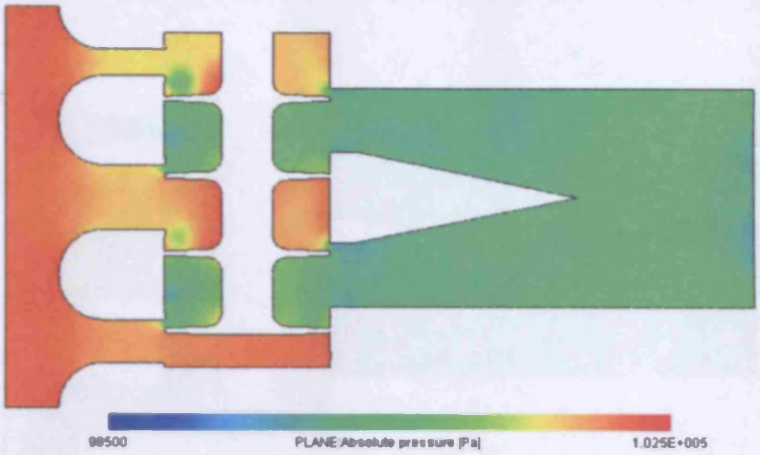

Figure 4.13 – Mark 3 Design, 2mm lift Pressure Field Results (T=0.006s)

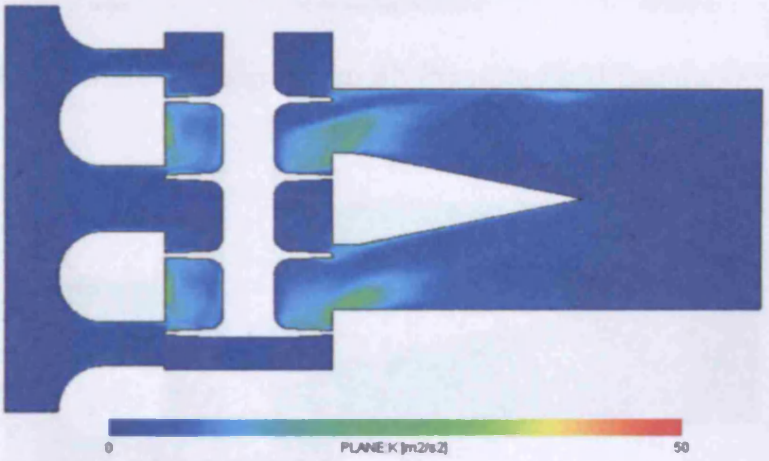

Figure 4.14 – Mark 3 Design, 2mm lift Turbulence Field Results (T=0.006s)

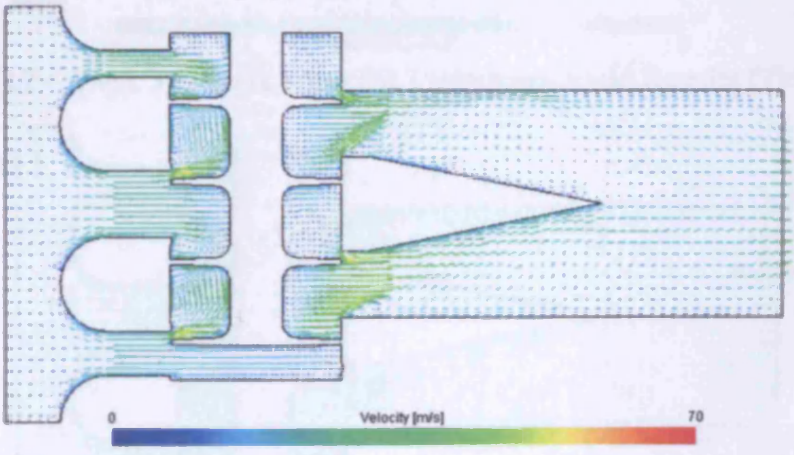

Figure 4.15 – Mark 3 Design, 2mm lift Velocity vector Results (T=0.006s)

Figures 4.19 – 4.21 show the pressure, turbulence intensity and velocity vectors for the Mark 3 EOCV apparatus with a 6mm valve lift. Comparing the results for the 6mm valve lift to that for the 4mm and the 2mm valve lifts it can be seen that the pressure difference across the valve spindle with a 6mm valve lift is more evenly distributed.

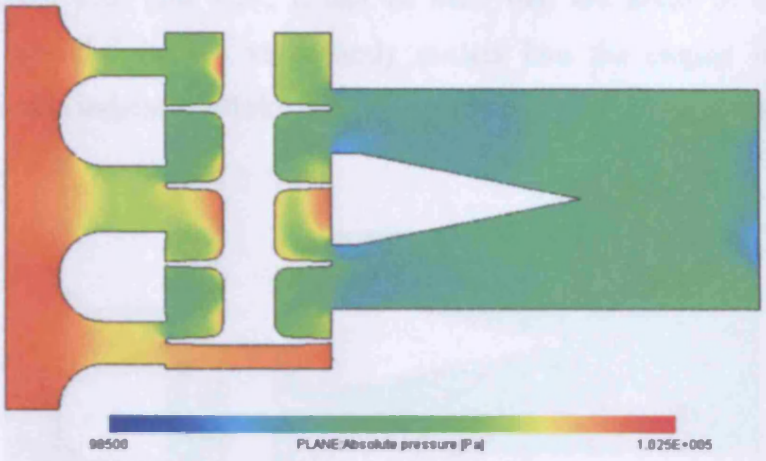

Figure 4.16 – Mark 3 Design, 4mm lift Pressure Field Results (T=0.006s)

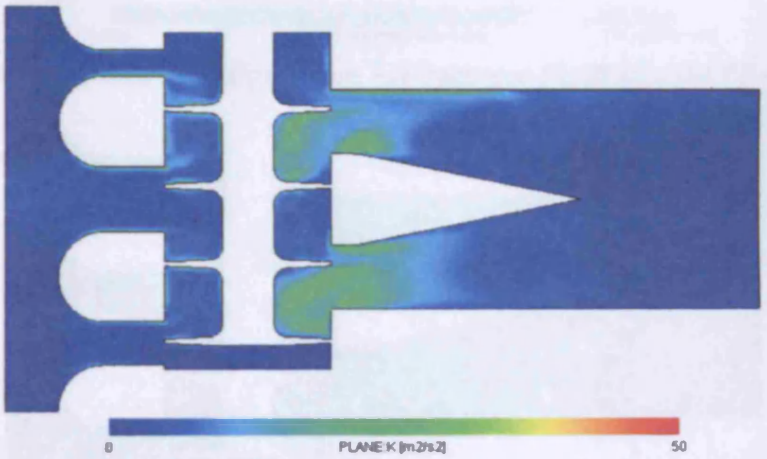

Figure 4.17 – Mark 3 Design, 4mm lift Turbulence Field Results (T=0.006s)

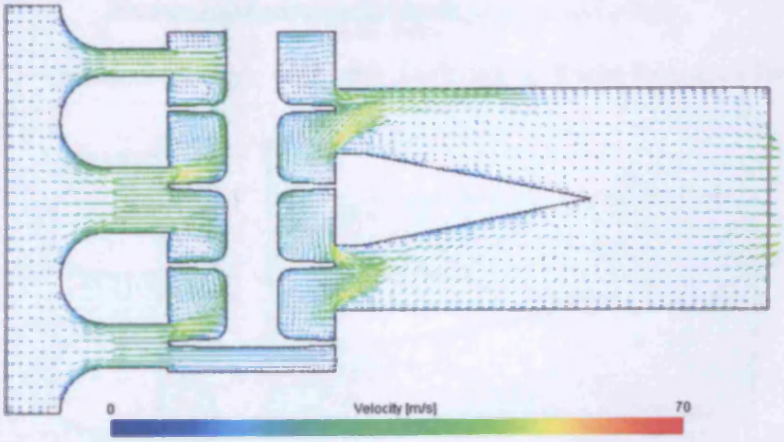

Figure 4.18 – Mark 3 Design, 4mm lift Velocity vector Results (T=0.006s)

Examining Figures 4.20 and 4.21, it can be seen that the areas of high turbulence intensity have spread from the valve body outlets into the engine inlet ports. The velocity vectors also indicate definite areas of recirculation within the valve and outlets.

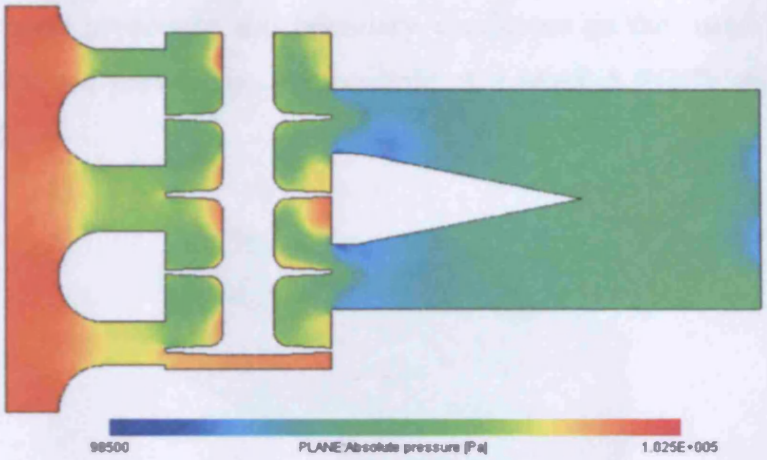

Figure 4.19 – Mark 3 Design, 6mm lift Pressure Field Results (T=0.006s)

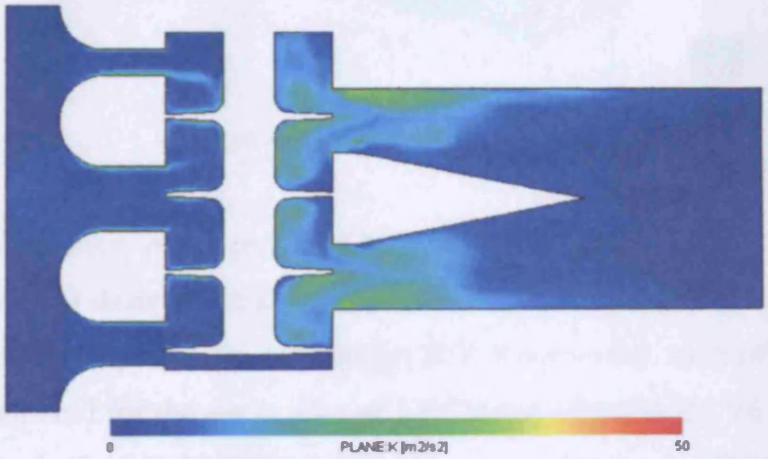

Figure 4.20 – Mark 3 Design, 6mm lift Turbulence Field Results (T=0.006s)

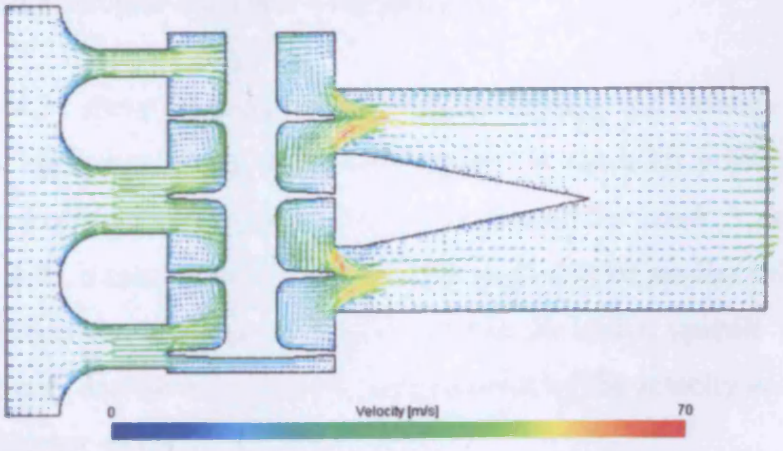

Figure 4.21 – Mark 3 Design, 6mm lift Velocity vector Results (T=0.006s)

4.3.2 Mark 4 EOCV Simulation Results

A CFD simulation of an initial design of the Mark 4 EOCV apparatus was constructed following the same procedure and boundary conditions as that used for the Mark 3 simulations described previously. An example of a Mark 4 EOCV mesh is shown in Figure 4.22 below.

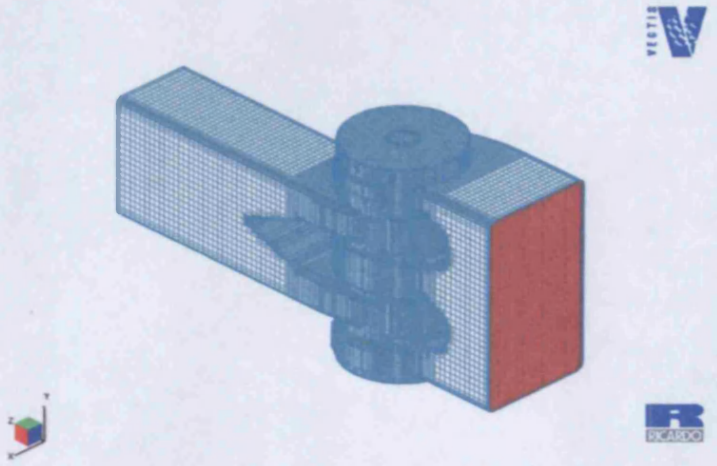

Figure 4.22 – Mark 4 CFD mesh.

Comparing the geometry of the proposed Mark 4 EOCV geometry shown in Figure 4.22 to that of the Mark 3 design seen in Figure 4.12, it can be seen that to accommodate the larger diameter valve spindle the inlet to the EOCV valve has been offset to one side. This offset it required for the application of EOCV apparatus to the V6 NoNOx engine, but may not be required if the EOCV technology is applied to a different engine while retaining the same actuator and control components.

Figures 4.23 – 4.31 show the pressure, turbulence intensity and velocity vectors for the Mark 4 EOCV apparatus at the 2mm, 4mm and 6mm valve lift positions. Comparing the results for the Mark 4 EOCV apparatus to that of the Mark 3 design shown in Figures 4.13 – 4.21 it can be seen that the two designs exhibit similar behaviour. As the valve lift increases the pressure difference across the valve spindle decreases. The turbulence intensity and the recirculation zones shown by the velocity vectors within the valve outlets increase as the valve lift increases.

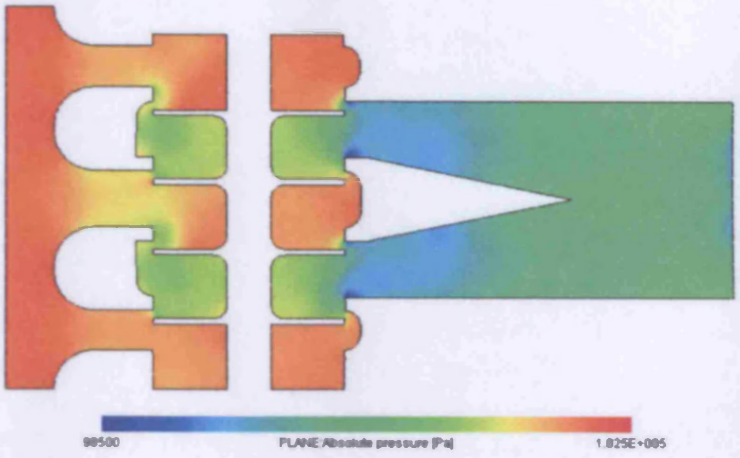

Figure 4.23 – Mark 4 Design, 2mm lift Pressure Field Results (T=0.006s)

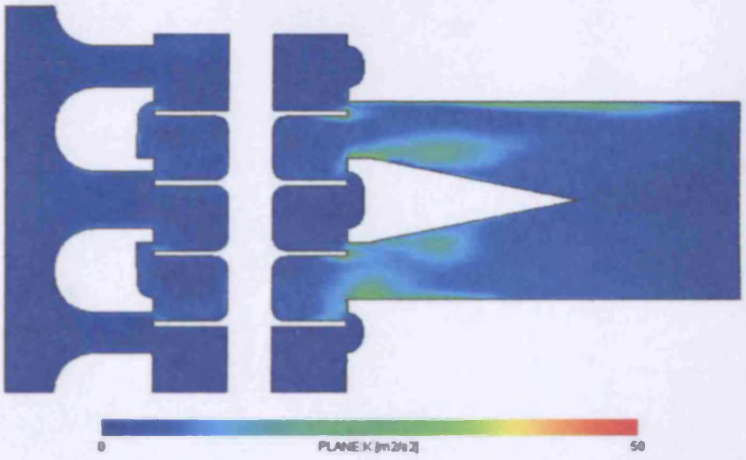

Figure 4.24 – Mark 4 Design, 2mm lift Turbulence Field Results (T=0.006s)

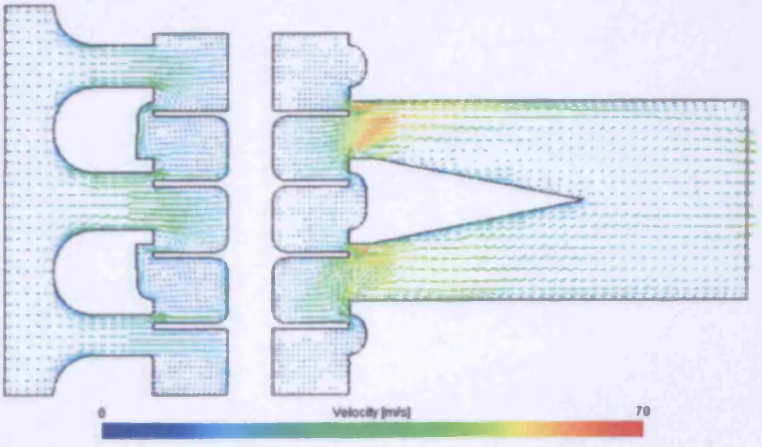

Figure 4.25 – Mark 4 Design, 2mm lift Velocity vector Results (T=0.006s)

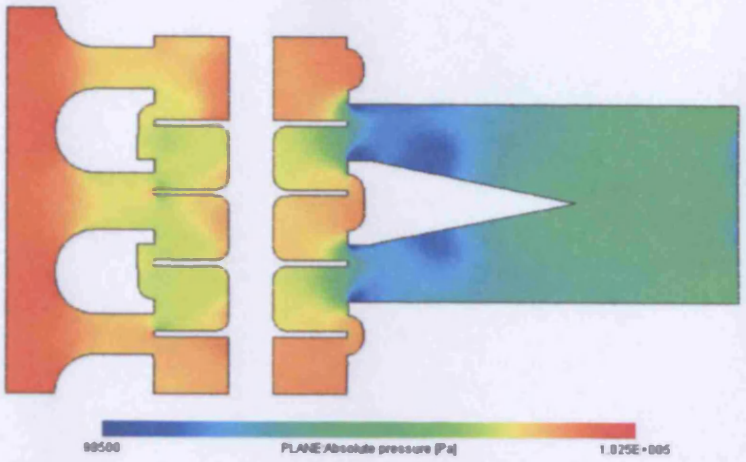

Figure 4.26 – Mark 4 Design, 4mm lift Pressure Field Results (T=0.006s)

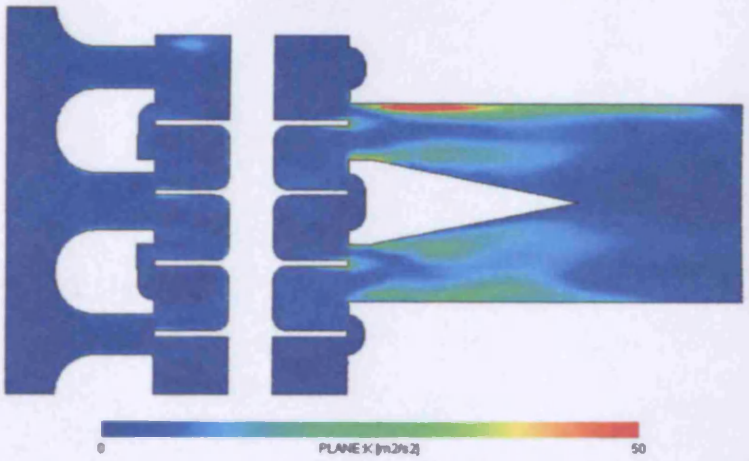

Figure 4.27 – Mark 4 Design, 4mm lift Turbulence Field Results (T=0.006s)

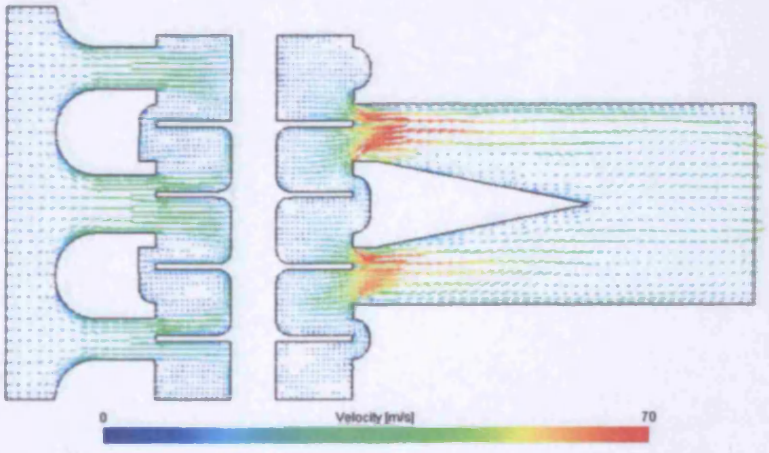

Figure 4.28 – Mark 4 Design, 4mm lift Velocity vector Results (T=0.006s)

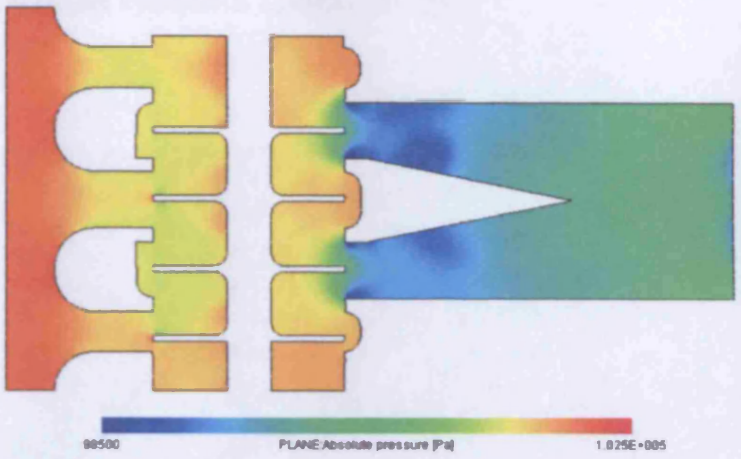

Figure 4.29 – Mark 4 Design, 6mm lift Pressure Field Results (T=0.006s)

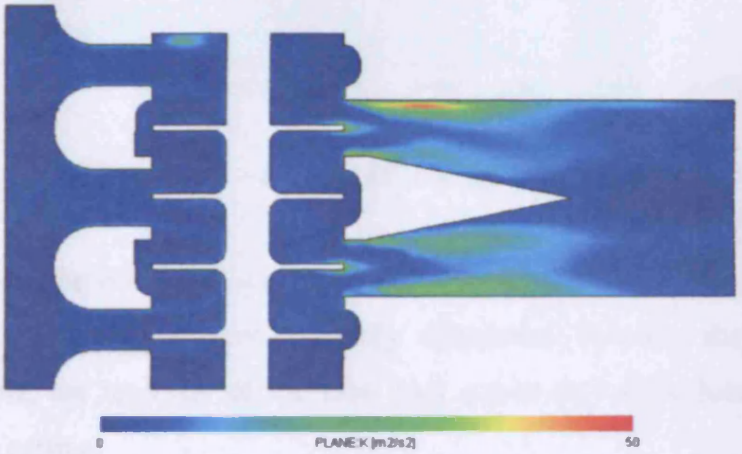

Figure 4.30 – Mark 4 Design, 6mm lift Turbulence Field Results (T=0.006s)

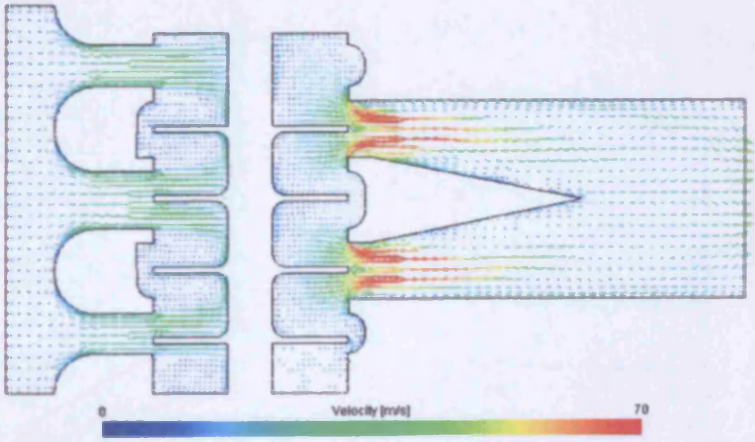

Figure 4.31 – Mark 4 Design, 6mm lift Velocity vector Results (T=0.006s)

4.3.3 Steady-State Results Discussion

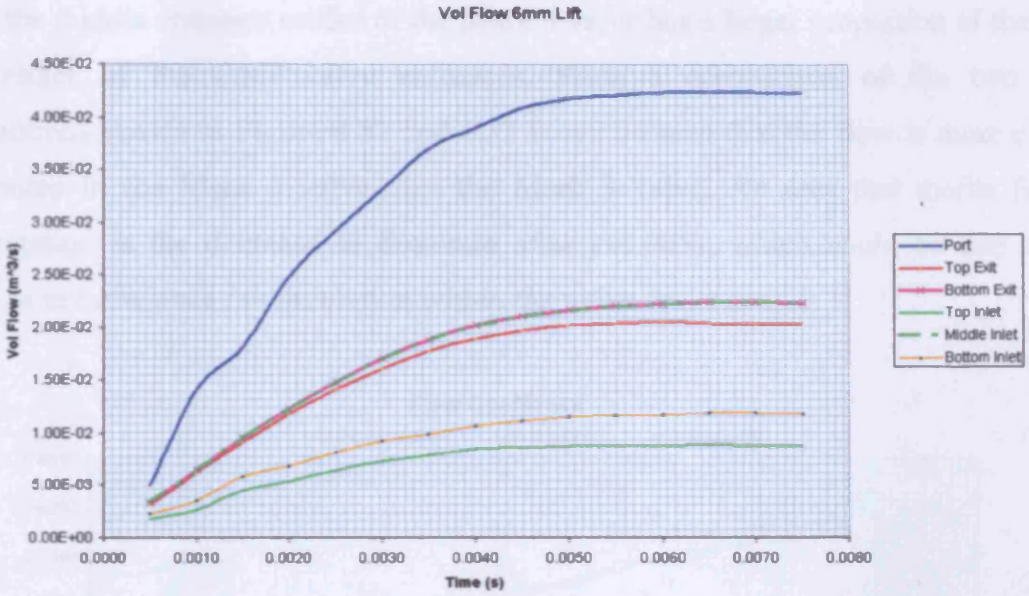

Figure 4.32 – Mark 3 EOCV flow proportion

Figure 4.32 shows the distribution of the flow within the Mark 3 valve at 6mm lift. It can clearly be seen that the flow is evenly distributed between the two valve exit orifices. However, the majority of the flow that enters the valve does so through the middle entrance orifice.

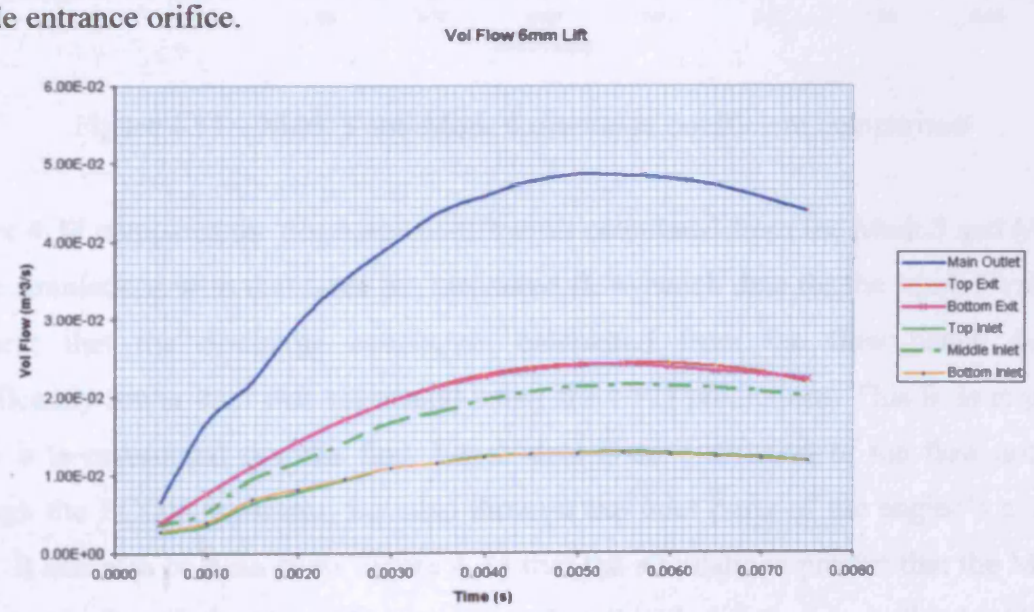

Figure 4.33 – Mark 4 EOCV flow proportion

Figure 4.33 shows how the flow is distributed within the proposed Mark 4 valve design at 6mm lift. The flow is evenly distributed between both valve exits. As with the Mark 3 valve the middle entrance orifice of the Mark 4 valve has a larger proportion of the flow than either of the other valve entrances. From a comparison of the two flow distributions shown in Figure 4.32 and 4.33 it can be seen that the flow is more evenly distributed in the Mark 4 valve than the Mark 3 valve. An area that merits further investigation is the decrease in flow-rate after t=0.005s, which could be due to the increase in turbulence / recirculation within the valve outlet area.

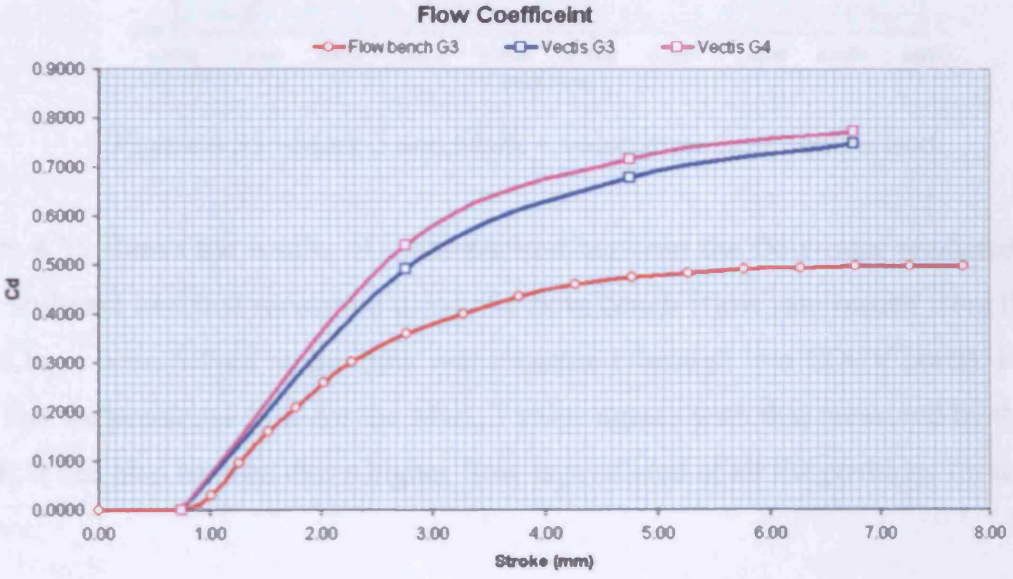

Figure 4.34 – Mark 3 and Mark 4 discharge coefficient comparison

Figure 4.34 compares the discharge coefficients calculated from the Mark 3 and Mark 4 valve simulations with that from the measured flow-bench data for the Mark 3 valve. It is clear that the discharge coefficient calculated from the flow bench data is significantly lower than that calculated using the CFD predictions. This is as expected when it is considered that the flow bench data is an evaluation of the flow not only through the ECOV apparatus, but also through the inlet ports of the engine's cylinder head. It can also be seen from Figure 4.34 that the simulations predict that the Mark 4 valve has higher discharge coefficient values than the Mark 3 design at all valve lifts.

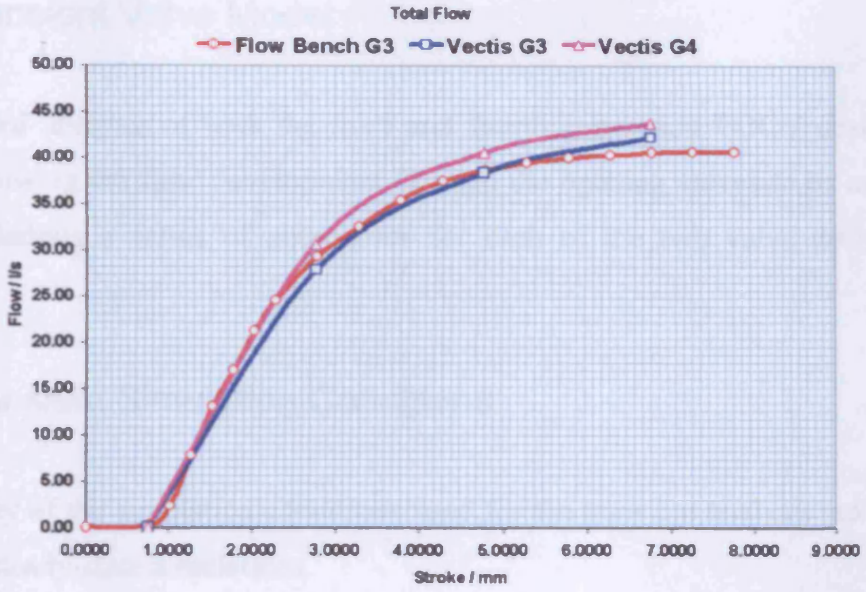

Figure 4.35 –Mark 3 and Mark 4 volumetric flow comparison

Figure 4.35 shows the results of a comparison between the flow-rates predicted by the CFD software and that measured using the flow bench (flow rate results from the flow bench have been halved as the flow was measured through two EOCV ports). It can be seen that the predicted flow for the Mark 3 valve agrees with that measured by the flow-bench, it can also be seen that a higher flow is predicted at all lift positions for the Mark 4 valve.

The results of the steady-state CFD simulations of the EOCV apparatus provides us with information similar to that which can be obtained by flow-bench testing, from these results the discharge coefficients for the EOCV designs at different valve lift positions can be determined. In reality however, the EOCV apparatus rapidly switches from a fully closed to a fully open position. This means that a transient simulation is required in order to obtain the actual discharge coefficients for the valve while opening, which are then to be included in the Wave engine simulation.

4.4 Transient Valve Model

A time-based analysis of both the third and fourth generation EOCV designs will be created; allowing the flow development through the opening valves to be assessed. For these simulations a series of geometries for each of the two valve designs will be created.

4.4.1 Transient Simulation Conditions

The majority of the simulation conditions used for the transient analysis are the same as that in the steady-state simulations.

Iteration Properties

The increased complexity of a transient analysis requires smaller time-steps to avoid instability in the results.

Global convergence criterion:	1e-008
Model start time:	0.0000s
Model end time:	0.0120s
Time step length:	2.5e-005s
Post-pro. Spacing:	0.0002s

Boundary Motion Properties

To simulate the opening of the EOCV apparatus, the surfaces that represent the valve head are defined as a separate 'boundary', this allows the valve-head to be moved (or distorted) such that it reflects the actual valve-heads motion when operating.

Figure 4.36 compares the measured valve-lift time profile with that used in the transient valve simulation. The valve lift data that is used for the CFD modelling is based upon the measured performance of the Mark 3 EOCV actuator.

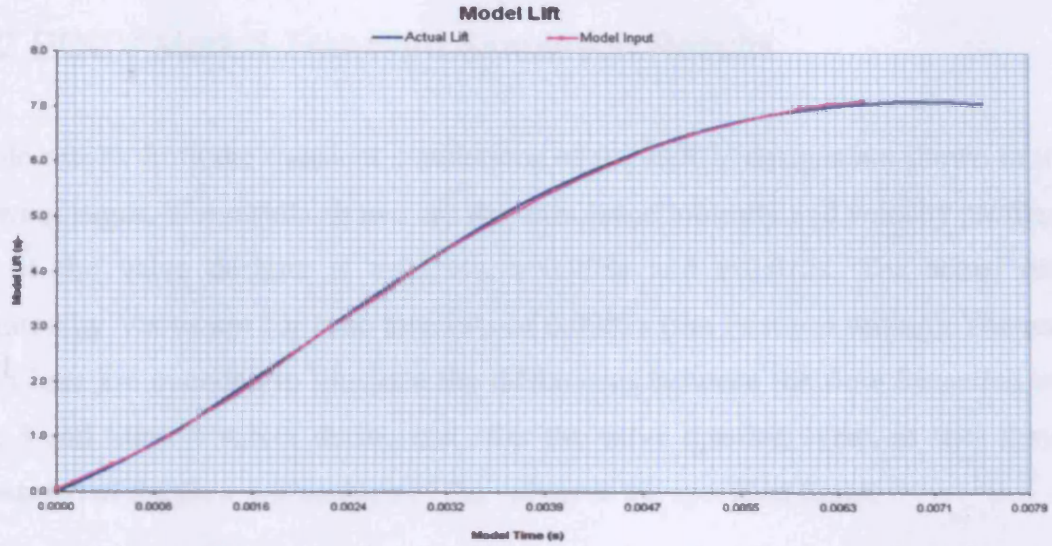

Figure 4.36 – Actual valve-lift and model valve-lift comparison

In order to model the opening of the EOCV apparatus, a series of different geometries must be created. At the beginning of the simulation the initial mesh is loaded, this mesh is then distorted to model the movement of the valve. The extent to which the mesh can be distorted is limited, as each of the individual cells must have dimensions of similar magnitudes. Therefore, at preset points throughout the valve opening procedure the simulation switches to a new mesh. A 'cross-linking' procedure is carried out in which the initial variable values for the new mesh are determined from the final values of the previous mesh based upon the Cartesian locations of the individual cells.

From the actuator timings of the Mark 3 EOCV apparatus shown in Figure 4.36 it can be seen that from the start of the simulation the EOCV reaches it's fully open position after only 7ms. The full motion of the actuator actually takes around 10ms, but for the first 3ms the EOCV is still effectively closed, as the valve spindle is moving within the valve body.

4.4.2 EOCV Mark 3 Transient Simulation Results

Sample results from the transient simulations of the EOCV designs are shown over the following pages. The results shown are the turbulence intensity and velocity profiles for each of the valve designs at t=0.004s, t=0.008s and t=0.012s. The actual results generated by Vectis are for time intervals of 0.0002s (the Post-pro setting). The results shown here are intended to illustrate the differences between the flow formation in the Mark 3 and Mark 4 valves during and after the valve opening event, as such they are 'snapshots' of the flow within each of the valves at the specified times.

Figure 4.37 shows the location of the side and top cross-sections through the Mark 3 EOCV model. These are the sectional views that the following results depict.

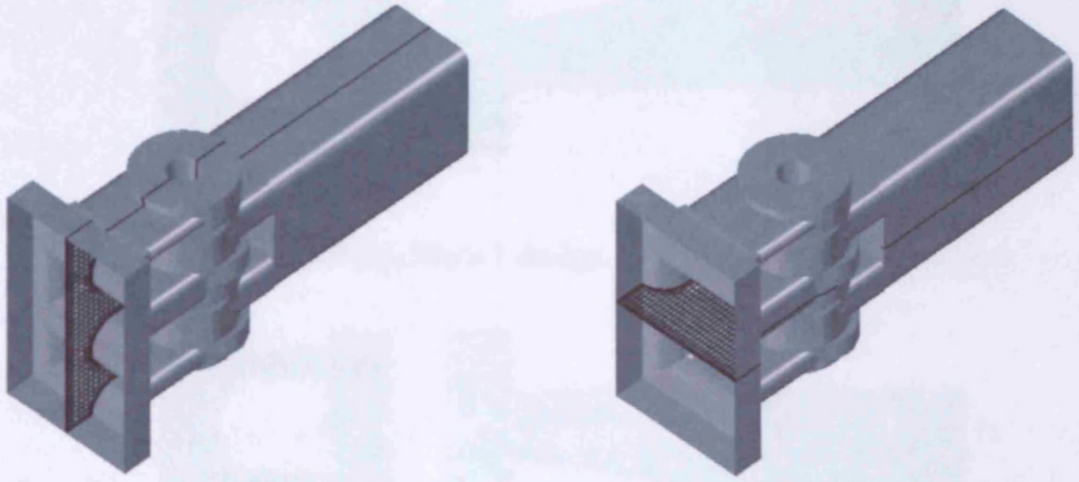

Figure 4.37 – Mark 3 EOCV side and top section locations

Figures 4.38 – 4.43 show the side and top sectional views through the Mark 3 valve design for each of the specified times, the turbulence intensity scalar *k* is illustrated on these plots. From Figures 4.38 – 4.43 it can be seen that the areas of largest turbulence intensity are the two outlets from the EOCV apparatus. It can also be seen that the distribution of the turbulence intensity within the Mark 3 EOCV design is nearly symmetrical, both in the vertical and horizontal plain.

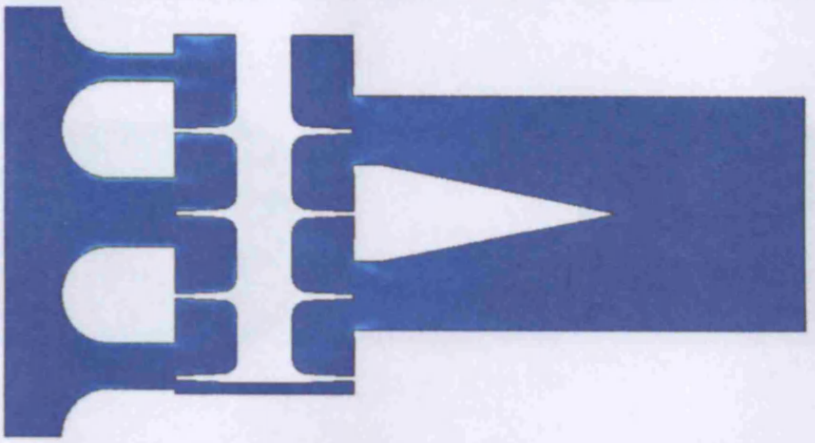

Figure 4.38 – T=0.004s, Mark 3 design, turbulence intensity side view

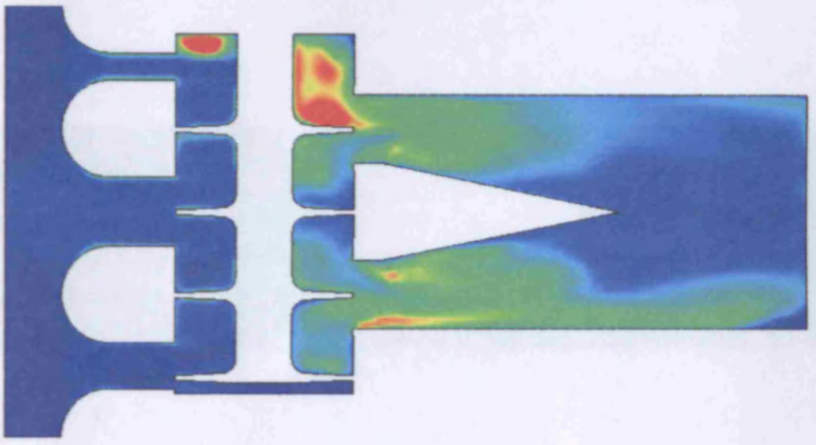

Figure 4.39 – T=0.008s, Mark 3 design, turbulence intensity side view

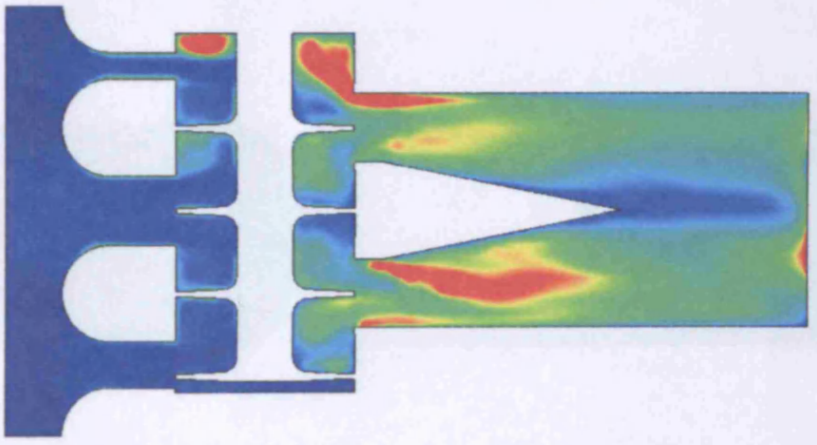

Figure 4.40 – T=0.012s, Mark 3 design, turbulence intensity side view

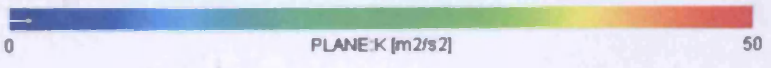

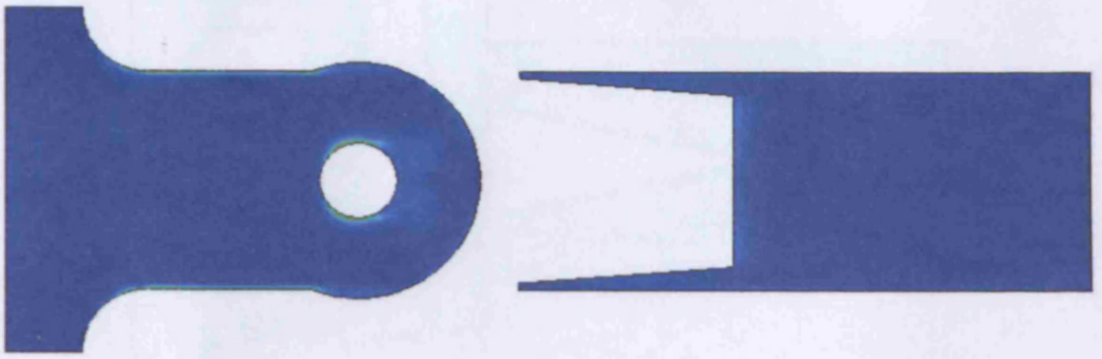

Figure 4.41 – T=0.004s, Mark 3 design, turbulence intensity top view

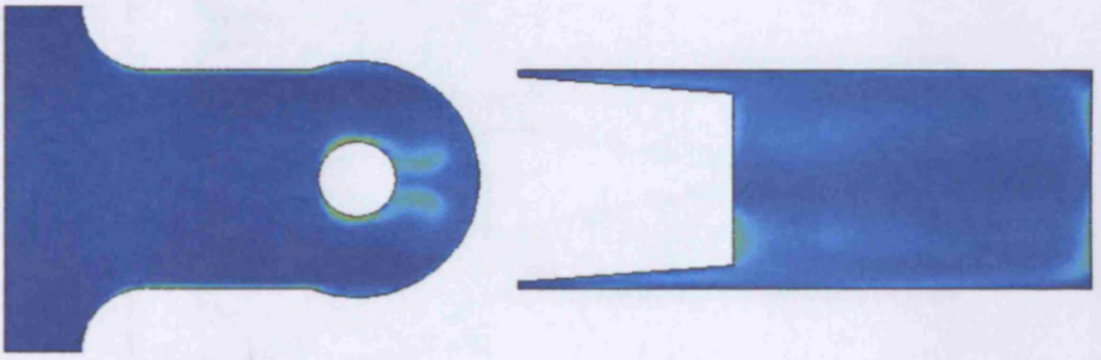

Figure 4.42 – T=0.008s, Mark 3 design, turbulence intensity top view

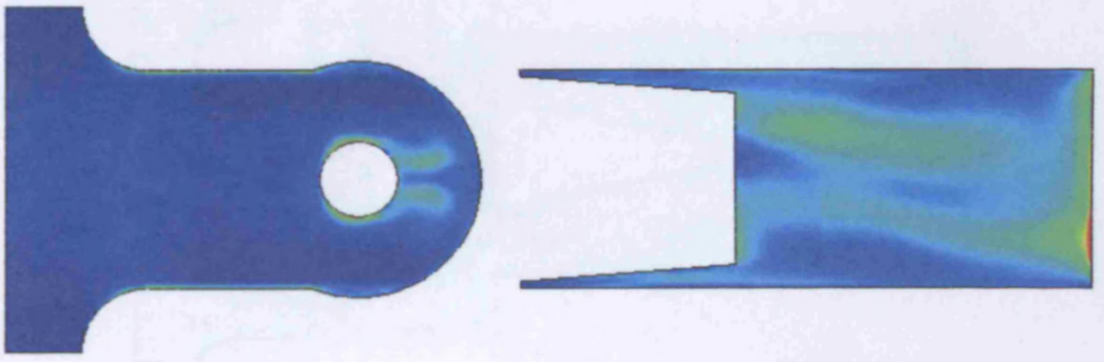

Figure 4.43 – T=0.012s, Mark 3 design, turbulence intensity top view

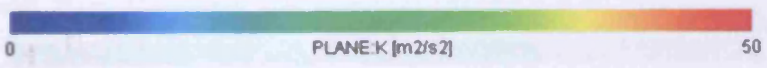

Figures 4.44 – 4.49 show the side and top sectional views through the Mark 3 valve design for each of the specified times, the velocity profiles are illustrated on these plots.

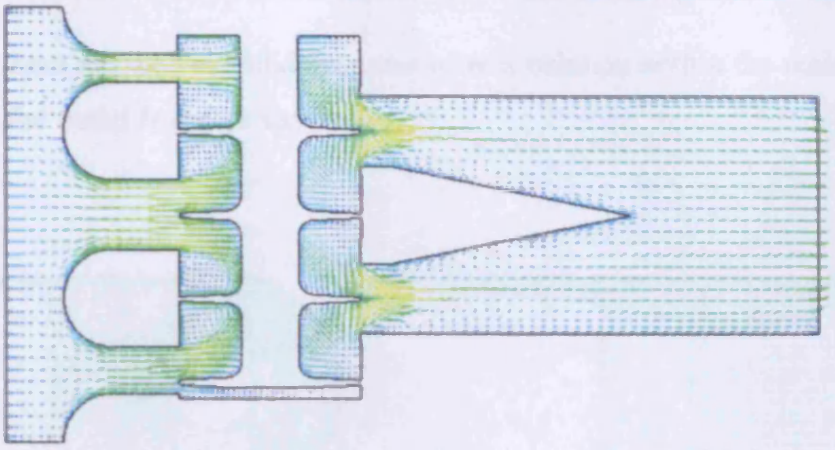

Figure 4.44 – T=0.004s, Mark 3 design, velocity profile side view

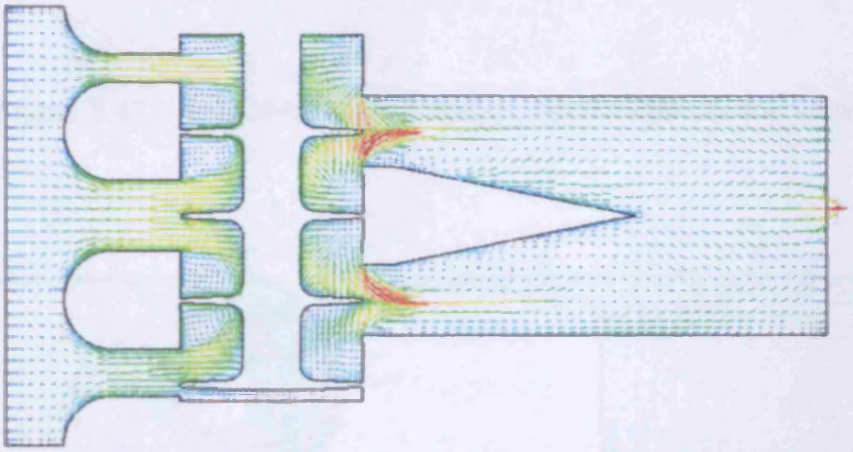

Figure 4.45 – T=0.008s, Mark 3 design, velocity profile side view

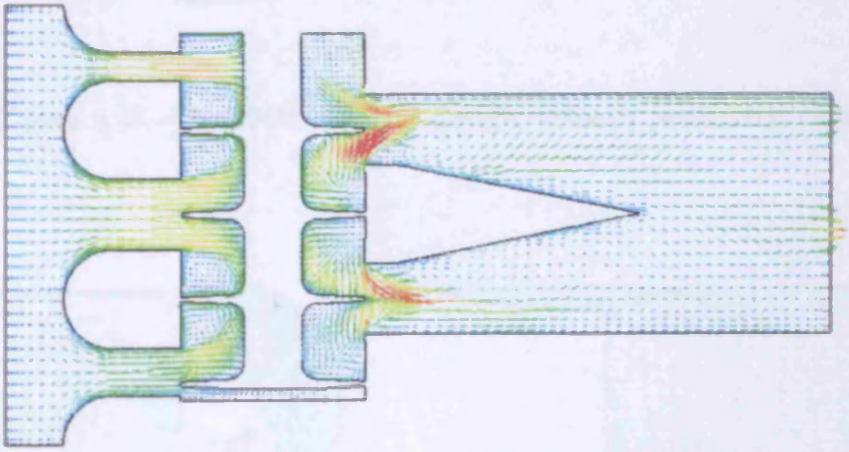

Figure 4.46 – T=0.012s, Mark 3 design, velocity profile side view

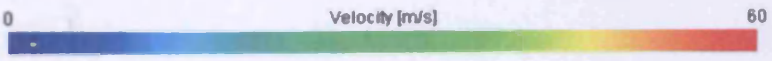

From Figures 4.44 – 4.49 it can be seen that the velocity distribution within the Mark 3 EOCV design is nearly symmetrical, both in the vertical and horizontal plain. It can also

be seen that there are well established areas of recirculation within the main valve body as well as in the outlet from the valve.

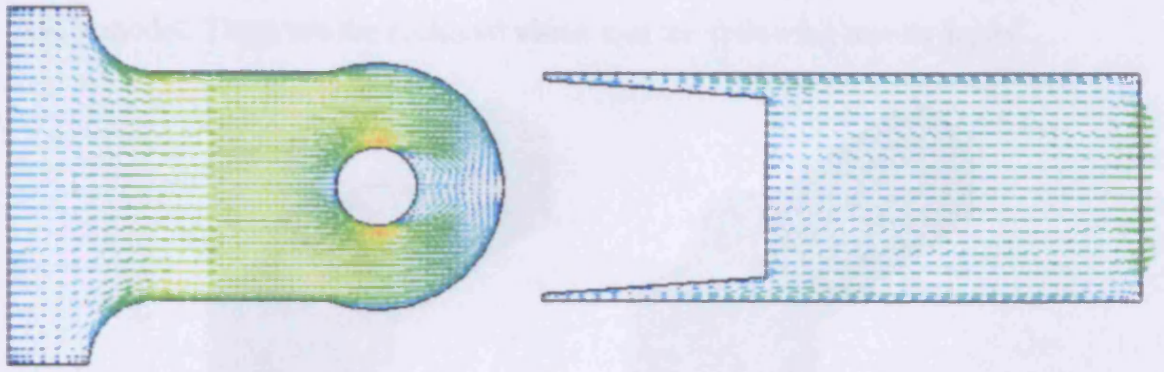

Figure 4.47 – T=0.004s, Mark 3 design, velocity profile top view

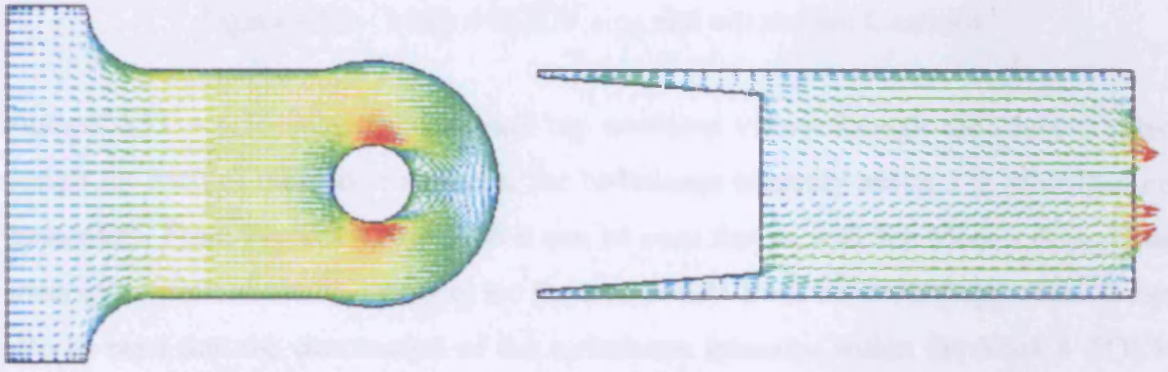

Figure 4.48 – T=0.008s, Mark 3 design, velocity profile top view

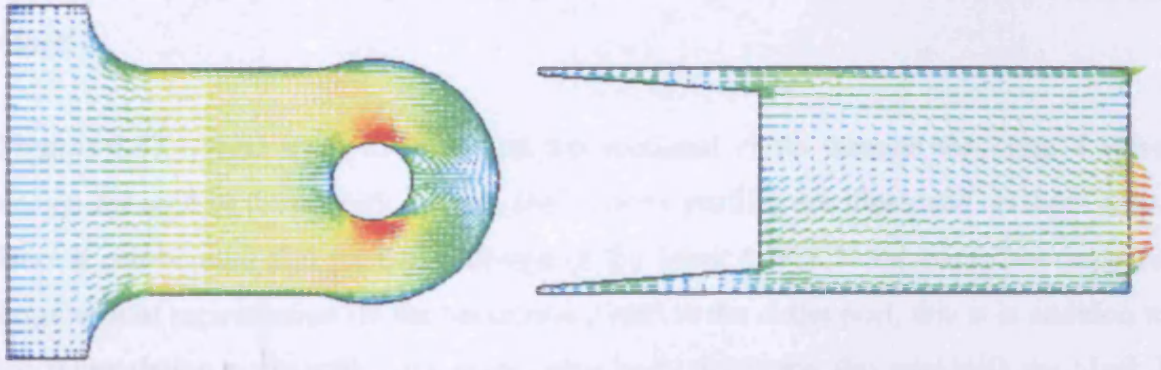

Figure 4.49 – T=0.012s, Mark 3 design, velocity profile top view

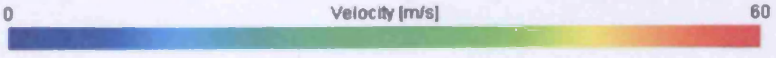

4.4.3 Mark 4 EOCV Transient Simulation Results

Figure 4.50 shows the location of the side and top cross-sections through the Mark 4 EOCV model. These are the sectional views that the following results depict.

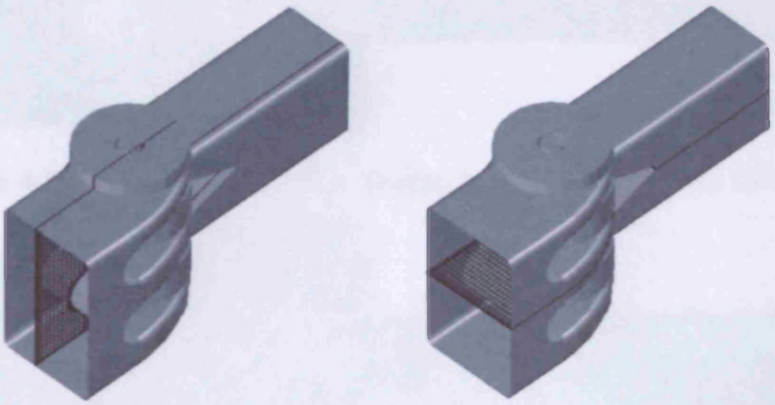

Figure 4.50 – Mark 4 EOCV side and top section locations

Figures 4.51 – 4.56 show the side and top sectional views through the Mark 4 valve design for each of the specified times, the turbulence intensity scalar k is illustrated on these plots. From Figures 4.51 – 4.56 it can be seen that as with the Mark 3 design, the areas of largest turbulence intensity are the two outlets from the EOCV apparatus. It can also be seen that the distribution of the turbulence intensity within the Mark 4 EOCV design is nearly symmetrical in the vertical plain, but in the horizontal plain there is a definite uneven distribution of turbulence. The offset design of the Mark 4 EOCV apparatus has caused one side of the outlet to be much more turbulent in nature than the other.

Figures 4.57 – 4.62 show the side and top sectional views through the Mark 4 valve design for each of the specified times, the velocity profiles are illustrated on these plots. Here it can be seen that the offset design of the Mark 4 EOCV apparatus has caused a large area of recirculation (in the horizontal plain) in the outlet port, this is in addition to the recirculation zones within the main valve body that were also seen with the Mark 3 EOCV design.

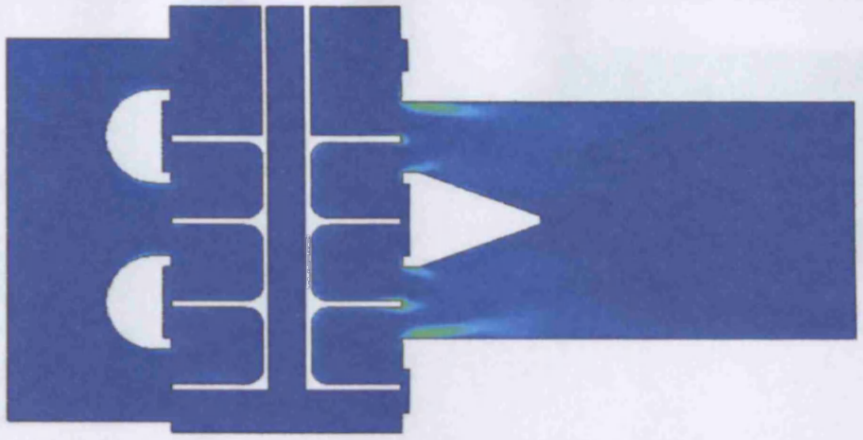

Figure 4.51 – T=0.004s, Mark 4 design, turbulence intensity side view

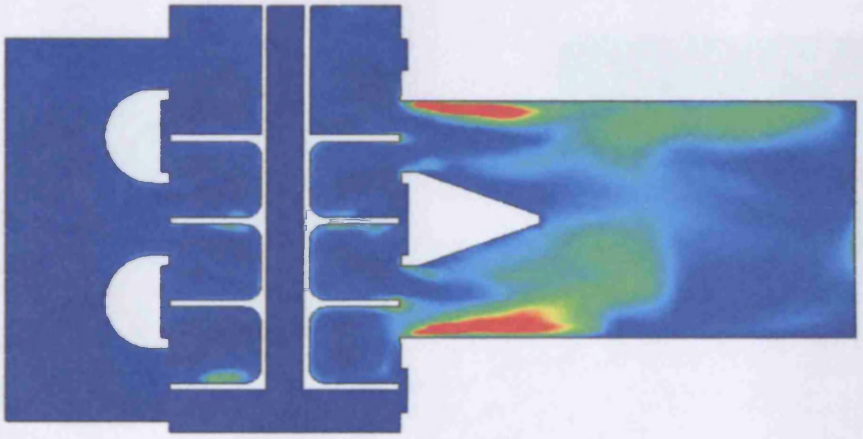

Figure 4.52 – T=0.008s, Mark 4 design, turbulence intensity side view

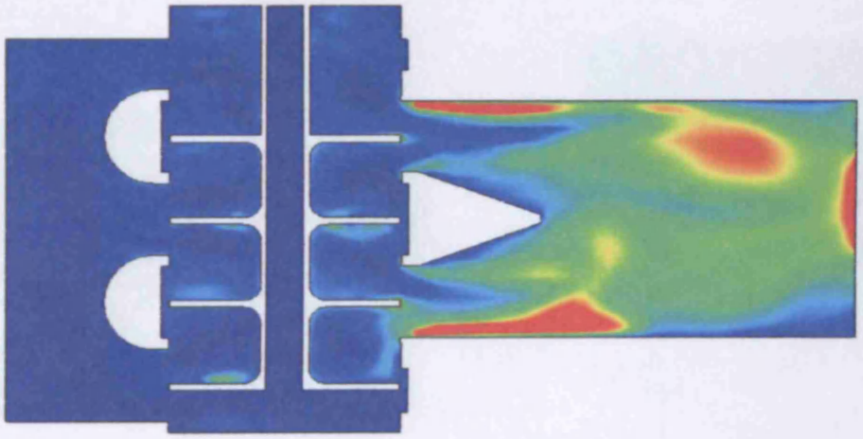

Figure 4.53 – T=0.012s, Mark 4 design, turbulence intensity side view

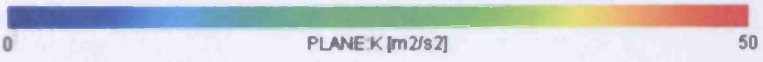

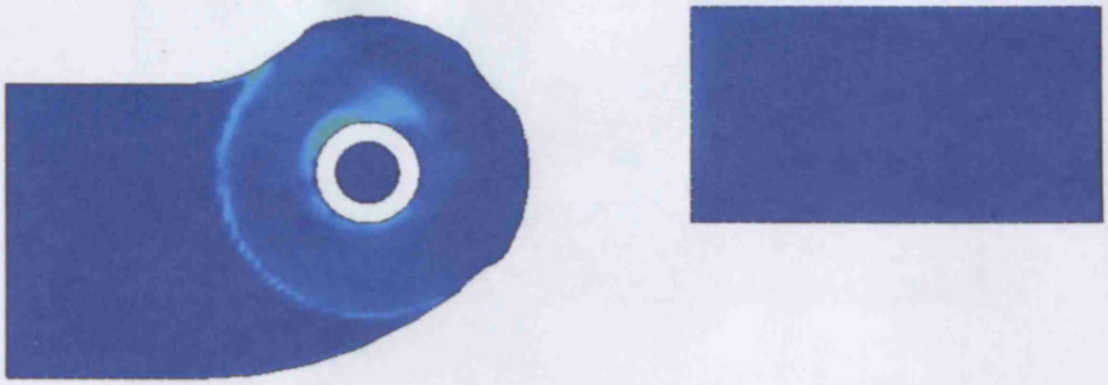

Figure 4.54 – T=0.004s, Mark 4 design, turbulence intensity top view

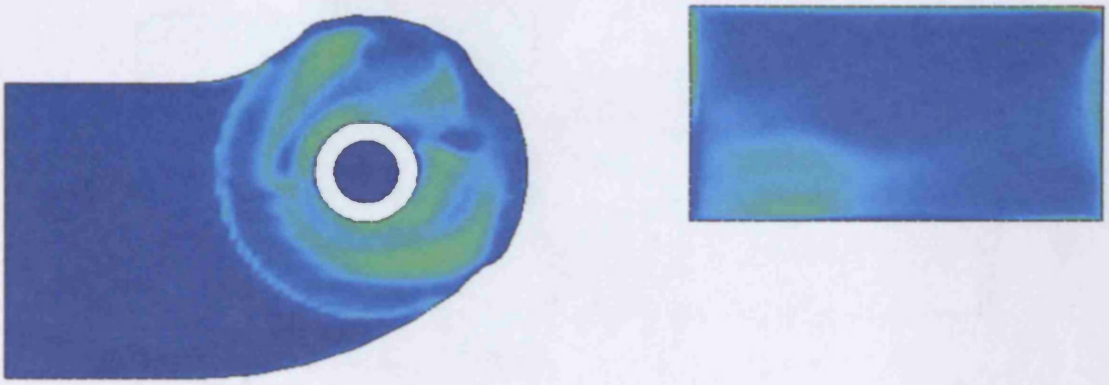

Figure 4.55 – T=0.008s, Mark 4 design, turbulence intensity top view

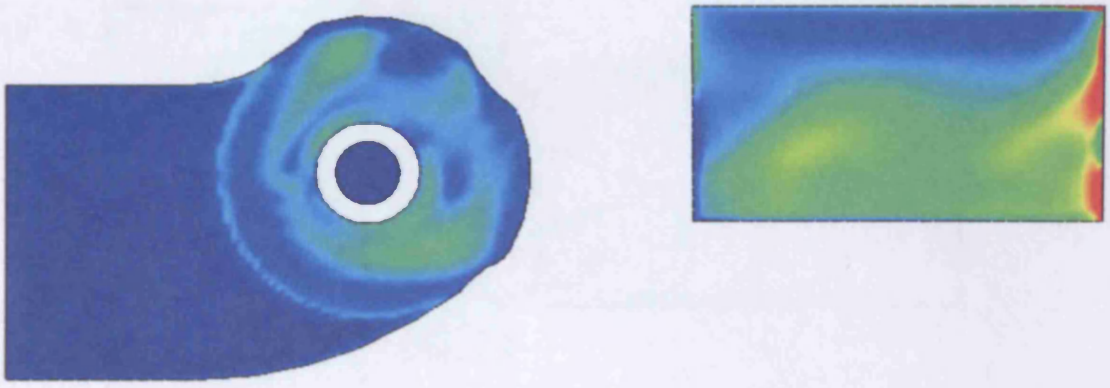

Figure 4.56 – T=0.012s, Mark 4 design, turbulence intensity top view

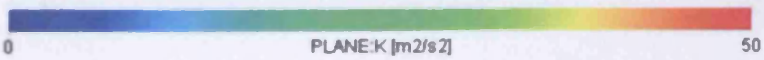

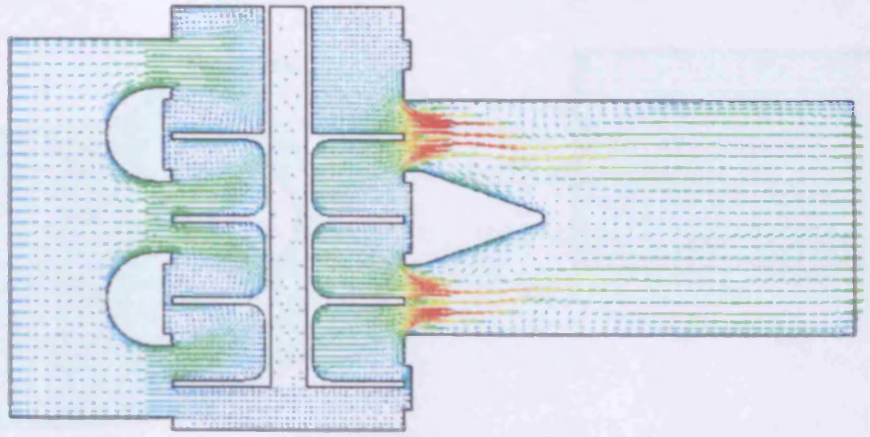

Figure 4.57 – T=0.004s, Mark 4 design, velocity profile side view

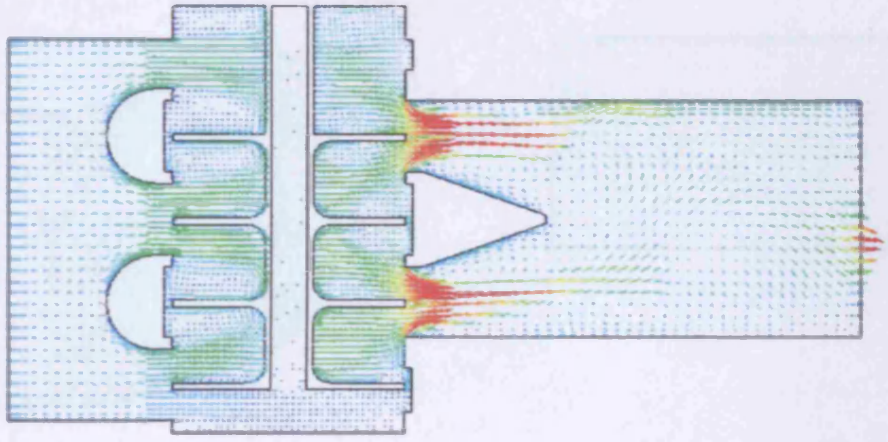

Figure 4.58 – T=0.008s, Mark 4 design, velocity profile side view

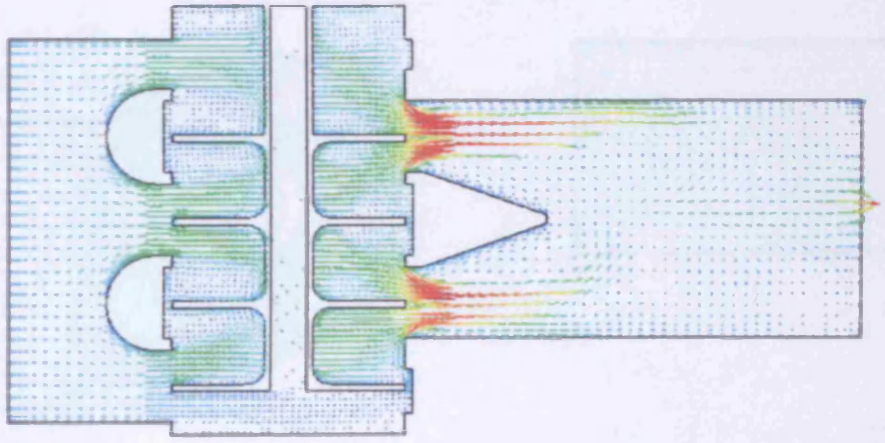

Figure 4.59 – T=0.012s, Mark 4 design, velocity profile side view

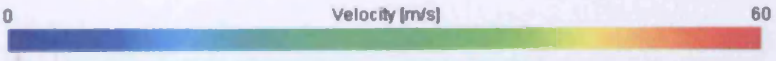

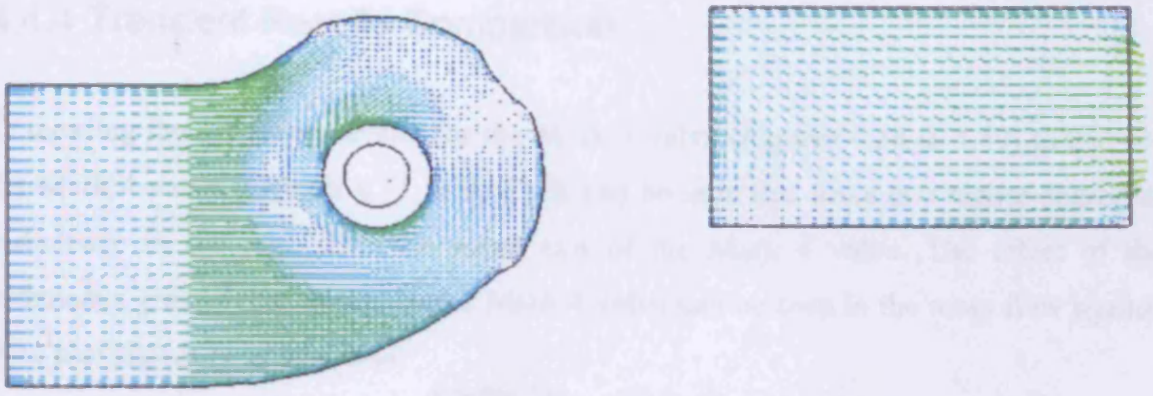

Figure 4.60 – T=0.004s, Mark 4 design, velocity profile top view

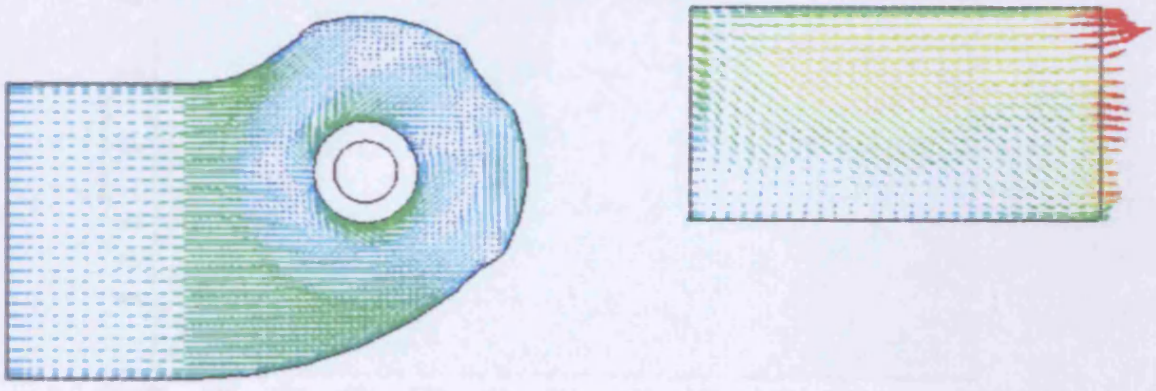

Figure 4.61 – T=0.008s, Mark 4 design, velocity profile top view

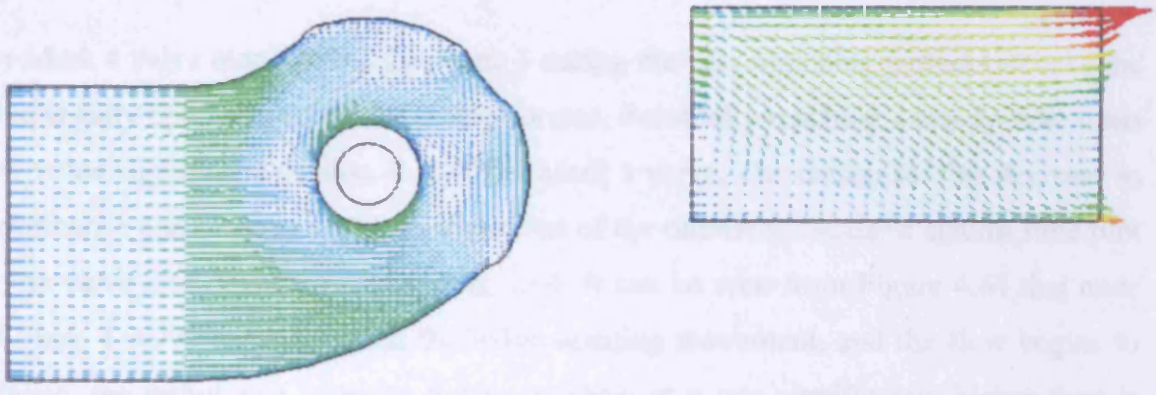

Figure 4.62 – T=0.012s, Mark 4 design, velocity profile top view

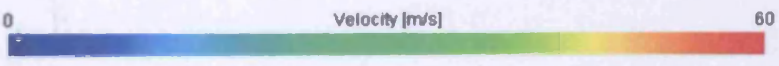

4.4.4 Transient Results Comparison

Comparing the graphical results for the Mark 3 valve (Figures 4.38 to 4.49) to that for the Mark 4 valve (Figures 4.51 to 4.62), it can be seen that there is a higher degree of turbulence in the port after the valve exit of the Mark 4 valve. The effect of the turbulence growth that occurs in the Mark 4 valve can be seen in the mass flow against time plot shown in Figure 4.63.

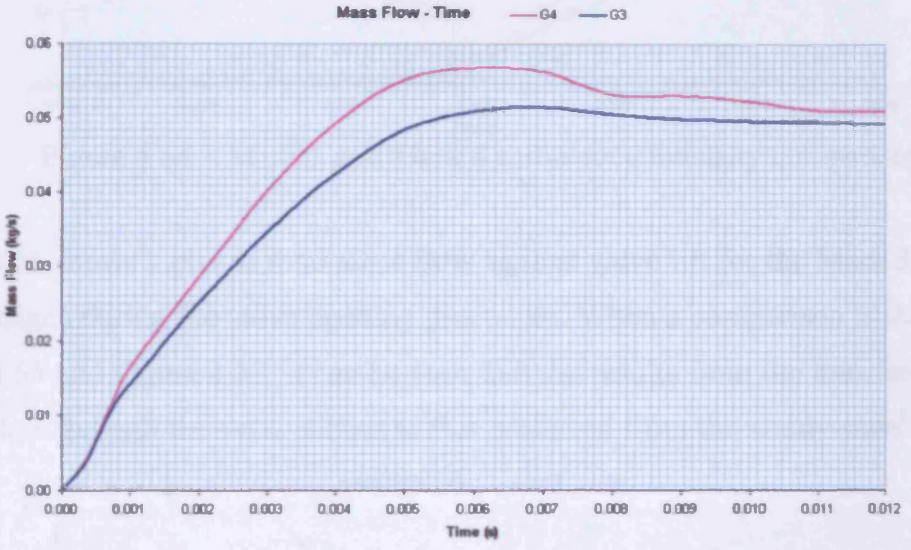

Figure 4.63 – Mark 3 and Mark 4 mass flow comparison

The Mark 4 valve outperforms the Mark 3 during the valve-opening period, but once the valve is fully open its performance deteriorates, eventually reaching a steady-state mass flow value slightly higher than that of the Mark 3 valve. The reason for this decrease in performance can be seen by the examination of the turbulence scalar k against time plot for the valve exit port shown in Figure 4.64. It can be seen from Figure 4.64 that once the Mark 4 valve has completed the valve opening movement, and the flow begins to stabilise, the turbulence intensity begins to grow at a rate significantly higher than is experienced by the Mark 3 valve design.

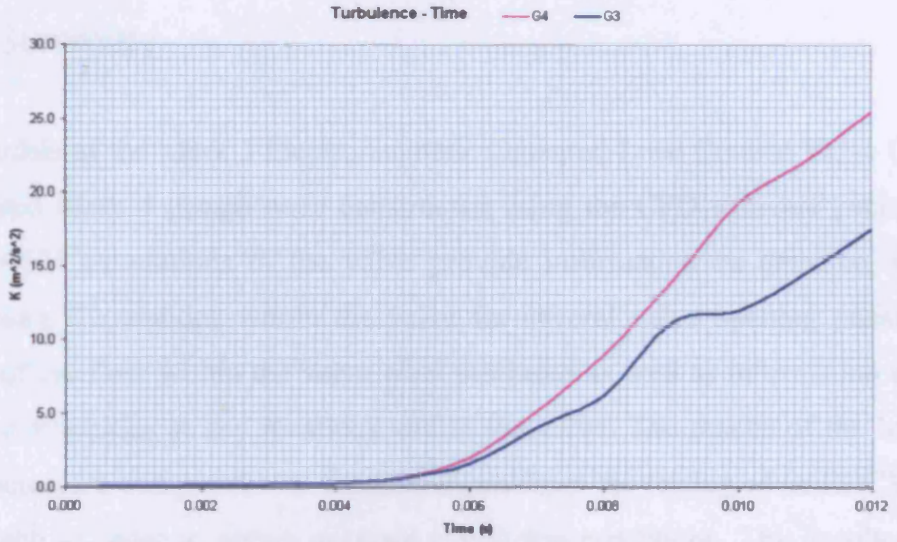

Figure 4.64 – Mark 3 and Mark 4 turbulence intensity comparison

Figure 4.65 shows a plot of total mass flow against valve lift for the Mark 3 and Mark 4 valve designs during the valve opening procedure. When a comparison is made between Figure 4.65 and Figure 4.35, it can be seen that the results from the transient simulation for the flow through the valve differs to that predicted from the steady-state simulations.

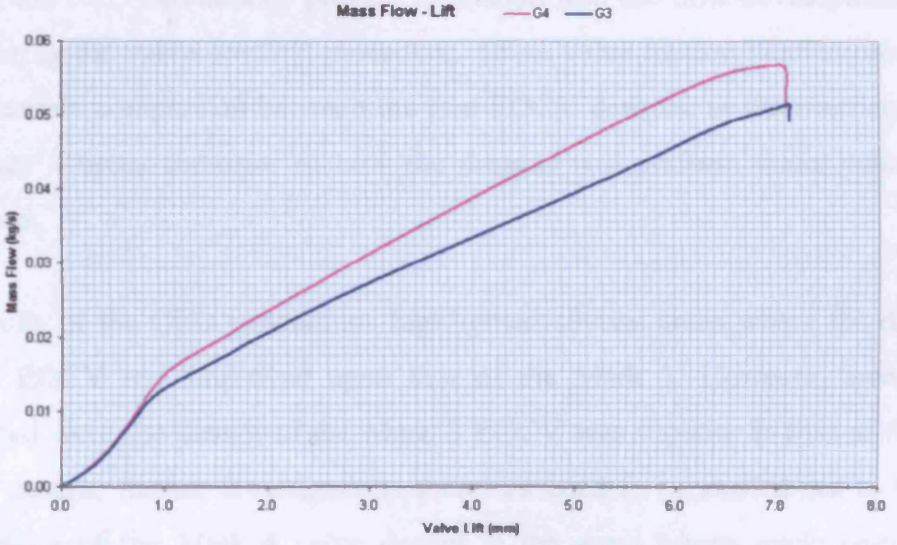

Figure 4.65 – Mark 3 and Mark 4 mass flow vs. valve-lift

4.5 Summary

CFD models of the Mark 3 Electromagnetic Operated-Load Control Valve (EOCV) and a proposed Mark 4 design were constructed using the CFD software package Ricardo Vectis. CFD simulations of the valve provide information on pressure, velocity and temperature fluctuations within the valve for several valve opening positions. Visual images of the flow within the valve were produced as well as information such as flow rates and velocities at key locations within the valve. The results of the Mark 3 valve simulation were compared with measurements from the testing of an EOCV valve on a flow-bench in order to obtain accurate simulation conditions. This resulted in a close agreement (less than 5% difference throughout valve stroke) between the CFD results and the practical flow-bench tests. For all valve lifts the steady-state CFD simulations predicted that the Mark 4 EOCV design would outperform the Mark 3 design.

Transient CFD models were created based upon data provided for the EOCV valve lift timings; the CFD simulations provide an insight into the flow development within the valve during the valve opening procedure. These valve motion simulations allow for a more accurate comparison between the two EOCV designs, as the transient simulation results are a better indicator of how the designs will perform under actual operating conditions.

The results of the CFD simulations highlighted several areas where the design of the Mark 4 EOCV had improved upon that of the Mark 3. However, areas were also discovered were the design of the Mark 3 EOCV was superior to that of the proposed Mark 4 design; further investigations therefore need to be carried out to improve the performance of the Mark 4 valve design in the areas where weaknesses have been discovered.

5 EOCV Development

A computer model of a natural gas fuelled engine featuring a novel secondary valve apparatus to allow Miller cycle operation was created in Chapter 3 of this work. It is anticipated that the combination of fuelling with CNG and adoption of the Miller cycle will allow an engine to operate with diesel equivalent power and economy while substantially reducing the emission of Carbon Monoxide, Carbon Dioxide and NO_X.

Using a commercially available three dimensional CFD code a computer model of the flow through the secondary Electronically Operated-load Control Valve (EOCV) was constructed in Chapter 4. The initial model was validated against flow-bench measurements before the simulation and evaluation of a potential future design. The simulation of an actual 'real-time' EOCV opening event was carried out in order to obtain discharge coefficients for the engine model.

The development of the EOCV design and its application to an operating engine is described within this chapter. Before the NoNOx engine is suitable for production, the dimensions of the inlet system, and the overall 'packaging' of the engine must be optimised. In addition to this, the design of the Mark 4 EOCV apparatus (specific to the NoNOx V6 engine) must be finalised. The discovery of a design problem, with prolonged use of the EOCV causing significant wear of the valve spindle and main valve body, which led to an increase in leakage, required a complete redesign of the valve spindle and bearings.

As a final requirement of the EU funded Mag-Move project, a preliminary investigation into the application of the EOCV apparatus to an engine running at speeds of up to 6000 RPM was required. A Cagiva Navigator / Suzuki TL-1000s motorcycle engine was chosen as the base engine for the 6000 RPM design. A computer model of the 6000 RPM engine as well as the results of a preliminary design of the EOCV apparatus is described.

During the investigation into alternative fuels carried out in Chapter 2, the possibility of the use of small amounts of hydrogen with natural gas is discussed. Karim et al. (1996) compared the combustion properties of a pure methane fuel with that of a 10% hydrogen – 90% methane mixture. For all equivalence ratios the 10% hydrogen – 90% methane mixture has a quicker flame propagation rate, higher apparent flame initiation speeds and therefore lower combustion durations. It is notable however, that the average maximum cylinder pressure increases with the addition of hydrogen, which may lead to an increase in NO_X formation.

Akansu et al. (2004) summarised the results of many different research papers on the use of natural gas-hydrogen mixtures in internal combustion engines. It was found that under certain conditions the addition of hydrogen can cause an increase in engine efficiency, whereas the emissions of hydrocarbons, CO_2 and CO generally decrease with an increasing hydrogen percentage. It was also found that the emission of NO_X increases with the addition of hydrogen. Mixtures of 10% and 20% hydrogen by volume with natural gas were found to on average increase the cost of the fuel by 8% and 15% respectively.

As an appraisal of hydrogen – methane mixtures, the final version of the NoNOx engine model is used to assess the effect of the addition of a small amount of hydrogen to the CNG fuel. A comparison of the computer models predictions of engine output and efficiency for CNG and a 10% hydrogen - 90% CNG mixture is made. The software predictions of NO_X formation and hydrocarbon and CO emissions are contrasted for both fuels.

5.1 Wave Engine Model

The one-dimensional computational fluid dynamics package Ricardo Wave, developed by Ricardo Software, was previously used to construct a working model of the NoNOx test engine incorporating the EOCV technology.

5.1.1 Model Development

5.1.1.1 Intake System

The inlet pipe network used on the NoNOx test engine includes a long length of pipe between the exit from each of the intercoolers and the inlet to the plenum servicing each bank of the engine. The effect of the length of these inlet pipes on the performance of the engine was investigated by a series of Wave simulations in which this length was varied between 400 and 5800 mm (the current design has a length of approximately 2000mm).

Figures 5.1 – 5.3 show how the predicted BMEP, overall engine efficiency and the volumetric efficiency of the engine vary with the length of the intercooler-plenum ducting for three engine operating speeds.

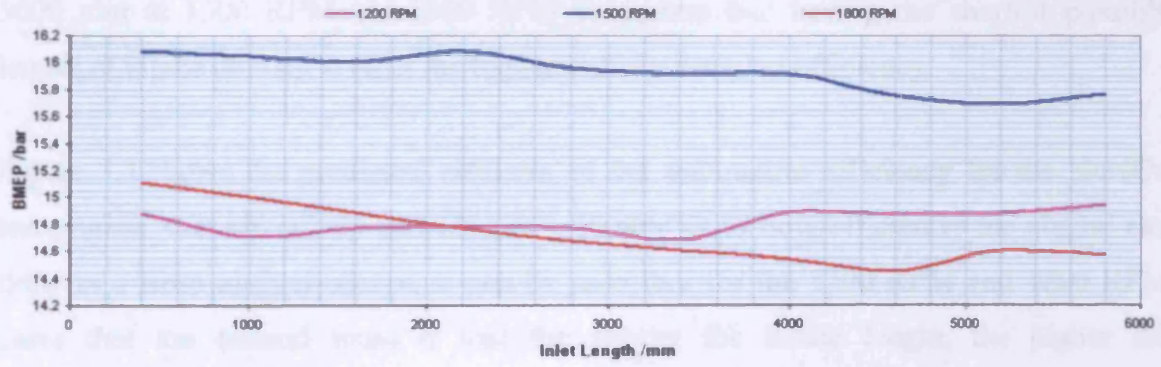

Figure 5.1 – Variation of BMEP with inlet duct length

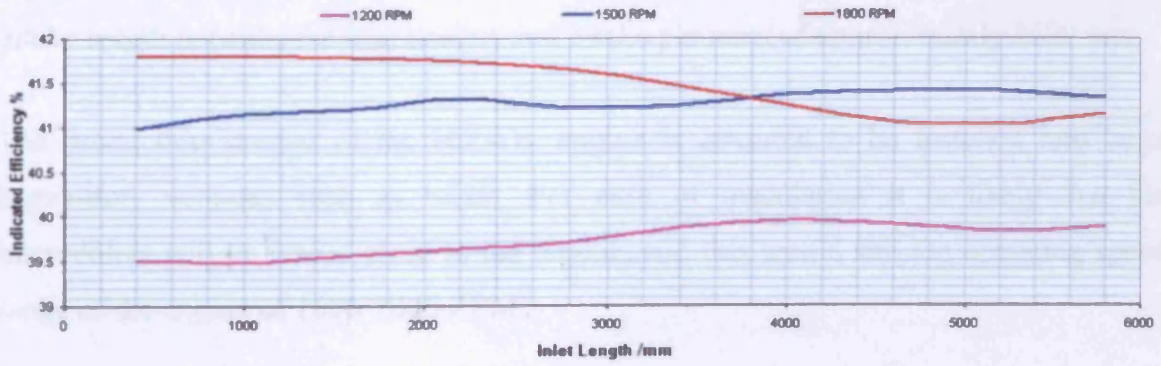

Figure 5.2 – Variation of indicated engine efficiency with inlet duct length

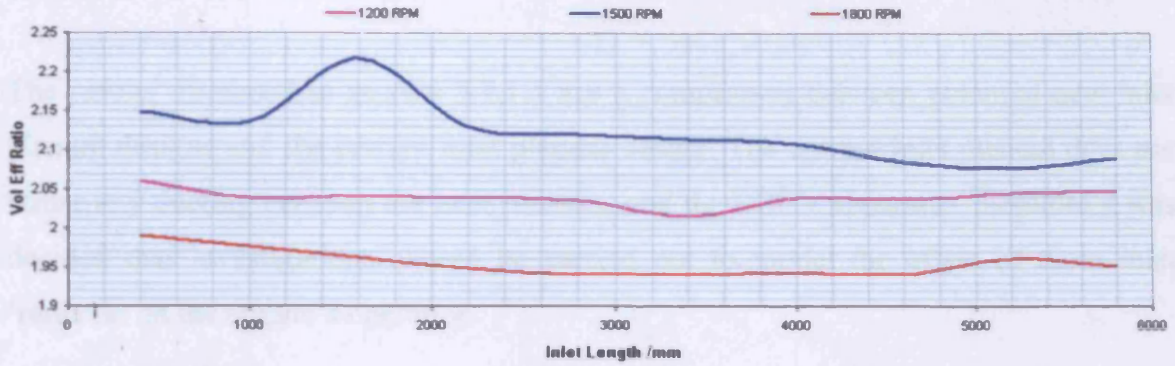

Figure 5.3 – Variation of volumetric efficiency with inlet duct length

The results shown in Figures 5.1 to 5.3 illustrate the effect of varying the length of intake ducting between the intercoolers and inlet plenums. It can be seen from Figure 5.1 that for higher engine speeds the BMEP produced by the engine reduces as the intake length increases. The results shown in Figure 5.2 predict that the optimum intake ducting length for high indicated efficiency of the engine is 4000 mm at 1200 RPM and 5000 mm at 1500 RPM. At 1800 RPM it appears that having the shortest possible length of intake ducting returns the higher indicated engine efficiency.

Figure 5.3 shows the predicted variation of the volumetric efficiency for the NoNOx test engine; this effectively provides an indicator as to how efficiently the engine can draw in a fresh air/fuel charge. It can be seen that for the 1200 RPM and 1800 RPM cases that the general trend is that the shorter the intake length, the higher the volumetric efficiency is for the engine. At 1500 RPM however there is a localised maximum in addition to the same general trend that occurs at other engine speeds. The highest volumetric efficiency for the test engine operating at 1500 RPM occurs with an intake length between the intercoolers and intake plenums of approximately 1600 mm.

The production version of the NoNOx engine is intended to be installed into large heavy-duty vehicles such as buses. For ease of installation it is likely that the intercoolers will be placed close to the engine, and this would suit the operating speed range of the engine of 1000-2000 RPM.

5.1.1.2 Inlet Runners

The results discussed in section 5.1.1.3 are a comparison between potential new inlet plenum designs and the current inlet plenum design. The current inlet plenum does not utilise any ducting between the inlet plenums and the EOCV apparatus, therefore it was decided that investigations should be carried out to model the effect of these inlet 'runners' on the engine's operation.

Simulations were carried out at three likely engine operating speeds in which the inlet runner length was varied between 5 and 600 mm. Figures 5.4 – 5.6 illustrate how the predicted BMEP, engine operating efficiency and volumetric efficiency varied with inlet runner length.

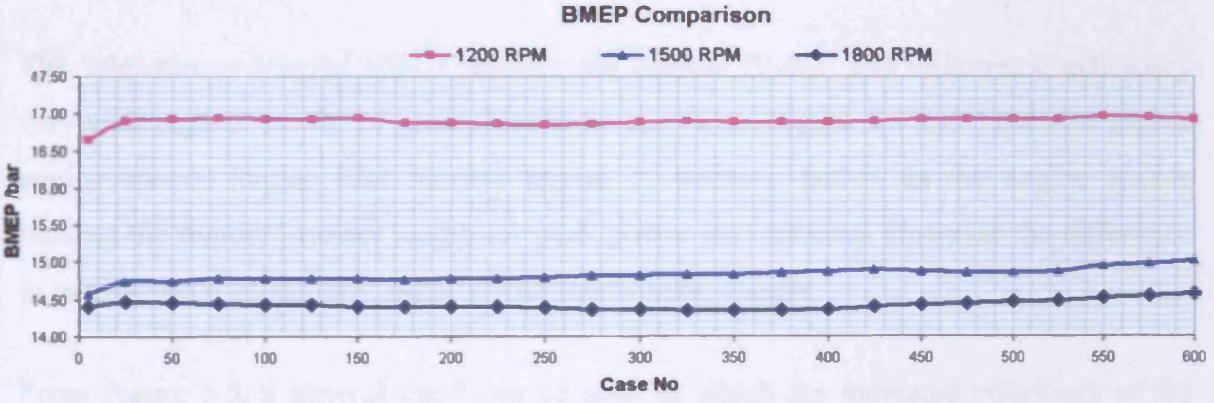

Figure 5.4 – Variation of BMEP with inlet runner length

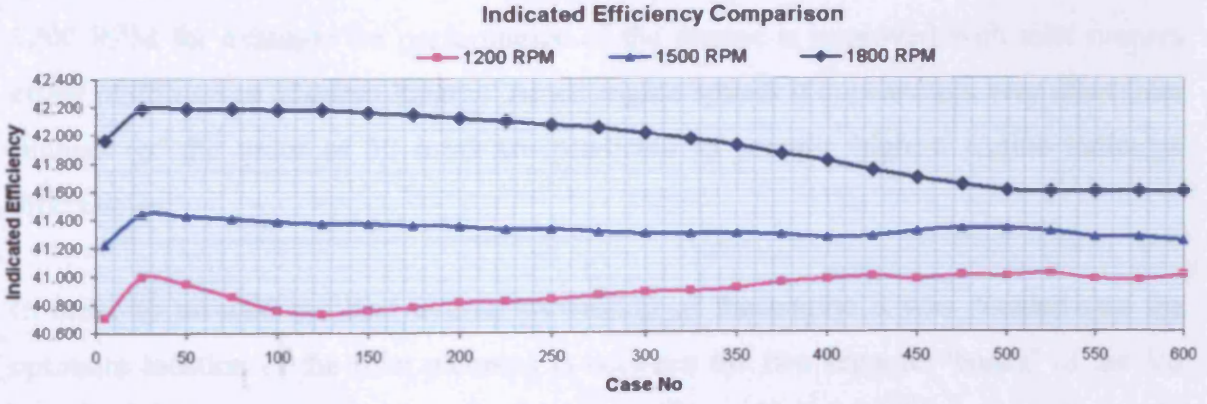

Figure 5.5 – Variation of indicated efficiency with inlet runner length

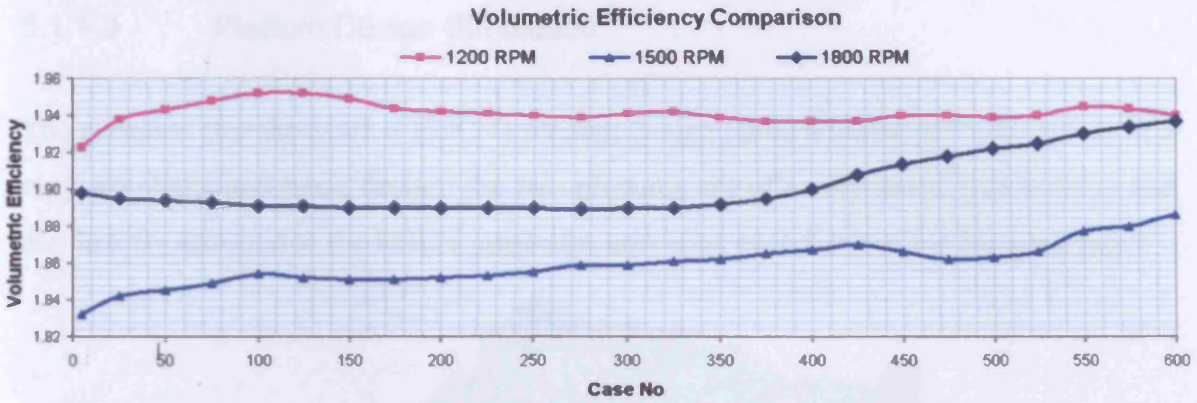

Figure 5.6 – Variation of volumetric efficiency with inlet runner length

A close examination of the results shown in Figures 5.4 – 5.6 reveals that there is no ideal inlet runner length, with individual engine speeds performing better with different length inlet runners.

The inlet runner lengths which produce the highest BMEP and volumetric efficiency vary with engine speeds. In general it can be seen from Figure 5.4 and 5.6 that at higher engine speeds longer inlet runners appear to perform better, as the engine speeds reduces the required runner length for peak power also reduces. However the difference in performance varies only slightly with inlet runner length.

From Figure 5.5, a general trend can be seen in which the indicated efficiency of the engine is higher with long inlet runners at low speeds and short inlet runners at high speeds. It is hard to determine an optimum inlet runner length from these results; at 1200 RPM for example the performance of the engine is improved with inlet runners either of 75 mm or 550 mm lengths. At all engine speeds it appears that very short inlet runners (of the order of 50 mm) are predicted to provide highest engine indicated efficiencies.

In order to provide the best overall packaging of the engine it was decided that the optimum location of the inlet plenums is between the two separate 'banks' of the V6 NoNOx engine, because of this the inlet runners are likely to be around 300 mm in length.

5.1.1.3 Plenum Design Simulation

The previous (for the Mark 3 EOCV) plenum design (shown below in figure 5.7) is of a very simplistic and basic design; the two plenums are of a very small total volume and are directly attached to the EOCV apparatus servicing each bank of the V6 test engine.

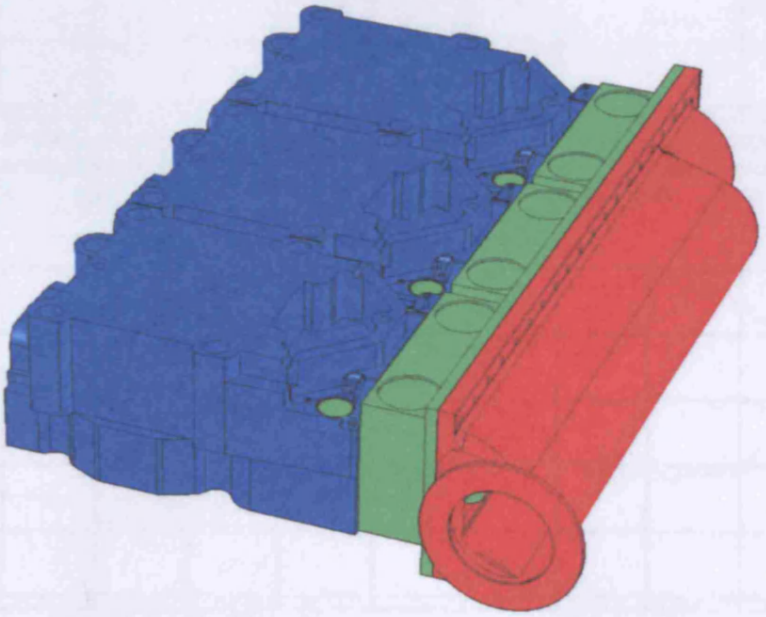

Figure 5.7 – Previous plenum design

The sample pressure trace diagrams shown in Figure 5.8 illustrate precisely a phenomenon that has been observed during operation of the NoNOx test engine. It can be seen that the pumping losses at higher engine speeds are substantially higher than that at lower speeds, and this is reducing the operating efficiency of the engine at the higher speeds. It is believed that these pumping losses are primarily due to the design of the inlet system installed on the engine, and that the engine's efficiency can be increased by improving the design of these components. However, other possible causes of these pumping losses include the current compressor specification as well as the design of the engine's cylinder head / inlet valves.

At this stage of the project NoNOx proposed three new plenum designs, which were to be modelled using the Wave computer software. All of the new plenum designs utilise inlet runners approximately 300mm in length between the plenum and the EOCV inlets.

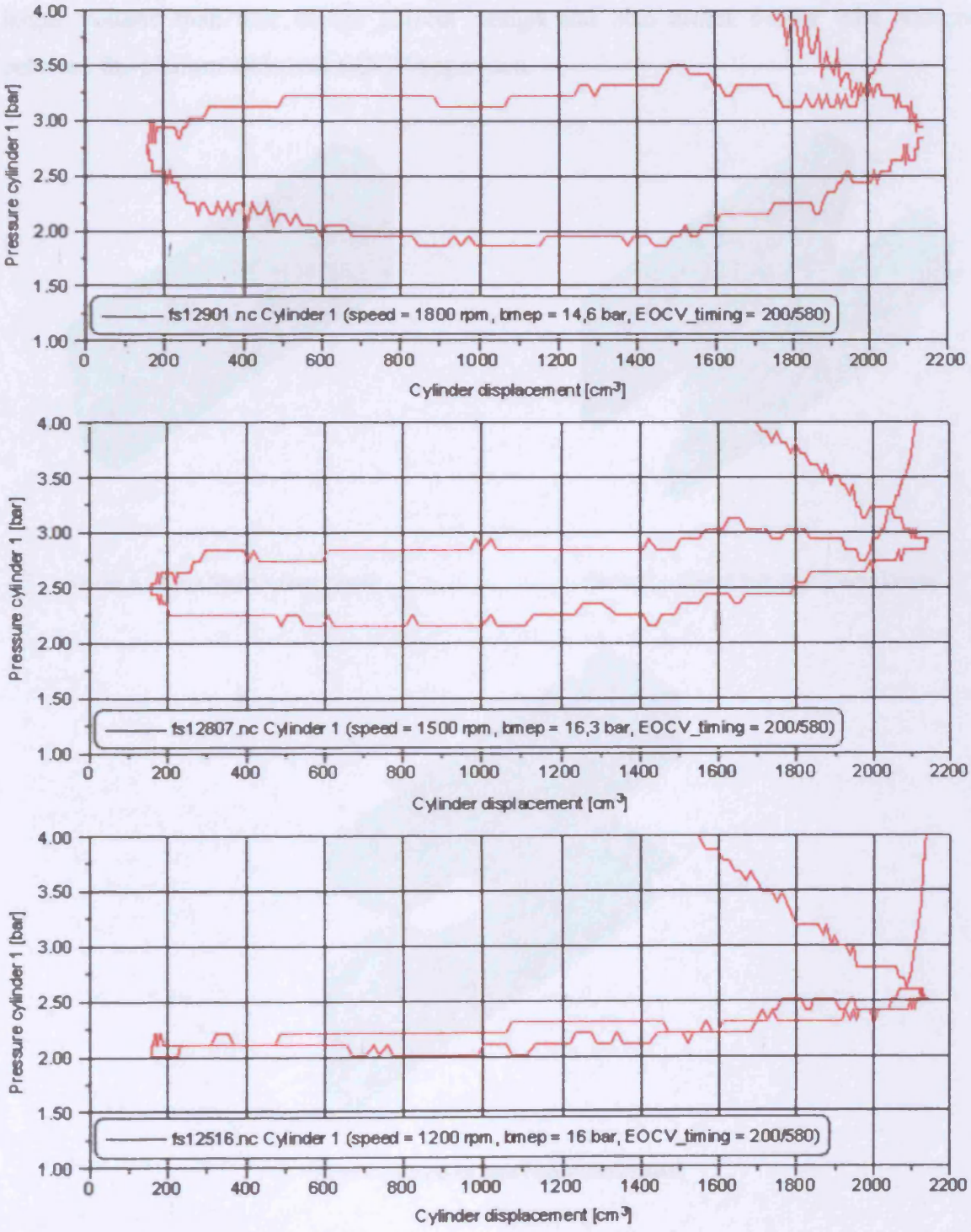

Figure 5.8 – Pumping loss pressure traces

The three plenum designs are shown in Figure 5.9. All of the new designs are of a much larger volume than that of the current design and also utilize longer inlet runners between the plenum and each EOCV apparatus.

Design A – Large Single Volume Plenum

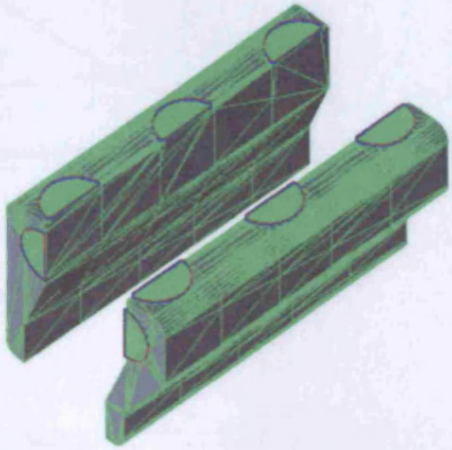

Design B – Vertical Split Twin Volume Plenum

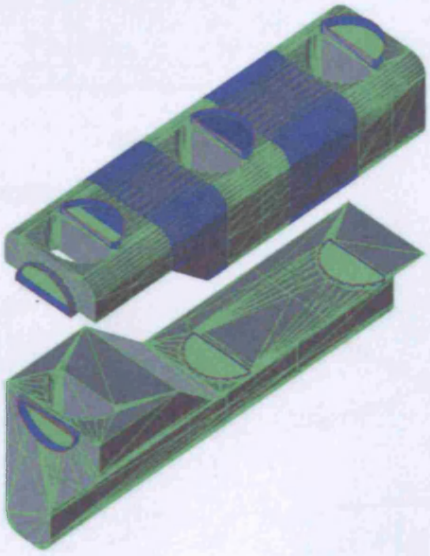

Design C – Horizontal Split Twin Volume Plenum

Figure 5.9 – New plenum designs

The new plenum geometries were imported into the Wave program using the Wavemesher software; for designs B and C this involved separating out the plenum into

two separate volumes and importing them separately. Simulations were then carried out for each plenum design at three engine operating speeds (Cases 1, 7 and 11 in Table 3.8). Comparisons of the new Wave simulation results are shown in Figures 5.10 – 5.12.

PV Diagram New Plenum Design A – 1200 RPM

PV Diagram New Plenum Design A – 1500 RPM

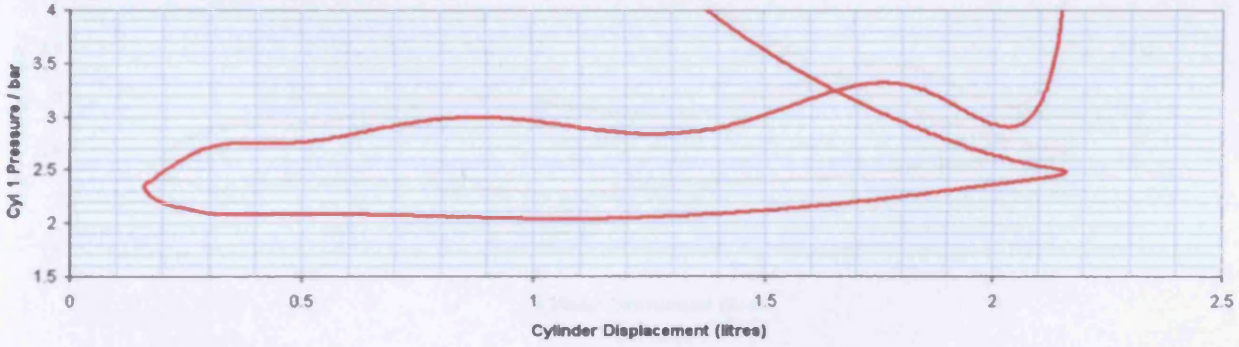

PV Diagram New Plenum Design A – 1800 RPM

Figure 5.10 – Wave simulation pressure traces plenum Design A.

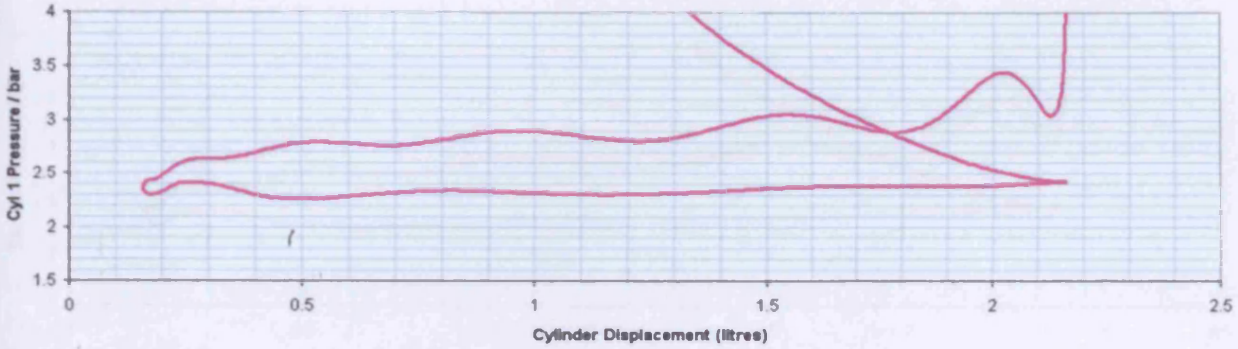

PV Diagram New Plenum Design B – 1200 RPM

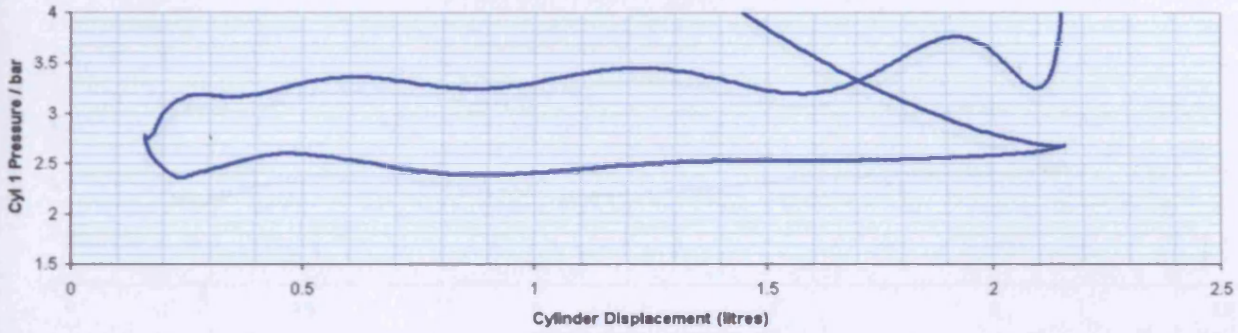

PV Diagram New Plenum Design B – 1500 RPM

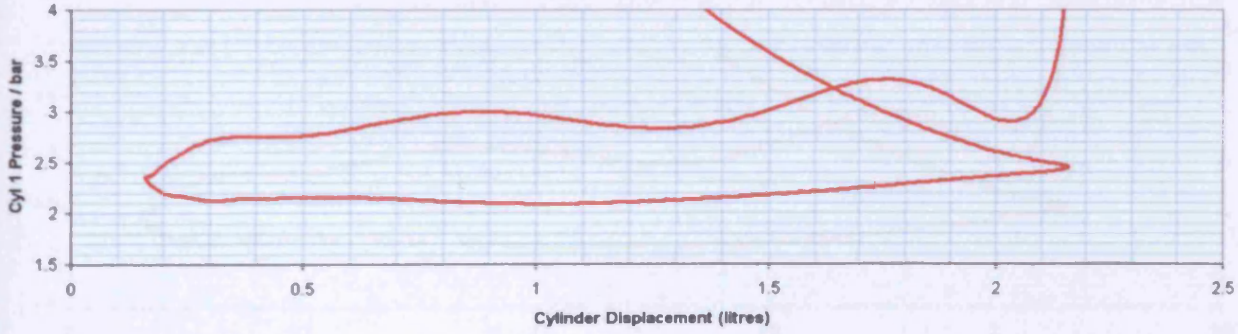

PV Diagram New Plenum Design B – 1800 RPM

Figure 5.11 – Wave simulation pressure traces plenum Design B.

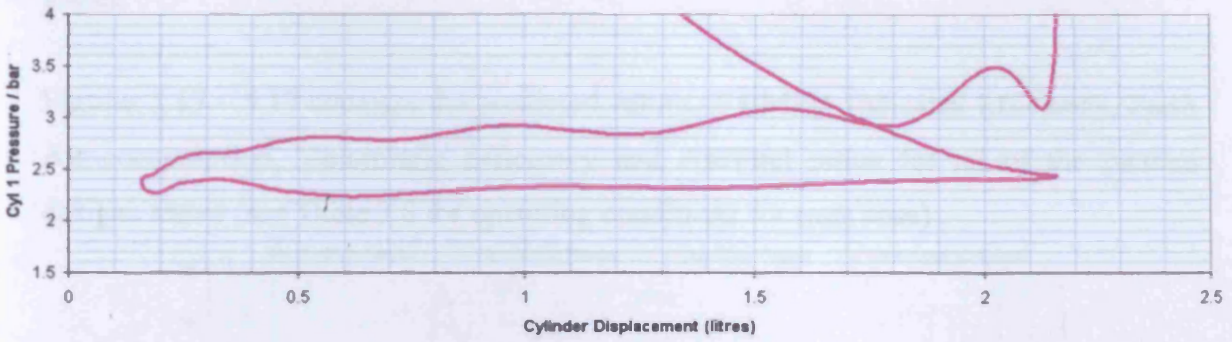

PV Diagram New Plenum Design C – 1200 RPM

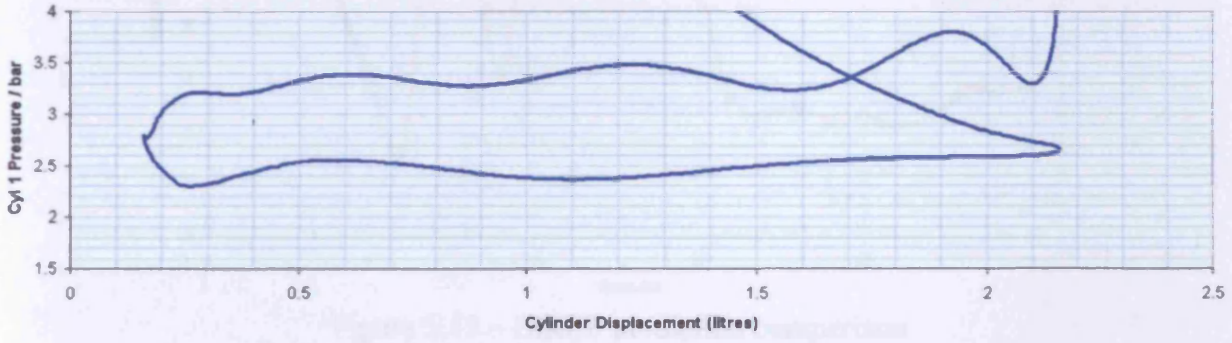

PV Diagram New Plenum Design C – 1500 RPM

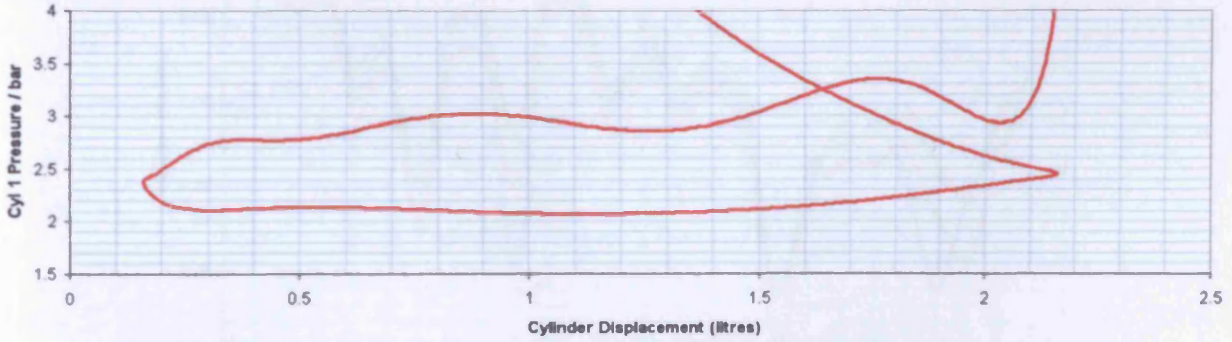

PV Diagram New Plenum Design C – 1800 RPM

Figure 5.12 – Wave simulation pressure traces plenum Design C.

Examining the PV pressure traces predicted by the Wave simulations in Figures 5.10 - 5.12, it can be seen that all of the new plenum designs have similar predicted pumping losses.

Figures 5.13 – 5.17 compare the predicted values of BMEP, Indicated Efficiency, Fresh Air consumption, Volumetric Efficiency and Air/Fuel ratios for all of the plenum designs tested (see Table 3.8 for operating conditions for each case) .

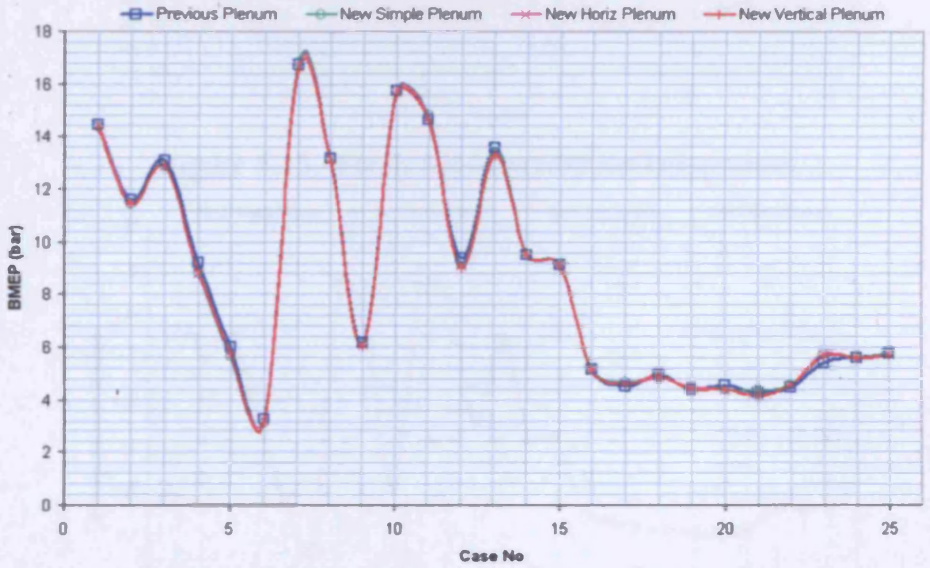

Figure 5.13 – BMEP prediction comparison

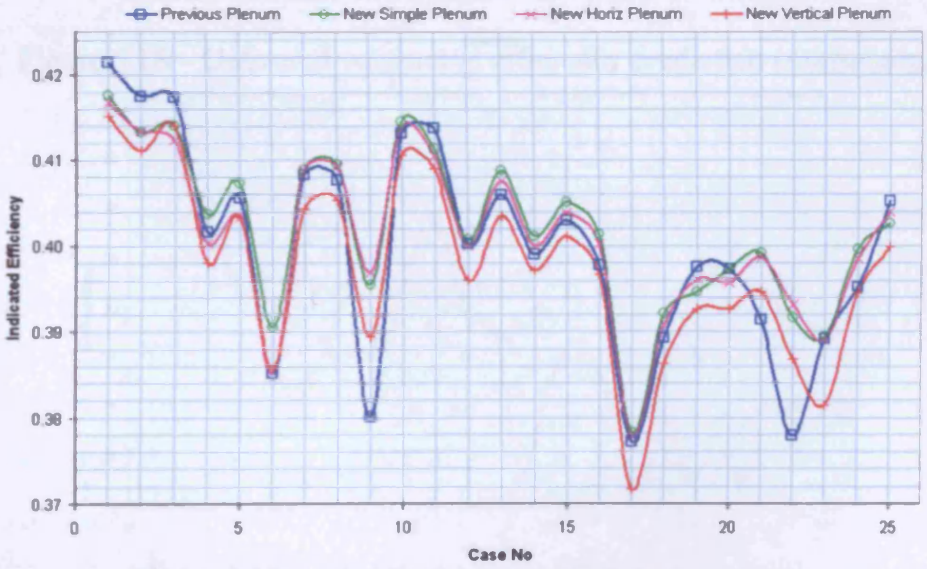

Figure 5.14 – Indicated efficiency prediction comparison

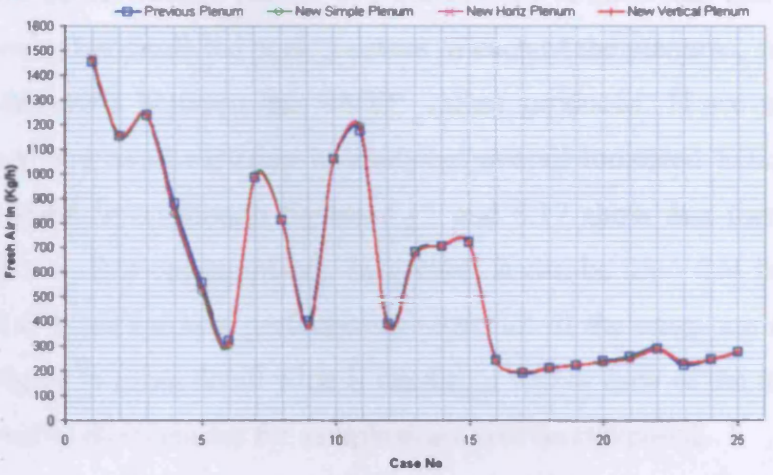

Figure 5.15– Fresh Air-in prediction comparison

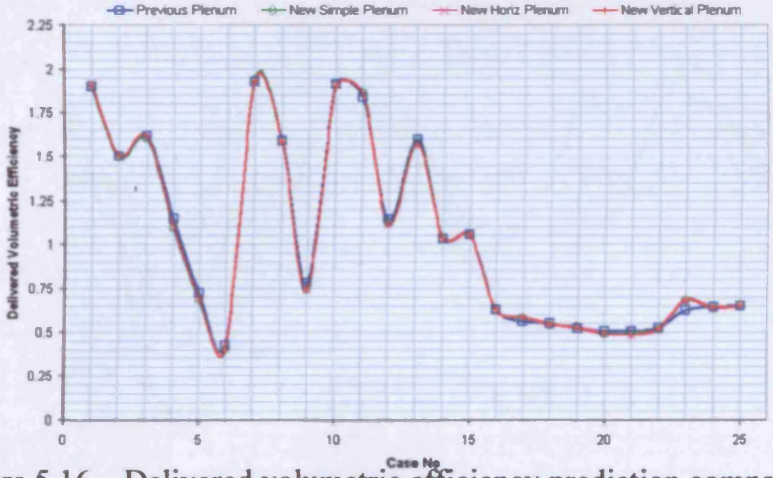

Figure 5.16 – Delivered volumetric efficiency prediction comparison

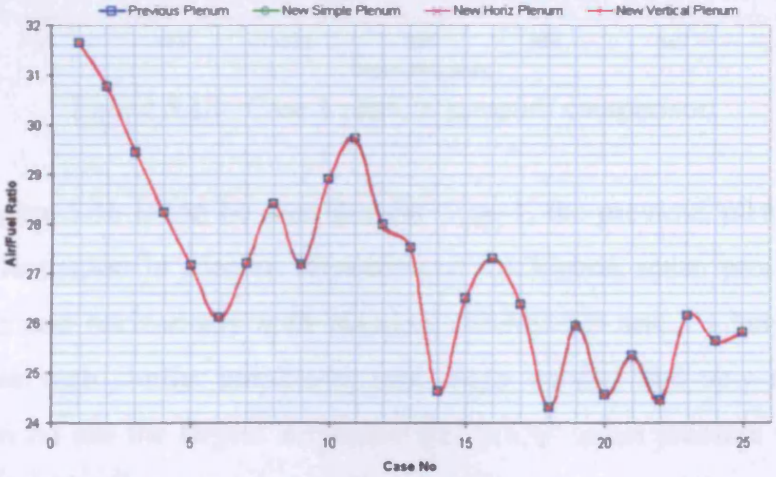

Figure 5.17 – Air / Fuel ratio prediction comparison

An examination of the results shown in Figures 5.13 reveals that there is very little difference between the predicted performances of each of the plenums, as there are only very small differences between the BMEP values produced. However, Figure 5.14 shows that there is a large variation in predicted overall Indicated Efficiency between the plenum designs (even though figures 5.15 and 5.17 show that there is very little variation in air and fuel consumption). In general it can be seen that the new plenum designs A and C have the best performance when all of the cases are considered. In order to investigate in more detail what is occurring within each of the plenum designs, the pressures within the plenums for sample cases will be compared.

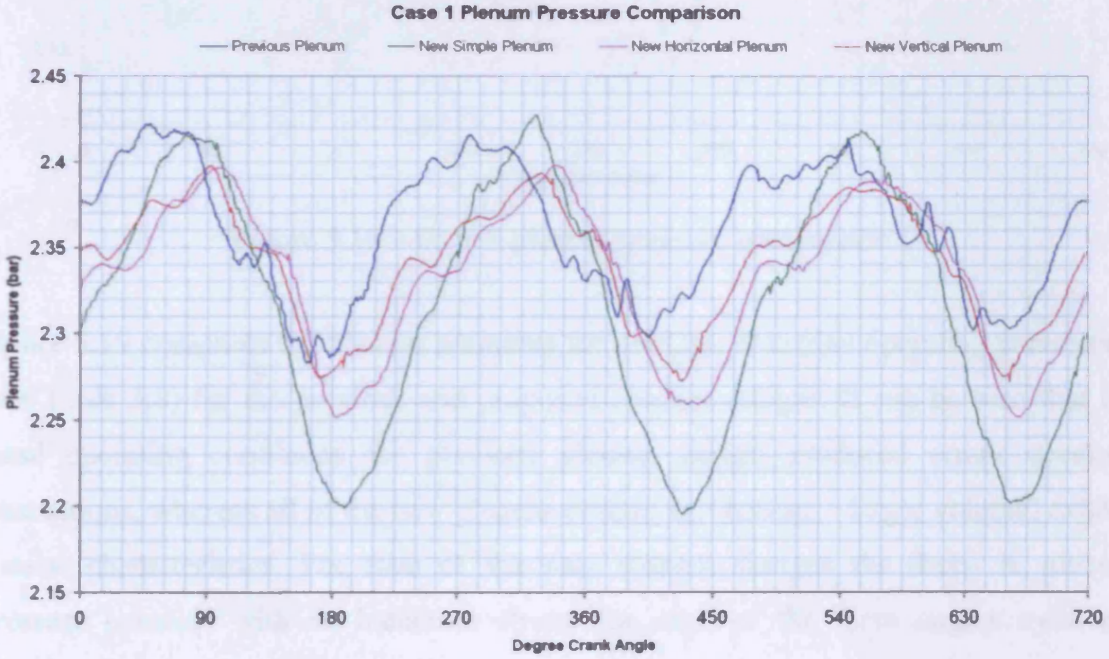

Figure 5.18– Case 1 plenum pressure comparison

Examining Figure 5.18 it can be seen that for Case 1, the previous plenum design has the smallest fluctuation in Plenum Pressure and the highest mean pressure. The new vertically split and horizontally split plenums (Designs B and C) have very similar pressure curves with similar amplitudes and mean values. The new simple plenum design (Design A) has the largest amplitude and lowest mean pressure value, but also has the smoothest curve.

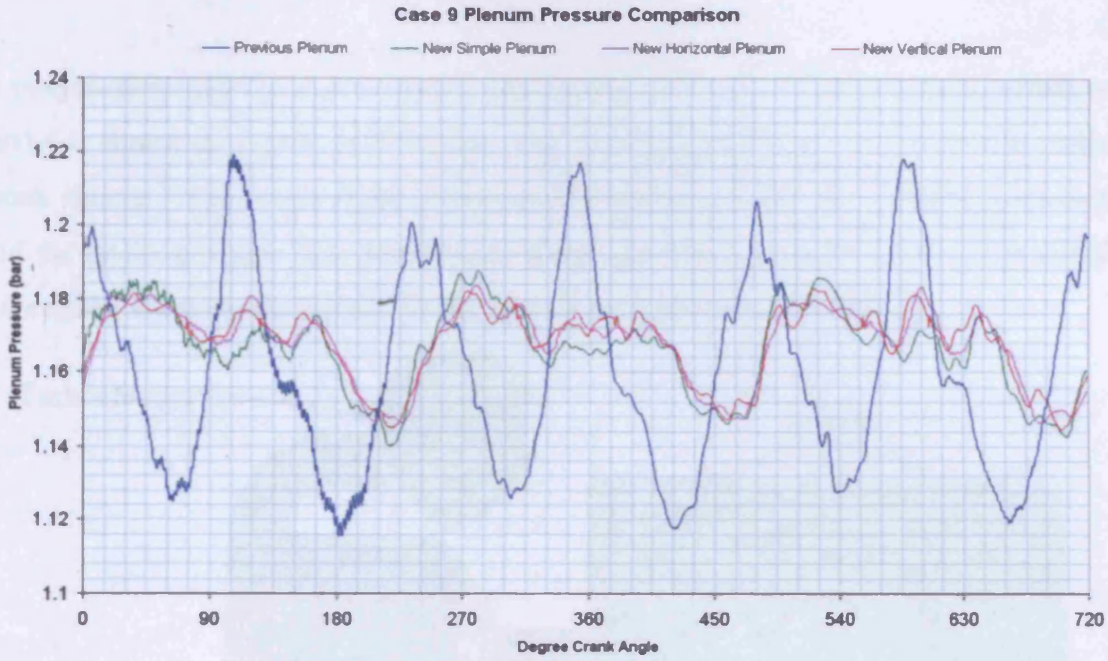

Figure 5.19 – Case 9 plenum pressure comparison

Figure 5.19 compares the plenum pressures for the Case 9 engine operating parameters (see Table 3.8) for the previous and proposed plenum designs. It can be seen that for these operating conditions the previous plenum design produced erratic pressure fluctuations, whereas all of the new plenum designs (all having a larger volume) exhibit similar characteristics. For each of the new plenum designs the drops in plenum pressure coincide with an induction stroke for each of the three engine cylinders connected to the plenum.

The simulations of the different plenum designs show that two of the new plenums (Design A and Design B) are predicted to increase the NoNOx engines average indicated efficiency over the range of operating conditions tested. Based upon the results of this simulation a new inlet plenum design was constructed by NoNOx in conjunction with a manufacturer. The new plenum design was tested and the results are shown in the following section.

5.1.1.4 Final Design Simulations

In conjunction with NoNOx a final design for the V6 EOCV engine's intake system was devised, shown in Figure 5.20 below. The final design for the intake system utilises much shorter ducts between the turbochargers and the intercoolers and the intercoolers and the intake plenum. New intercoolers have also been selected specifically to suit the V6 engine, allowing the overall intake system to be much more compact,

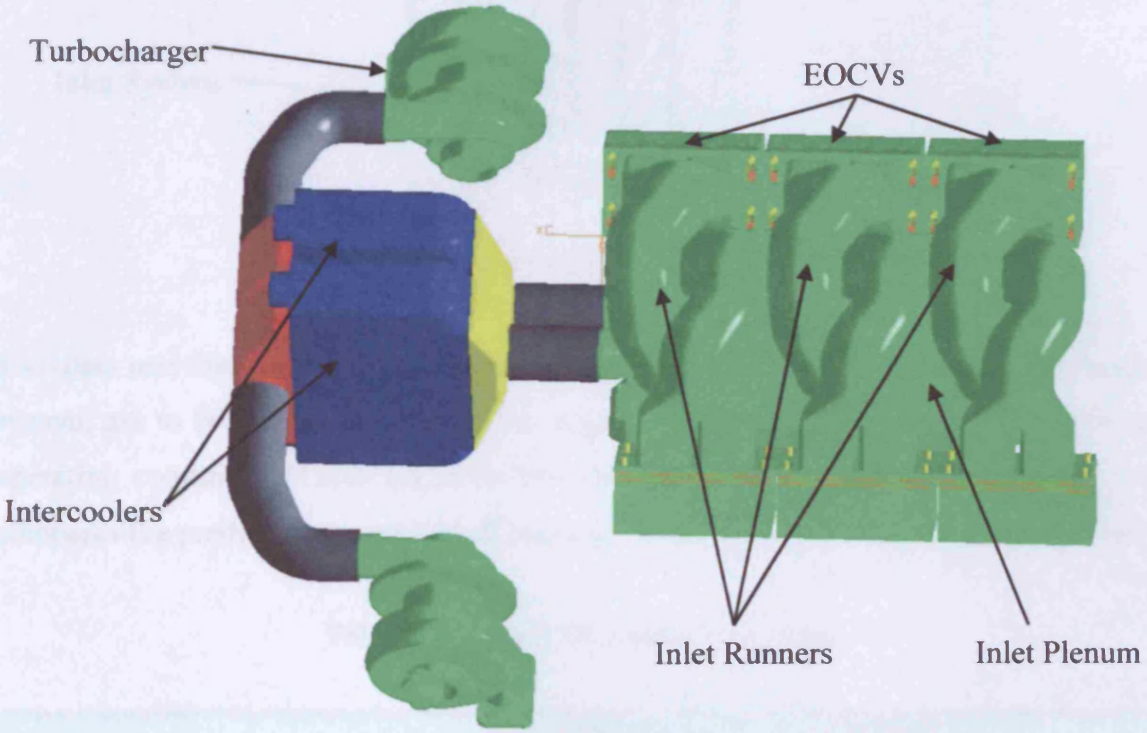

Figure 5.20 – Final design intake system

Figure 5.20 displays the complex new intake plenum design, which consists of two separate chambers, each supplied by one of the two turbochargers. The two separate plenum chambers either supply the "main" or "swirl" ports of each engine cylinder.

The Ricardo Wave model of the V6 NoNOx engine was altered using the new intake system geometry. The Ricardo Wave model of the NoNOx V6 test engine incorporating the final design intake plenum, intercooler etc. is shown in Figure 5.21. This model has been compared with some initial readings taken from the NoNOx test engine with a prototype version of the new inlet system as a final test of the Wave engine model.

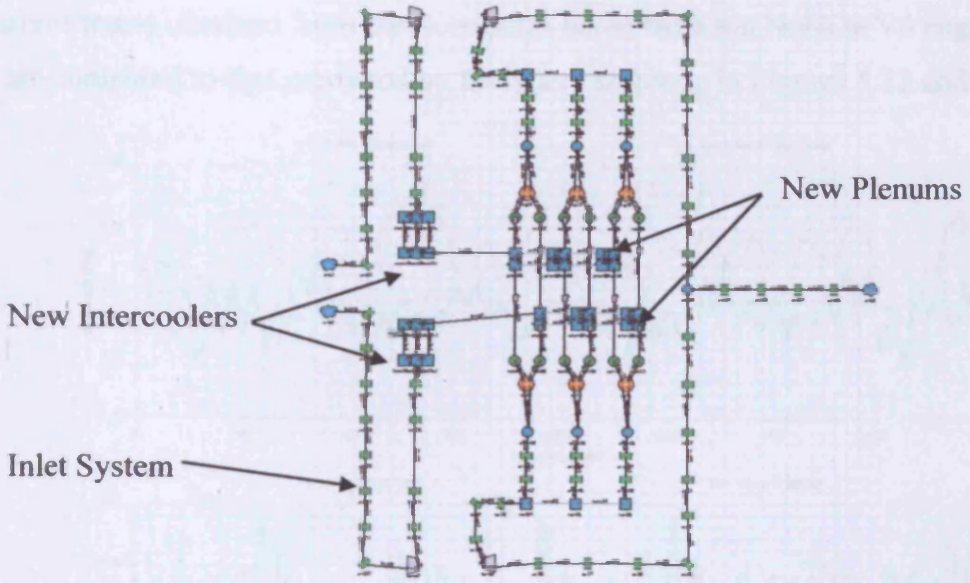

Figure 5.21 – Final EOCV V6 Wave engine model

Two data sets obtained from testing the NoNOx V6 engine, with the final design intake system, are to be compared to the Wave engine model predictions for the same engine operating conditions. Table 5.1 describes the operating conditions for each case and compares the predicted powers and efficiencies to that measured on the engine test-bed.

Table 5.1 – Final V6 engine validation

	OPERATING CONDITIONS			
	Case1		Case2	
Engine Speed	1800		1500	
Lambda	1.588		1.680	
Ignition Timing	24° BTDC		24° BTDC	
EOCV Open/Close	180° / 500°ATDC		180° / 540°ATDC	
VTG Position	23 mV		185 mV	
	Measured Values	Wave Prediction	Measured Values	Wave Prediction
BMEP	9.905 bar	9.905 bar	12.30 bar	12.30
Indicated Efficiency	-	40.10 %	-	41.27 %

Pressures traces obtained from measurements taken from the NoNOx V6 engine test-bed are compared to that predicted by the Wave software in Figures 5.22 and 5.23.

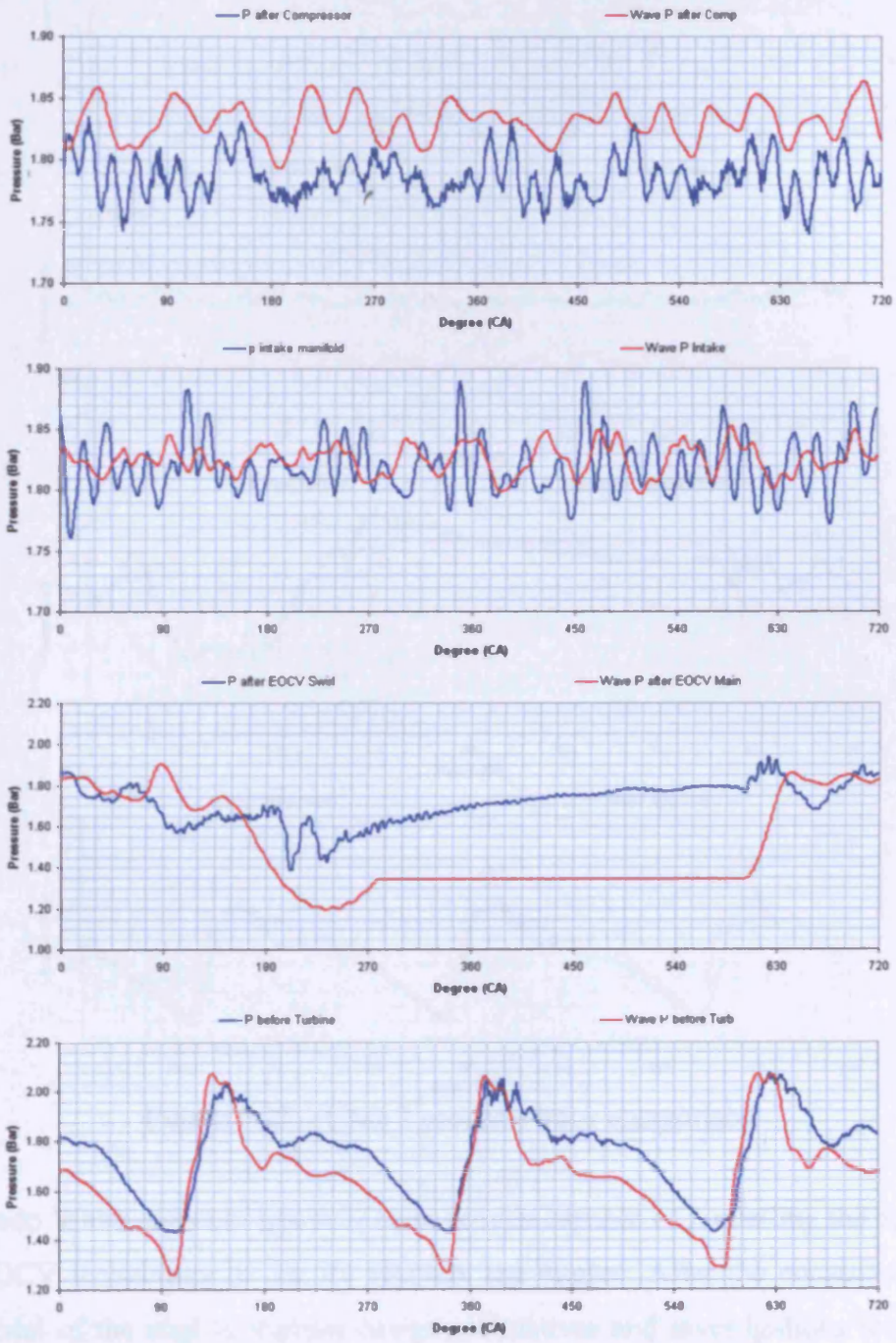

Figure 5.22 – Case 1 pressure trace comparison

The pressure traces shown in Figures 5.22 and 5.23 illustrate that the pressures predicted by Wave are very similar to the pressures measured on the test engine.

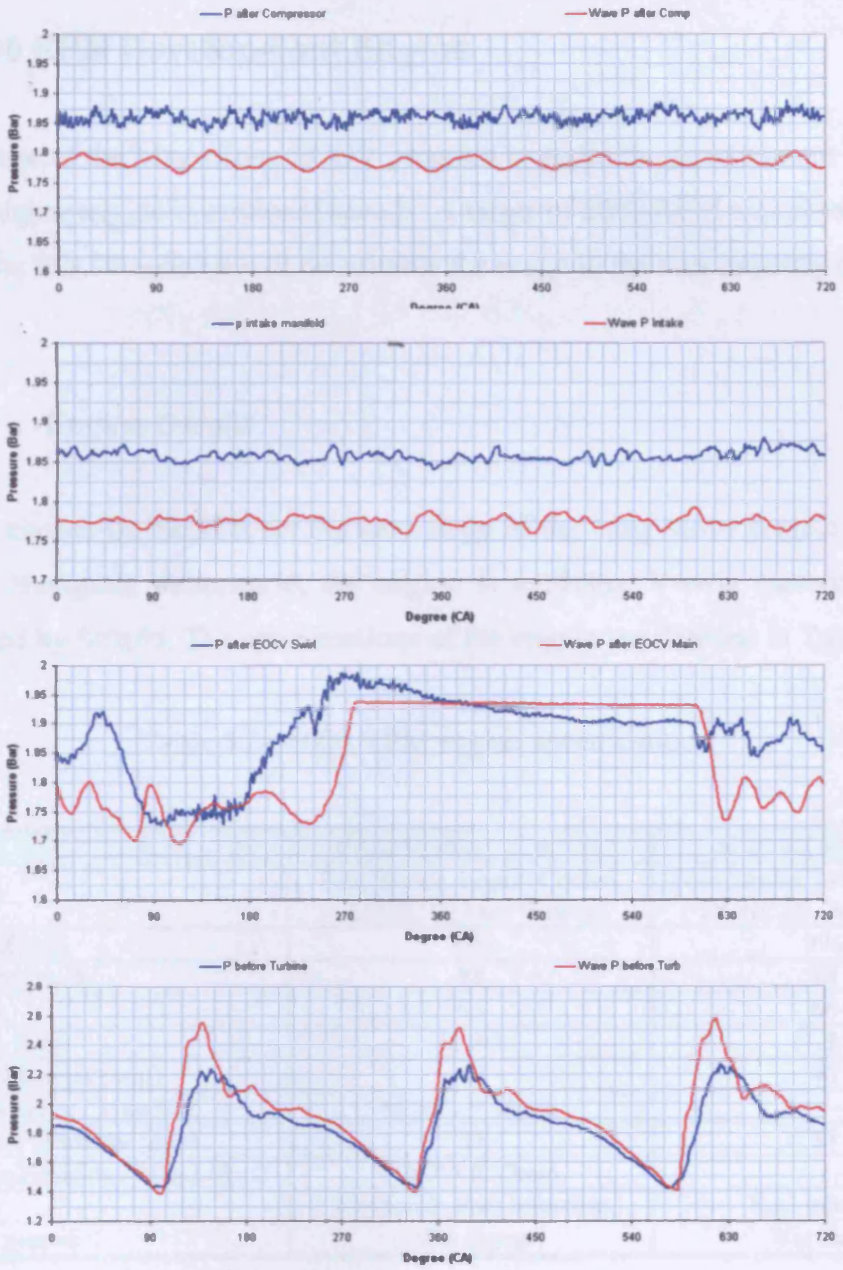

Figure 5.23 – Case 2 pressure trace comparison

The Ricardo Wave software has thus been proven capable of modelling the application of the EOCV technology to the V6 NoNOx test engine. After the construction of an initial model of the engine, various design alternatives and investigations were carried out. Reviewing the results of the Wave simulations and practical testing, a final design for the NoNOx V6 engine system was constructed. A model representing the final production geometry for the NoNOx V6 engine was created, which can be used in further investigations.

5.1.2 6000 RPM Development Engine

The final stage of the Mag-Move EOCV program includes the development of the valve design for higher engine operational speeds. A target of 6000 RPM was chosen as it will mean that the EOCV concept will be suitable for usage in the vast majority of passenger vehicles.

5.1.2.1 Engine Details

The engine chosen by NoNOx for the next stage of the Mag-Move project is that from the Cagiva Navigator motorcycle; the engine is a 1000cc V-twin motorcycle engine manufactured by Suzuki. The specifications of the engine are detailed in Table 5.2.

Table 5.2– 6000 RPM engine specifications

	CAGIVA NAVIGATOR	SUZUKI TL-1000S
Engine Type	Four Stroke, Liquid Cooled, DOHC 90 Deg V-twin	Four Stroke, Liquid Cooled, DOHC 90 Deg V-twin
Displacement (cc)	996	996
Cylinder Bore (mm)	98	98
Stroke (mm)	66	66
Compression Ratio	11.3:1	11.3:1
Inlet Valve Diameter (mm)	40	40
Inlet Cam Duration / Max Lift	≈270° / 9.45mm	- / -
Exhaust Valve Diameter (mm)	33	33
Exhaust Cam Duration / Max Lift	≈260° / 8.57mm	- / -
Fuel System	Electronic Fuel Injection	Fuel Injection
Lubrication System	Wet Sump	Wet Sump

Detailed geometric information for the Cagiva Navigator engine is not easily obtainable, mainly due to the rarity of the engine. However, the Cagiva Navigator engine is almost identical to the engine used in the Suzuki TL-1000s motorcycle for which information is readily available. Therefore, a working model of the TL-1000s engine is be constructed in Wave and compared to published performance data. This model can then be modified to incorporate the EOCV apparatus.

5.1.2.2 Model Construction

Inlet System

The standard inlet system fitted to the Suzuki TL-1000s is shown in Figure 5.24. The air flow enters through two separate inlets positioned either side at the front of the bike. The passage of the flow from the two separate inlets into the air filter is controlled by an inlet control valve; which partially closes at low-medium engine speeds. The air then passes through the air filter into the main body of the inlet plenum and into the inlet runners. The flow into the engine is then controlled by two individual throttles 52mm in size.

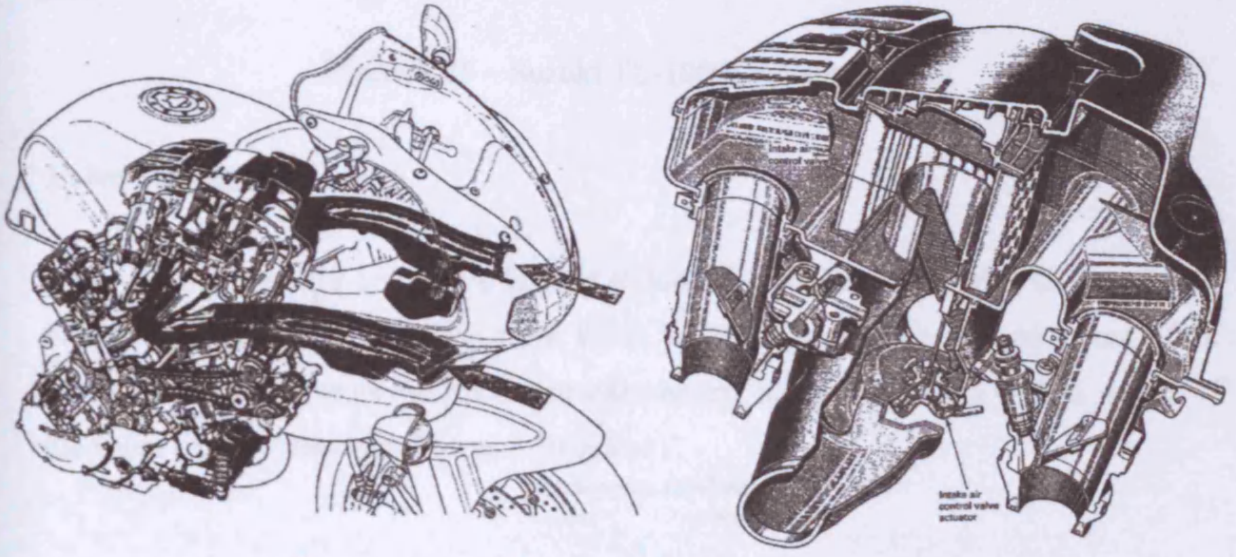

Figure 5.24 – Suzuki TL-1000s intake system

Exhaust System

The exhaust system used on the Suzuki TL-1000s is shown in Figure 5.25. The exhaust gases from each engine cylinder exit through two separate exhaust pipes, with a single connection between the two pipes allowing some of the exhaust gases to flow between the two exhaust "headers". The exhaust for the rear engine cylinder also has a short link pipe, connecting together a section of the exhaust before and after a sharp bend to act as an alternate route for the exhaust gases.

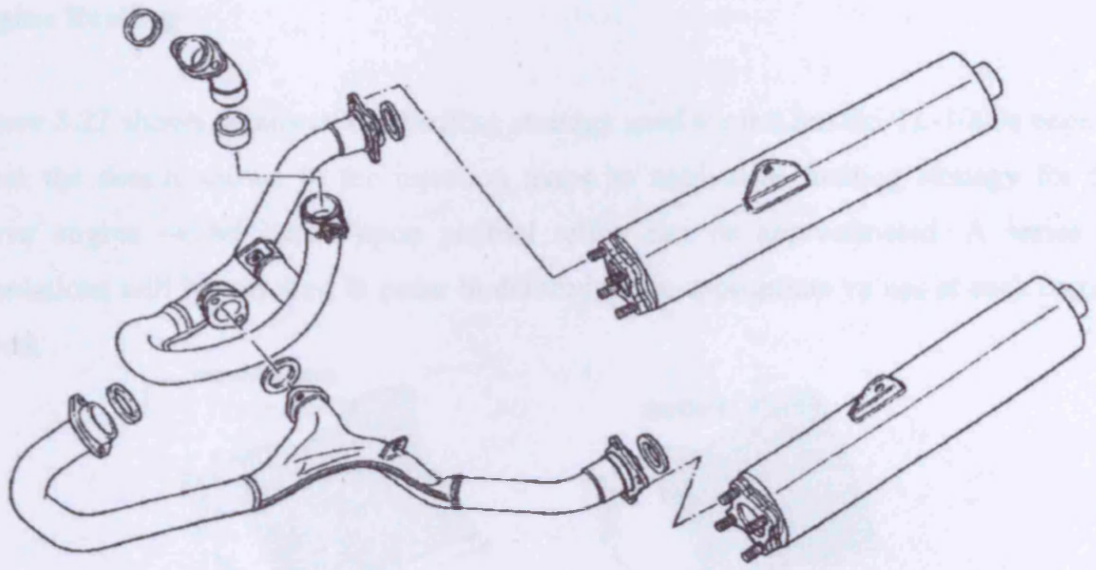

Figure 5.25 – Suzuki TL-1000s exhaust system

Valve Timing

Data was obtained for both the Inlet and Exhaust camshafts by NoNOx for the Cagiva Navigator engine. It can be seen from Table 5.2 that the duration and maximum lift of the cams are the same as the published information for the TL-1000s engine, details of the valve lifts are shown in Figure 5.26 below.

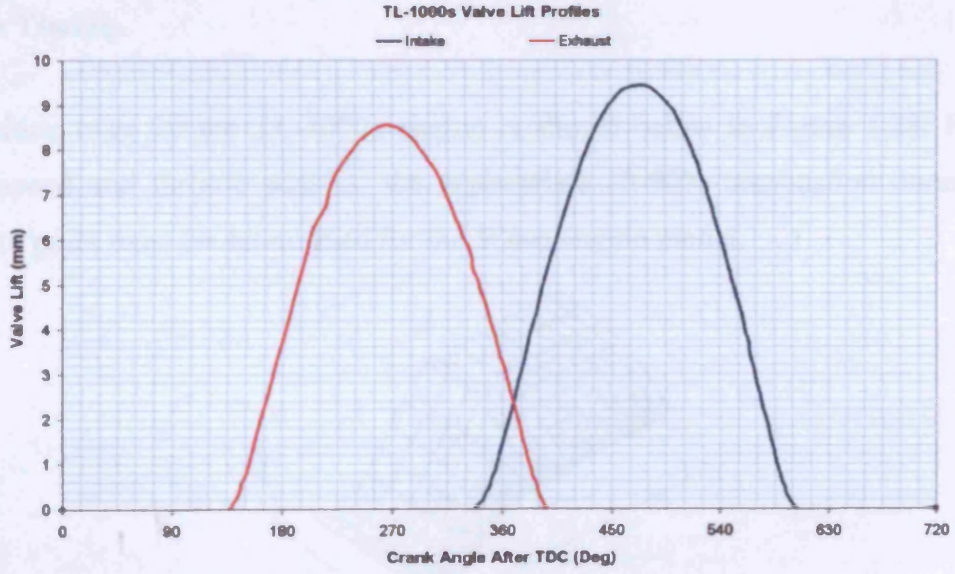

Figure 5.26 – Cagiva Navigator valve-lifts

Engine Fuelling

Figure 5.27 shows details of the fuelling strategy used for the Suzuki TL-1000s engine. From the details shown in the injection maps an equivalent fuelling strategy for the Wave engine model based upon air/fuel ratios can be approximated. A series of simulations will be required in order to determine the appropriate values at each engine speed.

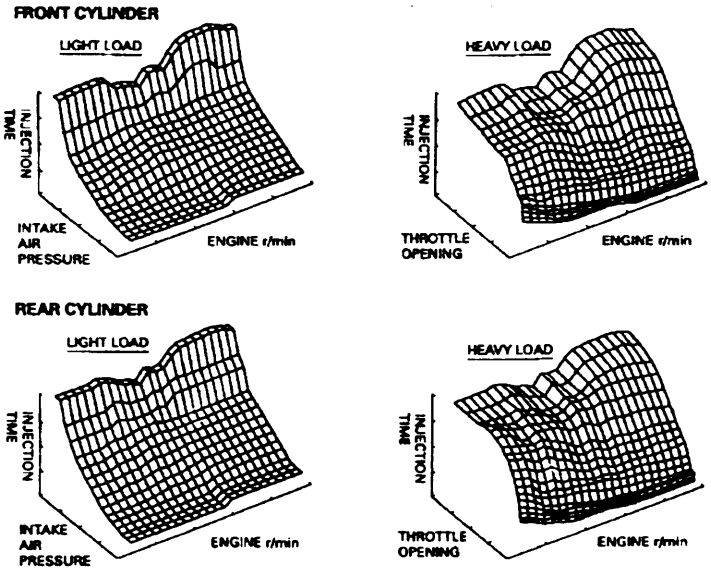

Figure 5.27 – Suzuki TL-1000s injection maps

Ignition Timing

The ignition map for the TL-1000s engine is shown below in Figure 5.28. For each engine speed and throttle position the appropriate 10-90% combustion duration and 50% burn point must be determined for the Wave engine model.

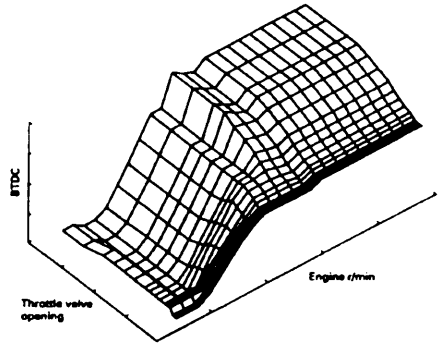

Figure 5.28 – Suzuki TL-1000s ignition map

Figure 5.29 shows the completed WaveBuild engine model for the Suzuki TL-1000s engine. The different engine operational values that have been determined to be appropriate for the initial TL-1000s engine simulations are listed in Table 5.3.

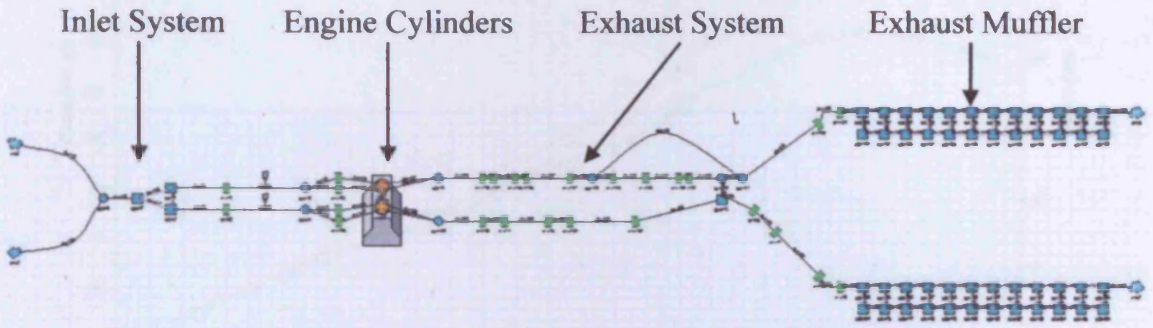

Figure 5.29 – Wave TL-1000s engine model

Table 5.3 – Wave TL-1000s engine settings

ENGINE SPEED (RPM)	1000	2000	3000	4000	5000	6000	7000	8000	9000	10000
Air/Fuel Mass Ratio	13.8	13.8	13.8	13.8	13.8	13.8	13.8	13.8	15.0	16.0
10-90% Burn Duration (Deg)	20	20	20	20	20	20	25	25	25	25
50% Burn Location (Deg ATDC)	16	16	12	8	4	0	1	1	1	1

The values listed in Table 5.3 are the fuelling values and combustion description parameters used by the Wave software to calculate the energy release and gas expansion within the engine cylinder. It is anticipated that these values may change when more detailed information is obtained from in-cylinder pressure sensors placed in the 6000 RPM test engine.

5.1.2.3 Model Results

Figure 5.30 compares the performance for the TL-1000s engine calculated by Wave to published values obtained by testing using a dynamometer. It can be seen that there is a reasonable agreement throughout the RPM range between the Dyno horsepower values and the brake horsepower (bhp) values calculated by the Wave model.

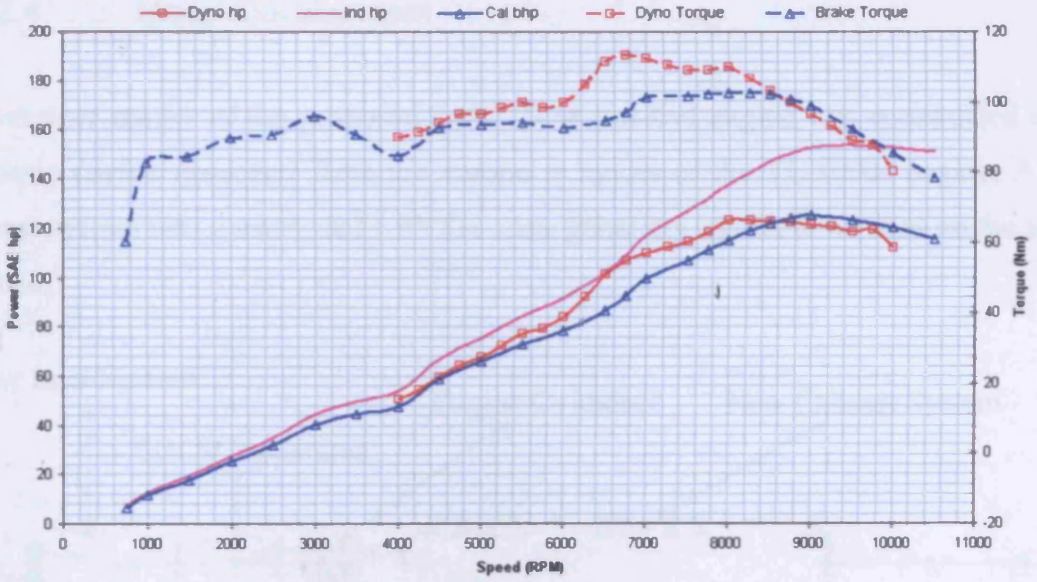

Figure 5.30 – TL-1000s Wave simulation results

The main difference between the values predicted by Wave for the Tl-1000s engine and the published values occur in the 5000-8000 RPM range, where the published torque and power values are higher than the Wave predictions. One possible reason for this performance difference is that the camshaft profiles used in the computer engine model were obtained by measurements of the Cagiva Navigator engine, and it is unknown whether the Suzuki TL-1000s engine uses exactly the same camshafts (the published performance figures for the Cagiva Navigator engine are lower than that for the Suzuki TL-1000s engine, and this may be in part due to a "milder" cam profile).

The next stage of the 6000 RPM model development is the modification of the model to include the EOCV apparatus. A new inlet system must be designed to incorporate two single EOCV's and the exhaust system must be replaced with that already constructed for the engine testing. See section 5.2.2 for the initial CFD analysis of a proposed 6000 RPM EOCV design.

5.1.2.4 Model Development

A computer model of the proposed 6000 RPM test-bed engine was constructed using the basic engine geometry from the computer model of the TL-1000s engine. A new exhaust system was constructed with the same geometry as that to be used on the actual test-bed.

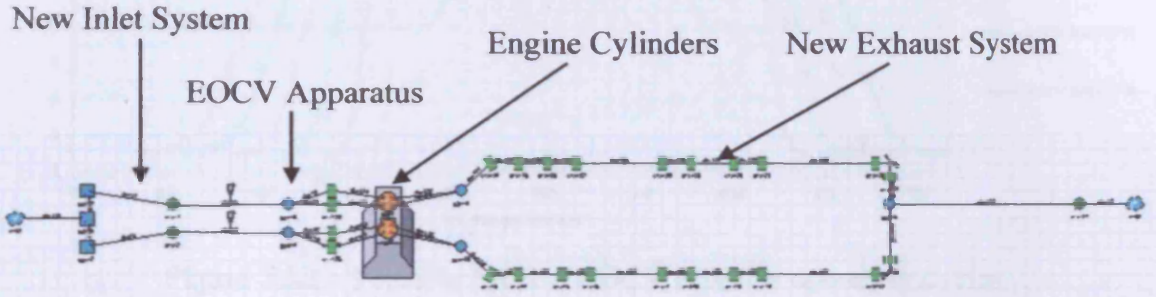

Figure 5.31 – 6000 RPM EOCV engine model

The design of the inlet system for the 6000 RPM engine is again investigated using the Wave software. The schematic view of the Wave engine model is shown in Figure 5.31 It was decided that a very simple inlet system would suffice for the 6000 RPM EOCV engine; with the air supply being drawn into a single plenum chamber. "Inlet-runners" then connect this plenum to an EOCV attached to each of the engine cylinders.

Initially, the 6000 RPM engine model will utilise the lift-flow characteristics predicted for the final Mark 4 EOCV design (see Figure 4.34). However, as the 6000 RPM engine has only a single inlet port for each engine cylinder a new design will ultimately be required. Measured actuator times for the Mark 4 actuator are significantly quicker than previous designs, and are almost suitable for an engine operating at speeds of up to 6000 RPM (see Figure 5.32). Figure 5.32 displays the possible EOCV opening and closing timings at different engine speeds. It can be seen that at speeds of up to 5000 RPM the EOCV can successfully open and close in the period when the main inlet valves are closed. At 6000 RPM however the EOCV must either open later or close earlier in order to complete its cycle.

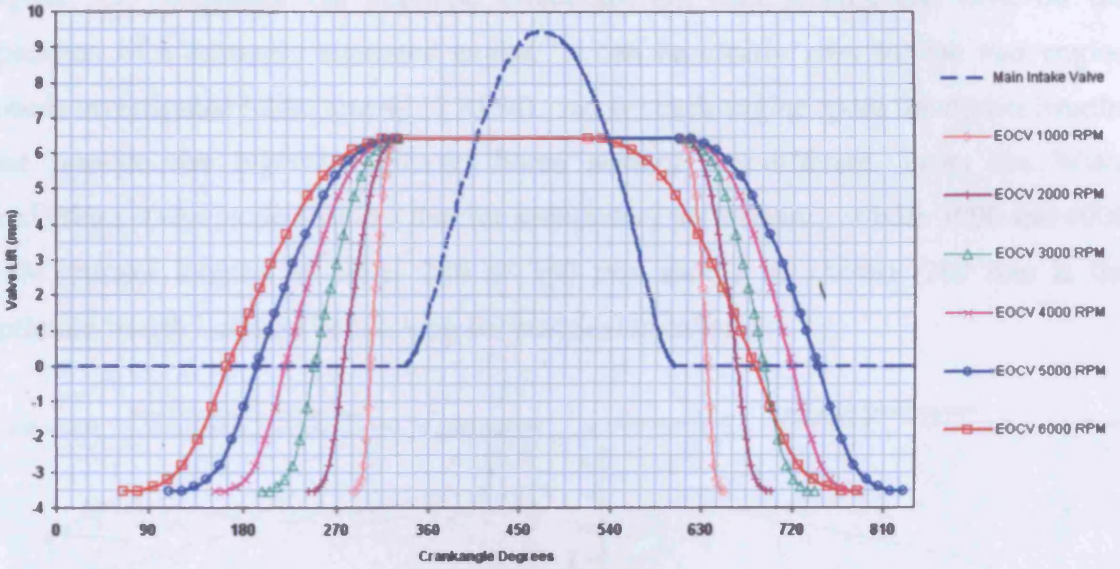

Figure 5.32 – Possible Mark 4 EOCV actuator operating cycles

It was decided that as the application of the EOCV technology to the Suzuki/Cagiva engine effectively reduces the operational rev limit down to around 6000 RPM, the inlet system should be optimised for speeds of 3000 - 4000 RPM. Using the fuelling and ignition specifications determined from the validation of the Suzuki model, a series of simulations were carried out to determine the effect of different inlet runner lengths on the engine's operation, the results of which are shown in Figure 5.33.

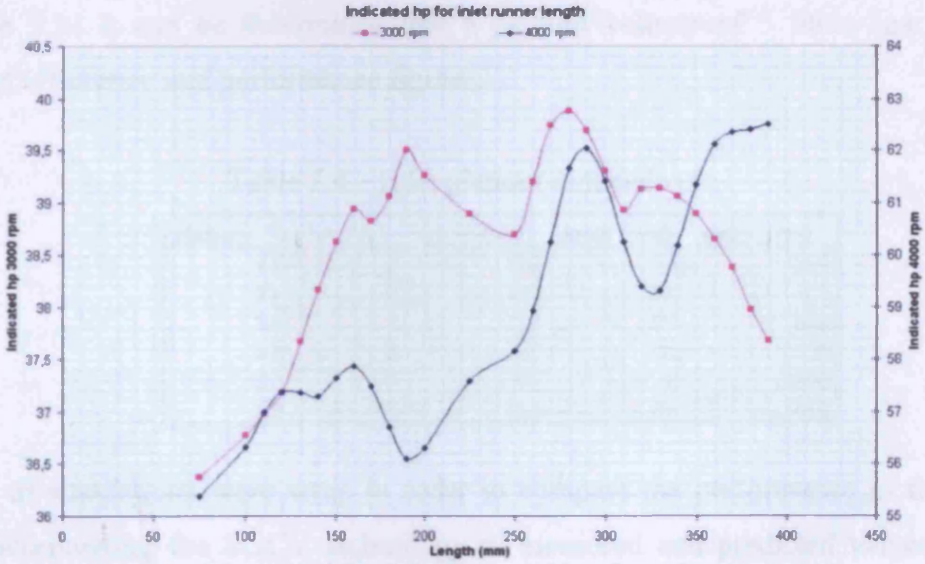

Figure 5.33 – Inlet runner length tuning

Figure 5.33 illustrates the dramatic effect altering duct lengths can have on the operation of a naturally aspirated engine. It can be clearly seen for the two engine speeds investigated (3000 and 4000 RPM), that for each engine speed the runner lengths that provide the highest indicated horse powers are different. From the Wave predictions it can be determined that for satisfactory performance at both 3000 and 4000 RPM, runner lengths of either 280 or 160 mm should be chosen (280 mm is the optimum length but may be too long for practical installation).

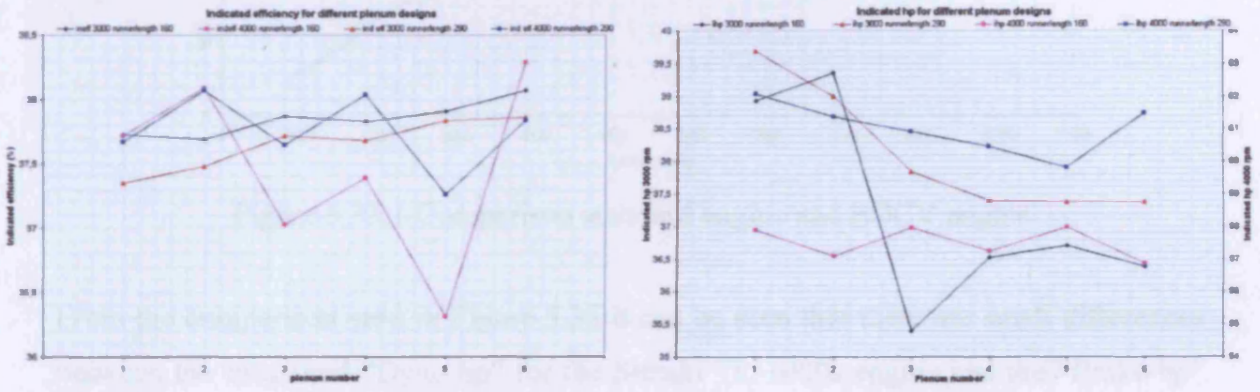

Figure 5.34 – Inlet plenum volume tuning

Several different shape and size plenum chambers were then tested using the Wave engine model (see Table 5.4 for the dimensions of the plenums). From the results shown in Figure 5.34 it can be determined that a plenum volume of 5 litres has the best combined efficiency and performance figures.

Table 5.4 – Inlet plenum dimensions

plenum	volume (L)	height (mm)	depth (mm)	width (mm)
1	5	150	150	285
2	5	120	120	450
3	3	115	115	285
4	3	92	92	450
5	2	92	92	300
6	8	150	150	450

A series of simulations were setup in order to compare the performance of the Wave model incorporating the EOCV technology to measured and predicted values for the standard Suzuki TL-1000s engine, the results of this comparison can be seen in Figure 5.35.

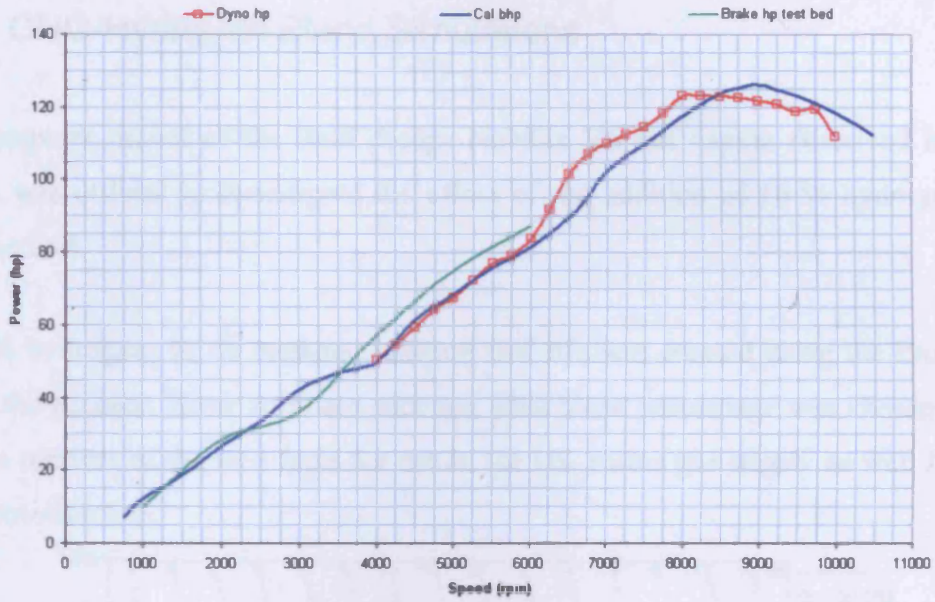

Figure 5.35 – Comparison standard engine and EOCV engine

From the comparison seen in Figure 5.35 it can be seen that there are small differences between the measured "Dyno hp" for the Suzuki TL-1000s engine and the "Brake hp" predicted by the Wave software, this may be because the cam profiles used in the model are from the Cagiva Navigator specification of the engine which may be different to the TL-1000s version.

The predicted "Brake hp" for the test bed engine shows an improved performance over much of its (shorter) speed range when compared to the predictions for the TL-1000s engine, this may be because the plenum and inlet runner configuration used in the EOCV model is more suitable for the lower engine speeds.

There is the possibility that the EOCV technology can be adapted such that it is suitable for much higher engine operating speeds, as the EOCV valve can also be used as a conventional throttle. This type of mixed-mode operation should be further investigated as it has the potential to allow the EOCV technology to be used on any type of internal combustion engine.

5.1.3 CNG-Hydrogen Blend Simulations

The computer model of the final design NoNOx V6 test engine described in section 5.1.1.4 was utilised to investigate the effect of the addition of 10 % hydrogen to the methane fuel.

A 10 % hydrogen, 90 % methane mixture fuel file was created using the Propty code within the Ricardo Wave software package. This blend percentage was chosen as it is a feasible mixture of the two fuels for use in the UK mains gas supply as well for use as an automotive fuel.

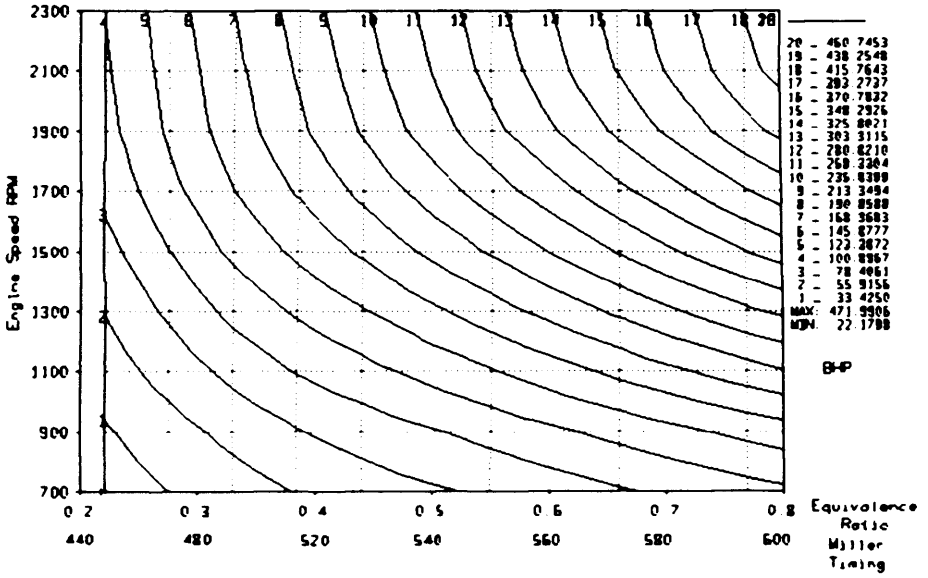

Figure 5.36 - Predicted power output for NoNOx engine (10% H_2, 90% CH_4)

If the predicted power output of the NoNOX test engine for the hydrogen / methane blend shown in Figure 5.36 is compared to the previous results for methane (see Figure 3.27), it can be seen that for equivalence ratios between 0.2 and 0.8 the hydrogen / methane fuel blend develops approximately 10 % more power at all engine speeds. This can be attributed to the addition of hydrogen increasing the combustion flame speed, which in turn increases the cylinder pressures.

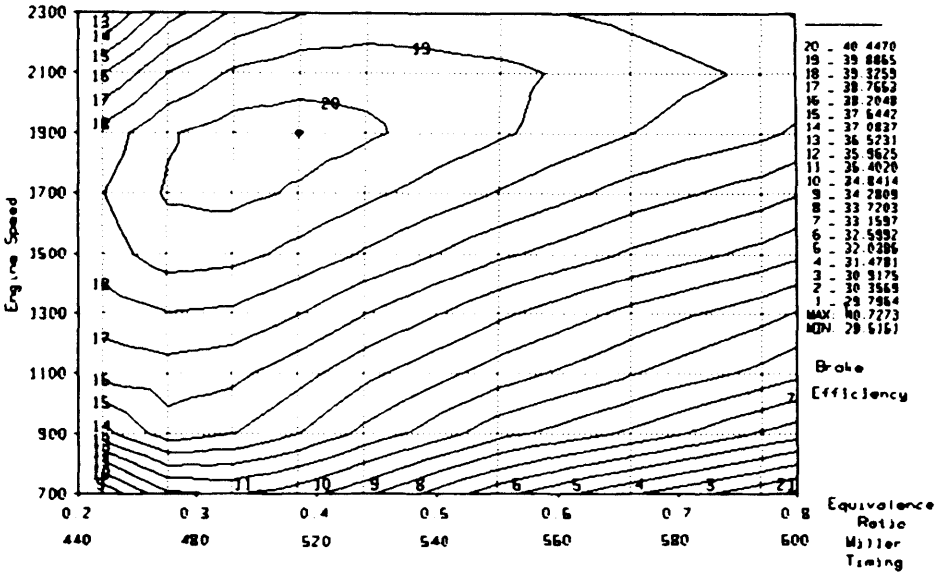

Figure 5.37 - Predicted engine efficiency for NoNOx engine (10% H_2, 90% CH_4)

The predicted engine efficiency for the hydrogen / methane blend is shown in Figure 5.37. When this is compared to that predicted for the methane fuel (see Appendix E for methane fuel results) it can be seen that for all engine speeds and equivalence ratios the efficiency obtained with the hydrogen / methane mixture is lower. This is due to the fact that the increase in flame speed leads to a shorter combustion duration of the hydrogen / methane mixture, which requires a later ignition timing for optimum efficiency.

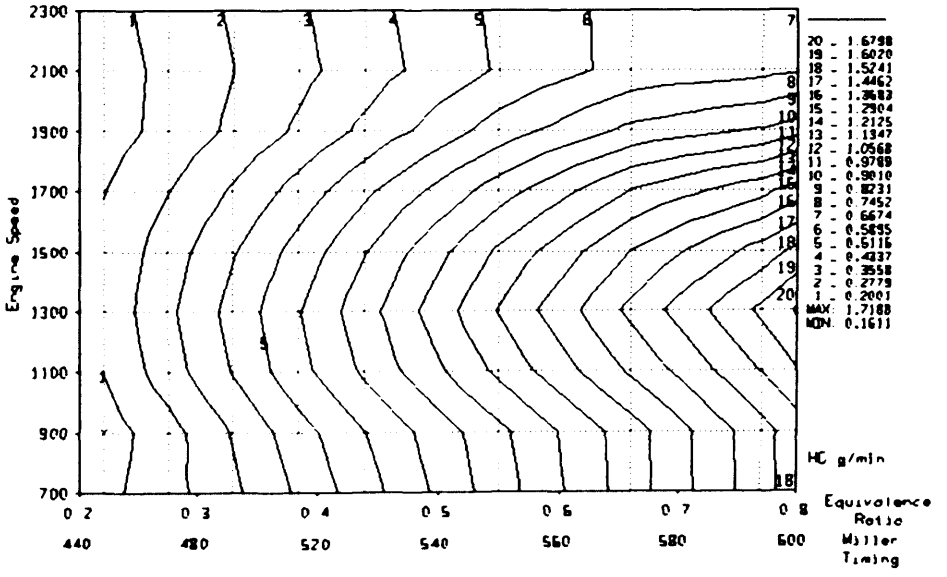

Figure 5.38 - Predicted hydrocarbon emissions for NoNOx engine (10% H_2, 90% CH_4)

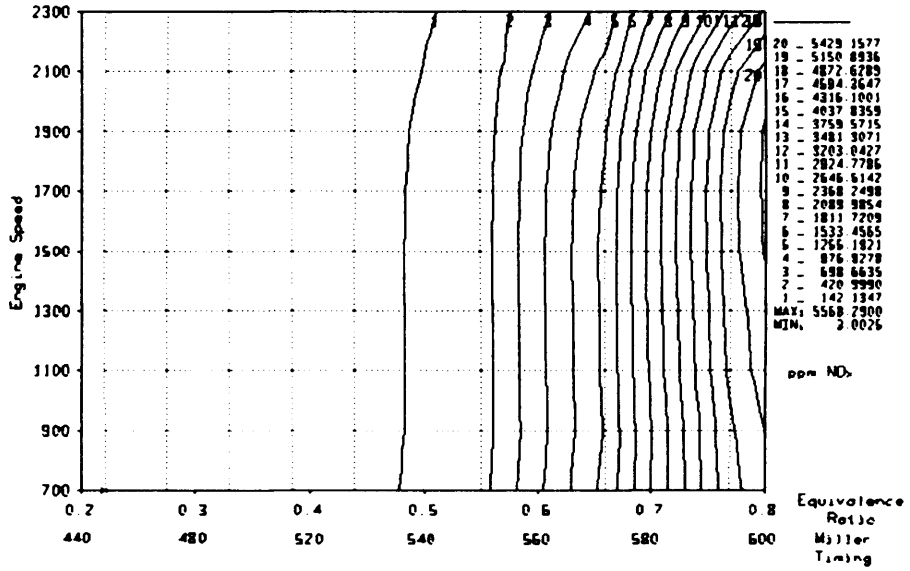

Figure 5.39 - Predicted NO_X emissions for NoNOx engine (10% H_2, 90% CH_4)

If the predicted emission of unburned hydrocarbons for the hydrogen / methane mixture shown in Figure 5.38 is compared to that for the methane fuel shown in Appendix E, it can be seen that the predicted hydrocarbons increase with the addition of hydrogen to the fuel. If the additional results for the hydrogen / methane mixture in Appendix G are compared to the methane results in Appendix E, it can also be seen that the emissions of CO are also predicted to increase with the addition of hydrogen. These results contradict that reported in literature, in which the addition of hydrogen to methane reduces the emissions of hydrocarbons and CO.

The predicted emissions of NO_X for the hydrogen / methane fuel mixture shown in Figure 5.39 are significantly greater than that previously predicted for the methane fuel (Appendix E). This is likely to be due to the increase in cylinder temperatures predicted with the addition of hydrogen. From the results of the Wave simulations it can be concluded that addition of a small percentage of hydrogen to the methane fuel of a spark ignition engine increases the power output, while having only a small detrimental effect on engine efficiency. However, with the addition of hydrogen there is a substantial increase in the predicted NO_X emissions.

5.2 Vectis EOCV Valve Model

3-Dimensional computer models were previously developed to simulate the air flow through the electromagnetically operated-load control valve (EOCV). Details of the EOCV model construction can be seen in chapter 4.

5.2.1 Mark 4 Development (V6 NoNOx Engine EOCV)

5.2.1.1 EOCV Inlet Design

In conjunction with the new plenum designs discussed in section 5.1, a new design for the inlet side of the EOCV apparatus was developed. Figure 5.40 below compares the previous EOCV intake "splitter" to the proposed new design. The function of the intake splitter is to efficiently split up the intake charge as it enters the EOCV apparatus.

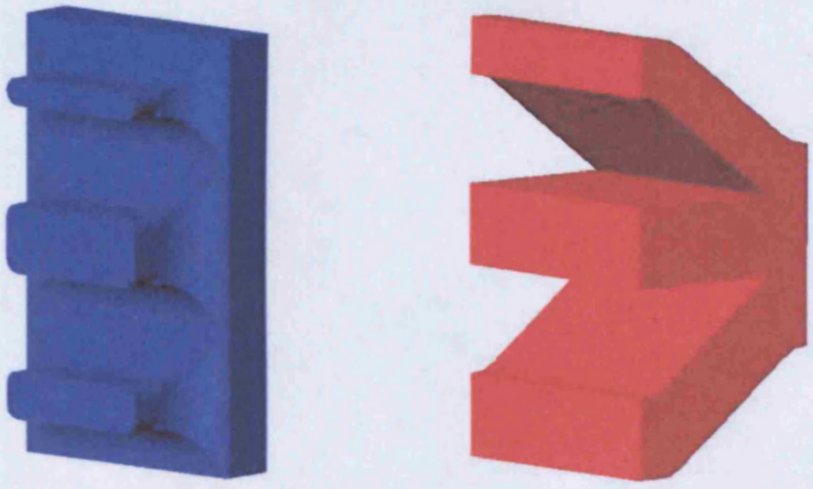

Figure 5.40 – EOCV intake splitter comparison

In order to test the effect of this new intake splitter, simulations were carried out using the Mark 4 EOCV geometry. The simulations are time-based simulations in which a pressure gradient is applied across the EOCV equipment, simulating the steady-state conditions that would occur on a flow-bench. By comparing the volumetric flow-rate values the performance of any design modifications can be assessed.

Figure 5.41 compares the previous steady-state flow results for the Mark 3 and Mark 4 EOCV designs with the results of the new simulations incorporating the new flow splitter.

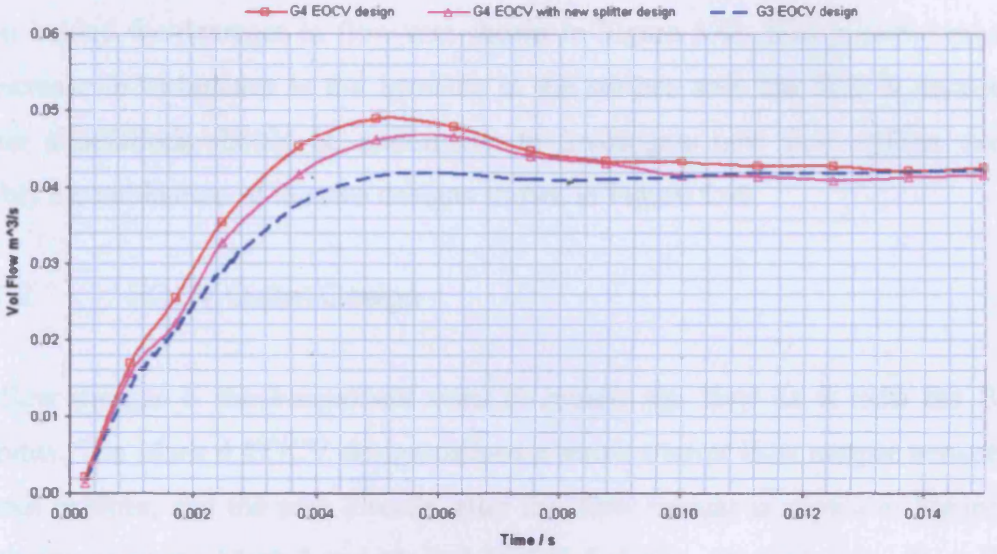

Figure 5.41 – Flow splitter EOCV design results

It can be seen from the results shown in Figure 5.41 that there is a marginal decrease in the flow-rate through the Mark 4 design when the new splitter is used. Figure 5.42 shows the turbulence intensity distribution for a cross-section through the Mark 4 EOCV model with the current flow splitter design and for the new flow splitter design.

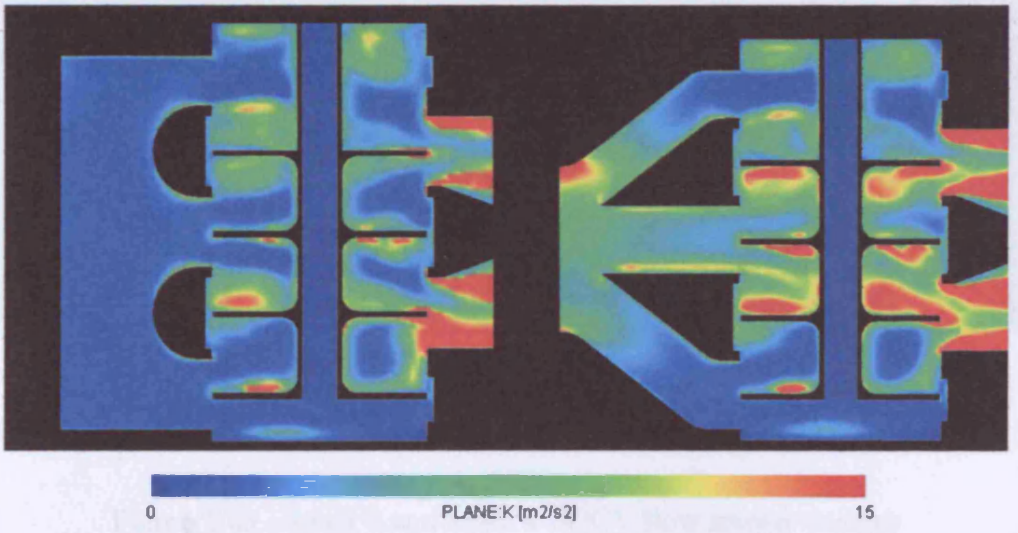

Figure 5.42 –Turbulence intensity distribution with old and new flow splitters

A comparison of the results shown in Figure 5.42 shows that the new flow splitter, which was designed to precisely split up the inlet flow, produces higher levels of turbulence than that seen with the current splitter design. This turbulence could be the reason behind the decrease in flow-rate shown in Figure 5.41. One possible cause for the increase in turbulence is the increase in the surface area the flow is exposed to. Further simulations should be undertaken to investigate new flow splitter designs, possibly a combination of the two designs shown in Figure 5.40.

5.2.1.2 EOCV Outlet Design

The flow merger is the component used to reunite the flow as it exits the EOCV apparatus. The Mark 4 EOCV design utilises a much shorter flow merger between the two exit orifices, and the area directly after this flow merger is shown in Figure 5.43 (which compares the Mark 3 and Mark 4 EOCV designs). As can be seen from Figure 5.43, this is an area with highly disrupted flow. The Mark 3 EOCV incorporated a much longer flow merger, which is seen to produce a much more even flow after the valve exit than that seen with the Mark 4 design.

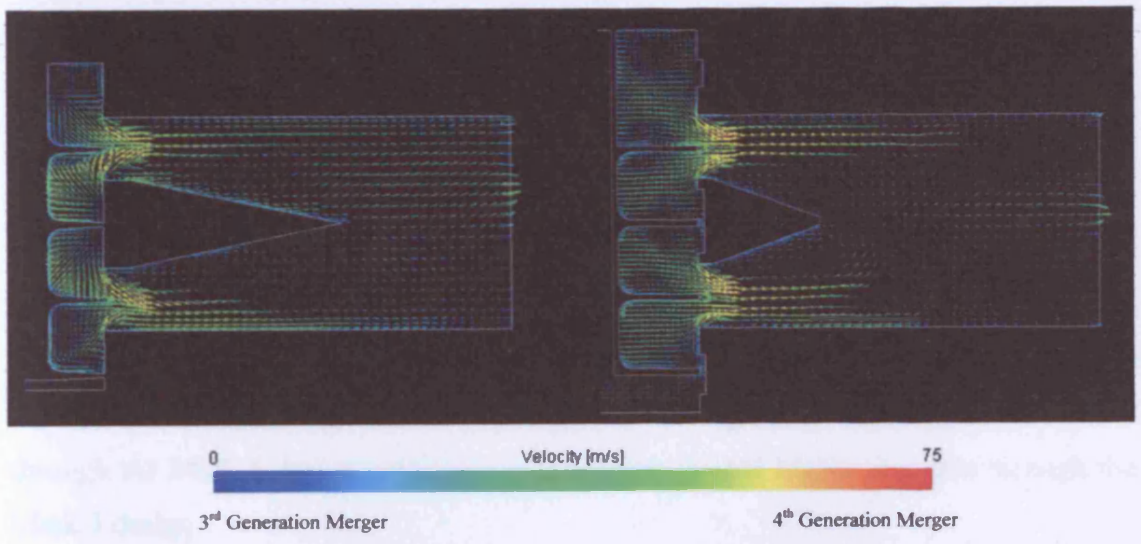

Figure 5.43 – Mark 3 and Mark 4 EOCV flow merger designs

As a consequence of the increased turbulence after the Mark 4 EOCV design reducing the potential flow, a series of simulations were carried out using several alternate flow merger designs, including the design of the flow merger used in the Mark 3 EOCV.

The graph shown in Figure 5.44 displays the predicted volumetric flow-rate result for the Mark 4 EOCV design modified to include the flow merger from the Mark 3 design.

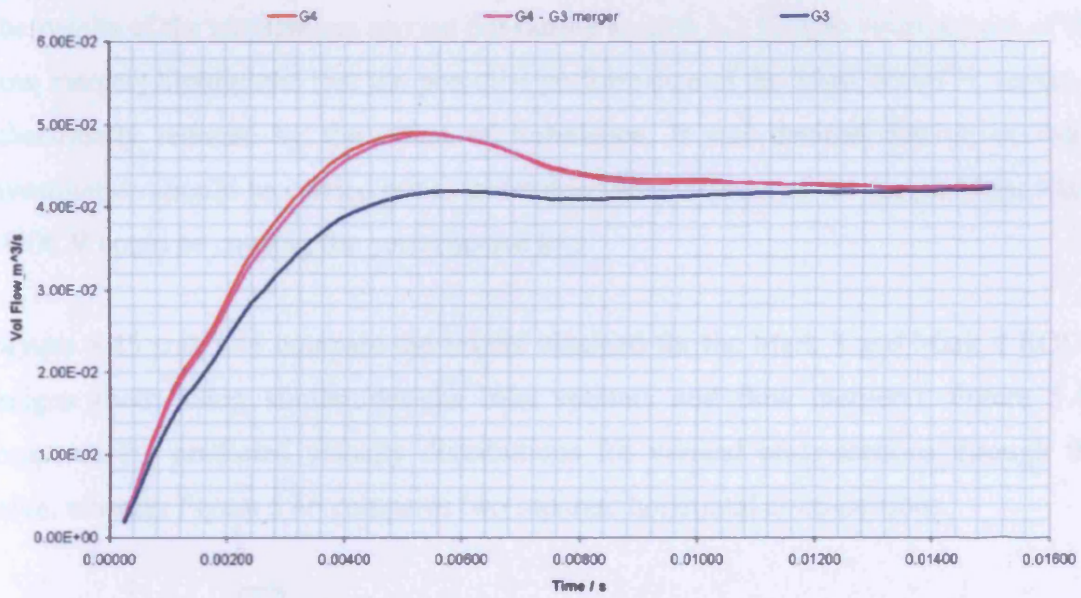

Figure 5.44 – Flow merger EOCV design results

The results shown in Figure 5.44 indicate that the inclusion of the Mark 3 flow merger has not improved the overall performance of the Mark 4 EOCV design. A closer examination of the results reveals that the Mark 4 EOCV exhibits different flow characteristics to the Mark 3 design. From the instant the simulation is started the improved design of the Mark 4 EOCV is apparent, with the flow-rate through the valve rising much more quickly than with the previous design. At T=0.0045s the flow-rate through the Mark 4 design peaks at a value which is 16% higher than that through the Mark 3 design.

After T=0.0045s the flow-rate through the Mark 4 EOCV design decreases, this is believed to be because of the onset of turbulence within the valve. The effect of the turbulence within the Mark 4 EOCV design is dramatic, with a much larger decrease in flow-rate than is seen in the predictions for the Mark 3 design.

5.2.1.3 Mark 3 / Mark 4 Design Comparison

The results of the simulations carried out during section 5.2.1.2 (the development of the flow merger) highlighted that the potential performance of the Mark 4 EOCV design is substantially reduced by the effect of turbulence. It was decided that an in depth investigation should be carried out to understand what aspects of the design of the Mark 4 EOCV could be causing the performance loss.

Figures 5.45 and 5.46 compare the results obtained for the Mark 3 and Mark 4 EOCV designs (both using similar designs inlet splitters and flow mergers). Figure 5.45 compares the predicted velocity distributions for vertical cross-sections through the valve, whereas Figure 5.46 compares two separate horizontal cross-sections.

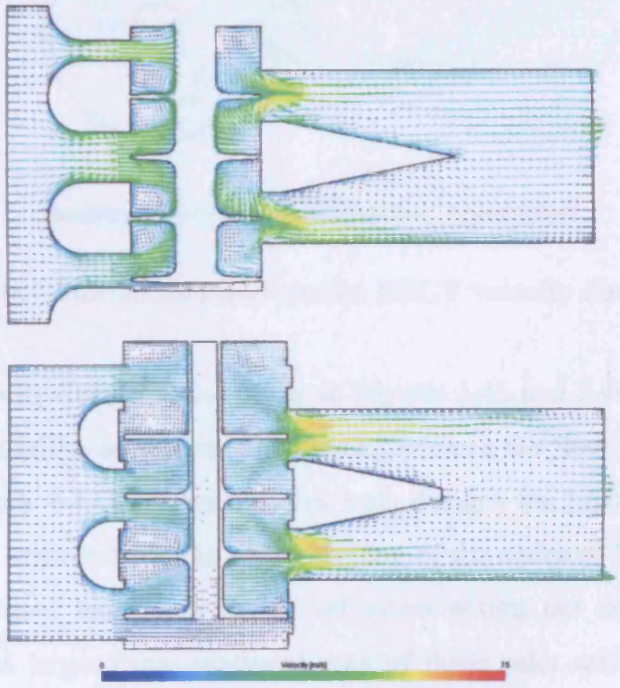

Figure 5.45 – Vertical cross-section EOCV velocity distribution

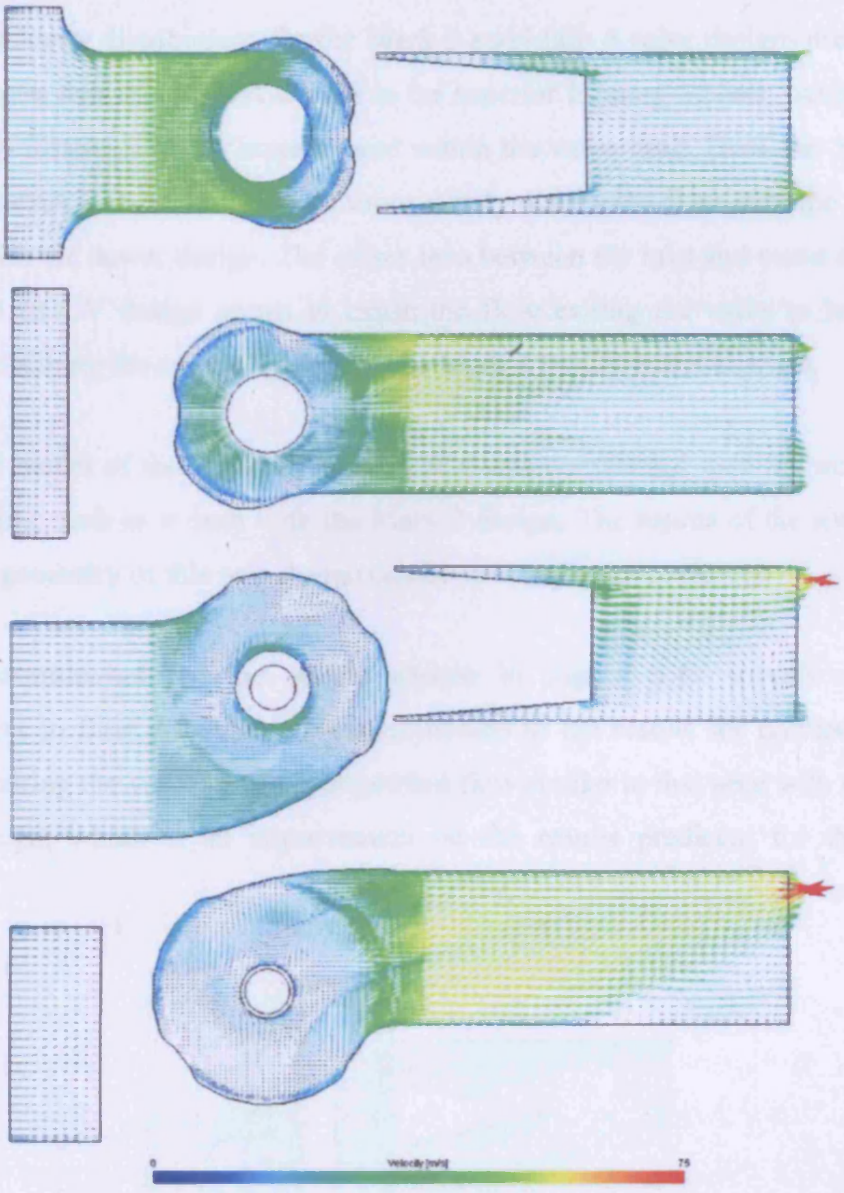

Figure 5.46 – Horizontal cross-section EOCV velocity distributions

Examining the velocity distributions shown in Figures 5.45 and 5.46 it can be seen that there are many similarities as well as differences between the flow predictions for both the Mark 3 and Mark 4 EOCV designs. For both designs the highest velocities occur within the two exit orifices from the valve and are of the order of 55 m/s. The Mark 4 EOCV design however has much lower velocities within the inlet orifices; this is probably due to the larger cross-sectional area of these inlet orifices in the Mark 4 design.

When the velocity distributions for the Mark 3 and Mark 4 valve designs are compared in can be seen that the Mark 4 design is far superior in most aspects; having a much more evenly distributed flow entering and within the valve itself. However ,the flow as it exits the Mark 3 valve has a much more evenly distributed flow after the valve than that seen with the newer design. The offset seen between the inlet and outlet channels of the Mark 4 EOCV design seems to cause the flow exiting the valve to be unevenly distributed, lacking the symmetry seen in the Mark 3 EOCV outlet channel.

A modified model of the Mark 4 EOCV design was constructed with the inlet and exit orifices inline, such as is seen with the Mark 3 design. The results of the simulation as well as the geometry of this new design can be seen in Figure 5.47.

A quick examination of the results shown in Figure 5.47 reveals an overall improvement in flow distribution when compared to the results for previous designs. The flow exiting the valve has an symmetrical flow similar to that seen with the Mark 3 EOCV design, which is an improvement on the results predicted for the Mark 4 geometry.

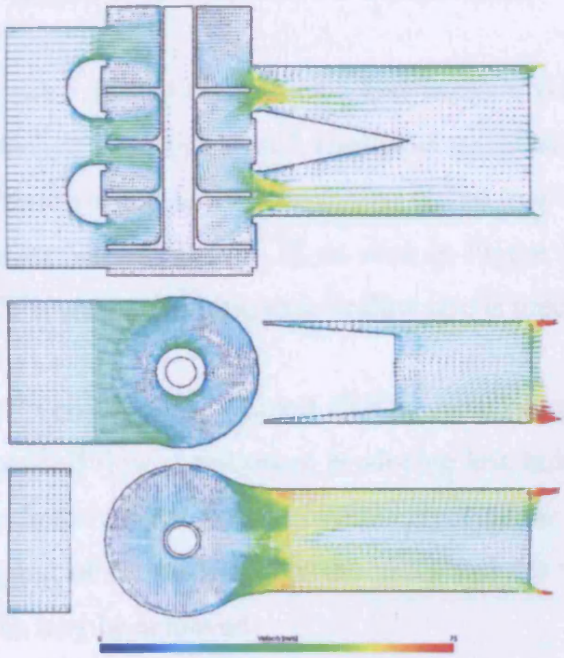

Figure 5.47 – CFD results for modified EOCV design

If the flow exiting the valve in Figure 5.47 is compared to that seen in Figures 5.45 and 5.46, it can be seen that the local velocities are much higher with the new design than with either of the previous designs. This indicates that the flow-rate through the new design is higher.

Figure 5.48 below compares the flow rate predictions for the new design to that for previous designs and their variants.

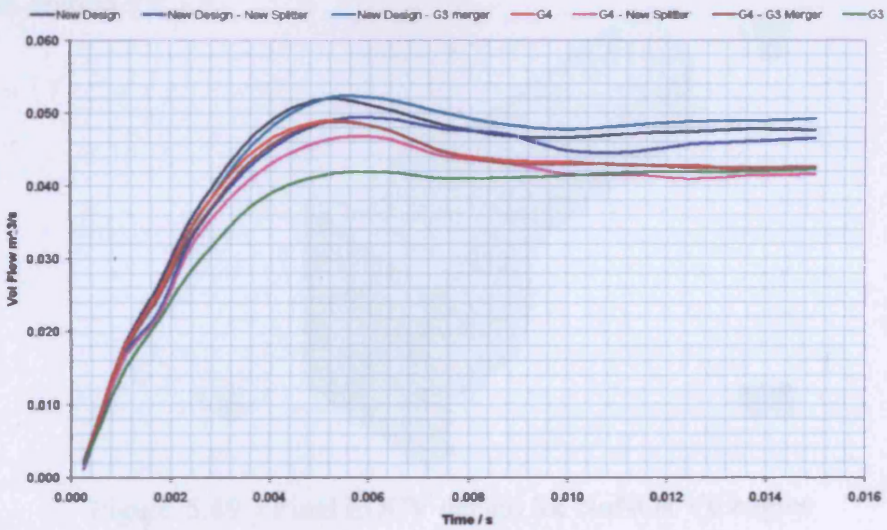

Figure 5.48 – New EOCV design results

It can be seen from Figure 5.48 that there is a marked improvement in flow through the new EOCV design, which is a "straightened" version of the Mark 4 EOCV design. The flow rate through the basic version of the new design settles to a value 12% higher than that seen with the similar Mark 4 design. If, as seen in Figure 5.48, the flow merger from the Mark 3 EOCV is used a 16% increase in flow rate is predicted.

The new "straightened" version of the Mark 4 EOCV valve has a proven improvement in both overall flow rate and flow distribution, producing less turbulence than is seen in previous designs. It is believed that further improvement of the EOCV design is still possible, with the shaping of the outlets from the valve and the flow merger being the area where largest gains may be achieved.

5.2.1.4 Final EOCV Design Simulation

The final design for the Mark 4 EOCV is shown below in Figure 5.49. There are several small changes to the shape of the valve, but it is very similar to the previous Mark 4 design. The offset that is present between the valve inlets and exits is required due to the design of the inlet ports of the NoNOx engine. However, subsequent EOCV designs may not require this offset and therefore could be based upon the modified design detailed in section 5.2.1.3.

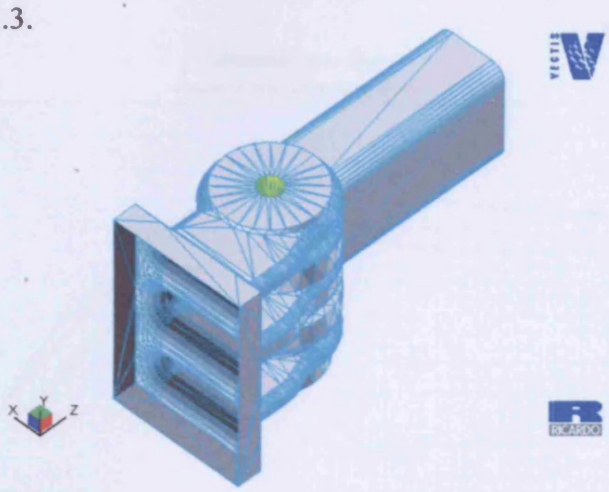

Figure 5.49 – Final EOCV design for NoNOx V6 engine

A simulation of the final Mark 4 EOCV opening was carried out using the new valve geometry and the new actuator times shown in Figure 5.50. It can be seen from Figure 5.50 that the new actuator is significantly quicker than the previous design.

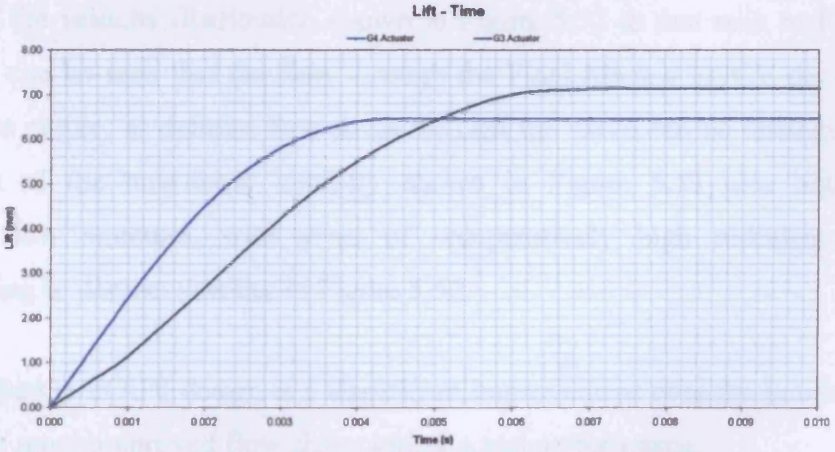

Figure 5.50 – Comparison of EOCV actuator performance

A comparison of the Final Mark 4 design performance to that of previous designs is shown in Figure 5.51. The velocity and turbulence intensity distributions are shown in Figures 5.52 and 5.53 respectively. It can be seen from the results for the Final Mark 4 design that the new actuator has not only improved the flow through the valve while it is opening, but the small changes that have been made to the design (particularly the recess areas around the valve spindle) have improved the overall performance of the valve (7.2% increase in flow).

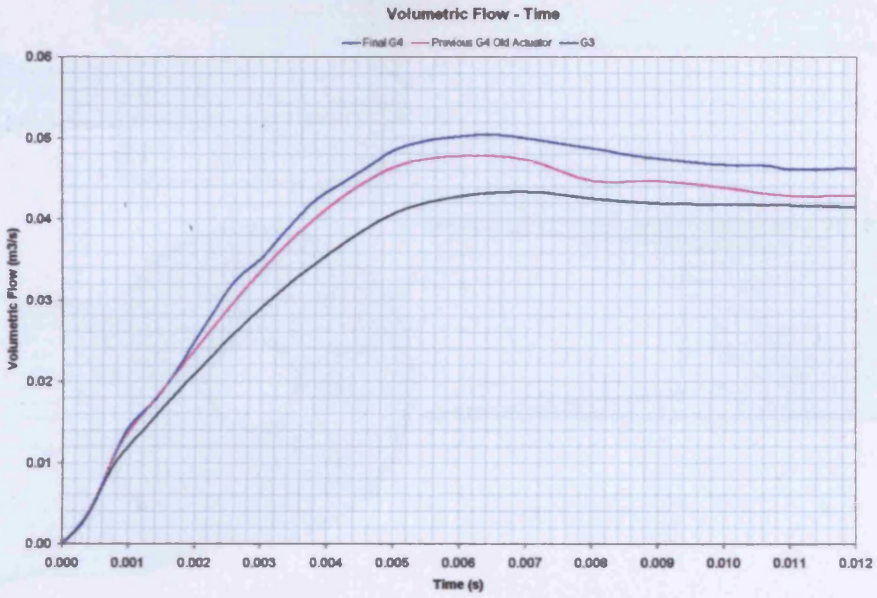

Figure 5.51 – Final design Mark 4 EOCV flow performance

Comparing the velocity distribution shown in Figure 5.52 to that seen in Figures 5.45 and 5.46 it can be seen that the flow through the Final Mark 4 EOCV design is more "ordered" in nature, as definite flow paths through the valve can be distinguished. The distribution of the turbulence intensity shown in Figure 5.53 also highlights the organized flow structure, with areas of comparatively high turbulence intensity corresponding to distinct vortices in Figure 5.52.

The final Mark 4 EOCV design is a significant improvement over the previous Mark 4 design, with much improved flow characteristics and performance.

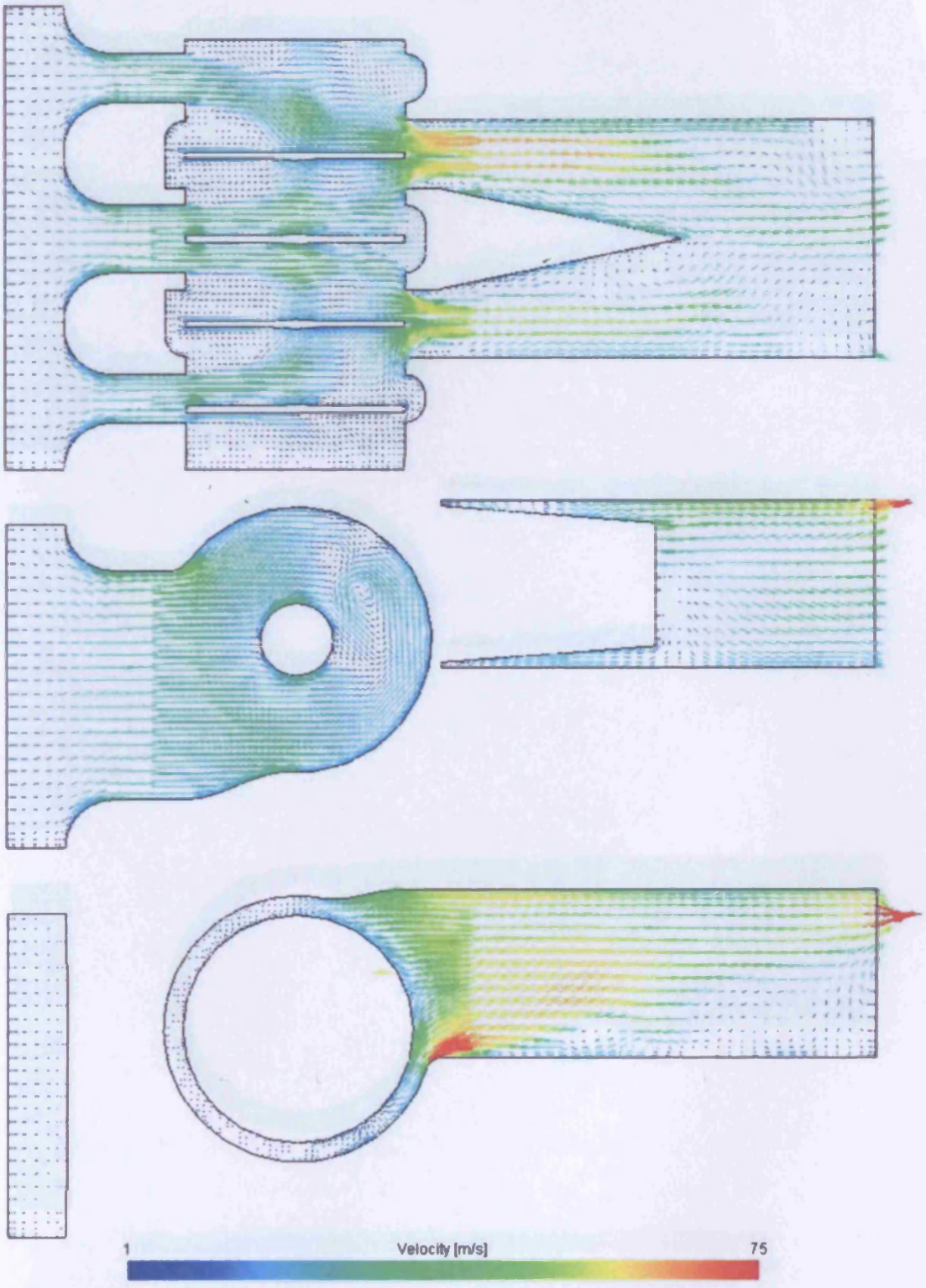

Figure 5.52 – Final design Mark 4 EOCV velocity distribution (Fully open)

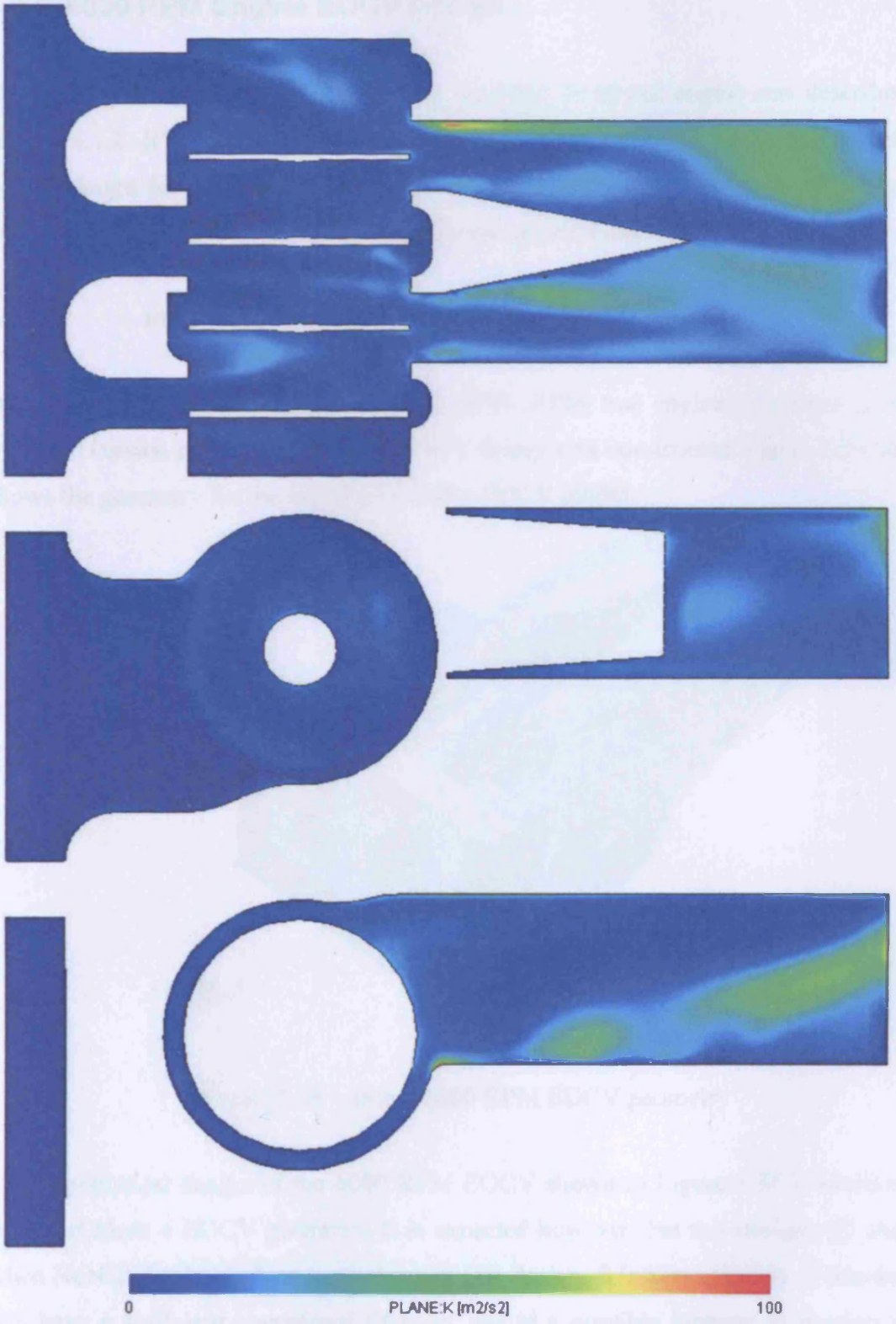

Figure 5.53 – Final design Mark 4 EOCV turbulence intensity distribution (Fully Open)

5.2.2 6000 RPM Engine EOCV Design

The development of an engine model for the 6000 RPM test engine was described in section 5.1.2. It was decided that for the initial Wave modelling work a hypothetical EOCV design for the Cagiva Navigator 6000 RPM test engine should be developed in order to obtain suitable flow coefficients for the engine model.

5.2.2.1 Initial Model Development

Based upon actual measurements of the 6000 RPM test engine's cylinder head, a modified version of the Final Mark 4 EOCV design was constructed. Figure 5.54 below shows the geometry for the initial 6000 RPM EOCV model.

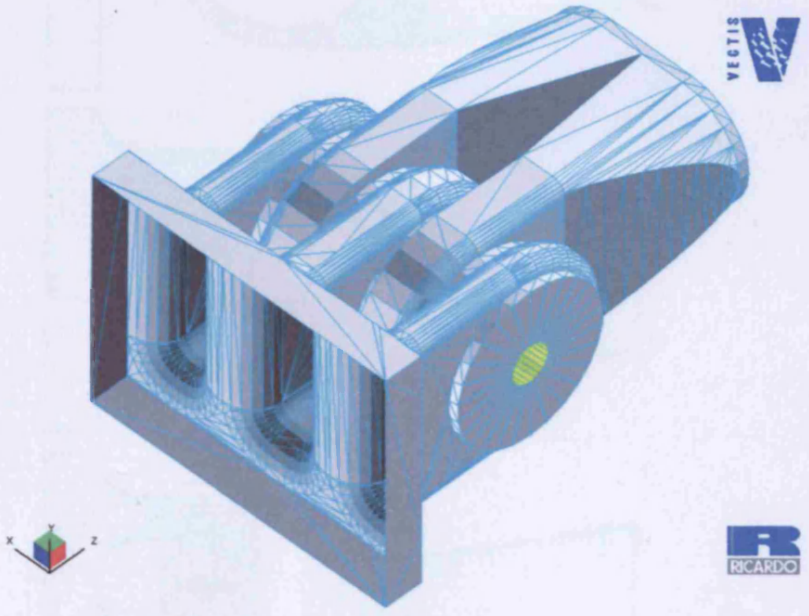

Figure 5.54 – Initial 6000 RPM EOCV geometry

The hypothetical design of the 6000 RPM EOCV shown in Figure 5.54 is based upon the Final Mark 4 EOCV geometry. It is expected however that this design will change when NoNOx begin work on a suitable actuator design. It is also unknown if this design will have a sufficient operational lifespan, due to a possible increase in bearing wear with the valve spindle motion being horizontal instead of vertical.

5.2.2.2 6000 RPM EOCV Results

Figure 5.55 shows the predicted velocity distribution for the 6000 RPM EOCV design. A comparison with Figure 5.55 reveals that flow through the 6000 RPM EOCV is similar in nature to that through the Final Mark 4 EOCV design, with defined vortices within the valve and a distinctive flow path through the valve.

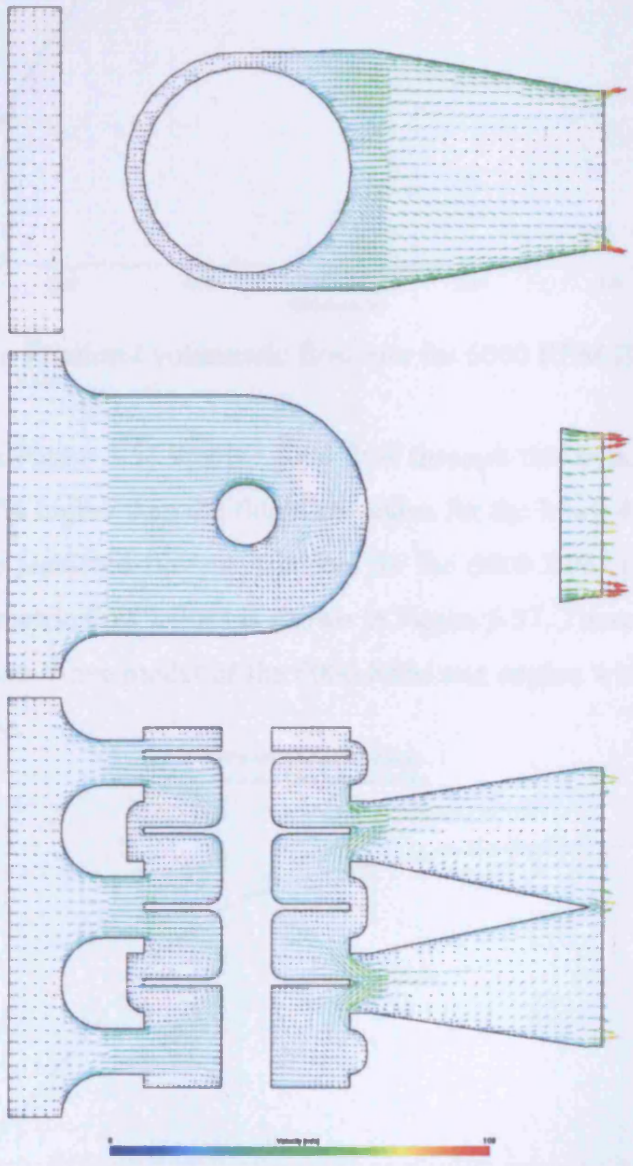

Figure 5.55 – 6000 RPM EOCV velocity distribution (Fully Open)

A comparison of the predicted volumetric flow-rate growth for the 6000 RPM EOCV design at three different valve lift positions is shown in Figure 5.56 (18.0 millibar pressure difference applied across the valve model).

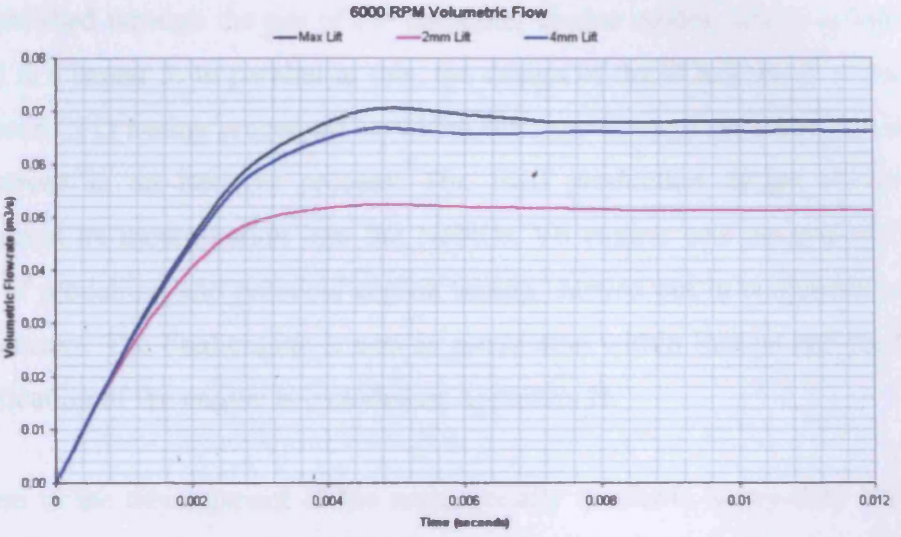

Figure 5.56 – Predicted volumetric flow rate for 6000 RPM EOCV design

It can be seen from Figure 5.56 that the final flow through this hypothetical 6000 RPM EOCV design is 47% higher than the final flow value for the Mark 4 EOCV design seen in Figure 5.51. The predicted flow coefficients for the 6000 RPM EOCV design based upon the final volumetric flow values is shown in Figure 5.57. These values can be used in the next generation Wave model of the 6000 RPM test engine which will incorporate the EOCV apparatus.

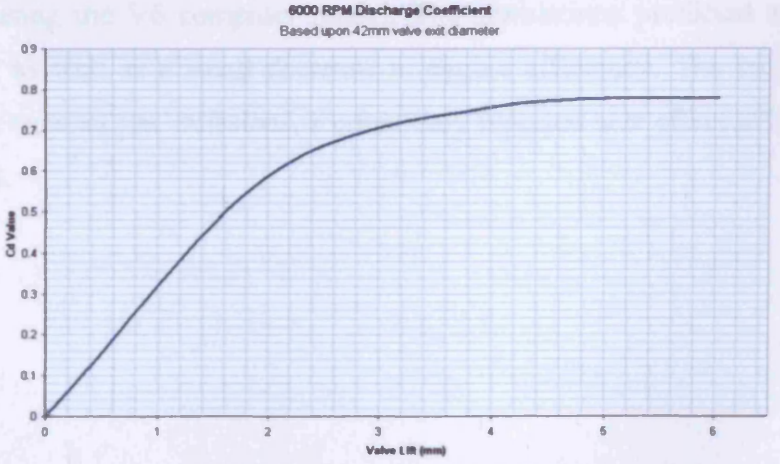

Figure 5.57 – Predicted 6000 RPM EOCV flow coefficients

5.3 Summary

The optimum designs of key engine components of a heavy-duty natural gas engine were established through the use of the computer engine model, whose construction is described in Chapter 3. In parallel to this, the design of the EOCV itself was subjected to a rigorous CFD testing procedure, in which the flow through the valve was evaluated and improved in an iterative process. The final production design of the EOCV apparatus and its incorporation into the NoNOx V6 engine was developed through a program of modelling and practical engine testing, carried out in conjunction with EU project partners. The final engine is now in production within Europe and the Far East, the specification of the engine is included in Appendix H.

In addition to the development of the commercially available heavy-duty V6 NoNOx engine, a design program was undertaken to develop the EOCV technology for a smaller higher speed engine, analogous to that used in modern passenger vehicles. A modified version of the EOCV design for the heavy-duty V6 engine was developed (which in simulations outperformed the design of the V6 EOCV apparatus) and was incorporated in a computer model of the test engine under construction at the NoNOx facility.

The effect of hydrogen addition to the CNG fuel of the NoNOx V6 engine was investigated using the V6 computer model. The simulations predicted an increase in power output as well as a small decrease in engine efficiency. The increase in NO_X content in the exhaust gas emissions, a commonly reported side effect in literature, was also predicted.

6 Miller Cycle Effect

The work described in Chapter 3 describes the initial construction of a CFD engine model of the NoNOx test engine, incorporating the Electromagnetically Operated-load Control Valve (EOCV). The purpose of the EOCV technology is to allow an engine to operate with throttle free load control and with various degrees of Miller cycle operation. The benefits are the ability to operate with high inlet boost pressures, while improving the operating efficiency and emissions of the engine.

A computer simulation of the airflow through an individual EOCV geometry has been carried out in Chapter 4. Within this Chapter present and future EOCV designs are evaluated and compared, with areas of possible improvement highlighted. The results of the simulations proved invaluable when materials problems required the EOCV apparatus to be redesigned, and in the development of the final design for use on the V6 NoNOx engine.

In order to investigate in detail the "Miller Cycle" effect of the EOCV apparatus on the flow into the engine cylinder, and to examine the design of the combustion chamber / piston crown, a detailed three dimensional CFD model was constructed using the Ricardo Vectis software. The Ricardo Vectis software package is widely used in industry for the simulation of the airflow and combustion within engines, and there are a number of research publications (e.g. Ryu et al. 2005 and Dekanski et al. 1996) in which fuel spray structure and changes in engine geometry are investigated. A precise recreation of the cylinder head geometry and the EOCV apparatus is created using the Ricardo Vectis software. Data obtained from the simulations of the NoNOx engine is used as the boundary conditions for the EOCV / cylinder head model, the results of which are compared with data for the NoNOx engine.

6.1 Simulation Parameters

It was decided that in total, three separate engine load settings will be simulated, the engine load being controlled through use of three different EOCV opening and closing timings. The settings for the three simulations are shown in Table 6.1 below. The computer simulation represents cylinder number 1 of the V6 NoNOx engine and will therefore use the corresponding boundary conditions.

Table 6.1 - Combustion model settings

	ENGINE SPEED	EOCV TIMING OPEN/CLOSE	LAMBDA VALUE	IGNITION TIMING
EOCV Simulation 1	1200 RPM	200/580 (°CA after TDC IGN)	1.59	17 (°CA before TDC)
EOCV Simulation 2	1200 RPM	200/540 (°CA after TDC IGN)	1.66	24 (°CA before TDC)
EOCV Simulation 3	1200 RPM	200/480 (°CA after TDC IGN)	1.59	27 (°CA before TDC)

Figure 6.1 shows the parameters that are used for the engine cylinder / valve simulation. The three separate EOCV opening and closing timings investigated are shown in Figure 6.1. The engine's standard valve lifts and the total cylinder volume are also shown for a comparison, it can be seen that the EOCV timings used for the first two computer simulations will partially limit the air into the engines cylinder. It is this charge limiting which induces the Miller cycle effect.

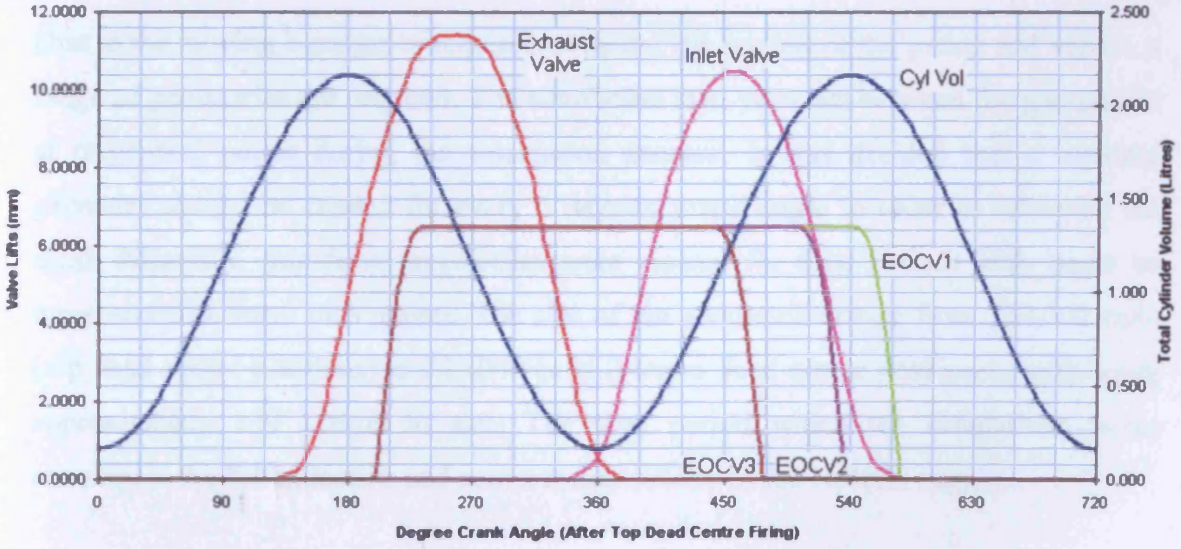

Figure 6.1 – Engine model parameters

Measurements were taken of the V6 NoNOx test engine's inlet and exhaust ports in order to generate an accurate CAD model of the flow geometry. The completed CAD model includes all of the required geometry to model a single engine cylinder, including the flow splitters, a pair of EOCVs, the inlet ports, the cylinder and the exhaust port. An example of a completed geometry is shown in Figure 6.2.

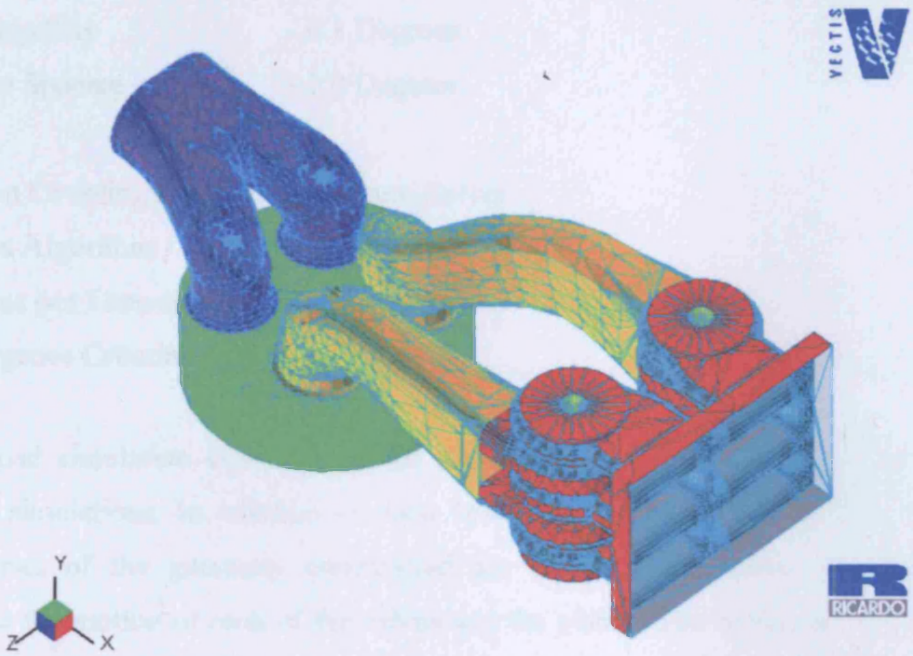

Figure 6.2 – Sample cylinder model geometry

Due to the moving boundaries required to model the motion of the piston and valves, a range of geometries are required. The simulation then switches between the geometries at prescribed points during the calculation process. It was decided that a separate geometry should be created for every 5 degrees crank angle in order to minimise the mesh distortion. Additional geometries were created for time periods with larger or more complex valve movements. The size of the geometries range from 250,000 cells (top dead centre positions) to 320,000 cells (bottom dead centre positions), each being approximately 130 MByte in size. The time period which the simulations cover encompass the full induction and compression strokes of the NoNOx engine.

The engine cylinder simulations are carried out using the following simulation parameters:

Simulation Duration	- 392.5 Degrees
Start Time	- 327.5 Degrees
End Time	- 720 Degrees
Time-step Size	- 0.1 Degrees
Post-pro Spacing	- 1.0 Degrees
Equation Coupling Scheme	- Pressure Solver
Solution Algorithm	- PISO
Iterations per Time-step	- 1
Convergence Criteria	- 1.0 x 10e-6

The broad simulation conditions listed above are used for all three of the 3D CFD EOCV simulations. In addition to these broad simulation parameters, the individual boundaries of the geometry constructed are assigned prescribed displacements to simulate the motion of each of the valves and the piston. The computational mesh then distorts according to the amount of movement for each of the boundaries in that time region.

In addition to specifying the movements of the boundaries that form the valves and the piston of the engine model, the boundaries that represent the inlet and outlet to the model need to be specified. The boundary conditions for the surfaces representing the inlets and outlets of the computer model are obtained from the Wave software, and are made up of defined absolute pressures and temperatures from which the flow into and out of the simulated geometry is calculated. For each of the separate closing times the inlet and outlet temperatures and pressures are shown in Figures 6.3 – 6.6.

Figures 6.3 and 6.4 show the predicted inlet boundary pressures and temperatures that are used for the Vectis simulations of the NoNOx engine geometry.

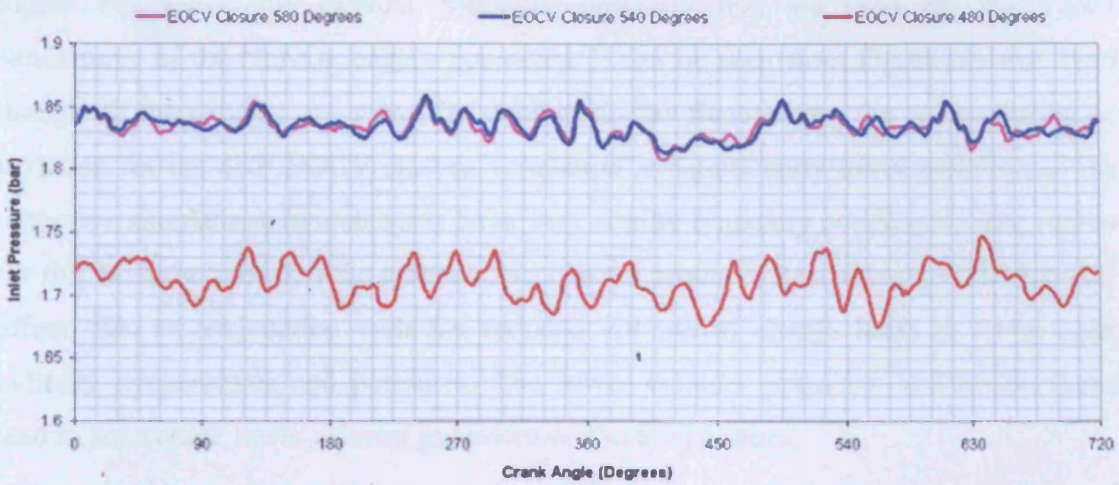

Figure 6.3 – Model inlet pressures

It can be seen from the Figures that the simulation with the earliest EOCV closure (480°), has a significantly lower range of inlet temperatures and pressures compared to the other two simulations. The reason for this is that the earliest EOCV closure corresponds to the case in which the engine produces the lowest load, i.e. the compressor speeds and therefore the flow rate into the engine is lower. The two simulations with later EOCV closure (540° and 580°) have very similar predicted inlet pressures and temperatures, indicating that the EOCV apparatus must restrict a significant proportion of the possible flow into the engine to have a measured effect on engine performance.

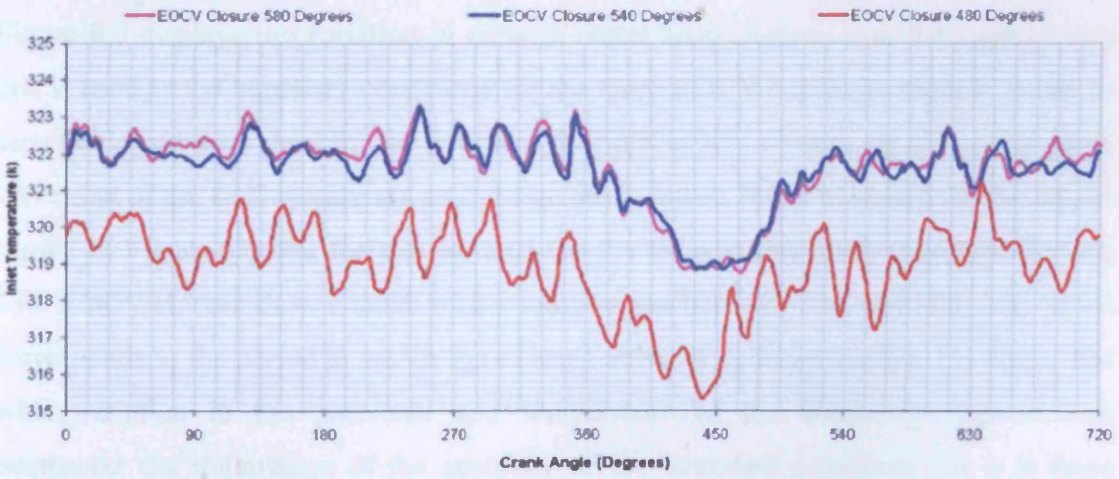

Figure 6.4 – Model inlet temperatures

Figure 6.5 shows the exhaust boundary pressures that are used for the Vectis simulations of the NoNOx engine geometry. It can be seen from Figure 6.5 that even though all the exhaust gas pressures exhibit similar fluctuations, the exhaust pressure variation for the 480° EOCV closure simulation is significantly lower than that of the other two simulations (which again have very similar boundary conditions). The reason for this is likely to be that the earlier valve closure produces a significant "Miller cycle" effect, this in conjunction with the reduced volume of charge leads to lower peak cylinder temperatures and pressures. The lower cylinder pressures and temperatures lead to an average lower exhaust gas pressure and temperature.

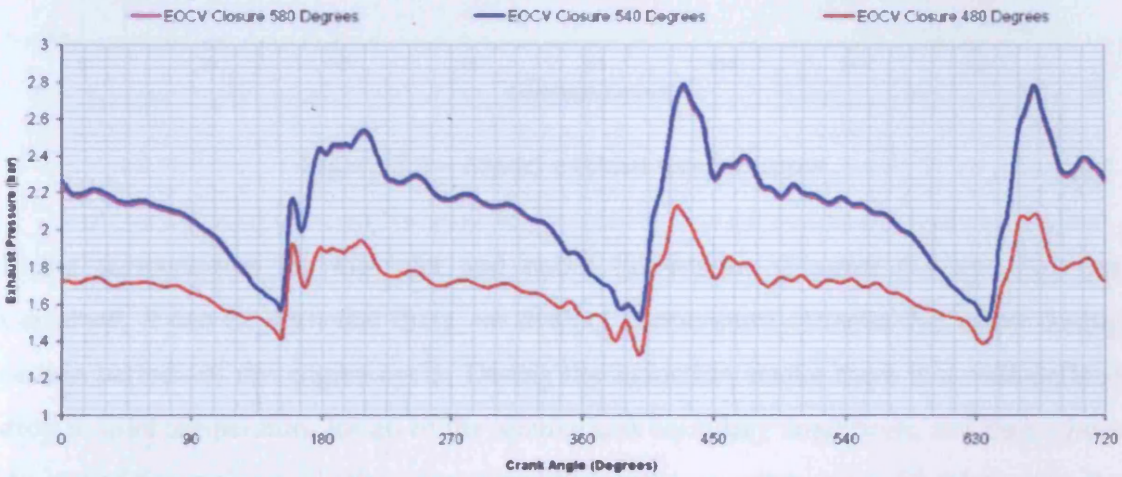

Figure 6.5 – Model exhaust pressures

Figure 6.6 displays the variation in exhaust outlet temperatures over the engine cycle that is used as the boundary conditions for the three EOCV / cylinder models. It can be seen that again the values for the 540° and the 580° EOCV closure are almost identical, while that of the 480° closure are on average much lower. It can be seen from the results shown in Figure 6.6 that the values used for the exhaust boundary conditions for the 480° EOCV closure show a much higher temperature between 150° and 360° CA, which corresponds to the period in which the exhaust valve of cylinder number 1 is open. The wide variation in the pressures and temperature of the boundaries shown here emphasize the importance of the accuracy of the boundary conditions, as it is these

conditions that are used by the software to calculate the flow into and out of the computer created geometry.

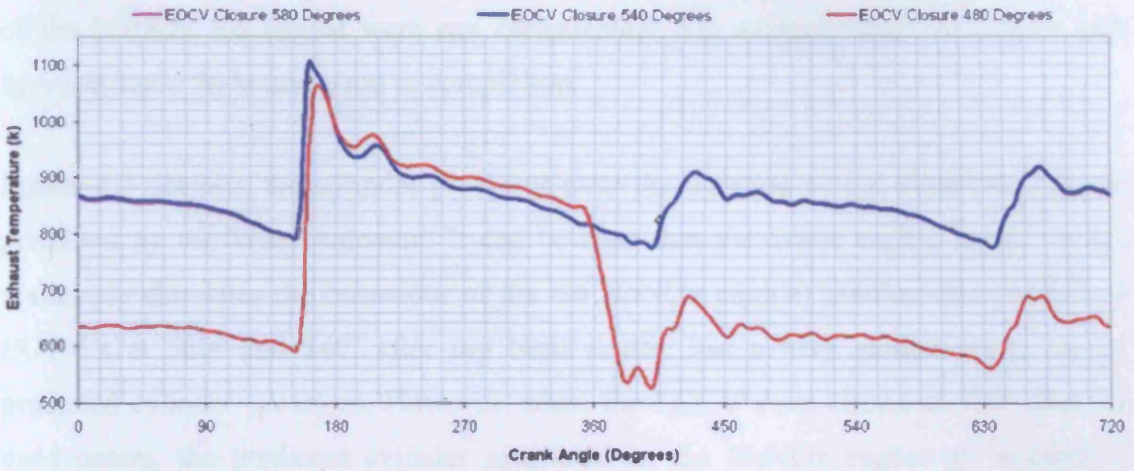

Figure 6.6 – Model exhaust temperatures

If the temperatures for the inlet and outlet boundaries (Figures 6.4 and 6.6) are examined, it can be seen that there are distinct temperature changes that occur during certain periods of the engine cycle. During the induction stroke there is a well-defined drop in inlet temperature for all of the simulations boundary conditions, and throughout the rest of the engine cycle the temperature fluctuations correspond to fluctuations in the inlet pressure. The variation in the exhaust temperature during the engine cycle has a much larger amplitude than that used for the inlet boundaries, with the peak temperatures corresponding to the exhaust valve opening of the three engine cylinders connected together by the exhaust manifold system of the V6 NoNOx engine. For all of the simulations the highest exhaust boundary temperature corresponds to the period in which the exhaust valves will be open in the model.

Once the basic specifications for the model were decided and incorporated into the input files for each of the simulations, the Vectis solver program was started. During the solving procedure possible errors and key calculation parameters are recorded into an output file; refinements to the model were then made through the adjustment of the simulation parameters and the creation of new geometries where needed.

6.2 CFD Predictions

The three simulations of the flow through the EOCV apparatus into the engine cylinder of the NoNOx V6 engine were run concurrently. On average, each simulation took approximately 96 hours to run to completion.

Figure 6.7 displays the cylinder pressures over the duration of the Vectis simulations predicted by the Wave software. It can be seen that the Wave engine model (which accurately simulates the behaviour of the V6 NoNOx engine) predicts that closing the EOCV's at 580° and 540° after top dead centre, has a very similar effect on the predicted cylinder pressures. However, when the EOCV's are closed at 480° after top dead centre, the predicted cylinder pressures for the NoNOx engine are substantial lower (illustrating the effect of the Miller cycle).

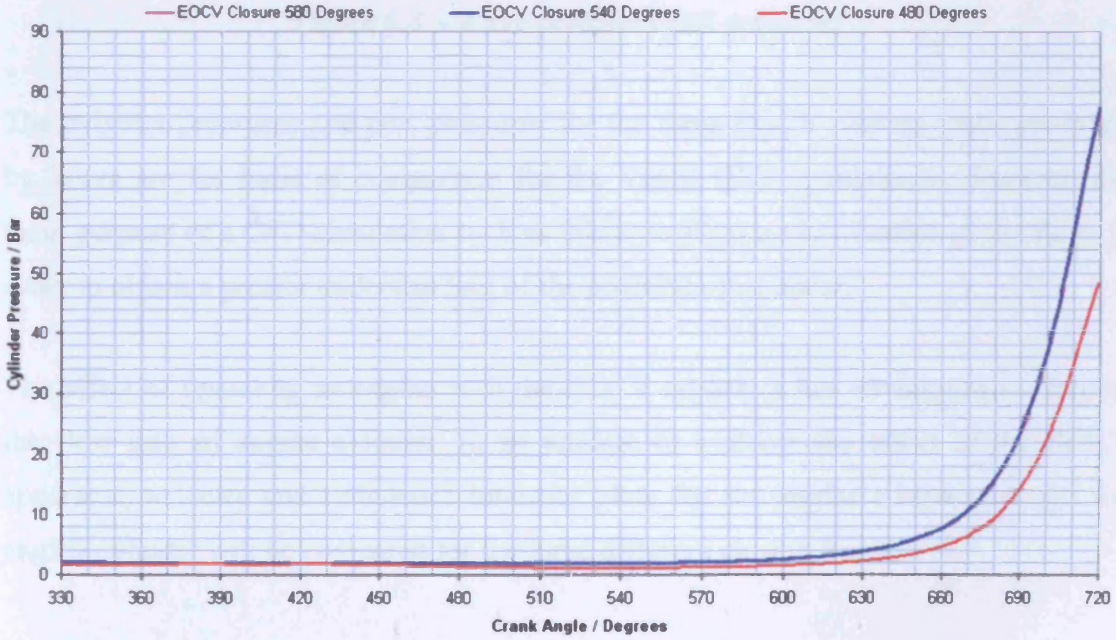

Figure 6.7 – Wave predicted cylinder pressures

Figure 6.8 displays the predicted engine inlet port pressures for the three different EOCV closure times. It can be seen that the closing of the EOCV at 480° after top dead centre is predicted to cause substantially lower port pressures than either the 540° or 580° EOCV closure times.

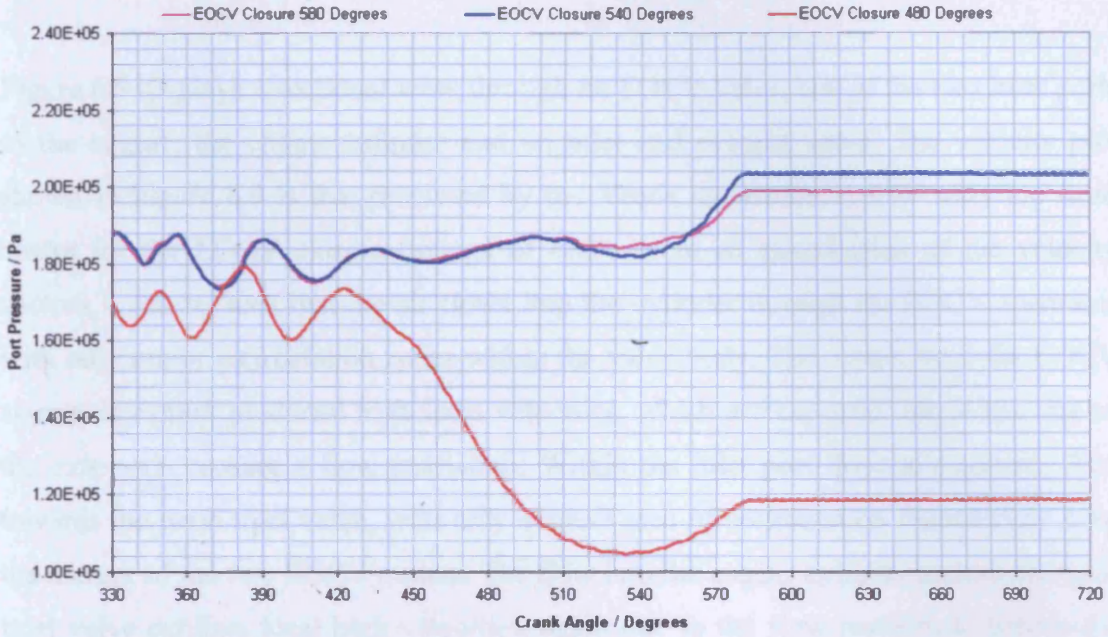

Figure 6.8 – Wave predicted port pressures

The cylinder pressures and port pressures for the three EOCV closure times predicted by Wave are the basis of comparison for the Vectis CFD simulations. However, the main purpose of a CFD simulation such as this is to allow a visualisation of the flow, in order to obtain a greater understanding of the processes that occur.

The effect of operating an engine with the EOCV apparatus has an unknown effect on the flow into an engine cylinder. In an attempt to evaluate the effect of the EOCV apparatus, velocity and turbulence intensity plots for the engine's inlet port and the engine cylinder will be compared for the three different closing times.

6.3 Results Comparison

Figure 6.9 displays a sectional view through an EOCV valve, one of the two inlet ports to the engine, the engine cylinder and an inlet and exhaust valve. The velocity plot shown in Figure 6.9 is that predicted by the Vectis simulation at 450° after top dead centre for the EOCV closure timings of 480°. From an examination of the velocity vectors it can be seen that the air flows into the cylinder through the EOCV apparatus with only minor recirculation zones within the valve body. The outlets from the EOCV apparatus exhibit predicted high local velocities, which are expected due to the size of the exit ports causing a flow restriction. Within the inlet port there is a smooth flow towards the main inlet valve, with only a small area of recirculation immediately after the merger of the two EOCV outlets. The flow into the engine cylinder around the main inlet valve exhibits local high velocities, again due to the flow restriction. Within the engine cylinder itself there are many recirculation zones, these are desirable in a spark ignition engine as they promote air and fuel mixing leading to a homogenous charge and improved combustion.

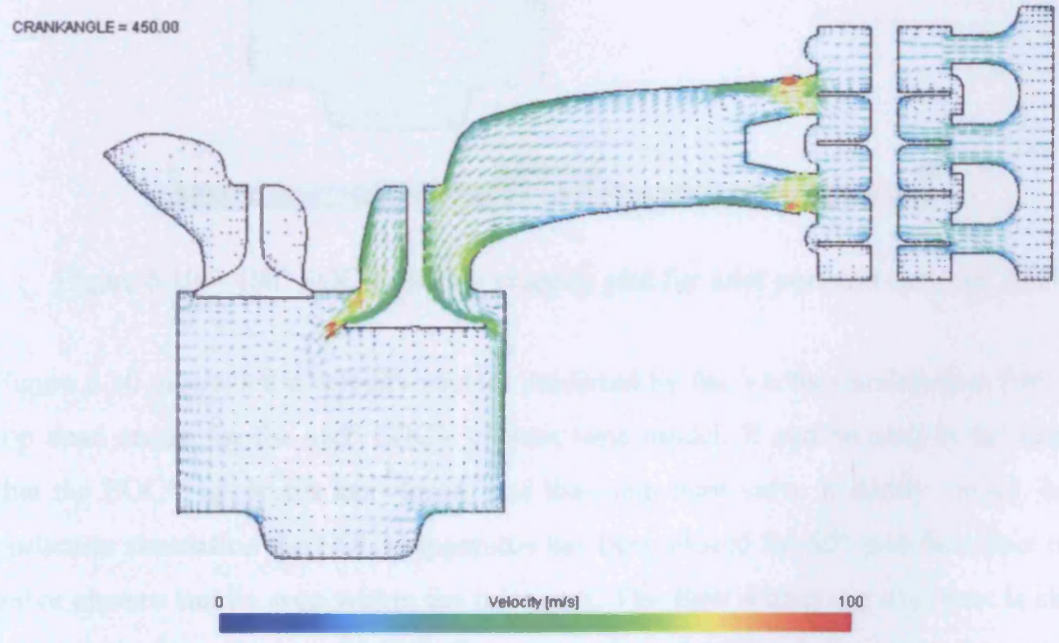

Figure 6.9 – 480° EOCV closure velocity plot for inlet port and cylinder, 450°

The contents of Appendix I include a comparison between the velocity vector plots for the three separate EOCV closure timings. An examination of the three velocity plots for 450° show that at this particular moment in the cycle (i.e. the EOCV apparatus are open in all three cases), the predicted flow pattern is nearly identical for the three separate simulations.

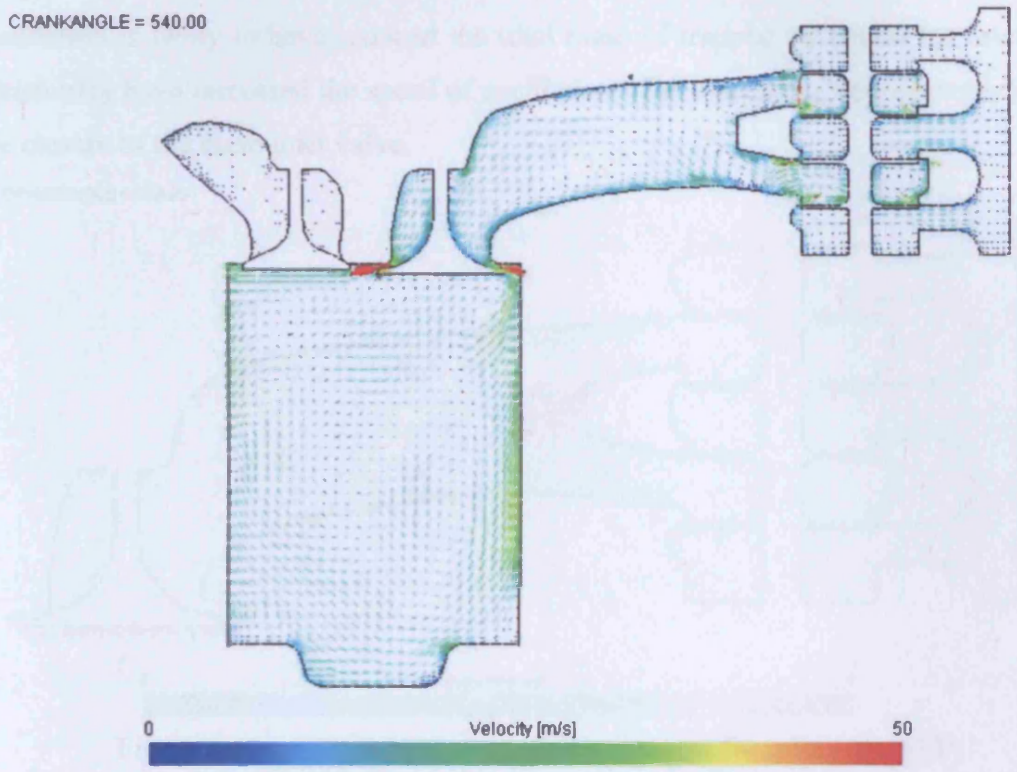

Figure 6.10 – 480° EOCV closure velocity plot for inlet port and cylinder, 540°

Figure 6.10 displays the velocity vectors predicted by the Vectis simulation at 540° after top dead centre for the 480° EOCV closure time model. It can be seen in the diagram that the EOCV apparatus has closed, and the main inlet valve is nearly closed. In this particular simulation the EOCV apparatus has been closed for 60°, and the effect of the valve closure can be seen within the inlet port. The flow within the inlet port is clearly less orderly than was seen at 450°. Comparing the velocities shown in the figure to that seen for the other two EOCV closure timings in Appendix I; it can be seen that in the 480° EOCV closure case the movement of the piston to its bottom dead centre and the resultant expansion of the trapped charge, has reduced the in cylinder air motion.

The velocity vectors predicted by the Vectis simulation at 630° after top dead centre for the 480° EOCV closure timing model are displayed in Figure 6.11. It can be seen from the velocities in Figure 6.11 that the flow within the port seems to be almost random in nature, with the closure of both the EOCV and the main inlet valve having isolating the air that remains. The diagrams for the other two EOCV closure timings in Appendix I exhibit a similar pattern, but reduced in intensity. The earlier EOCV closure in the 480° simulation is likely to have reduced the total mass of trapped air within the inlet port, which may have increased the speed of oscillation of any pressure waves resulting from the closure of the main inlet valve.

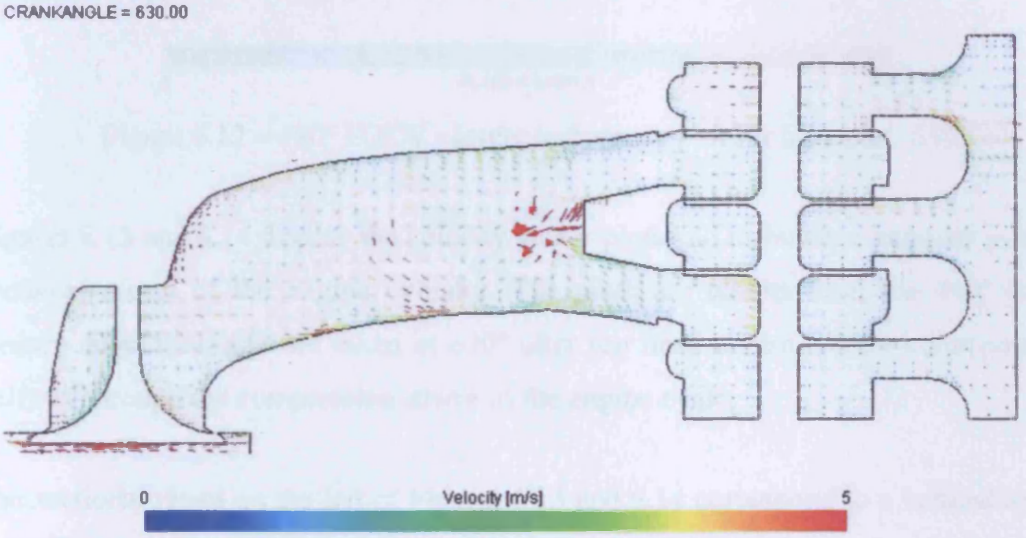

Figure 6.11 – 480° EOCV closure velocity plot for inlet port, 630°

Figure 6.12 displays the turbulence intensity plot for the 480° EOCV closure simulation case at 630° after top dead centre. It can be seen that there is a large area of turbulence located in the centre of the inlet port, which is significantly more intense than that for the other two EOCV closure timings displayed in Appendix I. From this it can be determined that the early closure of the EOCV apparatus, while also allowing Miller cycle operation, increases the turbulent kinetic energy of the trapped air within the inlet port. This trapped energy could explain a problem reported by NoNOx during testing, in which with EOCV induced miller cycle operation, there was a measurable increase in temperature of the EOCV apparatus.

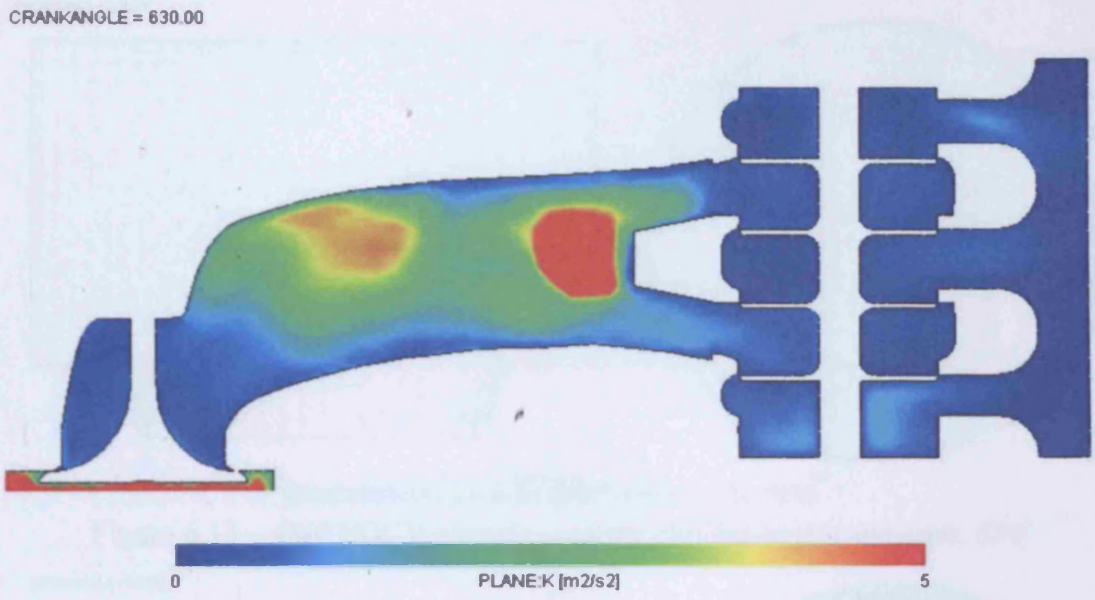

Figure 6.12 – 480° EOCV closure turbulence plot for inlet port, 630°

Figures 6.13 and 6.14 display the velocity vector plots and turbulence intensity plots for sectional views of the engine cylinder. The plots are results from the 480° EOCV closure simulation and are taken at 630° after top dead centre, which corresponds to halfway through the compression stroke of the engine cycle.

The sectional views on the left of Figures 6.13 and 6.14 correspond to a vertical section through the centre of the engine cylinder, at the top of which the spark plug is located. The sections on the right of Figures 6.13 and 6.14 correspond to a horizontal section through the cylinder, located approximately 2cm from the top of the engine cylinder.

Comparing the results shown in Figure 6.13 and 6.14 to that of the other EOCV closure timings in Appendix I, it can be seen that there is very little difference between the predicted in cylinder conditions. For all EOCV closure timings the air motion circulates within the engine cylinder in a similar manner, with the area of largest turbulence energy being in the centre of the cylinder volume. From this it can be determined that any differences that may have existed between the simulations at the completion of the induction stroke, are reduced by the compression of the air / fuel charge within the engine cylinder.

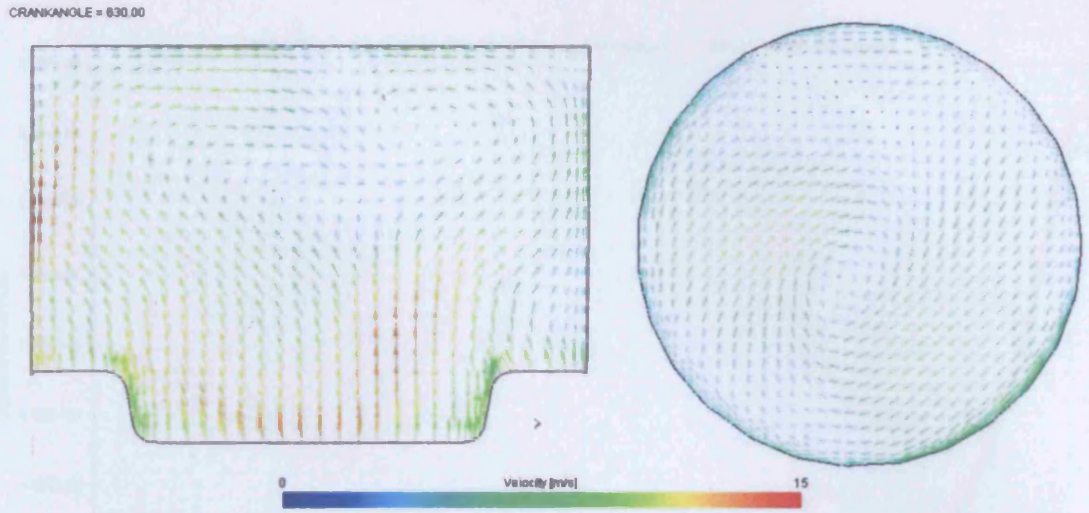

Figure 6.13 – 480° EOCV closure velocity plot for engine cylinder, 630°

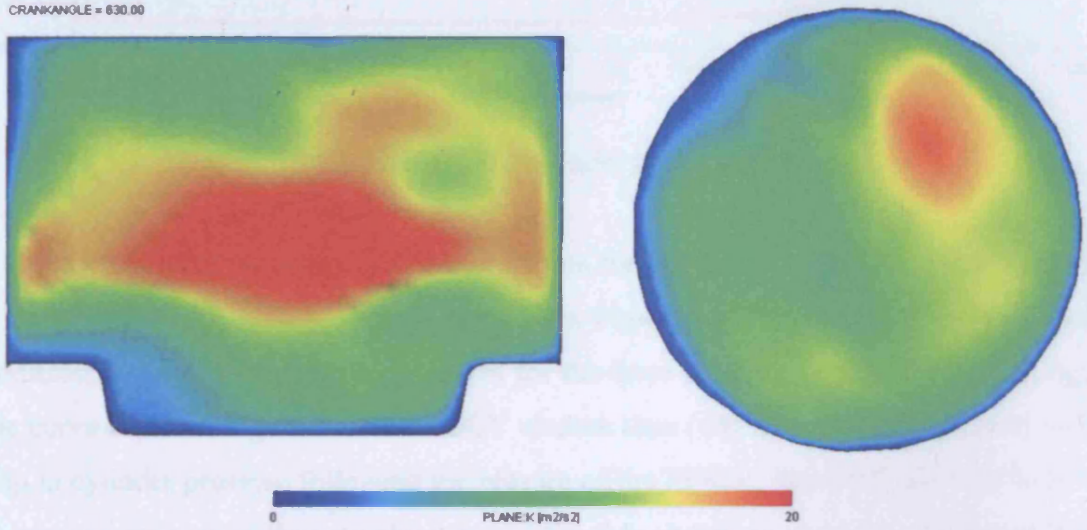

Figure 6.14 – 480° EOCV closure turbulence plot for engine cylinder, 630°

Figure 6.15 displays the predicted absolute pressure for a point located centrally near the top of the engine cylinder. It can be seen that the Vectis simulations predict similar cylinder pressures for all EOCV closure timings, even though the simulations with later EOCV closures should have higher pressures. Comparing the results in Figure 6.15 to that in Figure 6.7, it can be seen that the peak cylinder pressures (which occur at 720°, top dead centre) predicted by Vectis are approximately half the value of that predicted by Wave. With the Vectis simulations predicting a peak cylinder pressure of approximately 35 bar for the three EOCV closure timings.

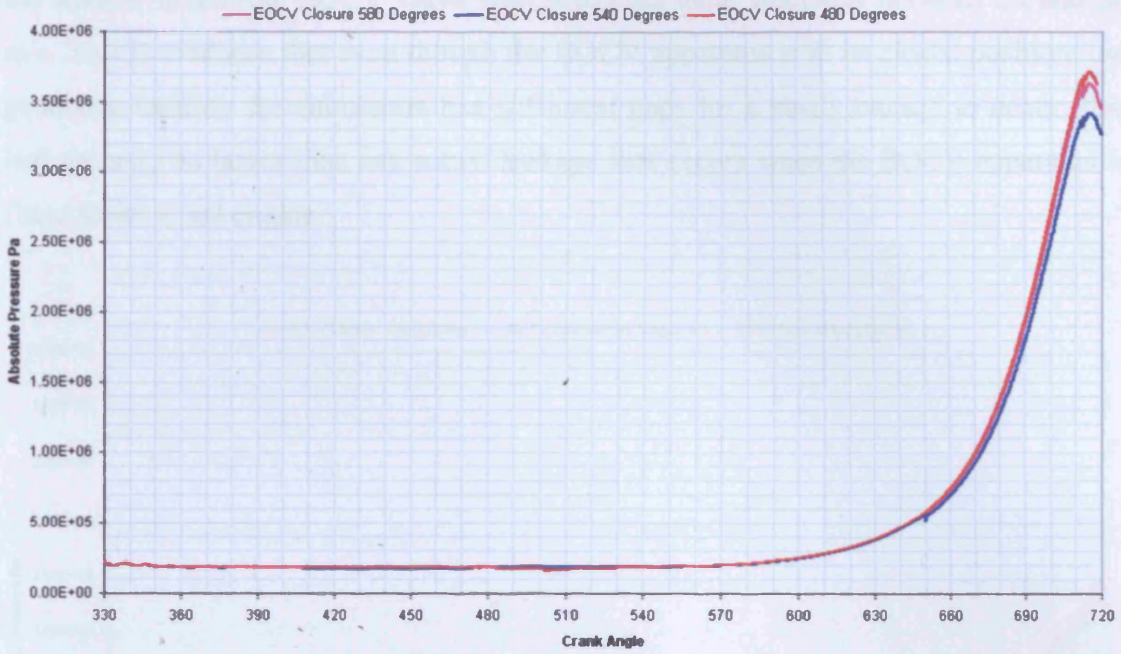

Figure 6.15 – Vectis CFD cylinder pressure predictions

A closure examination of the cylinder pressures for the duration of the induction stroke is shown in Figure 6.16. It can be seen from Figure 6.16 that there is only a small predicted difference in cylinder pressures for the three separate EOCV closure timings. The curve representing the earliest EOCV closure time (480°), does exhibit a noticeable drop in cylinder pressure following the closure of the EOCV. The 540° and 580° EOCV closure pressure traces do not exhibit any noticeable change in pressure after the EOCV closes. The explanation for this may be that the restriction in flow leading up to the closure of main inlet valve, which occurs at approximately 560°, has a larger effect on the flow into the cylinder than the EOCV apparatus. It is therefore evident that in order for a measurable Miller cycle effect to occur, the EOCV apparatus must limit a significant proportion of the normal flow into the cylinder, i.e. the closure of the EOCV apparatus must occur well before the closure of the main inlet valves.

The inability of the Vectis CFD simulations to produce similar in cylinder pressures to that of the Wave simulations (which are near to that actually measured at the NoNOx facility) could be due to the geometry used by the Vectis software. Examining the velocity vectors plotted in Figure 6.10, it can be seen that there are areas surrounding

the spindle within the EOCV valve with predicted local velocities between 20 and 30 m/s. This is evidence that even though the EOCV apparatus is in its closed position, the geometry used by the simulation has sufficient gaps for a small leakage to occur; this leakage may be larger than any actual leakage that occurs when the EOCV apparatus is fitted to an actual engine.

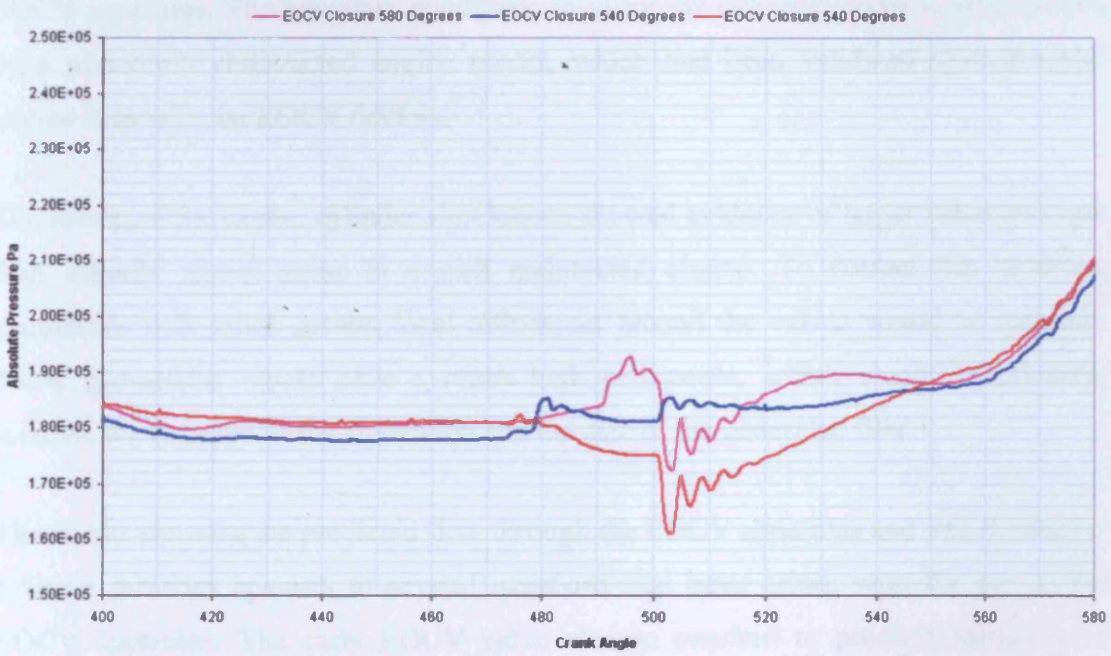

Figure 6.16 – Vectis CFD cylinder pressures (Induction stroke)

An examination of the velocity plots in Appendix I for the three EOCV closure times reveals evidence of leakage through the EOCV apparatus and possibly the main inlet valves of the engine. In the velocity results at 540° there is clear evidence of a small flow rate occurring though the EOCV apparatus for the 480° and 540° simulations, even though at this time the EOCV should be fully closed. There is also visible evidence of a small flow back into the inlet ports from the cylinder in the 630° velocity plots. The in-cylinder pressures that are created during the compression stroke are much greater than the pressures within the inlet and exhaust ports of the engine, therefore any small gaps in the geometry representing the inlet and exhaust valves could cause a "lack of compression", leading to a substantially lower predicted peak cylinder pressure.

6.4 Summary

In order to examine the effect of the EOCV induced Miller cycle on conditions within the engine cylinder and inlet ports of the V6 NoNOx engine, a three-dimensional CFD model of an engine cylinder was created. The geometry of the model included the engine cylinder, piston, main inlet and exhaust valves, inlet ports, exhaust ports and an EOCV apparatus. The boundary conditions used for the cylinder model were predicted by a previously constructed engine model, which had been validated against actual engine tests with the EOCV devices.

The results of the engine cylinder simulations showed evidence of larger valve leakages than actually would occur in a well maintained engine. To correct this problem, geometries with much greater local refinement around the valves would be required. These geometries would have a much high cell count, which would significantly increase the duration of the simulation and the size of the generated files.

The results showing the predicted flow through the EOCV apparatus and into the engine cylinder provides answers to several questions that have arisen with the use of the EOCV apparatus. The early EOCV valve closure required to produce Miller cycle operation causes a significant increase in turbulent kinetic energy of the trapped air within the inlet port, which may explain the measured increase in temperature of the EOCV apparatus during prolonged engine operation. From the results of the CFD simulations it can be seen that the conditions within the cylinder prior to combustion are unaffected by the use of the EOCV technology. The adoption of an EOCV induced Miller cycle does show evidence of a reduction in cylinder pressure, but the characteristics of the air / fuel charge prior to combustion remain similar to that for normal engine operation.

7 Diesel Test Engine Facility

Diesel powered vehicles on the market today have benefited, and will continue to benefit, from a great deal of research investment. However, from the trends in legislation and current research discussed in Chapter 2 it is clear that the emissions from diesel engines will have to significantly reduce in coming years. In order for new diesel engines to pass the future emission standards, developments must be made in particle filter/trap technology and NO_X absorbing catalysts.

Environmental engineering researchers at Cardiff University offer facilities capable of analysing exhaust gases and exhaust particulate matter (PM). In this chapter, a commercial heavy-duty diesel engine is considered with a view to concurrent appraisal of mechanical output and emission performance (with emphasis on PM) for commercially available diesel fuels. Both modelling (using Ricardo Wave) and experimental studies have been undertaken to offer a broader, integrated approach to the understanding of performance characteristics. The experimental test-bed facility described in this chapter was commissioned for the first time during this research programme, and this facility and data obtained will also serve as a bench mark for biodiesel analysis in Chapter 8

7.1 Diesel Engine Emissions

Modern diesel engines operate by injecting the fuel directly into the cylinder during the compression stroke. As the air/fuel mixture contained in the cylinder is compressed, the pressures and temperature conditions are eventually such as to initiate combustion. The initial combustion occurs rapidly due to the air/fuel charge being well mixed and the cylinder still compressing the ignited charge, which causes a rapid rise in cylinder temperature which promotes the formation of NO_X. At high engine loads, as the diffusion flame continues to burn the remaining fuel in the cylinder, the injector continues to inject fuel. The fuel that is injected late in the combustion process is exposed to the hot products of the premixed combustion and is cut off from the

remaining air in the cylinder, leading to incomplete combustion and the potential formation of soot. During the expansion stroke the majority of the soot formed is oxidized by the excess air in the cylinder, with less than 20% of the soot that is formed actual remaining in the exhausted gases. Figure 7.1 illustrates the process involved in the formation of soot particles.

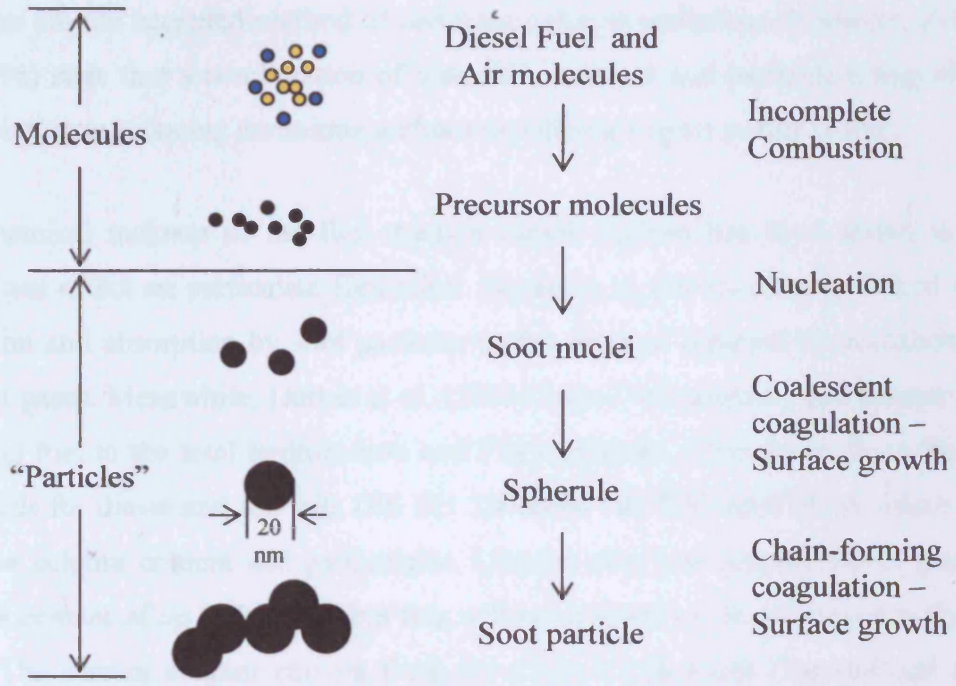

Figure 7.1 – Formation of soot particles in diesel combustion

Weingartner et al. (1997) and Funasaka et al. (1998) have shown that diesel powered vehicles are one of the primary sources of particulate matter (by mass) and NO_X emissions. Recent work carried out by El-Fadel et al. (2004) in which diesel powered vehicles were banned in the Greater Beirut area showed average reductions in airborne particulate matter of 44.9%. Severe health implications have been linked to diesel exhaust particles and it is because of this that future emission legislation requires the reduction of PM emissions.

The use of cooled EGR is an effective method of reducing the NO_X emissions of a diesel engine as it causes a decrease in peak cylinder temperatures. However, research carried out by Abu-Hamdeh (2003) showed that as a consequence the PM in the exhaust

gases increased. While Zheng et al (2004) highlighted that the sulphuric salts, abrasives and corrosive substances in the re-circulated exhaust gases could cause increased piston-cylinder wear.

In order for new diesel powered vehicles to meet future emission targets, the use of advanced catalytic converters and particulate traps will be required. Currently oxidation catalysts are the accepted method of reducing exhaust emissions. However, Zelenka et al. (1996) state that a combination of a de-NO_X catalyst and particulate trap offers the best solution to reducing emissions without sacrificing engine power output.

The chemical makeup of the fuel used in diesel engines has been found to have a significant effect on particulate formation. Durán et al. (2003) directly linked sulphate oxidation and absorption by soot particles to the mass of retained hydrocarbons in the exhaust gases. Meanwhile, Durbin et al. (2003) linked the aromatic and sulphur content of diesel fuel to the total hydrocarbon and PM emissions. Changes made to the British Standards for diesel and fuel oils (BS EN 590:2004 and BS 2869:2006) reflect the link between sulphur content and particulates. Current ultra low sulphur diesel can have a sulphur content of up to 50 ppm, but this will be reduced to 10 ppm towards the end of 2009. The current sulphur content limit for Class A2 fuel oils (Agricultural and off-highway fuel commonly known as red diesel) is 2000 ppm, but will be reduced to 1000 ppm from the beginning of 2008. The polycyclic aromatic hydrocarbon (PAH) content of commercial diesel fuel is limited to 11% by mass, whereas at present there is no PAH limit imposed for the agricultural red diesel. An interesting modification to the British Standards for diesel and fuel oils is the allowance of up to 5% by volume fatty acid methyl ester content, the common terminology for biodiesels.

As the sale of diesel powered vehicles throughout Europe continues to increase, automotive manufacturers are spending more on new innovative technology to make sure their vehicles can pass future emission legislation. The relative immaturity in the understanding of the impact upon health and the environment of PM emissions, together with the difficulties in sampling and measurement mean that it is likely to receive further attention in the future.

7.2 Test Engine Facility

The engine test-bed facility, although basic, will allow studies into engine performance, fuel economy and emissions testing. The test-bed facility will also be used for the testing of other engines (e.g. undergraduate projects such as the 'Formula Student' competition), and so needs to be able to accommodate differing engine specifications and measurement requirements.

7.2.1 Turbo-Diesel Test Engine

A diesel powered engine was purchased by Cardiff University to allow research orientated work to be undertaken. Details of the engine are listed in table 7.1.

Table 7.1 – Diesel test-engine specifications

Engine Model	Perkins 1000 Series 1004-4T
Number of Cylinders	4 in-line
Engine Displacement (Bore x Stroke)	4.0 litres (100mm x 127mm)
Rated Power Output (Speed)	83 kW - 111 bhp (2600 rev/min)
Rated Peak torque (Speed)	368 Nm – 271 lbf ft (1600 rev/min)
Compression Ratio	16:1
Firing Order	1-3-4-2

The 1004-4T Perkins engine is marketed as a 4-cylinder turbocharged diesel for agricultural and construction equipment. The official power and torque curves as well as a picture of the engine mounted on the test-bed can be seen in Figure 7.2. Further details of the engine can be seen in the specification sheet included in Appendix J.

7.2 Test Engine Facility

The engine test-bed facility, although basic, will allow studies into engine performance, fuel economy and emissions testing. The test-bed facility will also be used for the testing of other engines (e.g. undergraduate projects such as the 'Formula Student' competition), and so needs to be able to accommodate differing engine specifications and measurement requirements.

7.2.1 Turbo-Diesel Test Engine

A diesel powered engine was purchased by Cardiff University to allow research orientated work to be undertaken. Details of the engine are listed in table 7.1.

Table 7.1 – Diesel test-engine specifications

Engine Model	Perkins 1000 Series 1004-4T
Number of Cylinders	4 in-line
Engine Displacement (Bore x Stroke)	4.0 litres (100mm x 127mm)
Rated Power Output (Speed)	83 kW - 111 bhp (2600 rev/min)
Rated Peak torque (Speed)	368 Nm – 271 lbf ft (1600 rev/min)
Compression Ratio	16:1
Firing Order	1-3-4-2

The 1004-4T Perkins engine is marketed as a 4-cylinder turbocharged diesel for agricultural and construction equipment. The official power and torque curves as well as a picture of the engine mounted on the test-bed can be seen in Figure 7.2. Further details of the engine can be seen in the specification sheet included in Appendix J.

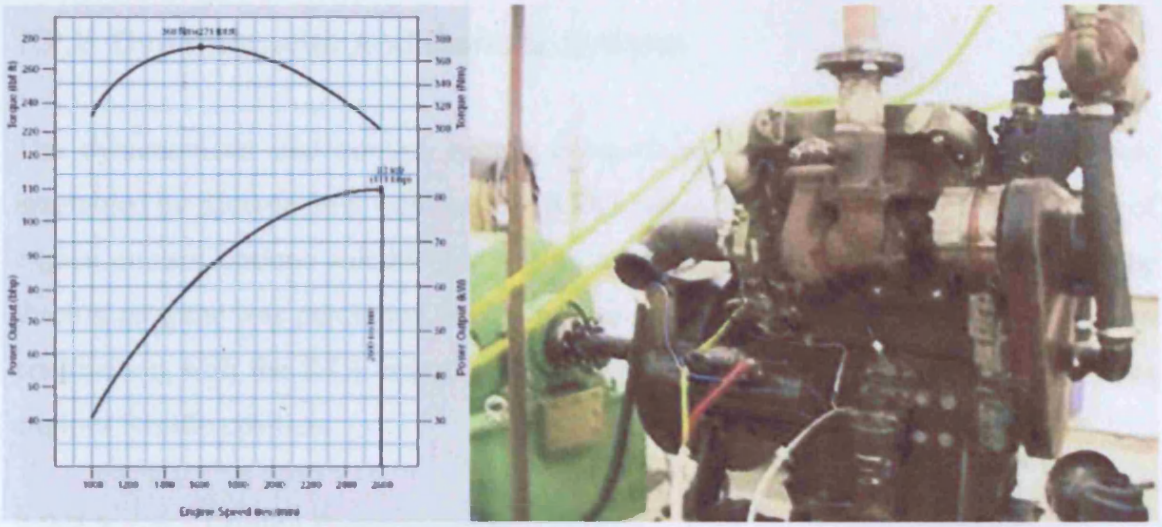

Figure 7.2 – Perkins 1004-4T output curves and installation picture

The initial set of experiments for the diesel test engine will concentrate on characterizing its emissions and performance, followed by the construction of a computer model of the engine in order to allow theoretical studies of the engine's operation.

The Perkins 1004-4T diesel engine is designed primarily as an engine for use in agricultural and construction equipment, both predominantly used off-highways. Therefore it is expected that the engine has been designed to run on fuel of the red diesel (Class A2 fuel oil) type. Red diesel can have vastly different chemical and physical properties to the most common road diesel fuel - ultra low sulphur diesel fuel. It should therefore be expected that the characteristics of the Perkins engine will be more suited to the lower Cetane rated red diesel fuel, and this can be confirmed by testing.

7.2.2 Dynamometer and Control System

The dynamometer and control system components of the engine test facility were assembled by Ricardo Test Automation (RTA) and are designed to offer a wide range of engine control options suitable for engine analysis, engine tuning and research. The throttle actuator was purchased from Dynamometer Services Group and when used in conjunction with the RTA control unit, allows precise control and monitoring of the engines throttle position.

7.2.2.1 Engine Dynamometer

The Engine Dynamometer to be used in the engine test facility at Cardiff University is an eddy-current dynamometer manufactured by Borghi and Saveri. An eddy-current dynamometer works using the principles of magnetic interaction between magnetic coils in the stator and the rotor, which is connected to the engine via a driveshaft. The torque produced by the engine is measured using a load cell mounted between the stator and the dynamometer body. The rotational speed of the engine is measured using an optical pickup and toothed gear arrangement mounted on the input shaft from the engine. The magnetic coils contained in the dynamometer produce a great deal of heat when the engine is operating, because of this a water cooling system is incorporated into the dynamometer which requires a constant supply of fresh water. Table 7.2 shows the specifications of the dynamometer whereas a picture of the dynamometer is shown in Figure 7.3.

Table 7.2 – Eddy-current dynamometer specifications

Dynamometer Type	Shaft / Rotor Diameter	Max. Torque / Power	Max. Speed	Moment of Inertia	Torsional Stiffness
Borghi & Saveri FE 260-s	50 mm / 380 mm	610 Nm / 260 HP (191.17 KW)	12000 RPM	0.176 kgm²	239.11 Nm/rad

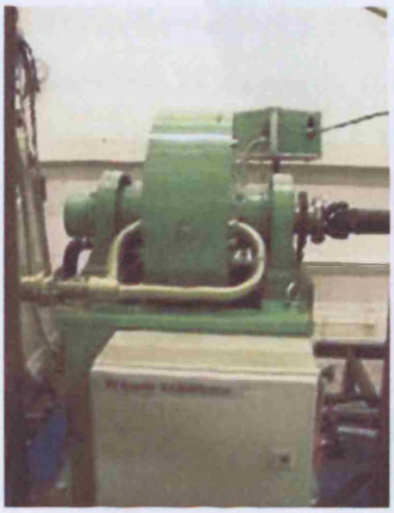

Figure 7.3 – Picture of dynamometer on test-bed

7.2.2.2 Dynamometer Controller

In order for studies into engine performance and emissions to be carried out using the dynamometer, a control system is required that can operate both the eddy-current dynamometer and the engine itself. For this purpose a Series 3000 Controller manufactured by Ricardo Test Automation was purchased. The Series 3000 Controller unit contains power modules for the dynamometer and throttle actuator as well as the control circuitry. A picture of the front panel of the Series 3000 controller is shown in Figure 7.4.

Figure 7.4 – Control panel of Series 3000 controller

The Series 3000 control system allows for the complete control of an engines speed and load condition. The operating conditions of an engine dynamometer are characterised by torque and speed. At the selected speed there exists a stable condition, providing the dynamometer is more powerful than the engine at that selected speed. This is shown in graphically in Figure 7.5.

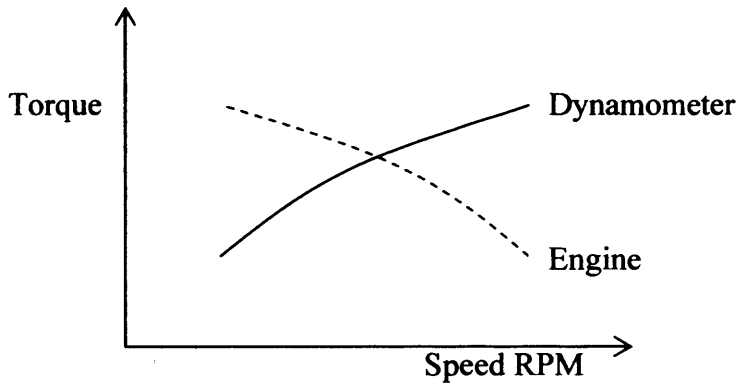

Figure 7.5 – Dynamometer/engine torque/speed characteristics

From Figure 7.5 it can be seen that for every engine setting (throttle position) and dynamometer control setting, there is a clearly defined point of intersection where the torque/speed characteristics match. The control system's electronics (through the dynamometer power module's amplifier) control the coil current of the dynamometer, providing a load for the engine.

The control cabinet allows for the complete control of the engine's operating conditions. The engine's running speed and load conditions are selected using the two controls shown in Figure 7.4. The engine's throttle position is selected as well as the desired engine's running speed, the control system then attempts to apply the correct load through the dynamometer such that the required speed is attained. Full details of the Series 3000 controller operation and calibration can be found in the Series 3000 User Manual available from Ricardo Test Automation (Schenk).

7.2.3 Emission Testing

The emission testing facilities within the engineering department at Cardiff University are comprehensive; with dedicated facilities for environmental sampling and large scale combustion tests. However, not all these facilities are suitable for sampling the emissions from an internal combustion engine. For the initial diesel engine tests, the exhaust emissions measurements taken will be compared against that stated in literature in order to evaluate the suitability of the selected equipment.

7.2.3.1 Exhaust Gas Analyser

To analyse the content of exhaust gases, a Testo 350 XL portable combustion analyzer will be used. The Testo exhaust gas analyzer is a portable unit designed for taking measurements in furnaces and combustors, and as such may not be entirely suitable for analysing the wide range and rapidly changing emissions of an internal combustion engine.

Figure 7.6 – Testo 350 XL unit and probe

The Testo 350 XL gas analyser, its control unit and sampling probe is pictured in Figure 7.6 and its specifications are listed in Table 7.3.

Table 7.3 – Testo 350 XL specifications

Gas \ Properties	O_2	CO	NO	NO_2	SO_2	$C_X H_Y$
Range	0-25% Vol.	0-10000 ppm	0-3000 ppm	0-500 ppm	0-5000 ppm	0-4%
Accuracy	< 0.8% F.V.	< 5 ppm (0 - 99) < 5 % m.v. (100 - 2000) < 10 % m.v. (2001 - 10000)	< 5 ppm (0 - 99) < 5 % m.v. (100 - 2000) < 10 % m.v. (2001 – 3000)	< 5 ppm (0 - 99) < 5 % m.v. (500)	< 5 ppm (0 - 99) < 5 % m.v. (100 - 2000) < 10 % m.v. (2001 - 5000)	< 0.04 % (0 - 0.4 %) < 10 % (0.41 - 4 %)
Resolution	0.1 Vol. %	1 ppm	1 ppm	0.1 ppm	1 ppm	0.01 Vol. %
Response Time	20s	40s	30s	40s	30s	40s

Although the Testo 350 XL analyzer purchased by the combustion department is capable of measuring SO_2 and C_XH_Y, this unit was unavailable during the testing period. The rental unit used was not capable of testing for these gases. Examining the accuracy and resolution of the Testo 350 XL instrument listed in Table 7.3 it can be seen that the unit is capable of detecting the required gases for diesel engine emission tests, namely CO (and therefore CO_2), NO_X, SO_X and gaseous hydrocarbons.

The main drawback with using the Testo 350 XL instrument to analyse the exhaust gases from a diesel engine is the response time. For O_2 detection the response time of the unit is twenty seconds, but for NO_X detection the response time is doubled. For measuring the emissions during transient engine studies a response time of less than a second is desirable.

The Testo 350 XL unit was chosen as it is capable of measuring the emissions from the diesel exhaust to a satisfactory degree of accuracy, without the need of sample preparation or the use of a dilution tunnel facility. However for future research projects, instruments with quicker response times would be desirable as they would allow for the accurate measurement of exhaust gas emissions during changes in engine loads and speed conditions.

7.2.3.2 Mass Concentration and Particulate Sizes

There are two methods by which the particulate matter emitted from the engine is to be measured and quantified.

The first method is a simple mass analysis, where a calibrated pump is used to sample the exhaust gases. A filter paper consisting of a three-dimensional fibre matrix acts as a particulate barrier, and the particulate aerosol within the exhaust gas is deposited on the filter through impaction, interception and diffusion. Through the correct choice of filters total deposition may be achieved allowing for bulk particulate analysis to be carried out. The sampling pipe, filter enclosure and pump used for the bulk particulate sampling are shown in Figure 7.7.

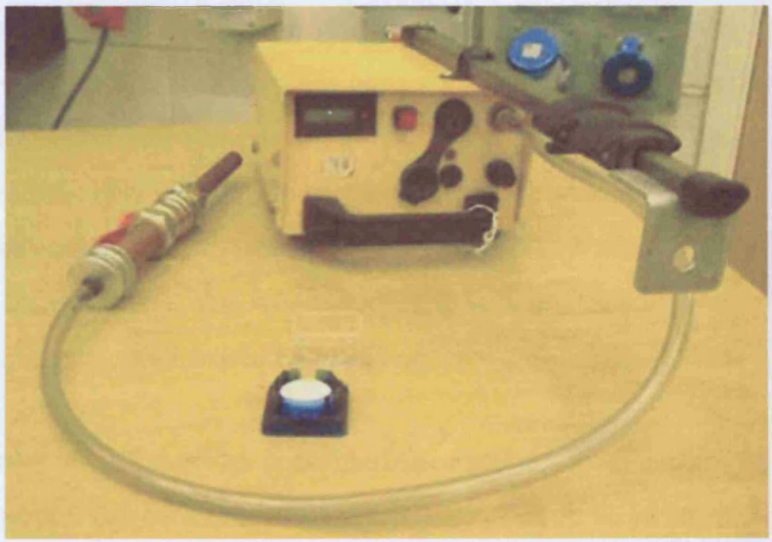

Figure 7.7 – Particulate sampling equipment

Prior to the sampling of the exhaust particulates, each filter paper is weighed using a precision balance with a 10μg resolution. After the particulates are sampled over a predefined sampling period the filter papers are reweighed, allowing the mass of PM retained by the filters to be calculated. As the flow-rate of the sampling pump is known, the mass of particulates as a function of volumetric exhaust gas flow can be derived. The flow to the pump can be shut off through the use of the valve within the sampling pipe, preventing the particulate matter from being sucked from the filter by the exhaust gas flow.

The second method used to measure the exhaust particulates is the characterisation of the particulate aerosol though the use of a Transmission Electron Microscope. The sampling tube, filter enclosure and pump shown in Figure 7.7 are again used, but this time with a nucleus pore filter which allows for single particle analysis. Nucleus pore filters consist of a thin polycarbonate film with a smooth surface, across which uniform sized holes are spaced. The holes are etched into the film through the irradiation of the surface with neutrons, and any particulates larger than the holes in the nucleus pore filter are deposited by the exhaust gas flow.

The nucleus pore filter particulate samples must be processed following collection to present the particles in a suitable condition for analysis. The particulates trapped on the surface of the nucleus pore filter are transferred onto a thin carbon film; the carbon film is only a few nanometres thick and is supported by a fine grid or mesh of a non-reactive metal. In this case the prepared samples used gold mesh grids of 5mm overall diameter. The carbon film is electron transparent, allowing the particles deposited to be viewed by an electron microscope. An alternate thermophoretic method (developed at Cardiff University) for sampling exhaust PM for analysis by an electron microscope is described by Jones (2003). For these studies it was decided that the simpler nucleus pore filter sampling method would be used.

The size distribution of the PM contained on each of the samples studied using the electron microscope can be assumed to be uniform. The sizes of the individual particles are often very difficult to determine, not only due to their small physical size (majority of the particulates in diesel exhaust are smaller than PM_{10}, i.e. less than 10μm in size) but also their irregular aggregated shape. The term "aerodynamic diameter" is often used to represent the particulates size, due to the difficulty of stating direct measurements. The aerodynamic diameter of an individual particle is the diameter of a particle of unit density possessing the same aerodynamic properties.

Through the use of these two particulate sampling methods it is hoped that the particulates contained in the exhaust from the Perkins diesel engine can be measured and characterised.

7.3 Diesel Engine Testing

For the initial diesel engine tests it was decided that the emissions and performance of the Perkins 1004-4T diesel engine would be characterised using a Class A2 fuel oil (an industrial/agricultural rebated heavy oil) hereafter known as red diesel, and a widely available ultra low sulphur No. 2 diesel fuel. The main physical and fuel properties of the two fuels used are listed in Table 7.4.

Table 7.4 – Fuel properties

	Low Sulphur Diesel Fuel	Red Diesel
Density kg/m^3	820-845	>820
Sulphur Content	< 50 ppm	< 2000 ppm
Viscosity @ 40°C g/ms	2.0 – 4.5	2.0 – 5.5
Flash Point °C	>55	>56
Cetane Number	51	45

Examining the fuel properties listed in Table 7.4 it can be seen that the low sulphur diesel fuel has significantly lower sulphur content than the red diesel. However, the density, viscosity and flash point of both the fuels are similar. It is also worthwhile noting that the Cetane number of the red diesel is lower than that of the regular diesel fuel; this should have a substantial effect on the combustion timing of the fuel and therefore the emissions that are produced. With the lower Cetane number of the red diesel delaying combustion, affecting cylinder temperatures and the amount of NO_X in the exhaust gases.

The initial diesel engine tests were carried out with the intention of characterising the performance of the Perkins diesel engine, by comparing the measurements taken to the official power ratings and computational predictions. The most important comparison is that between the measured torque curves for the two fuels, the computer predictions and that provided by Perkins.

7.3.1 Testing Procedure

For each of the two fuels tested a series of load-speed curves were obtained for different throttle (fuel pump) settings. In addition to obtaining the load/speed characteristics of the engine for both fuels, seven operating points were chosen to measure the fuel consumption and emissions of the engine. For the point corresponding to case 3 (80% throttle, 2100 RPM) particulate matter mass measurements were made and samples taken for examination by an electron microscope. Details of the seven tested operating points are shown in Table 7.5.

Table 7.5 – Engine operating test positions

Case Number	1	2	3	4	5	6	7
Throttle Position	70%	80%	80%	90%	90%	100%	100%
Engine Speed	2000 RPM	2100 RPM	2400 RPM	2200 RPM	2500 RPM	2300 RPM	2600 RPM

The engine tests were carried out in accordance with the EEC standard 80/1269 with the reference atmospheric conditions of 298 K and 99kPa (dry pressure). At all times during the testing, the actual atmospheric conditions during the tests were between the required limits, 283 K $\leq$ T $\leq$ 313 K and 80 kPa $\leq p_s \leq$ 110 kPa.

The power correction factor (α_d) for compression-ignition engines running at constant fuel rate is obtained by applying the formula 7-1.

$$\alpha_d = (f_a)^{f_m} \tag{7-1}$$

where

$$f_a = \left(\frac{99}{p_S}\right)^{0.7} \cdot \left(\frac{T}{298}\right)^{1.5} \tag{7-2}$$

and f_m is equal to 1.2 for all operating points of the Perkins engine. Therefore the actual corrected power (i.e. the equivalent power when operating under reference atmospheric conditions) is given by equation 7-3.

$$P_o = \alpha.P \tag{7-3}$$

where:

$$\alpha = \left(\frac{99}{p_S}\right)^{0.84} \cdot \left(\frac{T}{298}\right)^{1.8} \tag{7-4}$$

During each testing period, the temperature of the laboratory was carefully monitored and recorded. This, along with the published meteorological data for Cardiff during the testing times, allowed correction factors to be calculated for each batch of tests. Throughout the month in which the tests were carried out the correction factor varied from 0.9057 to 0.9525.

In order for approximate fuel flow-rates to be calculated, a digital scale is used to measure the fuel usage by mass over a prolonged period of time for each of the individual engine operating positions.

The exhaust gases from the diesel engine flow into a sampling cabinet of 0.38 cubic metres volume before they are extracted to the buildings exterior. An opening in the cabinet allowed the sampling probe of the Testo instrument to protrude into the sampling volume for the gaseous emission readings to be taken. The same cabinet opening is used for the sampling tube for the particulate measurements.

7.3.2 Dynamometer Results

The measured torque curves at 70%, 80%, 90% and 100% fuel pump settings for both diesel test fuels are shown in Figure 7.8. It can be seen that from the raw measured values, the low sulphur commercial diesel fuel produces slightly less power than the less refined red diesel rebated fuel oil.

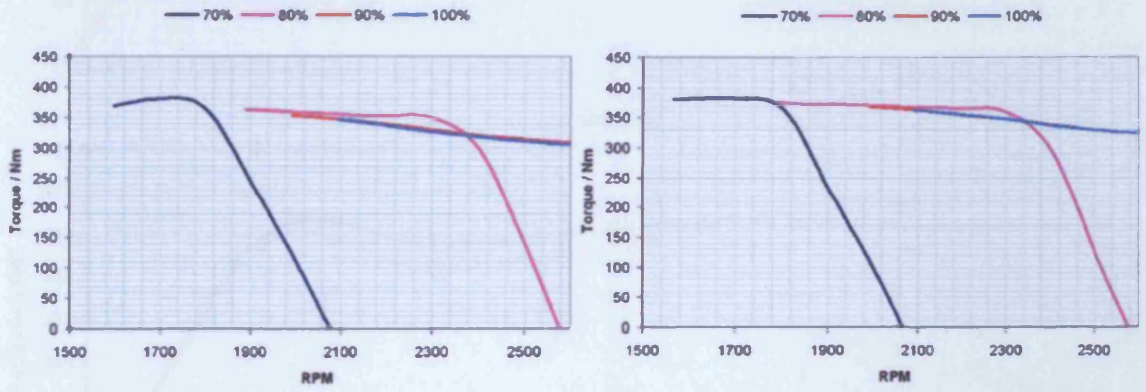

No. 2 Low Sulphur Diesel Red Diesel

Figure 7.8 – Comparison of torque / speed relationship for both diesel fuels

From Figure 7.8 it can clearly be seen that for all of the separate engine throttle positions, the engine appeared to produce higher torque figures when it was run on the red diesel fuel. However, the laboratory temperature was slightly colder on the day when the red diesel readings were taken. In addition to the slight difference in temperature between tests, the ambient air pressure in the laboratory was also significantly higher on the day of the red diesel tests to that of the low sulphur diesel tests.

In order for a fair comparison to be made between the two fuels, dynamometer correction factors were applied in accordance with the EEC 80/1269 directive relating to the engine power of motor vehicles. The corrected torque and BHP values for the two test fuels are compared for the seven test cases in Figures 7.9.

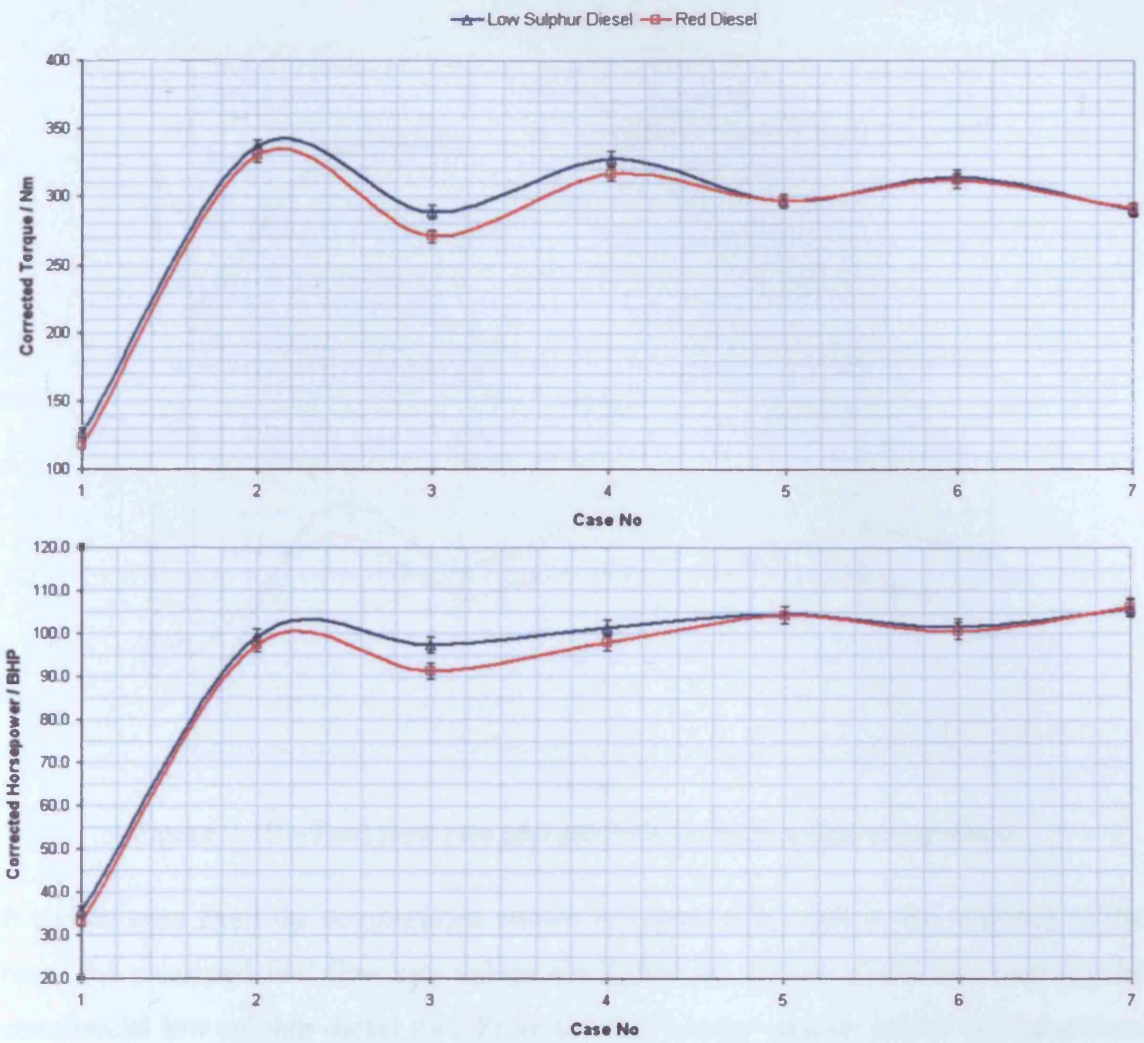

Figure 7.9 – Corrected diesel performance comparison

From Figure 7.9 it can be seen that once the differences in ambient laboratory conditions are taken into account, the torque produced by the engine is much higher for many of the test cases when the engine is fuelled by the commercial low sulphur diesel fuel. This can be explained by the fact that commercial low sulphur diesel fuels tend to have higher heating values than that used for agricultural purposes.

The results shown in Figure 7.10 compare the measured fuel flow rate for the seven engine operating points described in Table 7.5. From the fuel flow rate values and the calculated corrected power values, approximate values for the fuel energy content can be obtained for each fuel over the seven test cases.

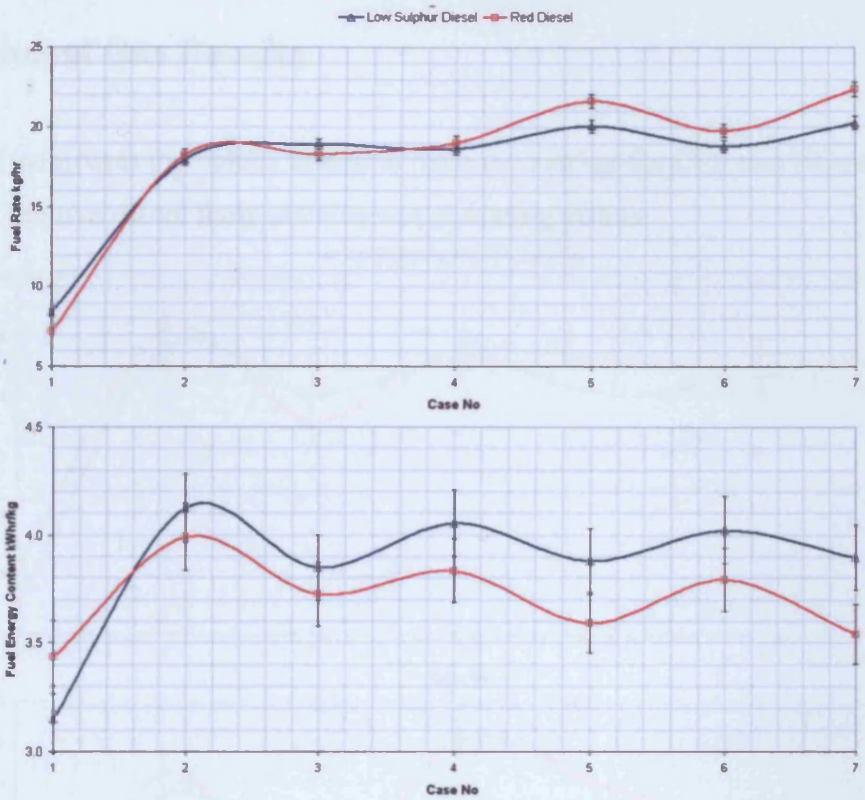

Figure 7.10 – Fuel flow rate and attributed energy value comparison

It can be seen from the comparisons shown in Figure 7.10, that in the majority of the cases the measured fuel flow rate values are higher for the red diesel fuel than for the commercial low sulphur diesel fuel. From the fuel energy content values that have been attributed to the two fuels for each of the test cases, it can be seen that in all cases except case number 1, the commercial low sulphur diesel fuel produced higher power values (per kilogram of fuel used by the engine).

Examining Figure 7.10 reveals that there is a large variation between test cases in the values obtained for the fuel energy content for each of the diesel fuels. This can be explained by the fact that each of the engine operating points represented by the test cases will have vastly different air to fuel ratios. The values obtained for the fuel energy content are higher for the commercial low sulphur diesel fuel than for the agricultural red diesel fuel, this again can be attributed to the higher heating values of the commercial diesel fuel.

7.3.3 Exhaust Gas Results

Figure 7.11 compares the values obtained from measuring the CO_2 and NO_X emissions for each of the two diesel fuels at the seven operating points.

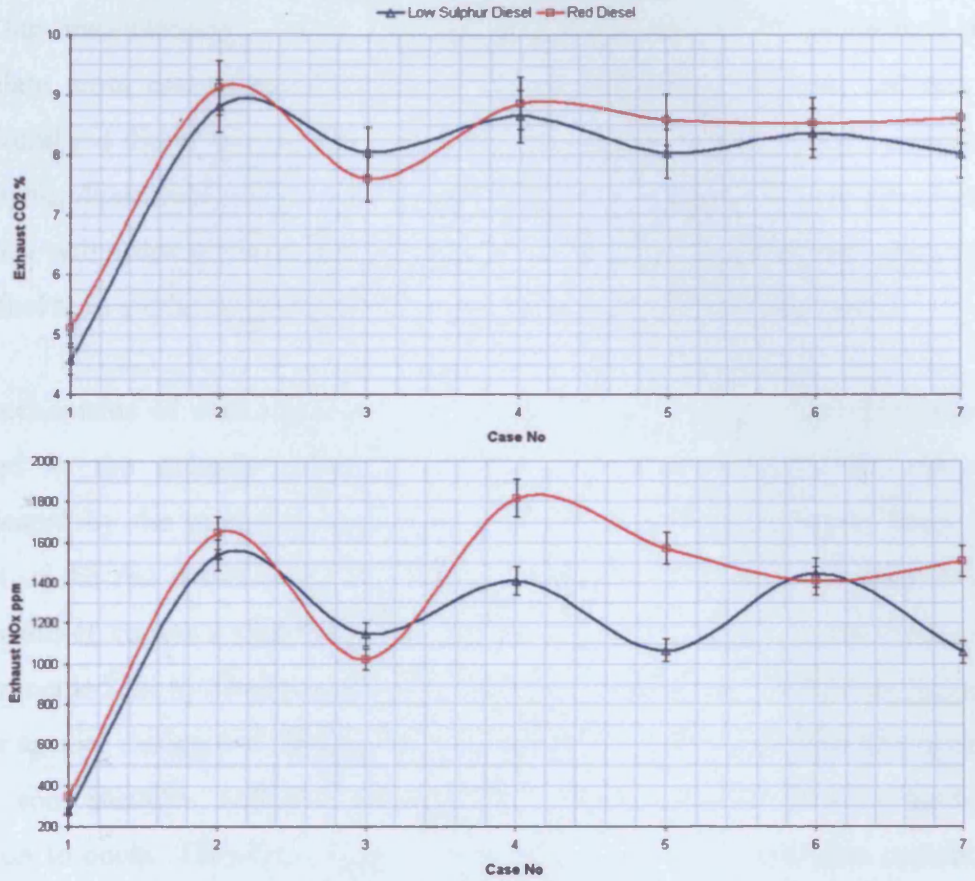

Figure 7.11 – Exhaust emission comparison

From the graphical comparison made in Figure 7.11 between the emissions measured for the commercial diesel and agricultural diesel fuel, it can be seen that in general the agricultural red diesel fuel produces higher levels of CO_2 and NO_X. The higher CO_2 levels could possibly indicate a higher percentage of carbon in the agricultural red diesel fuel, although this contradicts Lapuerta et al. (2003) who found that agricultural diesel contained 0.5% less carbon by weight than commercial diesel. The higher NO_X values recorded with the agricultural diesel fuel can be explained by the higher cetane number of the commercial diesel fuel, which reduces the fuel's ignition delay. This delay may reduce the NO_X formation by lowering the peak cylinder temperatures.

7.3.4 Exhaust Particulate Results

Using the equipment shown in Figure 7.7, particulate samples were taken from the exhaust gases when the engine was running at 2100 RPM with an 80% throttle setting. From the measurements taken, approximate values could be determined for the particulate mass concentrations. The particulate concentration in the exhaust of the agricultural red diesel was 0.0536 ±0.0040 mg/litre, while the value for the commercial low sulphur diesel fuel was 0.0502 ±0.0037 mg/litre. It can therefore be determined that an engine will produce more particulate matter when running on the red agricultural red diesel fuel than would be produced on commercial low sulphur diesel fuel.

The mechanisms of soot formation and the reactions in which the soot particles are oxidized in the exhaust gases of internal combustion engines are made more complicated by the presence of gaseous pollutants. The comparatively large sulphur content of the red diesel (class A2 fuel oil), when compared to the commercial low sulphur diesel, causes a significantly higher concentration of SO_X in the exhaust gases. As commented on by Durán et al. (2003) and Chughtai et al. (1998), the presence of sulphur species during and after combustion leads to reactions in which SO_2 is absorbed by the soot particles, reducing the available surface area on the soot particles for oxidation to occur. Therefore, a link can be made between the sulphur content of the fuel, and the proportion of the soot particles that remain in the exhaust gases. With higher sulphur content fuels producing more particulate matter by mass.

Figure 7.12 compares electron microscopy images of the particulate matter samples obtained from the exhaust of the diesel engine for both of the fuels. The images are taken at 26,000 and 235,000 times magnification, and show not only the large soot agglomerates but also the individual soot particles contained within the exhaust gases (see Figure 7.1 for mechanism of soot particle formation). It can be seen from Figure 7.12 (and the additional images in Appendices K and L), that the individual soot particles that make up a proportion of the particulate matter for both of the fuels tested are similar in nature, with the individual particles while only being 20 nm in magnitude joining together in the hundreds to form much larger soot particles.

Low Sulphur Diesel | Red Diesel

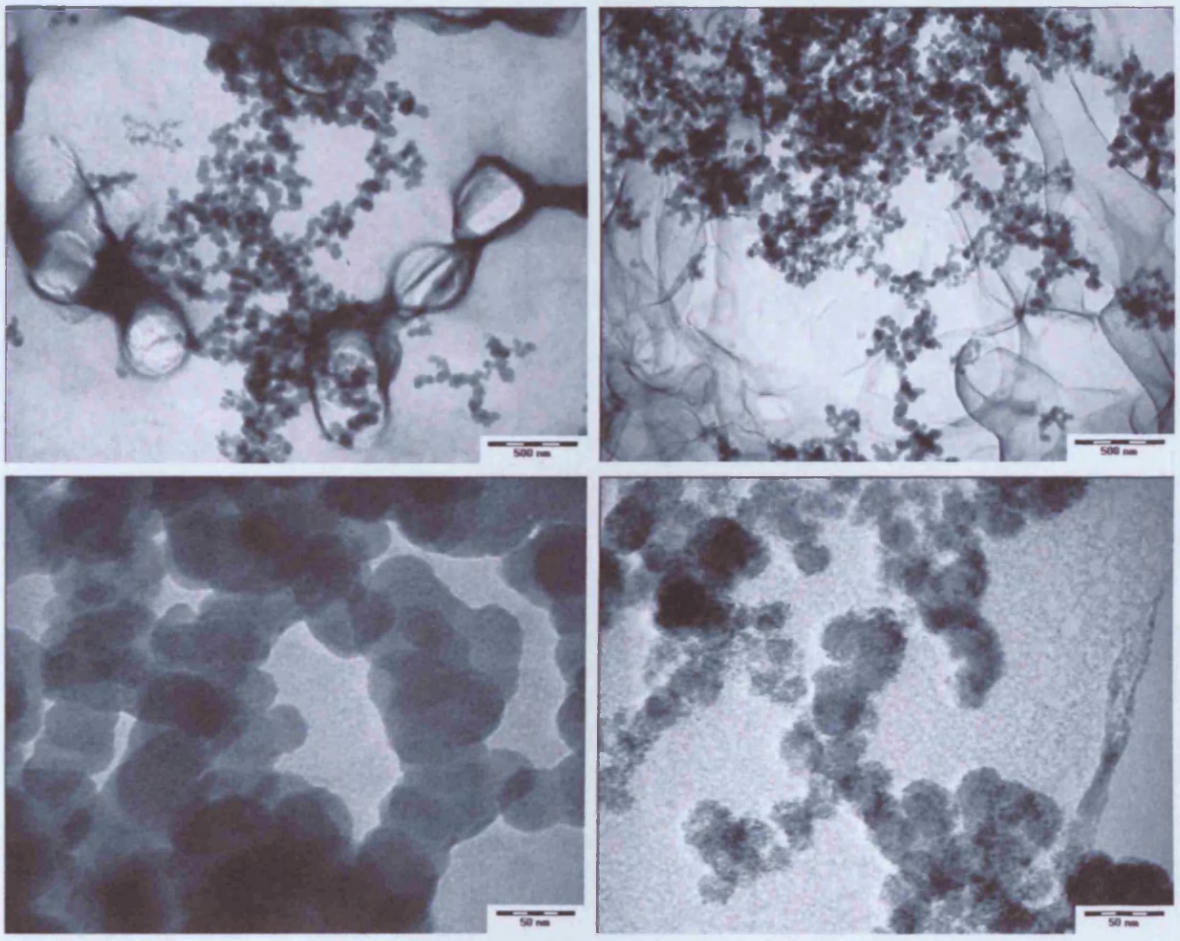

Figure 7.12 – Electron microscopy images of soot particles

Assuming that the particles seen in the images in Figure 7.12 are a fair representation of the PM contained in the exhaust gases, it can be concluded that the particulates emitted have similar size distributions. Studies such as that carried out by Durán et al. (2004) found that an increase in sulphur concentration in

a fuel is linked to an increase in the size of PM in the exhaust gases. The exact size distribution can only be accurately measured through the use of particle sizing equipment that can measure a suitably large number of particles so as to be statistically robust - no such equipment was available at Cardiff University at the time of this section of study.

7.4 Diesel Engine Model

From the results discussed in section 7.3, it can be seen that the engine testing facility constructed by Cardiff University can be used to carry out investigations into engine operation, fuel effects and emission studies. In addition to carrying out introductory investigations into the operation of a turbocharged Perkins diesel engine, it was decided that a computer model of the engine should be constructed to allow further detailed investigations into its operation.

7.4.1 Diesel Engine Model Construction

The Ricardo Wave software used to construct a model of the Deutz 1015 marine engine for the MagMove project was used to construct a detailed model of the Perkins 1004-4T turbo diesel engine.

Using detailed engine geometry provided by Perkins, the engine model shown in Figure 7.13 was constructed. It can be seen from Figure 7.13 that the geometry of the Perkins engine is fairly simple; with the fresh air being forced by the compressor of the turbocharger into a large plenum chamber which feeds each of the four engine cylinders. A simple 4-2-1 manifold is used to collect the exhaust gases, which then pass through the turbine before being vented to atmosphere through a simple exhaust. All the required information for valve-lifts and flow coefficients for the engine were provided by Perkins and incorporated into the model.

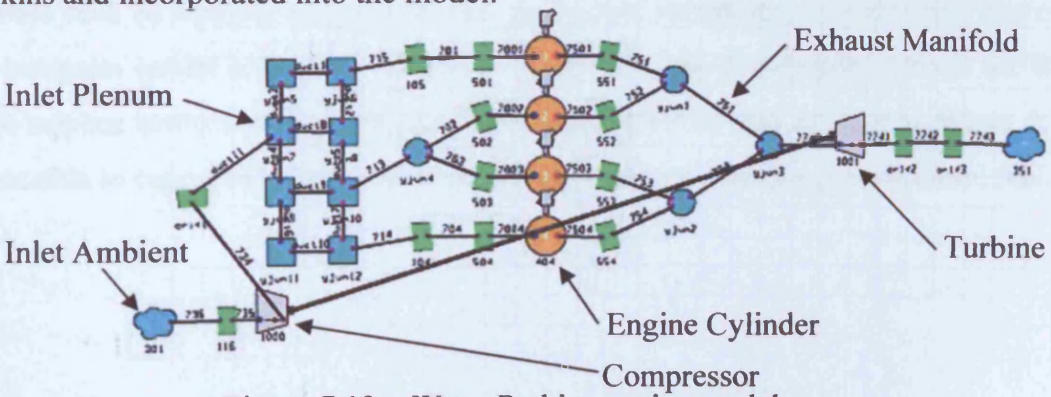

Figure 7.13 – Wave Perkins engine model

Using information provided by Perkins and Garrett, the turbine and compressor maps were constructed for the TA3123 turbocharger unit installed on the Perkins 1004-4T engine. The compressor and turbine maps generated by the TCMAP software are shown in Figure 7.14.

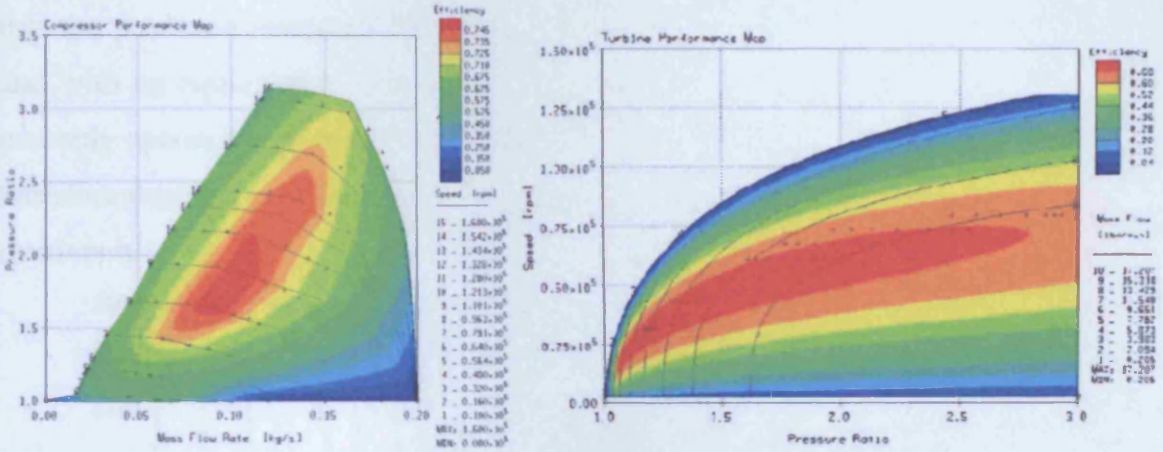

Figure 7.14 – Perkins turbocharger maps

The completed Perkins engine model is capable of predicting the performance of the actual test engine, therefore allowing changes in geometry of future exhaust and inlet modifications to be tested without the need for time consuming dynamometer testing.

The results of computer models such as Wave can be very helpful when investigations into the effect of significant engine modifications are to be carried out. However, the method by which Wave models the combustion of diesel fuels (while allowing for predictions of NO_X and CO emissions) does not take into account the effects of fuel impurities such as sulphur on gaseous and particulate emissions, and therefore the use of the computer model is limited when fuel effects are to be investigated. Due to the fact that the sulphur content of a diesel fuel is not a factor taken into account by Wave, it is only possible to carry out a generalised diesel fuel analysis, using a generic diesel fuel.

7.4.2 Diesel Engine Results

Figure 7.15 displays the predicted variation in power output of the Perkins 1004-4T diesel engine with equivalence ratio and engine speed. It can be seen from Figure 7.15 that the predicted maximum power occurs with an approximate speed of 2350 RPM, and with an equivalence ratio of about 0.72. In reality however, the Perkins engine probably operates with much lower equivalence ratios (leaner air to fuel mixtures). This therefore explains how the rated power of the engine is lower than the Wave predicted maximum.

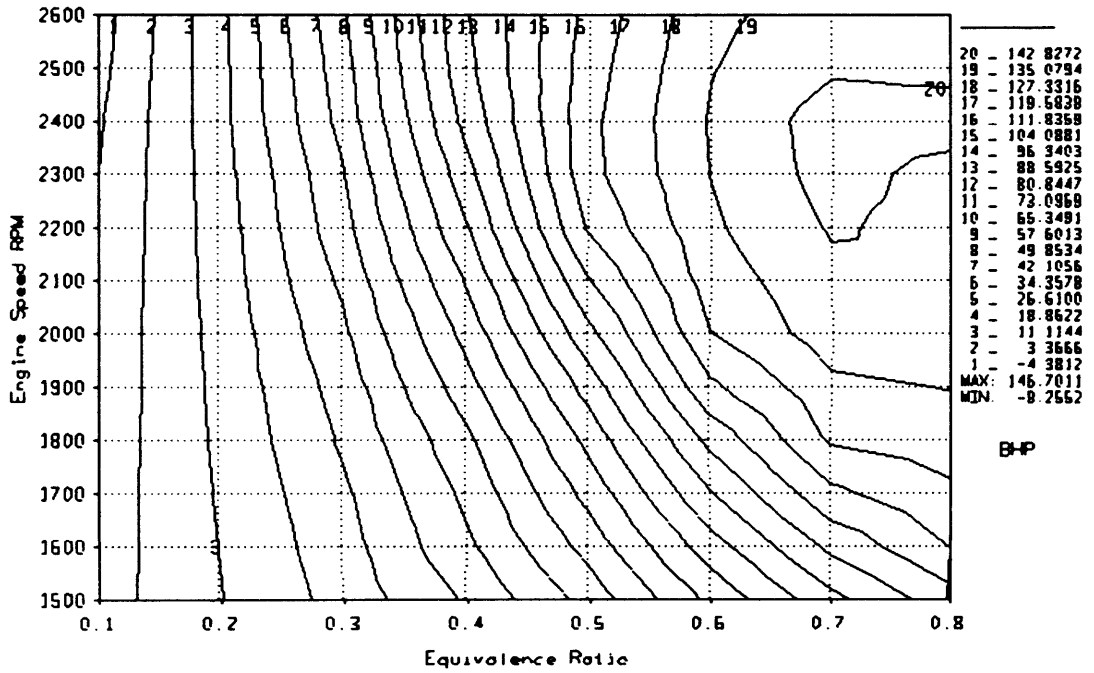

Figure 7.15 – Predicted BHP variation

Appendix M contains the predicted variation in brake efficiency, torque, fuel consumption, carbon monoxide emission, hydrocarbon emission and NO_X emission with equivalence ratio and engine speed. Using the output values from the Wave simulation a comparison can be made between the measured values for both the ultra low sulphur commercial diesel fuel, the agricultural red diesel (class A2 fuel oil) and the predicted values from the Wave software for a generic diesel fuel simulation. Table 7.6 displays a comparison of the measured values from dynamometer testing and the predicted values from the Wave computer model.

Table 7.6 – Dyno test and Wave software comparison

Case Number	1	2	3	4	5	6	7
Dyno Test Fuel	Commercial Ultra Low Sulphur Diesel Fuel						
Power (BHP)	35.58	99.27	97.27	101.29	104.37	101.50	105.90
Torque (Nm)	126.68	336.61	288.61	327.85	297.28	314.23	290.04
Fuel Flow rate (kg/hr)	8.43	17.95	18.85	18.63	20.07	18.81	20.27
NO_X Emissions (PPM)	275	1537	1146	1408	1066	1449	1058
PM Mass (mg/litre)	-	0.0502	-	-	-	-	-
Dyno Test Fuel	Agricultural Red Diesel (class A2 fuel oil)						
Power (BHP)	33.07	97.49	91.27	97.94	104.30	100.63	106.15
Torque (Nm)	117.74	330.58	270.80	317.00	297.07	311.56	290.74
Fuel Flow rate (kg/hr)	7.18	18.21	18.27	19.05	21.64	19.78	22.36
NO_X Emissions (PPM)	346	1646	1023	1818	1572	1411	1510
PM Mass (mg/litre)	-	0.0536	-	-	-	-	-
Wave Simulation Results							
Power (BHP)	33.71	97.64	94.37	98.84	104.25	100.76	105.92
Torque (Nm)	120.0	331.0	280.0	320.0	297.0	312.0	290.0
Brake Efficiency (%)	31.38	37.03	34.67	36.35	34.00	35.65	33.13
Fuel Flow rate (kg/hr)	6.72	16.50	17.04	17.00	19.21	17.67	20.03
NO_X Emissions (PPM)	1192	2072	1967	2050	2065	2055	2076
HC Emission (kg/hr)	3.23	7.80	8.04	8.04	9.06	8.35	9.43

From the results shown in Table 7.6 it can be seen that the predicted fuel flow rates to achieve comparable torque and power figures are lower than the values measured during the testing of the engine for both diesel fuels. In addition to this, it can be seen that the predicted levels of NO_X are far higher than the measured values; this indicates that the method in which the combustion process is initiated and simulated in the engine model is possibly causing higher cylinder temperatures than actually occur in the engine.

It can be seen from the results obtained from the Wave engine model of the Perkins diesel engine, that computer simulations can provide an alternative method to practical testing to investigate the changes that occur in engine behaviour. However, physical

engine testing is required to validate engine model results and provide detailed information to allow model improvements to be made for future investigations.

7.5 Summary

An engine test-bed facility was commissioned and used to investigate the emissions and performance of a 4-cylinder turbocharged diesel engine manufactured by Perkins. The gaseous and particulate emissions of the engine were measured for both a commercially available low sulphur diesel fuel and a Class A2 rebated heavy oil (red diesel).

It was found that the corrected torque values were higher when the engine was fuelled with the low sulphur diesel fuel; this was attributed to the low sulphur diesel fuel having a higher heating value than the red diesel fuel. From comparing the measurements made of the exhaust gases for both of the fuels, it was found that the red diesel fuel produced higher values of CO_2 and NO_X as well as producing a higher mass concentration of exhaust particulates.

A computer model of the Perkins diesel engine was constructed, the predictions of which were compared to the measured values obtained from the test-bed investigation. The computer model simulated the behaviour of the Perkins diesel engine with a reasonable degree of accuracy. However, the limitations of the Wave software with regards to simulating combustion were highlighted, primarily due to the software's inability to take into account the effect of fuel sulphur content on emissions.

8 Biodiesel Engine Performance

The use of biomass derived liquid fuels in internal combustion engines is not a new notion. Indeed, many of the first internal combustion engines were capable of running on a wide variety of liquid fuels. The use of biomass derived alcohols as an alternative to petrol is a fairly common occurrence world wide, and a great deal of research is being carried out searching for the diesel equivalent.

Biomass derived fuels for compression ignition engines vary widely in chemical properties, manufacture and performance. However, it is the methyl esters of vegetable oils that have shown the greatest compatibility with modern compression ignition engines. Here, a range of biodiesel blends is assessed in terms of mechanical performance and emissions. Both simulation and new data are presented and compared for the Perkins engine described in Chapter 7, with particular attention being paid to measurement and characterisation of particulate matter. From the combined set of results, conclusions are drawn concerning the potential of biodiesel utilisation

8.1 Performance and Emissions of Biodiesel

The phrase 'Biodiesel' refers to the methyl esters of many different vegetable oils, the most common being rapeseed methyl ester and sunflower seed methyl ester. Methyl esters have significantly better fuel properties than the raw (biomass derived) oils due to reductions in viscosity and density and improved stability. Altin et al. (2001) showed that the esterification of vegetable oils such as sunflower and soybean improved the torque and reduced fuel consumption compared to the raw oils; however emissions of CO_2 and NO_X increased with esterification while CO and smoke emissions were reduced.

Lapuerta et al. (2003) showed that for increasing concentrations of sunflower seed methyl ester and cardoon methyl ester a decrease in brake mean effective pressure and insoluble particulates emission occurred. The reduction in emissions was attributed to

the additional oxygen content of the biodiesel as well as the reduction in aromatic and sulphur content.

From the research carried out by Monyem et al. (2001) and Carraretto et al. (2004) it was concluded that an increasing content of biodiesel in No. 2 diesel fuel reduced the particulate matter, total hydrocarbon and CO emissions while increasing the NO_X emissions. The work by Monyem et al. (2001) also showed that the oxidization of biodiesel had no detrimental effects on performance or emissions. Schumacher et al. (1996) while finding similar results also found that a delay in the injection timing when using biodiesel was beneficial, as it reduced the NO_X emissions while still retaining the reductions in other emissions (this was shown to be due to a reduction in peak cylinder pressures). Kalligeros et al. (2003) found that for a large single cylinder diesel engine the substitution of diesel fuel with sunflower oil methyl ester or olive oil methyl ester decreased the particulate matter, CO, NO_X and hydrocarbon emissions, the only drawback was a slight increase in fuel consumption.

Çetinkaya et al. (2005) compared the performance of used cooking oil derived biodiesel to that of No. 2 diesel fuel. The comparison showed a significant reduction in torque (compared to that for diesel fuel) throughout the speed range of the engine when the engine was fuelled with biodiesel. The fuel consumption per engine stroke was comparable between the two fuels while the exhaust gas temperature was significantly lower with biodiesel. The work carried out by Çetinkaya et al. (2005) also highlighted possible problems with injector carbonization and clogging of the catalytic converter when biodiesel is used.

It can be seen from the changes made to the standards for diesel fuel (BS EN 590:2004) and agricultural/industrial fuel oils (BS 2869:2006) that biomass derived fuel for diesel engines are set to become an increasingly important resource in the future. At present up to 5% by volume of Fatty Acid Methyl Ester (FAME) conforming to the appropriate standard (BS EN 14214:2003) is allowed in both commercial diesel fuel and non-highway fuel oils. However, in the future, it is reasonable to assume that this proportion will increase as vehicle manufacturers approve the use of higher percentage mixtures.

8.2 Biodiesel Manufacture

The base catalyzed transesterification method of biodiesel production is the most widely used today, due to high relative yields and the good economics of the process. The transesterification process involves the reaction of triglycerides (vegetable or animal fats and oils) with an alcohol in the presence of a catalyst (usually a strong alkaline) to form esters (biodiesel) and glycerol. The process for the conversion of vegetable oils into biodiesel is illustrated in Figure 8.1.

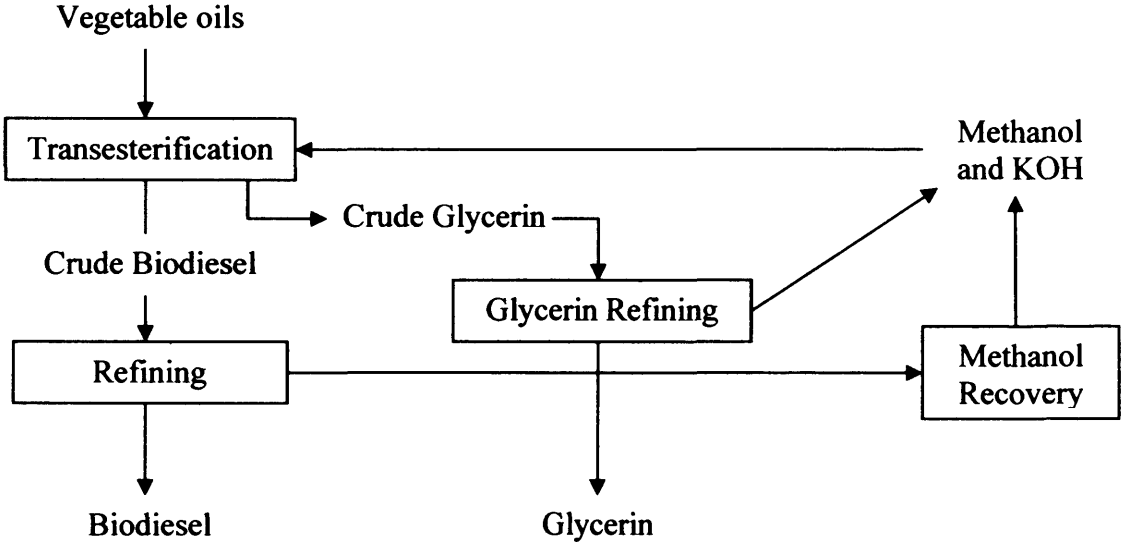

Figure 8.1 - Biodiesel production

Further details of biodiesel production methods are described by Demirbaş (2003), Alcantara et al. (2000), Bozbas (in print, 2006), Cvengroš and Považanec (1996) and Cvengroš and Cvengrošová (2004). The basic method of biodiesel production involves several separate stages, the first stage being the preparation of the oil through filtration, washing and drying. The cleaned and filtered oil is then added to a mixture of alcohol and catalyst (typically methanol and potassium hydroxide). The mixture is then heated to speed up the transesterification reaction. The crude glycerine (which is of much higher density than the biodiesel) is separated out, and then refined to remove un-reacted alcohol and unused catalyst. The biodiesel fraction is also refined to remove excess alcohol and is then sometimes washed and dried before being stored.

8.3 Engine Model Predictions

The construction of the Wave engine model of the Perkins 1004-4T Cardiff diesel test is described in section 7.4. Various blends of a widely available ultra low sulphur diesel fuel and used cooking oil originated biodiesel are to be tested to characterize the performance variations and emissions. The biodiesel to be used is manufactured by Sundance Renewables, and meets the ASTM B100 and BS EN 14214:2003 biodiesel standards. The fuel's exact chemical makeup is unknown but the used oils from which it is produced are mainly of the sunflower seed and rapeseed type.

8.3.1 Fuel Properties

The Wave engine model requires detailed chemical and physical information of the fuels to be used. Table 8.1 compares the properties of the ultra low sulphur diesel fuel to values for a B100 FAME biodiesel.

Table 8.1 – No. 2 Diesel and Biodiesel fuel properties

	No. 2 Diesel Fuel	Biodiesel Fuel
Density at 15°C kg/m^3	820 - 845	860 - 900
Specific heat J/kg/K	1675	2030
Viscosity at 40°C mm^2/s	2.0 – 4.5	3.5 – 5.0
Heat of Vaporization J/kg	-220000	-197000
Lower Heat Value MJ/kg	42.80	37.39
Composition C	15.0	19.5
H	25.05	36.4
O	0	2.35
Sulphur Content PPM	< 50	< 10
Cetane Number	> 51	> 51

Examinations of the properties of diesel and biodiesel shown in Table 8.1 show that the two fuels have similar heating values and liquid properties. There is a significant difference in chemical composition, with the biodiesel on average being made up of larger hydrocarbon molecules containing some oxygen. From the references in literature, the values of the Cetane number for both commercial diesel fuels and biodiesel fuels vary considerably, probably due to global differences in manufacturing However, in general the Cetane numbers for the two fuels are very similar.

From data presented by Yuan et al (2003) and Maxwell (1951) the variation of specific heat capacity, vapour pressure, viscosity and surface tension with temperature are shown in Figure 8.2 for both the commercial low sulphur diesel fuel and the B100 biodiesel - these values are also required by the Wave software.

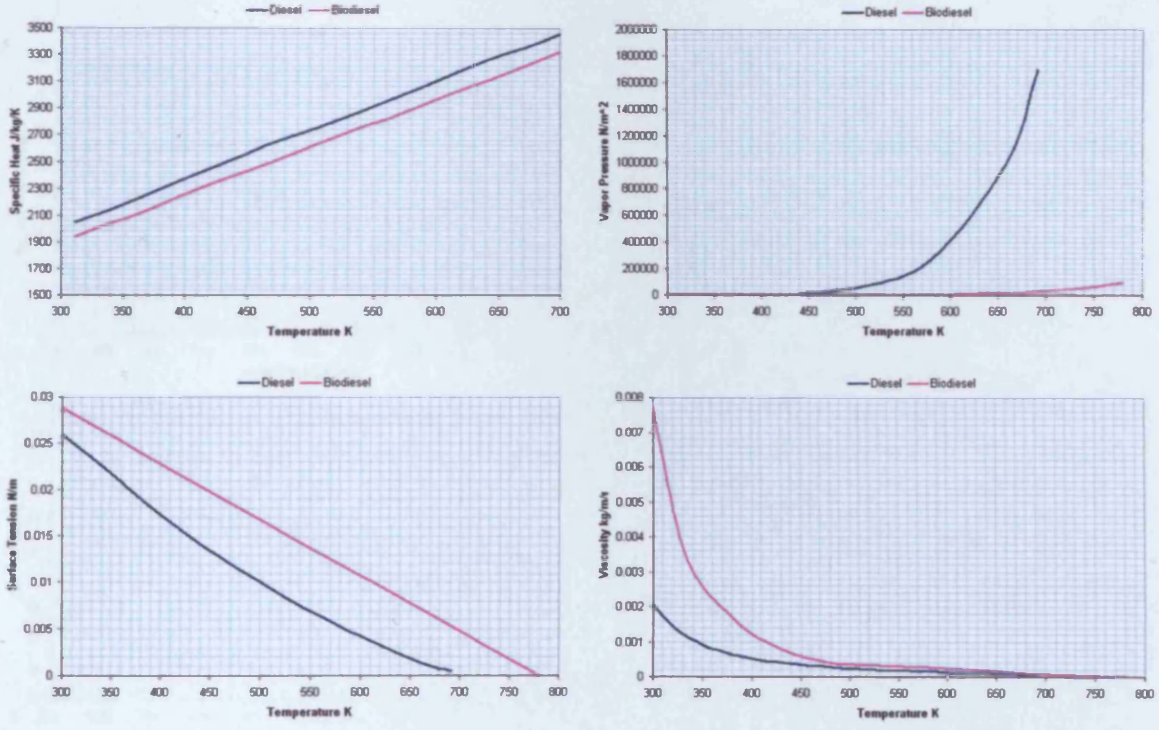

Figure 8.2 – Variation of physical properties of No. 2 Diesel and B100 Biodiesel fuels

From Figure 8.2, the variation in the specific heat capacity of diesel and biodiesel with temperature can be seen to be very similar. However, the viscosity of the biodiesel fuel at low temperatures is significantly higher than that for diesel fuel. There also seems to

be marked differences in the variation of vapour pressure and surface tension with temperature for the two fuels.

Figure 8.3 illustrates the variation in fuel properties of different blends of biodiesel in low sulphur diesel fuel.

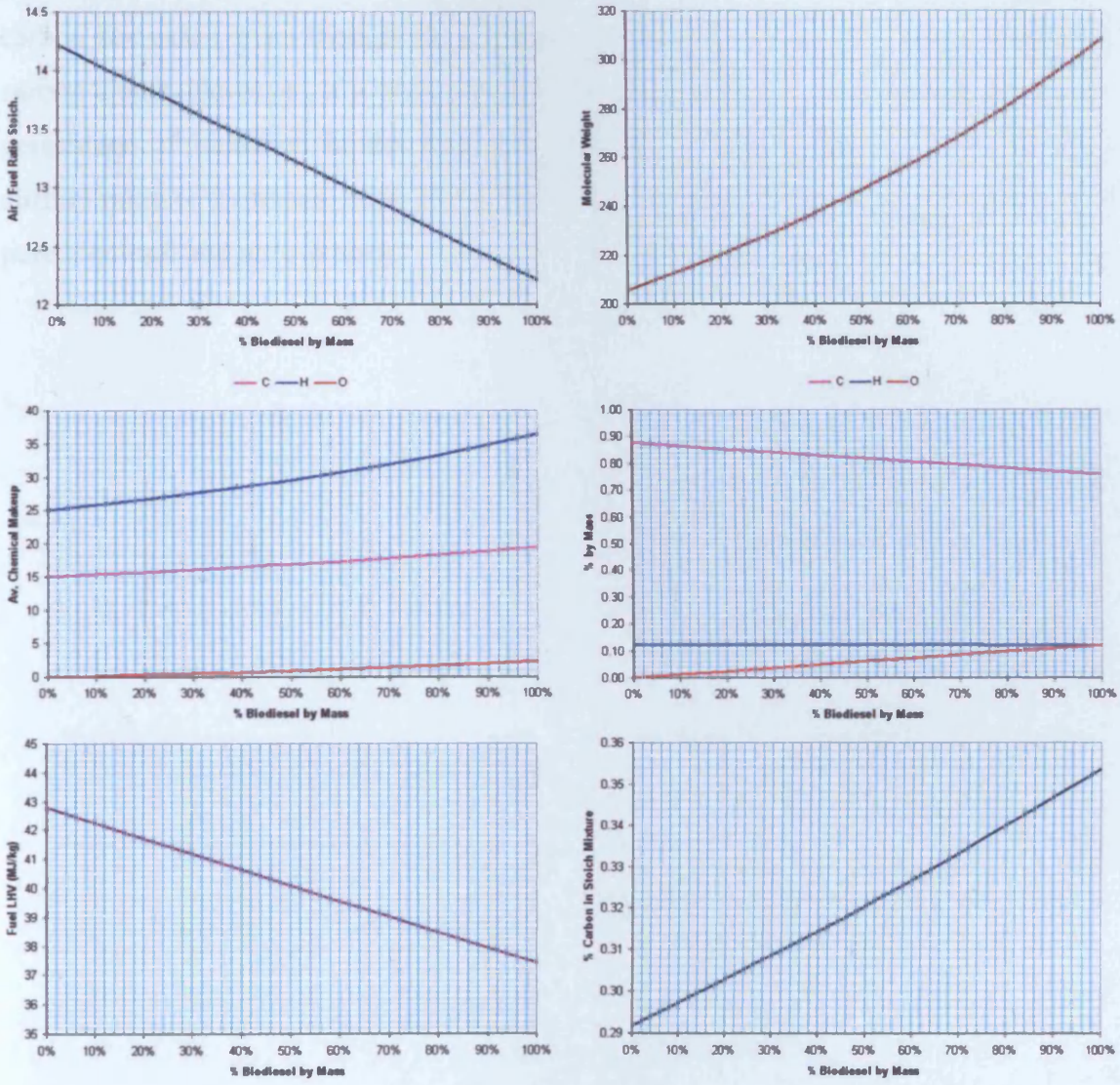

Figure 8.3 – Biodiesel blend properties

The effect of the oxygen content in the biodiesel becomes apparent when the change in stoichiometric air / fuel ratio with percentage biodiesel by mass (shown in Figure 8.3) is examined. As the percentage of biodiesel in the fuel mixture increases the air required

for combustion decreases; pure low sulphur diesel fuel requires an air / fuel ratio of 14.22:1, while pure biodiesel only requires an air / fuel ratio of 12.21:1.

Figure 8.3 also shows how the molecular weight of the fuel increases and the lower heat value decreases as the percentage by mass of biodiesel increases. As the biodiesel percentage of the fuel mixture increases, the percentage by mass of the fuel that is carbon decreases, even though the average fuel molecule contains a higher number of carbon atoms. However, if a stoichiometric mixture of fuel and air is considered; as the percentage of biodiesel in the fuel increases, the total percentage of carbon in the air/fuel mixture increases from 29 % (for a pure diesel and air mixture) to 35% (for a pure biodiesel and air mixture).

8.3.2 Engine Model Results

Using fuel files generated for mixtures of the low sulphur diesel and biodiesel fuels, simulations were carried out with engine speeds ranging from 1500 – 2600 RPM, and equivalence ratios between 0.1 and 0.8.

Figures 8.4 – 8.7 show how the brake torque, fuel economy, CO and NO_X vary with biodiesel percentage and equivalence ratios at an engine speed of 2600 RPM. As expected for the Perkins diesel engine, Figure 8.4 shows that the torque values increase as the equivalence ratios near 0.8. It can also be seen from the Wave predictions that for the same equivalence ratio, the torque values are slightly higher for diesel / biodiesel fuel mixtures containing between 25 % and 50 % biodiesel. There are however some anomalous results for diesel / biodiesel fuel mixtures containing around 75 % biodiesel by volume, with the torque predicted at high equivalence ratios being lower than that for fuel mixtures with both more and less biodiesel content. This may be due to the inlet or exhaust system of the engine not being 'tuned' for the precise flow rates and velocities of the inlet air / exhaust gases that occur at these operating points.

What can be determined from the results shown in Figure 8.4 is that torque is only marginally affected by biodiesel content, as long as the overall equivalence ratio remains constant. This reveals that the total energy content of the diesel and biodiesel fuel charges (i.e. mixture of fuel and air within engine cylinder prior to ignition) are similar even though the energy content of the biodiesel fuel is significantly lower than that of the diesel fuel.

An examination of the results shown in Figure 8.5 reveals that in order to keep the same equivalence ratios (and therefore similar power outputs), a higher fuel flow rate is required as the biodiesel content increases. From this it can be determined for the use of biodiesel in an actual running engine, unless modifications are made to the fuel pump settings to increase fuel flow rate, the power developed is likely to decrease.

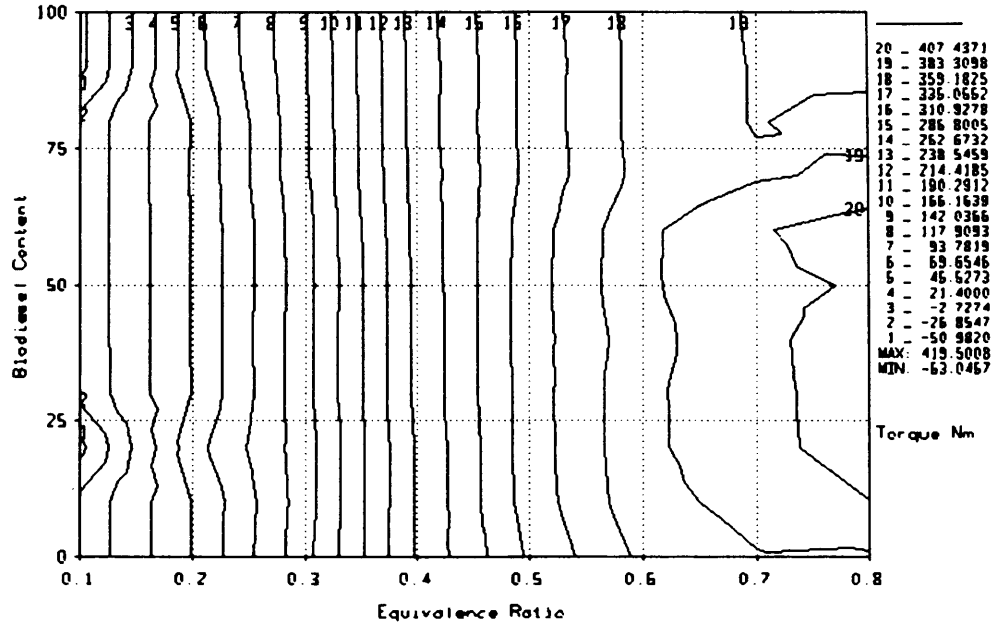

Figure 8.4 – Variation of brake torque with biodiesel percentage

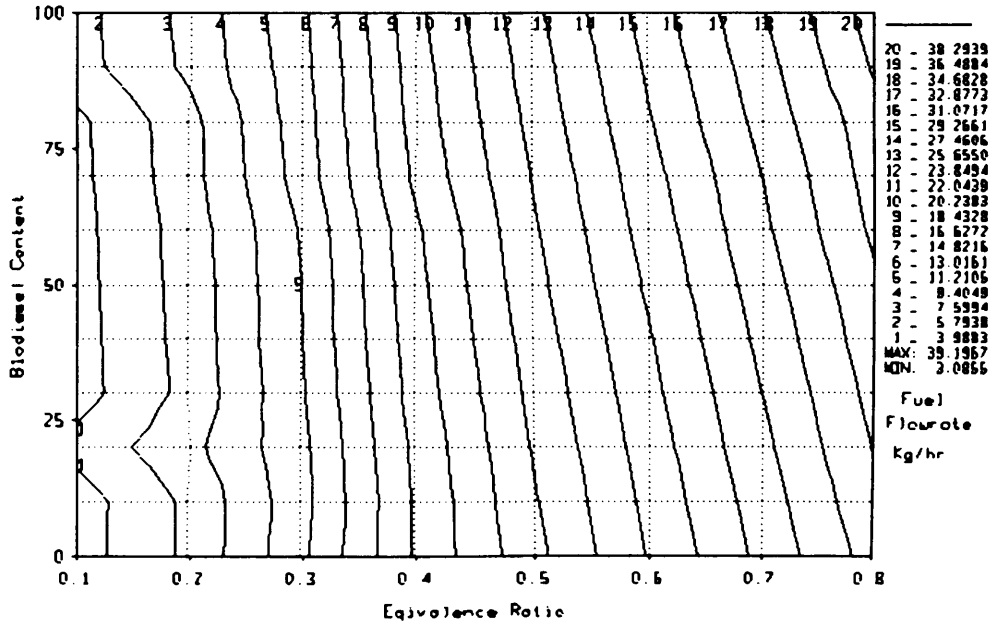

Figure 8.5 – Variation of fuel economy with biodiesel percentage

The variation in the predicted emission of CO with the equivalence ratio and biodiesel content is shown in Figure 8.6. There is very little variation in the amount of CO emitted with the percentage of biodiesel in the fuel mixture. Even though there is a much higher percentage carbon in the air fuel mixture for the biodiesel fuel than the diesel fuel, this has not caused an increase in the amount of carbon emitted as carbon

monoxide. For air-fuel mixtures closer to stoichiometric conditions, the emission of carbon monoxide may be higher for the biodiesel fuel than the diesel fuel, but as diesel engines predominantly operate with large amounts of excess air this is unlikely to be seen in an actual running engine.

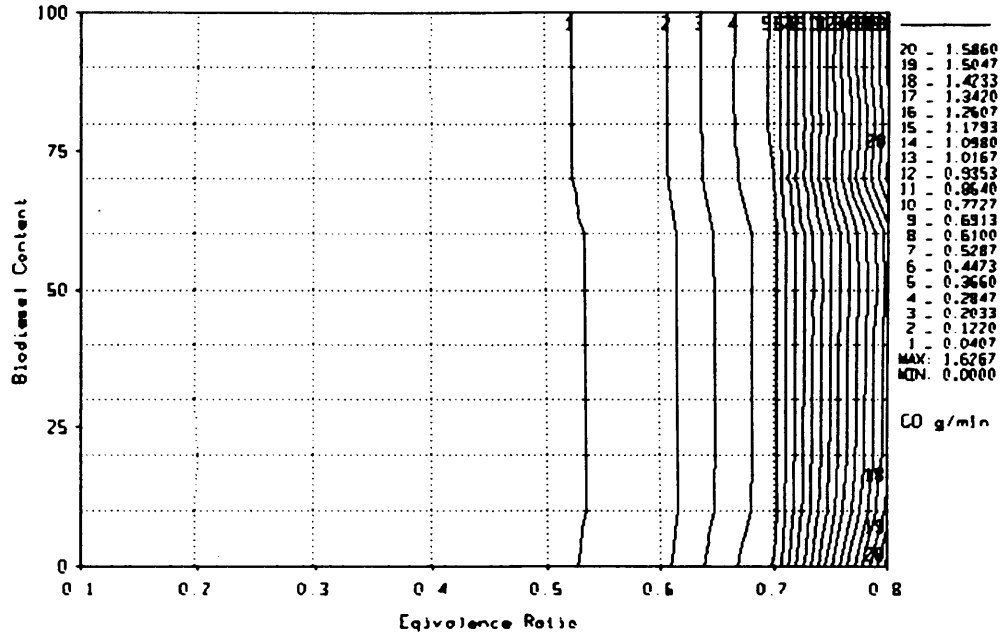

Figure 8.6 – Variation of CO emissions with biodiesel percentage

Figure 8.7 displays the predicted emission of NO_X with increasing content of biodiesel. It can be seen from Figure 8.7 that for higher percentage diesel fuel mixtures are predicted to produce more NO_X than the fuel mixtures composed mainly of biodiesel. However, it should be noted that the simulated injection timing in the computer model is not varied for increasing biodiesel fuel content, whereas the different fuel properties of biodiesel fuel to diesel fuel can lead to significantly different injection characteristics. In an actual engine this affects the injection timing and thus the combustion of the fuel. As the production of NO_X is directly linked to combustion timing, further computer model refinements are required if investigations into NO_X emissions are to be carried out.

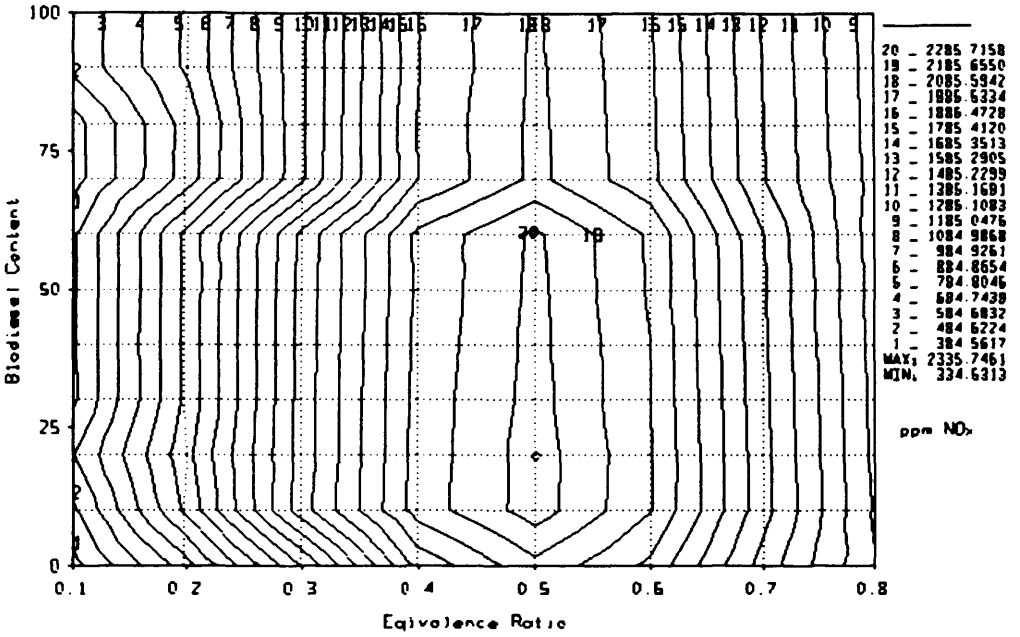

Figure 8.7 – Variation of NO_X emissions with biodiesel percentage

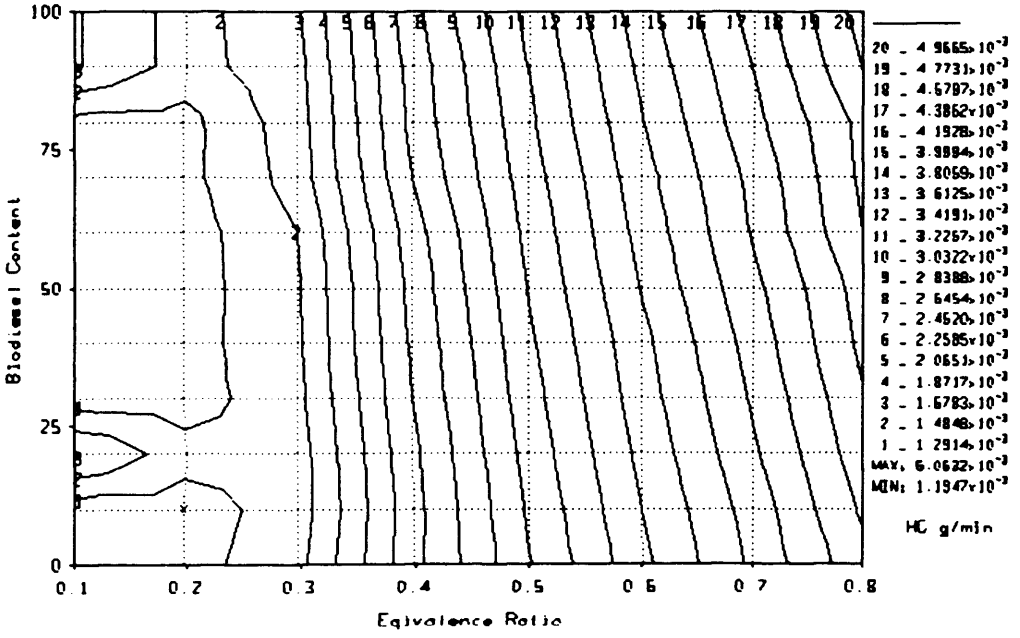

Figure 8.8 – Variation of predicted HC with biodiesel percentage

The variation in emission of unburned hydrocarbon with biodiesel content and equivalence ratio is shown in Figure 8.8. It can be seen that as the percentage of biodiesel increases, the predicted amount of unburned hydrocarbons in the exhaust increases. This is likely to be due to the reduction in the stoichiometric air/fuel ratio for mixtures of increasing biodiesel content.

8.4 Engine Testing

After the promising results of the computer simulations, the Perkins 1004-4T engine testing facility described in Chapter 7 has been utilised to consolidate the appraisal of the benefits of using biodiesel fuel blends. The fuels and fuel blends to be tested are a pure commercial ultra low sulphur diesel fuel, blends of 10%, 30% and 50% B100 by mass with No. 2 low sulphur diesel fuel and the pure B100 biodiesel fuel. Figure 8.9 shows samples of each of the fuels and fuel blends.

No. 2 Diesel Fuel 10% Biodiesel 30% Biodiesel 50% Biodiesel B100 Biodiesel

Figure 8.9 – Biodiesel and diesel fuels and blends

Figure 8.9 shows the dramatic difference in colour and transparency between the pure commercial ultra low sulphur diesel fuel, various blends of low sulphur diesel fuel and B100 biodiesel and the pure B100 biodiesel fuel.

As the percentage of biodiesel in the low sulphur diesel fuel increases, in addition to the predicted change in properties shown in Figures 8.2 and 8.3, there are other noticeable changes in the viscosity (when it is being poured) and odour of the fuel. The biodiesel has a noticeably sweet odour compared to the distinctive sharpness of the low sulphur diesel fuel.

Each of the fuels were mixed immediately prior to being used, and were thoroughly shaken to prevent separation.

8.4.1 Dynamometer Results

The same testing procedure that was used for the diesel engine tests (Chapter 7) was used to test the three blends of low-sulphur-diesel / biodiesel and the pure B100 biodiesel fuel. For each of the fuels a series of load-speed curves were obtained for different throttle (fuel pump) settings. The seven operating test points previously used were again chosen to measure the fuel consumption and emissions of the engine. For the point corresponding to case 3 (80% throttle, 2100 RPM), the particulate matter mass measurements were again made and samples taken for examination by electron microscope - details of the seven tested operating points are shown in Table 7.5. In addition, a Cambustion DMS500 particle sizer was used to analyse the particulate aerosol for the low sulphur diesel fuel and B100 biodiesel at the operating conditions specified by case 3. The results obtained from the testing of the exhaust gases using contemporary on-line PM analysis methodology can be compared with that obtained from the arguably more rigorous – though more time intensive – offline analysis technique.

All engine tests were again carried out in accordance to the EEC standard 80/1269 with the reference atmospheric conditions of 298 K and 99kPa (dry pressure). During the testing period, the actual atmospheric conditions were between the required limits, 283 $K \leq T \leq 313$ K and 80 kPa $\leq p_s \leq$ 110 kPa. The temperature of the laboratory was carefully monitored and recorded during each testing period, allowing correction factors to be calculated for each batch of tests. Approximate fuel flow-rates were calculated using a digital scale by measuring the mass of fuel used over a prolonged period of time, for each of the individual engine operating positions.

A Testo 350 XL portable gas analyser was used to monitor the exhaust gases from the diesel engine flow, sampling the exhaust gases from a cabinet of 0.38 cubic metres volume. Particulate measurements were taken for each of the fuel blends from the same cabinet using the sampling equipment shown in Figure 7.7. The DMS500 equipment sampled the exhaust gases from an orifice placed directly after the turbocharger exit, with the exhaust gases being diluted to appropriate levels within the instrument.

Figure 8.10 shows the corrected torque produced by the Perkins diesel engine at the seven operating test points for each of the fuels being compared. It can quite clearly be seen that the low sulphur diesel fuel produces the most torque, and the pure B100 biodiesel fuel produces the least torque. A general trend can also be seen in which there is a gradual decrease in corrected torque developed by the engine as the percentage of biodiesel in the fuel mixture increases.

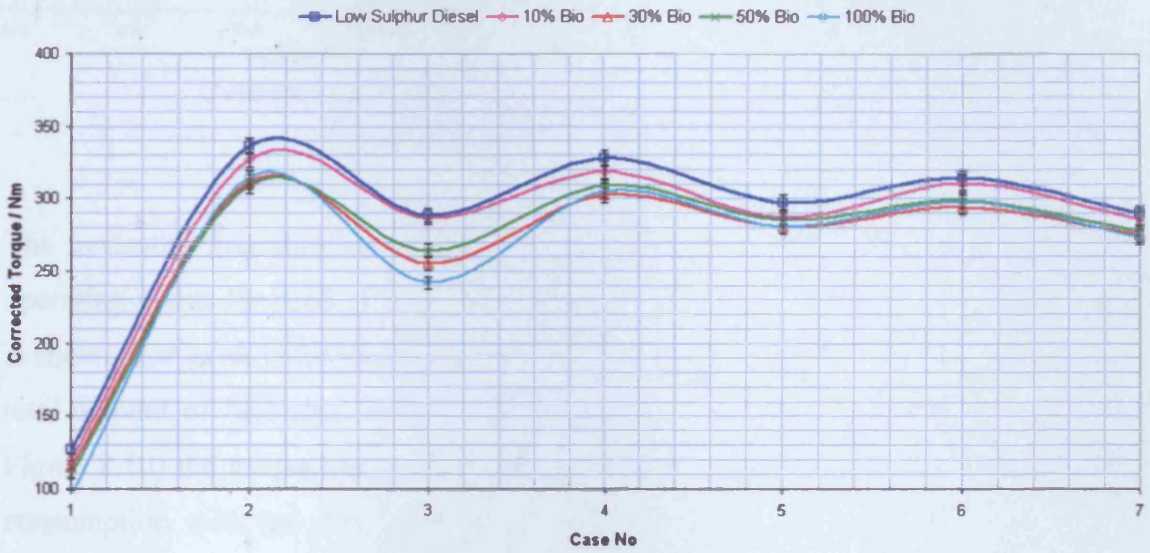

Figure 8.10 – Measured torque outputs for Diesel / Biodiesel blends

Comparing the sets of results displayed in Figure 8.11 (results published by Carraretto et al. (2004) and results obtained from tests at Cardiff), it can be seen that in both cases the torque developed by an engine decreases with the increase in concentration of biodiesel in the commercial diesel fuel. The Cardiff results shown in Figure 8.11 are for an 80% throttle setting, but as for all the results obtained using the Perkins engine, a very flat torque curve can be seen between 1800 and 2300 RPM. This is likely to be caused by the use of a turbocharger with no waste gate. The results shown for the investigation carried out by Carraretto et al. (2004) exhibit the typical characteristics of a naturally aspirated engine, with the torque curve exhibiting a definite peak torque value. The results shown in Figures 8.10 and 8.11 indicate that the addition of the waste vegetable oil derived biodiesel to diesel fuel reduces the resultant torque produced by an engine. These results agree with a large proportion of results in published literature.

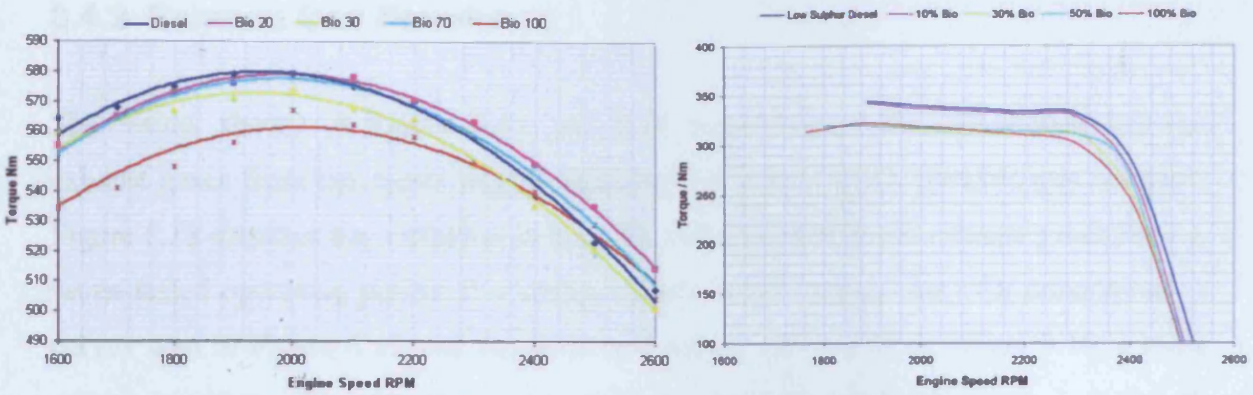

Carraretto et al. (2004) Cardiff Tests

Figure 8.11 – Torque curve comparison

The measured fuel flow rate for the Perkins engine operating at the seven different operating points for each of the aforementioned fuel blends in shown in Figure 8.12. It is shown that as an increasing concentration of biodiesel is used in the fuel mixture, the total amount of fuel used by the engine increases, even though (as can be seen from Figure 8.10) the torque produced by the engine decreases. The increase in overall fuel consumption with the percentage of biodiesel in the fuel seen here agrees with the trends reported in the literature.

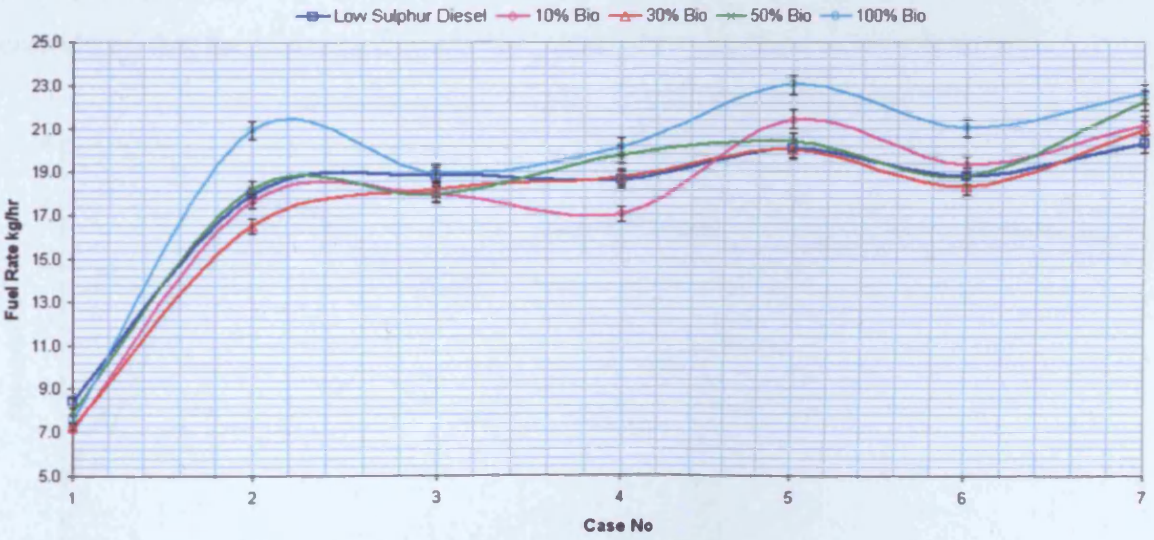

Figure 8.12 – Measured fuel flow rate comparison

8.4.2 Exhaust Gas Results

The results shown in Figure 8.13 and 8.14 were obtained through monitoring the exhaust gases from the diesel engine utilising the Testo 350 XL portable gas analyser. Figure 8.13 displays the variation in the CO_2 concentration in the exhaust gases for the seven tested operating points. If a comparison is made between the CO_2 concentration curves seen in Figure 8.13 and the corrected torque curves seen in Figure 8.10, a clear pattern emerges. The operating points with higher load conditions (cases 2, 4 and 6) produce the highest concentration of CO_2 in the exhaust gases, indicating that when running at these settings the engine may be using a higher equivalence ratio (richer air/fuel mixture).

It can also be seen that the increase in biodiesel concentration, while reducing torque, increases the amount of CO_2 produced. The most likely reason for this increase in exhaust CO_2 concentration can be seen from Figure 8.3, in which the percentage carbon in the air/fuel mixture increases significantly as the percentage of biodiesel in the fuel increases; this leads to an increase in production of exhaust CO_2, even if 'perfect' combustion is achieved. However, when interpreting the exhaust CO_2 results, it must be considered that the biomass derived biodiesel fuel is regarded as carbon neutral.

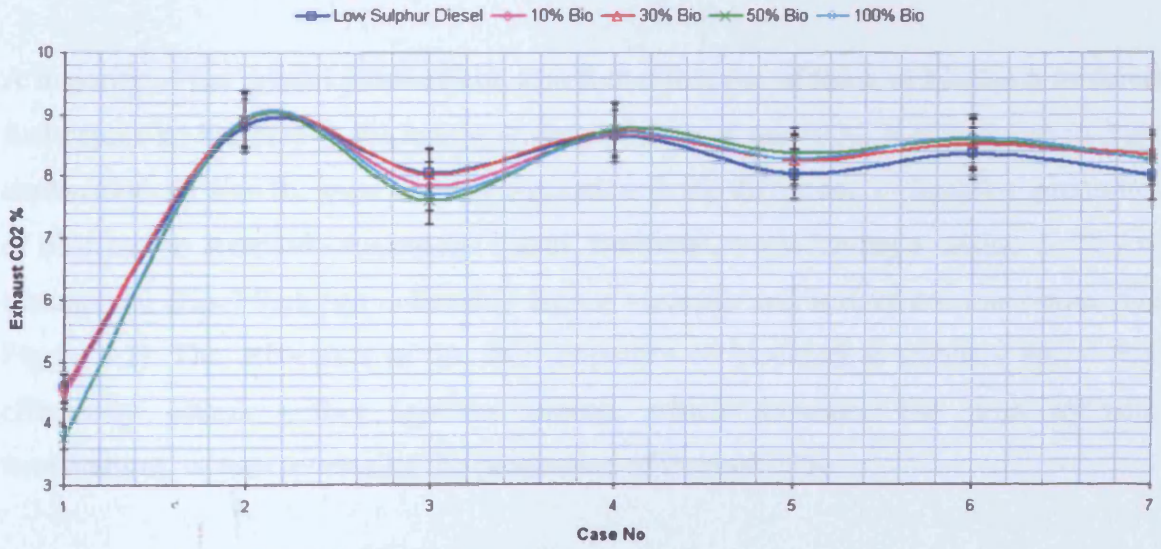

Figure 8.13 – Measured exhaust CO_2 concentration

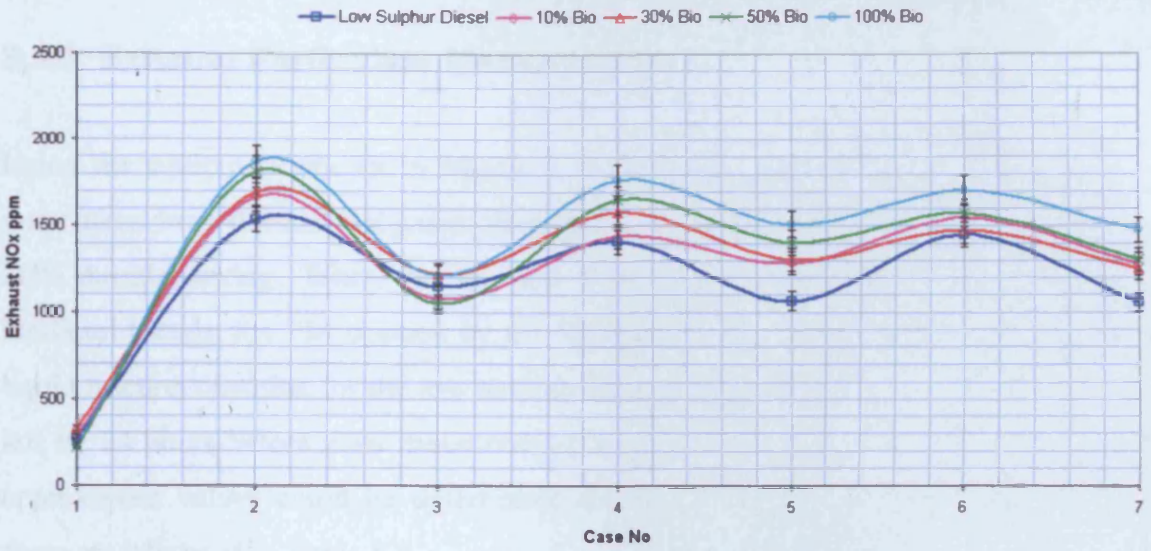

Figure 8.14 – NO_X exhaust gas concentration

The measured exhaust gas NO_X concentration for the seven test cases is shown in Figure 8.14. It can again be seen that at the higher loaded operating points, the concentration of the pollutant in the exhaust gases increases. The production of NO_X is predominantly linked to high cylinder temperatures, and at high load conditions more fuel is required, which releases more energy during the combustion process. An examination of the effect of biodiesel concentration on the production of NO_X reveals that higher concentrations of NO_X are present in the exhaust gases of fuels containing a higher biodiesel percentage.

A majority of the related publications also found that the addition of biodiesel to diesel fuel causes an increase in the concentration of exhaust gas NO_X. It is believed that the explanation for this increase in NO_X formation is the difference in injection properties of biodiesel to standard commercial diesel. Biodiesel, while having a similar density to commercial diesel fuel, has noticeably higher viscosity and surface tension values (see Figure 8.2). The difference in the fuel properties of biodiesel to standard diesel fuel effectively causes earlier ignition timing, which increases the peak cylinder temperatures, in turn increasing the production of thermal NO_X.

8.4.3 Exhaust Particulate Measurement

Using the equipment shown in Figure 7.7, particulate samples for each fuel mixture were taken from the exhaust gases when the engine was running at 2100 RPM with an 80% throttle setting. When the samples were taken from the exhaust gases of the biodiesel blends, the PM trapped by the filter papers was noticeably of a much higher liquid fraction than that for the low sulphur diesel fuel, and due to this the samples were left for 24 hours before mass measurements were taken. From the measurements taken, approximate values could be determined for the particulate mass concentrations and these are tabulated in Table 8.2.

Table 8.2 – PM mass measurement comparison

Fuel Blend	Low Sulphur Diesel	10% Biodiesel	30% Biodiesel	50% Biodiesel	100% Biodiesel
Exhaust PM Concentration mg/litre	0.1169 ± 0.0086	0.0836 ± 0.0062	0.0902 ± 0.0067	0.0902 ± 0.0067	0.0636 ± 0.0047

From the data presented in Table 8.2 it can be determined that an engine will produce a greater global *mass* of particulate matter when running commercial low sulphur diesel fuel than would be produced if a pure biodiesel fuel were used. It can also be seen that adding biodiesel fuel to a commercial low sulphur diesel can significantly reduce the mass concentration of particulate matter in the exhaust gases.

In Figure 8.15 a display of the PM filter paper samples can be seen for the ultra low sulphur diesel fuel, the pure biodiesel and each of the biodiesel / diesel blends tested. It can be seen from a comparison of the filter paper samples that whereas the low sulphur diesel fuel mass PM samples mainly contains black carbonaceous material, the sample taken from the exhaust of the pure biodiesel fuel is composed mainly of a liquid aerosol. As the proportion of the biodiesel in the fuel mixture increase the PM samples also

noticeably lighten in colour, indicating that the PM samples contain a lower percentage of soot.

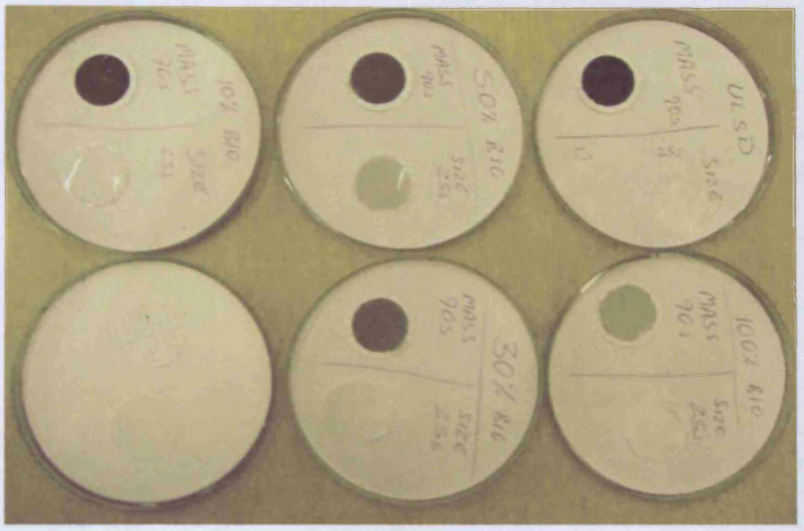

Figure 8.15 – Biodiesel and Diesel blends PM samples

In a series of studies carried out by Lapuerta et al. (2003 and 2004) and Durán et al. (2004) links were made between the sulphur content and aromatic content of fuels and the tendency of soot particles to agglomerate to form larger particles. Since biodiesel has a very low sulphur and aromatic content, a larger percentage of the soot particles formed during combustion are oxidized by the excess air reducing the number of particles emitted.

Figure 8.16 compares electron microscopy images of the particulate matter samples obtained from the exhaust of the Perkins diesel engine for the pure ultra low sulphur diesel and biodiesel fuels. The images are taken at 26,000 and 235,000 times magnification. If a comparison is made between Figures 8.16 and 7.12 it can be seen that the soot particle content for the biodiesel fuel is of a similar nature to that of both the commercial low sulphur and the agricultural red diesel - the individual soot particles (of magnitude 20 nm) again joining together randomly to form much larger complex soot agglomerates. Additional images of the low sulphur diesel and the biodiesel particulate samples are included in Appendices K and N.

Low Sulphur Diesel Biodiesel

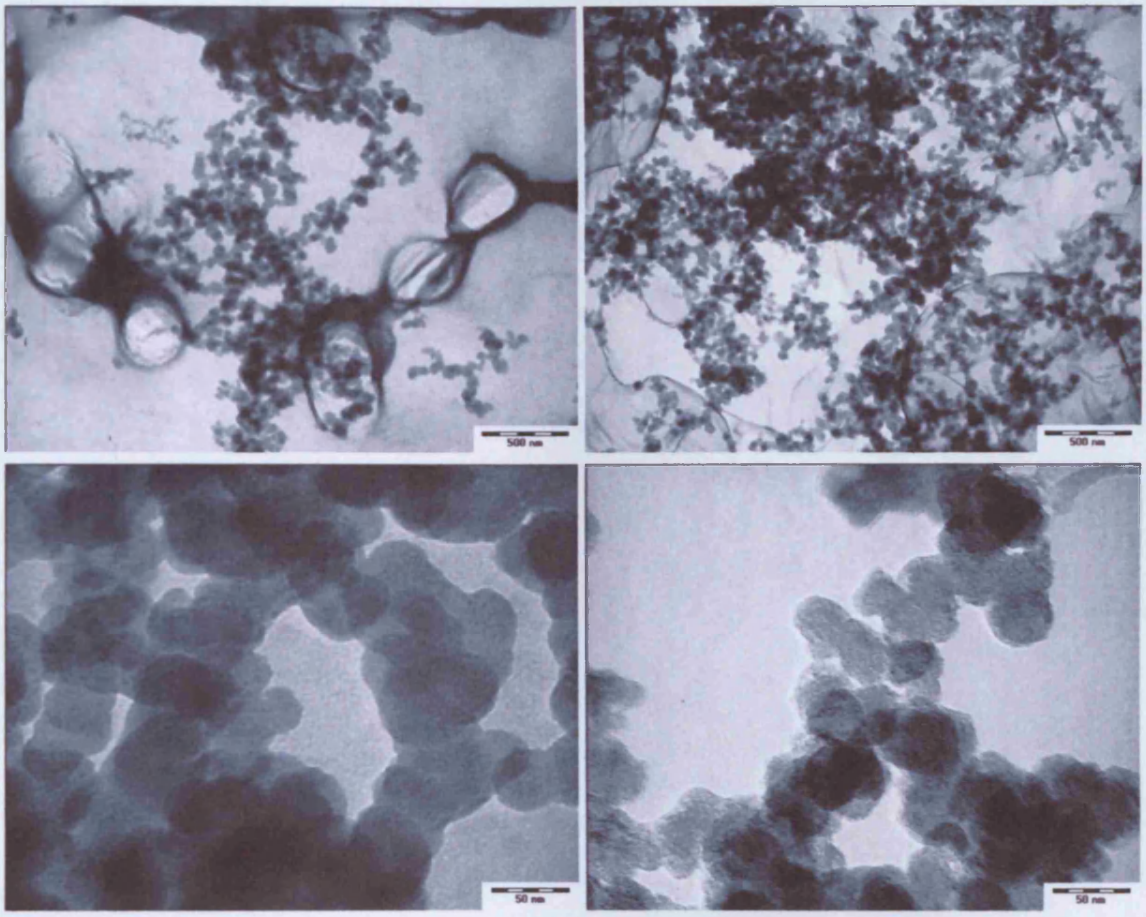

Figure 8.16 – Electron microscopy images of soot particles

A comparison of the electron microscopy images of the PM for both the commercial ultra low sulphur diesel fuel and the biodiesel fuel reveals no evidence of the difference in the characteristics that are evident in Figure 8.15. In order to reveal the differences between the particulate aerosols in the exhaust from both fuels it was decided that size distributions should be obtained.

A Cambustion DMS500 differential mobility spectrometer was selected to obtain size distributions for the particulate content of the exhaust gases. The DMS500 unit obtains the size distribution of a particulate sample by measuring the electrical mobility of the individual particles. The ease to which a charged particle is deflected by an electric field is a function of the charge on the particle and its aerodynamic drag, and is termed its

electrical mobility. As the charge on the particle and its aerodynamic drag are functions of the diameter of the particle, the size of a particle can be calculated from knowing its electrical mobility.

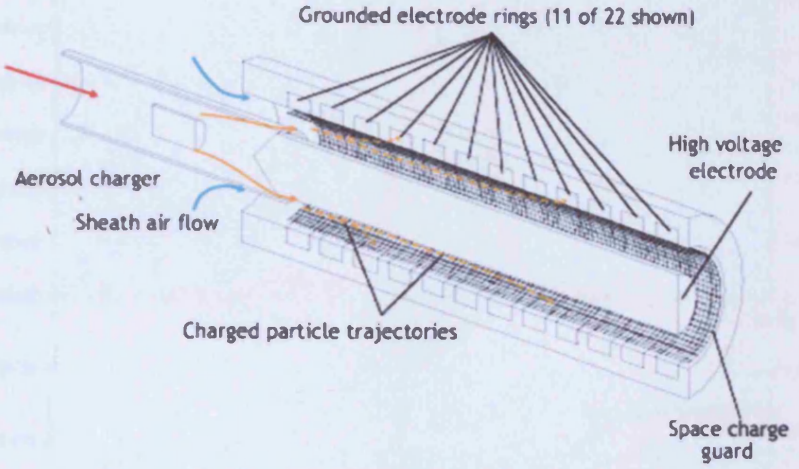

Figure 8.17 – DMS500 classification column

The DMS500 unit incorporates a two stage dilution system in which the exhaust gases are diluted by fresh clean air to a ratio of up to 2000:1. The diluted particulate aerosol sample from an engine exhaust is electrically charged through collisions with air ions. The charged particles then enter the low pressure classification column (shown in Figure 8.17) and are carried along by an additional fresh air supply. The central high voltage electrode produces a radial electric field which repels the charged particles, pushing them towards the grounded electrode ring forming the outside of the column. Particles of low electrical mobility are repelled to the outside slower than particles with higher mobility, and therefore travel further down the classification column before impinging upon one of the electrometer rings along the length of the column.

The DMS500 calculates the particle size spectrum of a aerosol sample from the electrometer currents through the use of a computer modelled transfer function. This transfer function takes into account the amount of charge given to particles of each size and geometry combination. The calibration of the DMS500 instrument is carried out through the use of NIST traceable solid nanospheres of known size, and a comparison with a calibrated Scanning Mobility Particle Sizer (SMPS).

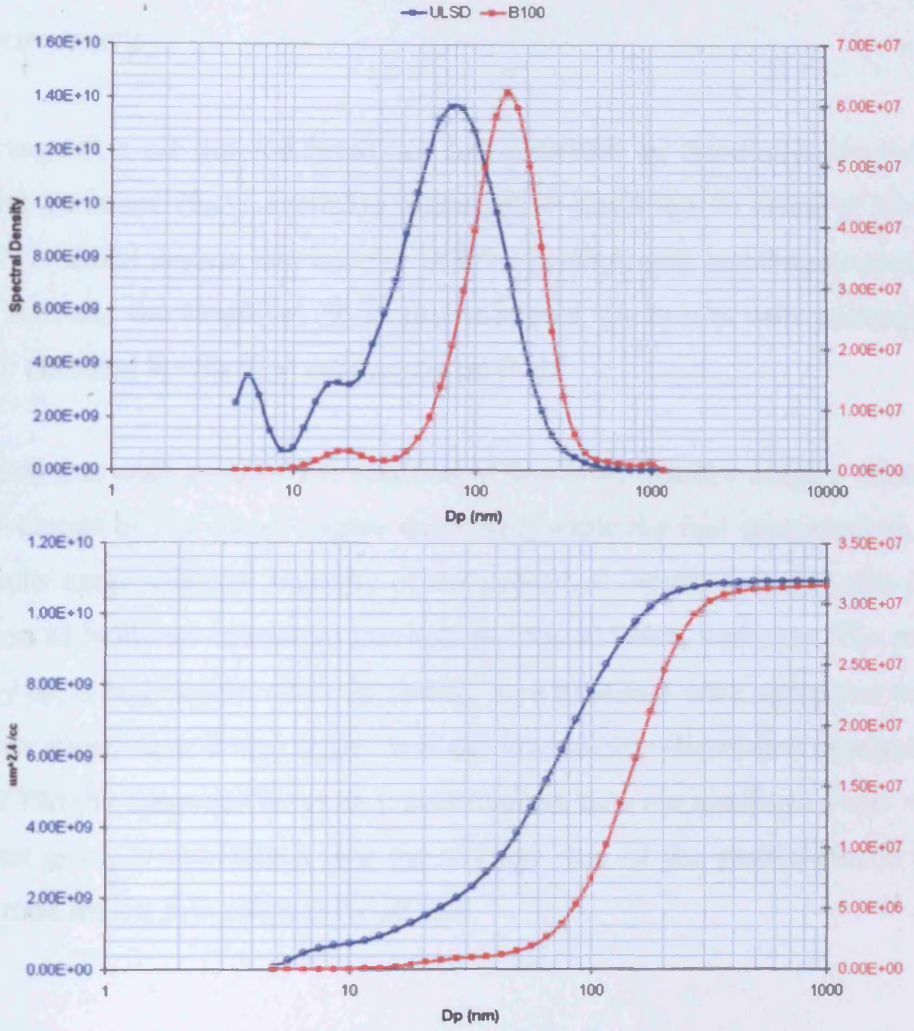

Figure 8.18 – Diesel and biodiesel PM size distribution comparison

Figure 8.18 displays the average size distribution and cumulative concentration comparison obtained, over a prolonged period of sampling, from the exhaust gases of the Perkins diesel engine when it was fuelled by ultra low sulphur diesel and pure biodiesel. The results shown in Figure 8.18 agree with those published by Lapuerta et al. (2005), in that the number of particles in the exhaust emissions from biodiesel is significantly less when compared to that from a low sulphur diesel fuel. It is also of note that the average size of the particulates in the biodiesel sample is larger than that in the low sulphur diesel sample. If the trend in current medical concerns regarding the number counts of ultra-fine particulates being of more importance than the mass undersize continues, then this evidence indicates another potential benefit of biodiesel.

8.5 Summary

A waste vegetable oil derived biodiesel fuel provided by Sundance Renewables was mixed with a commercially available low sulphur diesel fuel to ratios of 10:90, 30:70 and 50:50. A diesel engine was used to test the performance and emissions of the pure biodiesel fuel and the biodiesel/diesel fuel mixtures, the results were compared to that previously obtained for the low sulphur diesel fuel.

It was found that with incremental addition of biodiesel to a low sulphur diesel fuel the power developed by the diesel engine decreases, while the fuel consumption increases. These results agree with the majority of the published literature. It was also found that the addition of biodiesel causes an increase in CO_2 and NO_X emission. The particulates emitted by the diesel engine when fuelled by pure biodiesel were compared to that for a low sulphur diesel fuel, it was found that the low sulphur diesel fuel produces a larger amount of PM (by mass and number concentration), than the biodiesel. From analysis of the exhaust gases it was found that the average size of the particulates is larger for biodiesel than for the low sulphur diesel fuel.

9 Conclusions and Suggestions for Further Work

A number of conclusions have been drawn as a result of this study, which has allowed the achievement of each of the aims and objectives described in Chapter 1. An overview of these conclusions is given below, as well as suggestions for further work.

9.1 Main Achievements of Work

A review of the various drivers currently influencing developments in engine technology, with specific focus on improvements in engine efficiency and emission reductions was carried out. It was found that the signing of the Kyoto Protocol proved to be a watershed moment in the global technological development of the internal combustion engine. Tighter emission legislation imposed after the Kyoto agreement resulted in advances in the understanding of the concepts behind internal combustion engines; this together with developments such as variable valve timing, direct injection and exhaust gas treatment has improved the economy of modern motor vehicles while reducing their emissions of CO_2 and particulate matter.

Current trends indicate that alternative internal combustion engine fuels will, in the short to medium term future, partially replace petrol and diesel. This together with developments in technology will further reduce the pollutants emitted by the transport sector. There is evidence that the use of biomass derived fuels will increase through the increased supplementation of both petrol and diesel, and as separate transport fuels. In the long term future, developments in engine technology and global infrastructure will make CNG and hydrogen based fuels increasingly important.

As part of an EU funded project entitled "Magnetic Movement Valve for Miller Cycle operation of engines", the application of a novel secondary valve apparatus to an internal combustion engine was investigated. The software package Ricardo Wave was used to construct computer models of a marine diesel engine both before, and after, modifications were made to allow the use of gaseous fuels and to incorporate the

secondary valve apparatus. It was shown that the secondary valve concept is capable of controlling the output of an internal combustion engine, while increasing the operating efficiency and reducing the emission of NO_X through the use of Miller cycle operation and throttle free load control.

Through a series of comparisons the computer engine model was tested against measurements obtained from a test engine incorporating the secondary valves, it was shown that the computer model closely simulated the behaviour of the physical test engine. The optimum designs of key engine components were established through the use of the computer model. In addition, the design of the EOCV apparatus was improved though a CFD testing procedure, in which the flow through the valve was evaluated and improved in an iterative process, carried out in conjunction with testing by EU project partners. This development program resulted in a marketable engine incorporating the EOCV technology, which has now gone into production within Europe and the Far East.

The effect of the EOCV induced Miller cycle on conditions within the engine cylinder and inlet ports of the V6 NoNOx engine was examined through the use of a three-dimensional CFD model. The simulation results showed that the early EOCV valve closure required to produce Miller cycle operation caused a significant increase in turbulent kinetic energy of the trapped air within the inlet port. Over a prolonged period of operation, this could possibly lead to an increase in temperature of the EOCV apparatus.

An engine test-bed facility was commissioned and used to investigate the emissions and performance of a 4-cylinder turbocharged diesel engine manufactured by Perkins. The gaseous and particulate emissions of the engine were measured for both a commercially available low sulphur diesel fuel, a Class A2 rebated heavy oil (red diesel) and a variety of biodiesel / diesel fuel blends. A comparison of the low sulphur diesel fuel and the red diesel fuel showed that the red diesel fuel produced less power and significantly higher emissions of CO_2 and NO_X, as well as producing a higher mass concentration of exhaust particulates.

It was found that with incremental addition of Biodiesel to a low sulphur diesel fuel the power developed by the diesel engine decreases, while the fuel consumption increases – these results agree with the majority of the published literature. It was also found that the addition of Biodiesel causes an increase in CO_2 and NO_X emission. The particulates emitted by the diesel engine when fuelled by pure biodiesel were compared to that for a low sulphur diesel fuel; it was found that the low sulphur diesel fuel produced higher levels of particulate matter in the exhaust gases (by mass and number concentration), than the biodiesel. From analysis of the exhaust gases it was also found that the average size of the particulates is larger for the biodiesel fuel than for the low sulphur diesel fuel.

9.2 Further Work

This study has illustrated that the use of technological developments such as the EOCV, and alternative fuels such as CNG and biodiesel, can substantially reduce the emissions from an internal combustion engine. However a number of further studies would be of use to supplement these findings.

It has been shown that through the use of Miller cycle operation and throttle free load control, the emissions of a CNG powered engine can be reduced without any associated decrease in power or efficiency. A preliminary investigation was carried with a hydrogen / methane fuel blend, but the application of this technology to engines utilising different fuels should be investigated further.

During the development and investigation of the EOCV's effect on the in-cylinder properties of an engine prior to combustion, it was discovered that the outlet design of the EOCV apparatus has a large effect on overall flow through the valve and the inlet port of an engine. In the case of the V6 NoNOx engine, the outlet design of the EOCV caused turbulence within the inlet port of the engine which reduced the total flow-rate into the cylinder as well as causing undesired pressure oscillations. The design of the EOCV outlet should be investigated further, with emphasis on ensuring a smooth flow into the engine cylinder.

The investigation carried out into the emissions and performance of a diesel engine fuelled with biodiesel / diesel blends highlighted several areas of possible future study. The difference in the liquid properties of the biodiesel to normal diesel fuel affected the injection timing of the engine, ultimately leading to an increase in NO_X formation. The pre-heating of the biodiesel fuel prior to injections may reduce this effect, and should be investigated for a variety of biodiesel blends. In addition to this, injection studies of biodiesel / diesel fuel blends should be carried out in order to characterize the effect of the differing liquid properties on injection timing and atomisation.

Further work is required in developing the understanding of the mechanisms of particulate matter formation for biodiesel / diesel fuel blends. Analysis of the products of combustion (carried out under controlled conditions) should be carried out to investigate the effect of equivalence ratio and biodiesel percentage on particulate size and quantity.

References

Altin R., Çetinkaya S. and Yücesu H. S. (2001) The potential of using vegetable oil fuels as fuel for diesel engines. *Energy Conversion and Management, Vol. 42, pp. 529-538.*

Abu-Hamdeh N. H. (2003) Effect of cooling the recirculated exhaust gases on diesel engine emissions. *Energy Conversion and Management, Vol. 44, pp. 3113-3124.*

Akansu S. O., Dulger Z., Kahraman N. and Veziroğlu T. N. (2004) Internal combustion engines fuelled by natural gas – hydrogen mixtures. *International Journal of Hydrogen Energy, Vol. 29, pp. 1527-1539.*

Alcantara R., Amores J., Canoira L., Fidalgo E., Franco M. J. and Navarro A. (2000) Catalytic production of biodiesel from soy-bean oil, used frying oil and tallow. *Biomass and Bioenergy, Vol. 18, pp. 515-527*

Ali Y., Hanna M. A. and Leviticus L. I. (1995) Emissions and power characteristics of diesel engines on methyl soyate and diesel fuel blends. *Bioresource Technology, Vol. 52, pp. 185-195.*

Aslam M. U., Masjuki H. H., Kalam M. A. Abdesselam H., Mahlia T. M. I. and Amalina M. A. (2006) An experimental investigation of CNG as an alternative fuel for a retrofitted gasoline engine. *Fuel, Vol. 85, pp. 717-724..*

Bozbas K. (In print) Biodiesel as an alternative motor fuel: Production and policies in the European Union. *Renewable and Sustainable Energy Reviews*

British Standards Institution. (2003) BS EN 14214:2003 Automotive fuels – Fatty acid methyl esters (FAME) for diesel engines – Requirements and test methods. *London: BSI. ISBN 0 580 43281 5.*

British Standards Institution. (2004) BS EN 590:2004 Automotive fuels – Diesel – Requirements and test methods. *London: BSI. ISBN 0 580 44119 9.*

British Standards Institution. (2006) BS 2869:2006 Fuel oils for agricultural, domestic and industrial engines and boilers - Specification. *London: BSI. ISBN 0 580 47928 5.*

Burtscher H., Matter U. and Skillas G. (1999) The effect of fuel additives on diesel engine particulate emissions. *Journal of Aerosol Science, Vol. 30, Suppl. pp. S851-S852.*

Carbon Dioxide Information Analysis Centre. . (Online) Available from – http://cdiac.ornl.gov

Carraretto C., Macor A., Mirandola A., Stoppato A. and Tonon S. (2004) Biodiesel as alternative fuel: Experimental analysis and energetic evaluations. *Energy, Vol. 29, pp. 2195-2211.*

Çetinkaya M., Ulusoy Y., Tekìn Y. and Karaosmanoğlu F (2005) Engine and winter road test performances of used cooking oil originated biodiesel. *Energy Conversion and Management, Vol. 46, pp. 1279-1291.*

Ceviz M. A. and Yüksel F. (2005) Effects of ethanol-unleaded gasoline blends on cyclic variability and emissions in an SI engine. *Applied Thermal Engineering, Vol. 25, pp. 917-925.*

Cherry R. S. (2004) A hydrogen utopia? *International Journal of Hydrogen Energy, Vol. 29, pp. 125-129.*

Choi C. Y. and Reitz R. D. (1999) An experimental study on the effects of oxygenated fuel blends and multiple injection strategies on DI diesel engine emissions. *Fuel, Vol. 78, pp. 1303-1317.*

Chughtai A. R., Atteya M. M. O., Kim J., Konowalchuk B. K. and Smith D. M. (1998) Adsorption and adsorbate interaction at soot particle surfaces. *Carbon, Vol. 36, No. 11, pp. 1573-1589.*

Clerc J. C. (1996) Catalytic diesel exhaust after treatment. *Applied Catalysis B: Environmental, Vol. 10, pp. 99-115.*

Corson D. W. (2002) High power battery systems for hybrid vehicles. *Journal of Power Sources, Vol. 105, pp. 110-113.*

Cvengroš J. and Považanec F. (1996) Production and treatment of rapeseed oil methyl esters as alternative fuels for diesel engines. *Bioresource Technology, Vol. 55, pp. 145-152.*

Cvengroš J. and Cvengrošová Z. (2004) Used frying oils and fats and their utilization in the production of methyl esters of higher fatty acids. *Biomass and Bioenergy, Vol. 27, pp. 173-181.*

Dekanski C. W., Bloor M. I. G. and Wilson M. J. (1996) A parametric model of a 2-stroke engine for design and analysis. *Computer methods in applied mechanics and engineering, Vol. 137, pp. 411-425.*

Demirbaş A. (2003) Biodiesel fuels from vegetable oils via catalytic and non-catalytic supercritical alcohol transesterifications and other methods: a survey. *Energy Conversion and management, Vol. 44, pp. 2093-2109.*

Department for Environment Food and Rural Affairs. . (Online) Available from - www.defra.gov.uk

Department of Transport (2005) Transport Trends 2005 Edition. *Department of Transport, National Statisitcs, London.*

Drake M. C., Fansler T. D. and Lippert A. M. (2005) Stratified-charge combustion: modelling and imaging of a spray-guided direct-injection spark-ignition engine. *Proceedings of the Combustion Institute, Vol. 30, pp. 2683-2691.*

Durán A., Carmona M. and Balleateros R. (2003) Competitive diesel engine emissions of sulphur and nitrogen species. *Chemosphere, Vol. 52, pp. 1819-1823.*

Durán A., Carmona M. and Monteagudo J. M. (2004) Simulation of diesel particulate matter size. *Atmospheric Environment, Vol. 38, pp. 6203-6209.*

Durbin T. D., Zhu X. And Norbeck J. M. (2003) The effects of diesel particulate filters and a low-aromatic, low-sulfur diesel fuel on emissions for medium-duty diesel trucks. *Atmospheric Environment, Vol. 37, pp. 2105-2116.*

El-Fadel M., Aldeen R. A. F. and Maroun R. (2004) Impact of diesel policy banning on PM levels in urban areas. *International Journal of Environmental Studies, Vol. 61(4), pp. 427-436.*

Energy Information Administration, Department of Energy. (Online) Available from - http://www.eia.doe.gov

European Commission (1970-2003) Directive 70/220/EEC. Laws of Member States on Measures to be taken against air pollution by emissions from motor vehicles. *Official Journal of the European Communities.*

European Commission (1998) Directive 98/70/EC. Quality of petrol and diesel fuels. *Official Journal of the European Communities.*

European Commission (1999) Directive 1999/32/EC. Reduction in the sulphur content of certain liquid fuels. *Official Journal of the European Communities.*

European Federation for Transport and Environment (Unknown date) Waiting for Euro 5 and Euro 6. New Emission Standards for Passenger Cars, Vans and Lorries.

Figler B., Sahle W., Krantz S. and Ulfvarson U. (1996) Diesel exhaust quantification by scanning electron microscope with special emphasis on particulate matter size distribution. *The Science of the Total Environment, Vol. 193, pp. 77-83.*

Funasaka K., Miyazaki T., Kawaraya T., Tsuruho K. and Mizuno T. (1998) Characteristics of particulates and gaseous pollutants in a highway tunnel. *Environmental Pollution, Vol. 102, pp. 171-176.*

Ge Y., Chen L., Sun F. and Wu C. (2005) Reciprocating heat-engine cycles. *Applied Energy, Vol. 81, pp. 397-408.*

Granovskii M., Dincer I. and Rosen M. A. (2006) Life cycle assessment of hydrogen fuel cell and gasoline vehicles. *International Journal of Hydrogen Energy, Vol. 31, pp. 337-352.*

Hansen A. C., Zhang Q. and Lyne P. W. L. (2005) Ethanol-diesel fuel blends-a review. *Bioresource Technology, Vol. 96, pp. 277-285.*

Haraldsson K., Folkesson A. and Alvfors P. (2005) Fuel cell buses in the Stockholm CUTE project- First experiences from a climate perspective. *Journal of Power Sources, Vol. 145, pp. 620-631.*

Harris S. J. and Maricq M. M. (2001) Signature size distributions for diesel and gasoline engine exhaust particulate matter. *Aerosol Science, Vol. 32, pp. 749-764.*

Hatamura K., Hayakawa M., Goto T. and Hitomi M. (1997) A study of the improvement effect of Miller-cycle on mean effective pressure limit for high-pressure supercharged gasoline engines. *Society of Automotive Engineers of Japan – Review, Vol. 18, pp. 101-106.*

Heck R. M. and Farrauto R. J. (2001) Automobile exhaust catalysts. *Applied Catalysis A: General, Vol. 221, pp. 443-457.*

Hekkert M. P., Hendriks F. H. J. F., Faaij A. P. C. and Neelis M. L. (2005) Natural gas as an alternative to crude oil in automotive fuel chains well-to-wheel analysis and transition strategy development. *Energy Policy, Vol. 33, pp. 579-594.*

Her Majesty's Treasury. (2006) Economic and Fiscal Strategy Report and Financial Statement and Budget Report – March 2006

Höhlein B., von Andrian S., Grube Th. And Menzer R. (2000) Critical assessment of power trains with fuel-cell systems and different fuels. *Journal of Power Sources, Vol. 86, pp. 243-249.*

Hsieh W., Chen R., Wu T. and Lin T. (2002) Engine performance and pollutant emission of an SI engine using ethanol-gasoline blended fuels. *Atmospheric Environment, Vol. 36, pp. 403-410.*

Jia L., Shen M., Wang J. and Lin M. (2005) Influence of ethanol-gasoline blended fuel on emission characteristics from a four-stroke motorcycle engine. *Journal of Hazardous Materials, Vol. A123, pp. 29-34.*

Johansson B. (1999) The economy of alternative fuels when including the cost of pollution. *Transportation Research Part D, Vol. 4, pp. 91-108.*

Jones D. A. (2003) Characterisation and fundamental studies of particulate matter from combustion processes. *Thesis (PhD) Cardiff University.*

Kalligeros S., Zannikos F., Stournas S., Lois E., Anastopoulos G., Teas Ch. and Sakellaropoulos F. (2003) An investigation of using biodiesel/marine diesel blends on the performance of a stationary diesel engine. *Biomass and Bioenergy, Vol. 24, pp. 141-149.*

Kano M., Saito K., Basaki M., Matsushita S. and Gohno T. (1999) Analysis of mixture formation of direct injection gasoline engine. *Society of Automotive Engineers of Japan – Review, Vol. 20, pp. 31-39.*

Karim G. A., Wierzba I. and Al-alousi Y. (1996) Methane – hydrogen mixtures as fuels. *International Journal of Hydrogen Energy, Vol. 21, No. 7, pp. 625-631.*

Karim G. A. (2003) Hydrogen as a spark ignition fuel. *International Journal of Hydrogen Energy, Vol. 28, pp. 569-577.*

Kato T., Saeki K., Nishide H. and Yamada T. (2001) Development of CNG fuelled engine with lean burn for small size commercial van. *Society of Automotive Engineers of Japan – Review, Vol. 22, pp. 365-368.*

Kim H., Lee S., Kim J., Cho G., Sung N. And Jeong Y. (2005) Measurement of size distribution of diesel particles: effects of instruments, dilution methods, and measuring positions. *International Journal of Automotive Technology, Vol. 6, No. 2, pp 119-124.*

Kojima T., Tange A. and Tamatsu K. (1999) Developments of diesel particulate filter systems with mesh laminated structures. *Society of Automotive Engineers of Japan – Review, Vol. 20, pp. 117-136.*

Kumar M. S., Ramesh A. and Nagalingam B. (2003) Use of hydrogen to enhance the performance of a vegetable oil fuelled compression ignition engine. *International Journal of Hydrogen Energy, Vol. 28, pp. 1143-1154.*

Labeckas G. and Slavinskas S. (2006a) Performance of direct-injection off-road diesel engine on rapeseed oil. *Renewable Energy, Vol. 31, pp. 849-863.*

Labeckas G. and Slavinskas S. (2006b) The effect of rapeseed oil methyl ester on direct injection diesel engine performance and exhaust emissions. *Energy Conversion and Management, Vol. 47, pp. 1954-1967*

Lapuerta M., Hernández J. J., Ballesteros R. and Durán A. (2003) Composition and size of diesel particulate emissions from a commercial European engine tested with present and future fuels. *Proceedings of the Institution of Mechanical Engineers Vol. 217, Part D. Journal of Automobile Engineering, pp. 907-919.*

Lapuerta M., Armas O., Ballesteros R. and Fernández J. (2005) Diesel emissions from Biofuels derived from Spanish potential vegetable oils. *Fuel, Vol. 84, pp. 773-780.*

Lee S. (1996) Alternative fuels. Applied energy technology series *Taylor and Francis, ISBN 1-56032-361-2.*

Lee K. H., Lee C. H. and Lee C. S. (2004) An experimental study on the spray behaviour and fuel distribution of GDI injectors using the entropy analysis and PIV method. *Fuel, Vol. 83, pp. 971-980.*

Leicester A. (2005) Fuel Taxation. *The Institute for Fiscal Studies Briefing Note No. 55. ISBN 1-903274-09-5*

Lin C. and Lin H. (2006) Diesel engine performance and emission characteristics of biodiesel produced by the peroxidation process. *Fuel, Vol. 85, pp. 298-305.*

Lin C. and Wang K. (2004) Diesel engine performance and emission characteristics using three-phase emulsions as fuel. *Fuel, Vol. 83, pp. 537-545.*

Lu X., Huang Z., Zhang W. And Li D. (2005) Combustion visualization and emissions of a direct injection compression ignition engine fuelled with Bio-Diesohol. *International Journal of Automotive Technology, Vol. 6, No.1, pp. 15-21.*

Maher A. R., Sadiq A., Haroun A. K. and Shahad A. (2003) A prediction of a spark-ignition supercharged hydrogen engine. *Energy Conversion and Management, Vol. 44, pp. 3143-3150.*

Maher A. R. and Sadiq A. (2004) Effect of compression ratio, equivalence ratio and engine speed on the performance and emission characteristics of a spark ignition engine using hydrogen as a fuel. *Renewable Energy, Vol. 29, pp. 2245-2260.*

Marland, G,. and T. A. Boden. (2001) The Increasing concentration of atmospheric CO_2; How much, when, and why? *Oak Ridge National Laboratory*

Marland, G,. T. A. Boden, and R. J. Andres. (2005) Global, regional, and national CO_2 emissions. In trends: A compendium of data on global change. *CDIAC. ORNL. US Department of Energy. Oakridge, Tenn. USA.*

Matsumoto S., Ikeda Y., Suzuki H., Ogai M. and Miyoshi N. (2000) NO_X storage-reduction catalyst for automotive exhaust with improved tolerance against sulphur poisoning. *Applied Catalysis B: Environmental, Vol. 25, pp. 115-124.*

Matsumoto S., Inaba A. and Yanagisawa Y. (1997) Technology assessment of alternative fuels by CO_2 fixation use in passenger cars. *Energy Convers. Management, Vol. 38, Suppl. pp. S455-S460.*

Maxwell J. B. (1951) Data Book on Hydrocarbons. *D. Van Nostrand.*

Monyem A. and Van Gerpen J. H. (2001) The effect of biodiesel oxidation on engine performance and emissions. *Biomass and Bioenergy, Vol. 20, pp. 317-325.*

Nagaya K., Kobayashi H. and Koike K. (2006) Valve timing and valve lift control mechanisms for engines. *Mechatronics, Vol. 16, pp. 121-129.*

Powers W. F. and Nicastri P. R. (2000) Automotive vehicle control challenges in the 21st century. *Control Engineering Practice, Vol. 8, pp. 605-618.*

Ricardo Software (2004) VECTIS Computational Fluid Dynamics Release 3.8 Theory Manual *RD.03/1267.2 Ricardo Software.*

Ricardo Test Automation (1998) Series 3000 User manual. *Ricardo Test Automation Ltd. Lowesmoor Wharf, Worcester. WR1 2RS.*

Ristovski Z. D., Morawska L., Hitchins J., Thomas S., Greenaway C. and Gilbert D. (2000) Particle emissions from compressed natural gas engines. *Journal of Aerosol Science, Vol. 31, No. 4, pp. 403-413.*

Rotondi R. and Bella G. (2006) Gasoline direct injection spray simulation. *International Journal of Thermal Sciences, Vol. 45, pp. 168-179.*

Ryu J., Kim H. and Lee K. (2005) A study on the spray structure and evaporation characteristic of common rail type high pressure injector in homogeneous charge compression ignition engine. *Fuel, Vol. 84, pp. 2341-2350.*

Sasaki S., Sawada D., Ueda T. and Sami H. (1998) Effects of EGR on direct injection gasoline engine. *Society of Automotive Engineers of Japan – Review, Vol. 19, pp. 223-228.*

Schumacher L. G., Borgelt S. C., Fosseen D., Goetz W. And Hires W. G. (1996) Heavy-duty engine exhaust emission tests using methyl ester soybean oil / diesel fuel blends. *Bioresource Technology, Vol. 57, pp. 31-36.*

Shi X., Pang X., Mu Y., He H., Shuai S., Wang J., Chen H. and Li R. (2006) Emission reduction potential of using ethanol-biodiesel-diesel fuel blend on a heavy-duty diesel engine. *Atmospheric Environment, Vol. 40, pp. 2567-2574.*

Stamatelos A. M. (1997) A review of the effect of particulate traps on the efficiency of vehicle diesel engines. *Energy Convers. Management, Vol. 38, No. 1, pp. 83-99.*

Stansfield P. (2005) The Hotfire Project: Studying the interaction between homogeneous GDi and fully variable valve trains. *Presentation: Institute of Physics*

Young Researcher Meeting 21/09/05. Available from – http://groups.iop.org/CB/events/YR2005.htm

Stojkovic B. D., Fansler T. D., Drake M. C. and Sick V. (2005) High-speed imaging of OH* and soot temperature and concentration in a stratified-charge direct-injection gasoline engine. *Proceedings of the Combustion Institute, Vol. 30, pp. 2657-2665.*

Smith Z. (2000) The Petrol Tax Debate. *The Institute for Fiscal Studies Briefing Note, No. 8, ISBN 1-903274-09-5*

Song C., Zhang W., Pei Y., Fan G. And Xu G. (2006) Comparitive effects of MTBE and ethanol additions into gasoline on exhasut emissions. *Atmospheric Environment, Vol. 40, pp. 1957-1970.*

Topgül T., Yücesu H. S., Çinar C. and Koca A. (In Press) The effects of ethanol-unleaded gasoline blends and ignition timing on engine performance and exhaust emissions. *Renewable Energy.*

Transport for London. (2004) Greater London Authority Act 1999, Transport Act 2000. The Greater London (Central Zone) Congestion Charging Order 2004.

Transport for London. (2005) Central London Congestion Charging – Impacts Monitoring. Third Annual Report April 2005.

United Nations Framework Convention on Climate Change. (Online) Available from - http://www.unfccc.int

UNFCCC Kyoto Protocol to the United Nations Framework Convention on Climate Change.

Vandenborre H. and Sierens R. (1996) Greenbus: A hydrogen fuelled city bus. *International Journal of Hydrogen Energy, Vol. 21, No. 6, pp. 521-524.*

Verhelst S. and Sierens R. (2001) Aspects concerning the optimisation of a hydrogen fuelled engine. *International Journal of Hydrogen Energy, Vol 26, pp. 981-985.*

Weingartner E., Keller C., Stahel A., Burtscher H. and Baltensperger U. (1997) Aerosol emission in a road tunnel. *Atmospheric Environment, Vol. 31, No. 3, pp. 451-462.*

Weitschel M., Hasenauer U. and de Groot A. (2006) Development of European hydrogen infrastructure scenarios - CO_2 reduction potential and infrastructure investment. *Energy Policy, Vol. 34, pp. 1284-1298.*

White C. M., Steeper R. R. and Lutz A. E. (In Press) The hydrogen-fuelled internal combustion engine: a technical review. *International Journal of Hydrogen Energy.*

Williamson A. and Badr O. (1998) Assessing the viability of using Rape Methyl Ester (RME) as an alternative to mineral diesel fuel for powering road vehicles in the UK. *Applied Energy, VOl 59, No2-3, pp. 187-214.*

Wu C., Puzinauskas P. V. and Tsai J. S. (2003) Performance analysis and optimization of a supercharged Miller cycle Otto engine. *Applied Thermal Engineering, Vol. 23, pp. 511-521.*

Wu C., Chen R., Pu J. And Lin T. (2004) The influence of air-fuel ratio on engine performance and pollutant emission of an SI engine using ethanol-gasoline-blended fuels. *Atmospheric Environment, Vol. 38, pp. 7093-7100.*

Yamin J. A. A., Gupta H. N., Bansal B. B. and Srivastave O. N. (2000) Effect of combustion duration on the performance and emission characteristics of a spark ignition engine using hydrogen as a fuel. *International Journal of Hydrogen Energy, Vol. 25, pp. 581-589.*

Yuan W., Hansen A. C. and Zhang Q. (2003) Predicting the physical properties of biodiesel for combustion modelling. *American Society of Agricultural Engineers, Vol. 46(6), pp. 1487-1493*

Zelenka P., Cartellieri W. and Herzog P. (1996) Worldwide diesel emission standards, current experiences and future needs. *Applied Catalysis B: Environmental, Vol. 10, pp. 3-28.*

Zeng K., Huang Z., Liu B., Liu L., Jiang D., Ren Y. and Wang J. (2006) Combustion characteristics of a direct-injection natural gas engine under various fuel injection timings. *Applied Thermal Engineering, Vol. 26, pp. 806-813.*

Zhao F., Lai M. C. and Harrington D. L. (1999) Automotive spark-ignited direct-injection gasoline engines. *Progress in Energy and Combustion Science, Vol. 25, pp. 437-562.*

Zheng M., Reader G. T. and Hawley G. (2004) Diesel engine exhaust gas recirculation – a review on advanced and novel concepts. *Energy Conversion and Management, Vol. 45, pp. 883-900.*

1015. The marine engine.

195-440 kW (261 - 590 BHP) at 1500-2100 rpm

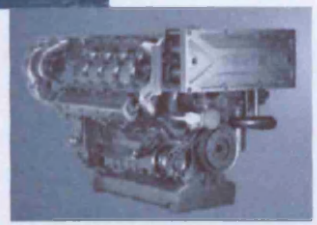

These are the characteristics of the 1015:

Modern water-cooled four stroke 6- and 8-cylinder V-engines.
Water-cooled turbocharger and exhaust manifolds.
PTOs gear driven.
Modern injection system with mechanical governor.
Electronical governor for gen set application.
Charge-air-cooled by engine cooling liquid.
Innovative DEUTZ Multi-Parallel-Cooling System.
Compact design.

Your benefits:

- High return on investment due to high fuel economy and low oil consumption.
- Plate type sea water heat exchanger guarantees low maintenance costs.
- The innovative cooling system reduces fuel consumption and is a further example of the outstanding reliability and durability.
- Low operating noise level eliminates the need for elaborate and costly noise abatement measures.
- Designed according to maritime classification rules.
- Integrated piping works for additional operating safety.

Standard specification

Types of cooling:	Single-circuit mixed cooling as indirect cooling (DEUTZ Multi-Parallel-Cooling system) raw water cooled version with engine mounted plate-type heat exchanger, coolant circulating pump, expansion tank, thermostat and raw water pump. As keel-cooling with coolant circulating pump and integrated thermostat. Integrated expansion tank optional
Crankcase:	Crankcase of grey cast iron with wet liners
Crankcase breather:	Closed-circuit system, vacuum controlled
Cylinder head:	Individual cylinder heads of grey cast iron of crossflow design
Valve arrangement / timing	Overhead valves in cylinder head, four valve technology, actuated via tappets, pushrods and rocker arms, driven by gears and central camshaft
Piston:	Three-ring aluminium piston with cooling channel and ring carrier for top ring groove
Piston cooling:	Oil cooled with spray nozzles
Connecting rod:	Drop-forged steel rod
Crankshaft:	Drop-forged steel crankshaft with screwed-on counterweights. V6 with 30° offset crankpins (split pin).
Turbocharging:	Two liquid-cooled turbochargers and possible intercooler mounted at flywheel end
Exhaust manifolds:	Liquid-cooled exhaust manifolds
Topsional vibration damper:	Viscous-fluid damper
Lubrication system:	Forced-feed circulation lubrication with gear pumps, integrated engine oil cooler, paper type microfilter as replaceable cartridge, integrated in main oil circuit, double filter as option
Injection system:	In-line injection pump with mechanical (propulsion engine) or electronic (gen-set) governor
Fuel injection pipes:	High pressure fuel injection pipes double walled as option
Fuel system:	Mechanical reciprocating pump, replaceable cartrige-type for fuel filter, double filter as option
Alternator:	Three-phase alternator, 28 V, 55 or 80 A
Starting system:	24 V, 5.4 kW
Heating system:	Optional connection for heating or warm water boiler to engine cooling circuit
Options:	Hydraulic pumps, flywheels, adapter housings SAE 1, oil pans, air cleaners, elastic engine mounting feet, starters, alternators, engine monitoring system, marine gears
Classification:	By all major classification societies

Technical data

Engine type			BF6M1015M	BF6M1015MC	BF8M1015MC
Number of cylinders			6	6	8
Bore		mm/in	132/5.2	132/5.2	132/5.2
Stroke		mm/in	145/5.71	145/5.71	145/5.71
Displacement		l/cu.in.	11.91/727	11.91/727	15.81/968
Compression ratio			17	17	17
Power ratings for marine propulsion units					
acc. to power category A	at 1800 rpm	kW/BHP	203/272	272/365	364/488
	at 1900 rpm	kW/BHP	214/287	287/385	383/513
	at 2100 rpm	kW/BHP	214/287	287/385	383/513
acc. to power category B	at 1800 rpm	kW/BHP	228/306	313/420	418/560
	at 1900 rpm	kW/BHP	240/322	330/442	440/590
	at 2100 rpm	kW/BHP	240/322	330/442	440/590
Power ratings for on-board generating sets					
	at 1500 rpm	kW/BHP	210/282	285/382	380/509
	at 1800 rpm	kW/BHP	228/306	310/416	413/554
Weight dry incl. heat exchanger		kg/lbs	1080/2381	1180/2602	1380/3043
Weight as keel-cooling		kg/lbs	1020/2250	1110/2448	1310/2890

The values given in this data sheet are for information purposes only and not binding.
The data provided in the offer is decisive.

Standard specification

Engine type		A	B	C	D	E
BF6M1015M	mm	1191	1316	1138	443	695
	in	469	518	448	174	274
BF6M1015MC	mm	1482	1316	1138	443	695
	in	583	518	448	174	274
BF8M1015MC	mm	1661	1333	1138	443	695
	in	654	525	448	174	274

Definitions of power ratings

Power category A: Net brake fuel stop power for continuous operation unlimited time, SCFN or ICFN to ISO 3046.

Power category B: Net brake fuel stop power for continuous operation, SCFN or ICFN to ISO 3046.

Power for on-board generating sets: Continuous power, overloadable by 10% for one hour within an operating period of 12 hours. SCXN or ICXN to ISO 3046.

Dimensions

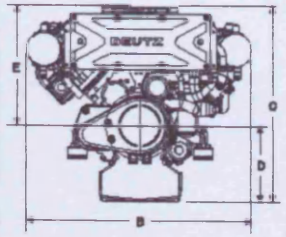

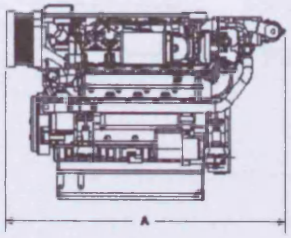

DEUTZ®

We move your world.

DEUTZ AG
DEUTZ MOTOR
Deutz-Mülheimer Str. 147-149
D-51063 Köln
Phone: +49 (0) 2 21-8 22-0
Fax: +49 (0) 2 21-8 22-22 34
Internet: www.deutz.de
eMail: marine.sales@deutz.de

Appendix B – IHI Turbocharger Details

IHI RHF5V -VGS Turbo-
TURBINE PERFORMANCE

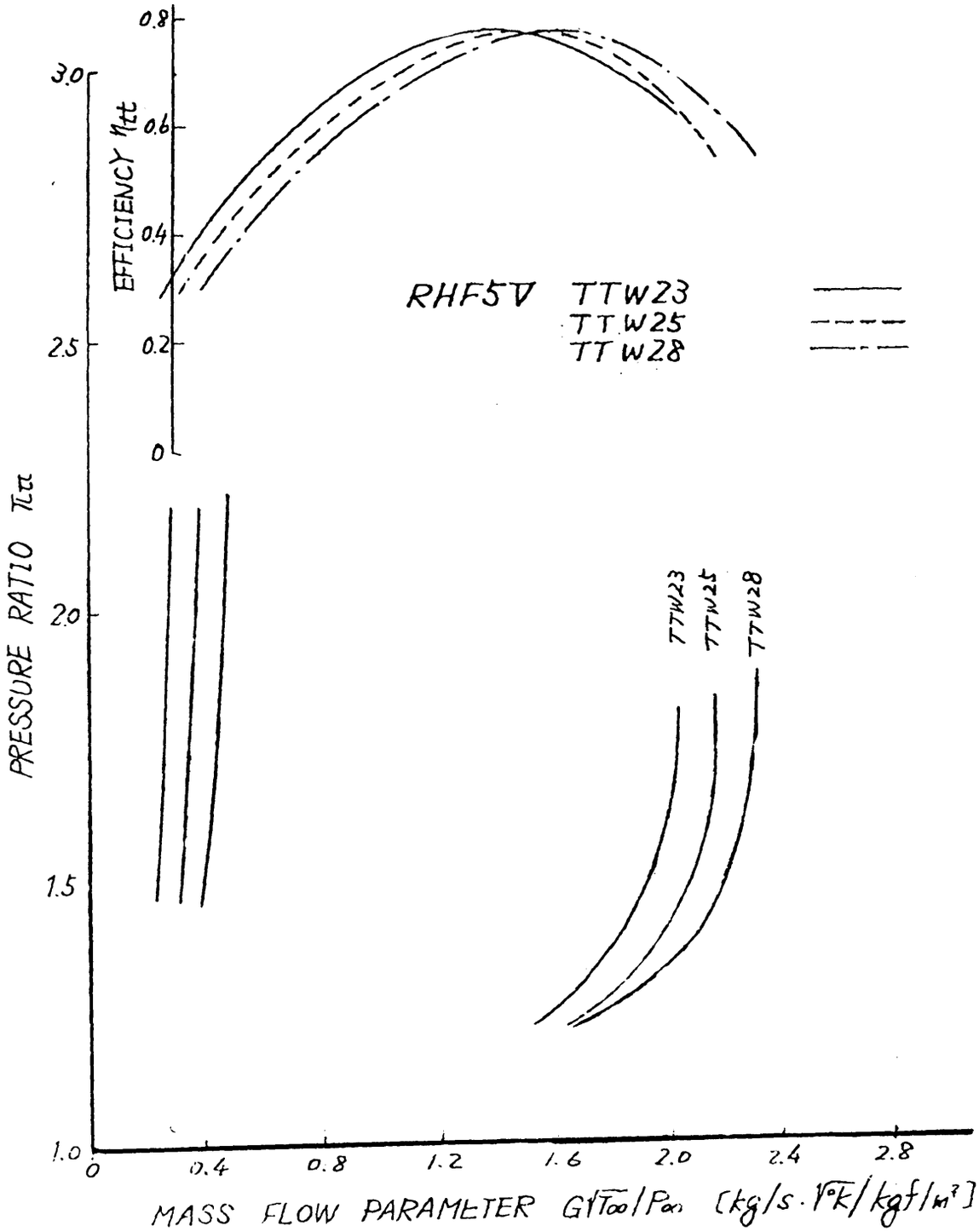

Appendix C – Sample Wave Output

FINAL OUTPUT OF JUNCTIONS

Junction	TWALL K	TAV K	PAV BAR	PMAX BAR	PMIN BAR	HTKW KW
erun01	900.0	1005.6	2.220	3.439	1.522	0.076
erun04	900.0	1001.9	2.225	3.453	1.514	0.074
erun07	900.0	991.8	2.234	3.487	1.519	0.064
erun10	900.0	1000.7	2.224	3.433	1.520	0.072
erun13	900.0	1017.6	2.265	3.884	1.537	0.086
erun16	900.0	1008.9	2.271	3.945	1.547	0.078
icool1	300.0	353.9	1.820	1.981	1.703	0.137
icool2	300.0	300.9	1.723	1.880	1.604	0.006
icool3	300.0	354.1	1.822	1.986	1.704	0.137
icool4	300.0	300.9	1.725	1.887	1.606	0.006
man1	900.0	1019.1	2.168	2.940	1.585	0.455
man2	900.0	1020.8	2.173	2.950	1.588	0.355
man3	900.0	1008.1	2.183	2.964	1.579	0.158
man04	900.0	1022.3	2.171	2.892	1.585	0.465
man05	900.0	1025.8	2.184	2.926	1.597	0.366
man06	900.0	1012.4	2.193	2.938	1.589	0.161
out00	900.0	939.4	1.049	1.114	0.974	0.197
plen01	300.0	299.3	1.715	1.867	1.578	-0.001
plen02	300.0	299.2	1.716	1.878	1.579	-0.001
plen03	300.0	299.2	1.716	1.887	1.574	0.000
plen04	300.0	299.1	1.717	1.898	1.570	0.000
plen05	300.0	299.1	1.717	1.905	1.571	0.000
plen06	300.0	298.9	1.717	1.912	1.564	0.000
plen07	300.0	299.3	1.717	1.875	1.580	-0.001
plen08	300.0	299.2	1.718	1.886	1.580	-0.001
plen09	300.0	299.2	1.719	1.895	1.576	0.000
plen10	300.0	299.2	1.719	1.907	1.571	0.000
plen11	300.0	299.3	1.719	1.915	1.570	0.000
plen12	300.0	299.0	1.720	1.923	1.564	0.000

COMPRESSOR			SUMMARY			TURBINE		
INLET TEMP	(K) =	295.1	COMPRESSOR:comp1			INLET TEMP	(K) =	1008.
(TOTAL)	(F) =	71.42	TURBINE:turb1			(TOTAL)	(F) =	1355.
OUTLET TEMP	(K) =	362.3	RPM =	116715.		OUTLET TEMP	(K) =	957.3
(TOTAL)	(F) =	192.5	CONTROL MECHANISM =	NONE		(TOTAL)	(F) =	1263.
INLET PRESS.	(BAR) =	0.9901	CONTROL VARIABLE =	NONE		INLET PRESS.	(BAR) =	2.145
(TOTAL)	(PSI) =	14.36	WASTEGATE AREA (CM2) =	0.000		(TOTAL)	(PSI) =	31.12
OUTLET PRESS.	(BAR) =	1.842	TURBINE RACK POSITION =	0.000		OUTLET PRESS.	(BAR) =	1.136
(TOTAL)	(PSI) =	26.72	COMPRESSOR VANE POSITION =	0.000		(TOTAL)	(PSI) =	16.48
PRESSURE RATIO	=	1.861				PRESSURE RATIO	=	1.888
MASS FLOW	(KG/HR) =	602.1	SHAFT TORQUE (N-M) =	0.9258		MASS FLOW	(KG/HR) =	651.4
	(LB/HR) =	1327.	(FT-LB) =	0.6829			(LB/HR) =	1436.
POWER	(KW) =	11.38	SHAFT POWER (KW) =	11.32		POWER	(KW) =	11.25
	(HP) =	15.26	(HP) =	15.17			(HP) =	15.09
EFFECTIVE DIAMETER	(M) =	0.5030E-01	EXTERNAL POWER [kW] =	0.000		EFFECTIVE DIAMETER	(M) =	0.5066E-01
ISEN. EFF. (INST.	%) =	84.17				ISEN. EFF. (INST.	%) =	35.68
(AVG.	%) =	84.90				(AVG.	%) =	36.43
BLADE SPEED RATIO(INST)	=	0.9108				BLADE SPEED RATIO(INST)	=	0.5345
(AVG)	=	0.9045				(AVG)	=	0.5299
MECH. EFFICIENCY	(%) =	100.0				MECH. EFFICIENCY	(%) =	100.0
INLET TEMP	(K) =	295.1	COMPRESSOR:comp2			INLET TEMP	(K) =	1011.
(TOTAL)	(F) =	71.44	TURBINE:turb2			(TOTAL)	(F) =	1360.
OUTLET TEMP	(K) =	362.5	RPM =	116544.		OUTLET TEMP	(K) =	960.0
(TOTAL)	(F) =	192.9	CONTROL MECHANISM =	NONE		(TOTAL)	(F) =	1268.
INLET PRESS.	(BAR) =	0.9902	CONTROL VARIABLE =	NONE		INLET PRESS.	(BAR) =	2.140
(TOTAL)	(PSI) =	14.36	WASTEGATE AREA (CM2) =	0.000		(TOTAL)	(PSI) =	31.04
OUTLET PRESS.	(BAR) =	1.843	TURBINE RACK POSITION =	0.000		OUTLET PRESS.	(BAR) =	1.135
(TOTAL)	(PSI) =	26.74	COMPRESSOR VANE POSITION =	0.000		(TOTAL)	(PSI) =	16.46
PRESSURE RATIO	=	1.862				PRESSURE RATIO	=	1.885
MASS FLOW	(KG/HR) =	598.6	SHAFT TORQUE (N-M) =	0.9244		MASS FLOW	(KG/HR) =	648.5
	(LB/HR) =	1320.	(FT-LB) =	0.6818			(LB/HR) =	1430.
POWER	(KW) =	11.35	SHAFT POWER (KW) =	11.28		POWER	(KW) =	11.22
	(HP) =	15.22	(HP) =	15.13			(HP) =	15.04
EFFECTIVE DIAMETER	(M) =	0.5030E-01	EXTERNAL POWER [kW] =	0.000		EFFECTIVE DIAMETER	(M) =	0.5066E-01
ISEN. EFF. (INST.	%) =	83.97				ISEN. EFF. (INST.	%) =	35.69
(AVG.	%) =	84.72				(AVG.	%) =	36.45
BLADE SPEED RATIO(INST)	=	0.9098				BLADE SPEED RATIO(INST)	=	0.5340
(AVG)	=	0.9027				(AVG)	=	0.5289
MECH. EFFICIENCY	(%) =	100.0				MECH. EFFICIENCY	(%) =	100.0

ENGINE SUMMARY

NC	MASS IN KG/HR	VOL.EFF.	TRAP.RATIO	IMEP BAR	PMEP BAR	IHP	TEXH K	RES(%)	EGR(%)	PHI	PMAX BAR	HTR KW
1	205.4	1.606	0.9957	15.42	-0.6053	61.57	1031.	1.737	0.000	0.6220	92.45	10.76
2	206.6	1.615	0.9966	15.46	-0.6215	61.72	1028.	1.824	0.000	0.6155	92.83	10.80
3	209.8	1.641	0.9956	15.55	-0.6375	62.06	1017.	1.712	0.1157E-01	0.6076	94.36	10.78
4	206.6	1.615	0.9943	15.48	-0.5926	61.78	1027.	1.610	0.000	0.6198	92.82	10.73
5	204.7	1.601	0.9990	15.39	-0.6808	61.43	1036.	2.239	0.000	0.6201	92.61	10.95
6	207.9	1.626	0.9992	15.47	-0.7054	61.76	1025.	2.165	0.1287E-01	0.6115	94.39	10.95

BREATHING QUANTITIES:

AMB.VOL.EFF	(AIR IN / AMB. REF.) =	1.617	TRAP.RAT.	(FRESH TR./ FRESH IN) =	0.997
DEL.EFF.	(FRESH IN / PLEN. REF.) =	0.963	SCAV.RAT.	(GAS IN / GAS TR.) =	0.984
CHARG.EFF.	(FRESH TR./ PLEN. REF.) =	0.960	SCAV.EFF.	(FRESH TR./ GAS TR.) =	0.981
TOT.DEL.EFF	(GAS IN / PLEN. REF.) =	0.963	RESID.FR.	(RESID TR./ GAS TR.) =	0.019
EGR FR.	(RESID IN / GAS IN) =	0.000			

E N G I N E G E O M E T R Y

DISPL./CYL. (LIT.)	= 1.984	NUMBER OF CYLINDERS	= 6.000				
(IN3)	= 121.1	COMPRESSION RATIO	= 17.00	EFFECTIVE CR (VC-TDC)	= 15.49		
BORE (MM)	= 132.0	BORE/STROKE	= 0.9103				
(IN)	= 5.197	CON. ROD LENGTH(MM)	= 261.7				
STROKE (MM)	= 145.0	WRIST PIN OFFSET(MM)	= 0.000				
(IN)	= 5.709	CLEARANCE VOL. (M3)	= 0.1240E-03	ENGINE TYPE	= DIESEL		
INT. VALVE DIA.(MM)	= 40.70	EXH. VALVE DIA.(MM)	= 36.70	#1 EVO	= 130.8		
MAX. LIFT (MM)	= 10.23	MAX. LIFT (MM)	= 11.10	#1 EVC	= 379.4		
				#1 IVO	= 342.4		
NO. INTAKE VALVES	= 2.000	NO. EXHAUST VALVES	= 2.000	#1 IVC	= 581.3		

O P E R A T I N G C O N D I T I O N S

RPM	= 1800.	#1 INT.PORT PR(BAR)	= 1.711	#1 IGN DELAY (CA)	= 2.326
AMB. PRESSURE (BAR)	= 1.004	(IN.HG)	= 50.68	#1 COMB. START (CA)	= -0.1743
(IN.HG)	= 29.73	#1 INT.PORT TEMP(K)	= 296.3	INJ.TIMING (ATDC)	= -2.500
AMB. TEMP. (K)	= 291.9	(F)	= 73.61	MID.INJ.PRESS.(BAR)	= 500.0
(F)	= 65.75	#1 EXH.PORT PR(BAR)	= 2.212	(PSI)	= 7252.
FUEL TYPE (C:H:O) C	= 15.00	(IN.HG)	= 65.49	INJ.DURATION (CA)	= 15.00
H	= 25.05			FUEL RATE (KG/HR)	= 53.58
O	= 0.000	PISTON VEL. (M/S)	= 8.700	(MULTI) (LBM/HR)	= 118.2
FUEL LHV (MJ/KG)	= 42.80	(FT/MIN)	= 1713.	#1 FUEL / SHOT (KG)	= 0.1656E-03
(BTU/LBM)	= 0.1840E+05			CYL. FUEL TEMP. (K)	= 350.0
(A/F) STOICH	= 14.22			1% FUEL PWR/CYL (W)	= 1062.
FUEL MOLEC. WEIGHT	= 205.4				
CETANE NUMBER	= 60.00			PREMIXED BURN FR.	= 0.1005E-01

P R E D I C T E D P E R F O R M A N C E

INDIC. POWER (HP)	= 370.3	BRAKE POWER (HP)	= 356.8	PMEP (BAR)	= -0.6405
IND.EFFICIENCY (%)	= 43.35	BRAKE EFFICIENCY(%)	= 41.77	(PSI)	= -9.290
IMEP(NET) (BAR)	= 15.46	BMEP (BAR)	= 14.90	FMEP (BAR)	= 0.5645
(PSI)	= 224.3	(PSI)	= 216.1	(PSI)	= 8.188
ISFC (KG/KWH)	= 0.1940	BSFC (KG/KWH)	= 0.2014	IMEP(GROSS) (BAR)	= 16.10
(LBM/BHP-HR)	= 0.3190	(LBM/BHP-HR)	= 0.3311	(PSI)	= 233.6
IND. TORQUE (N-M)	= 1465.	BRAKE TORQUE (N-M)	= 1412.	FRICT. TORQUE (N-M)	= 53.48
(FT-LB)	= 1080.	(FT-LB)	= 1041.	PUMP. TORQUE (N-M)	= -60.69
AUXILIARY POWER [hp]	= 0.000			#1 EXHAUST TEMP (K)	= 1031.
AUXILIARY POWER [kW]	= 0.000			(F)	= 1397.
IND. ENERGY BALANCE:(MULTI)		FRESH AIR IN (KG/H)	= 1241.	#1 PMAX (BAR)	= 92.45
NET PISTON WORK (%)	= 43.35	(WET) (LBM/HR)	= 2736.	(PSI)	= 1341.
AVAIL.EXH.ENTH. (%)	= 9999.	TRAPPING RATIO	= 0.9967	#1 CA AT PMAX	= 11.15
DEBIT INTK.ENTH.(%)	= 9999.	VOL.EFF.(DELIVERED)	= 1.617	#1 MAX DP/DTH (BAR)	= 2.670
H. TRAN.(IN-CYL)(%)	= 10.20	#1 VOL.EFF.(PLENUM)	= 0.9561	(PER DEG) (PSI)	= 38.73
BLOWBY AT RING1 (%)	= 9999.	A/F TRAPPED	= 23.08	#1 CA AT MAX DP/DTH	= -13.01
IMBALANCE (%)	= 9999.	PHI TRAPPED	= 0.6161	#1 MAX AVG.GAS T(K)	= 1818.
PUMPING WORK (%)	= -1.796	RESIDUAL FRAC. (%)	= 1.882	(F)	= 2813.
		BRAKE POWER (KW)	= 266.1	FRIC. (%FUEL ENER.)	= 1.583
				H.TRAN.(IN-CYL)(KW)	= 64.96

E N G I N E O U T E M I S S I O N S

NOx (PPM)	= 1241.	HC EMISSIONS (PPMC1)	= 42.97	CO EMISSIONS (PPM)	= 395.1
NOx AS NO2 (g/hr)	= 2563.	(g/hr)	= 26.41	(g/hr)	= 496.7
(g/bkW-hr)	= 9.633	(g/bkW-hr)	= 0.9928E-01	(g/bkW-hr)	= 1.867

ENGINE CYLINDER BACKFLOW

CYL	BEFORE EVC AMOUNT(KG)	BEFORE EVC % OF TOTAL	AFTER EVC AMOUNT(KG)	AFTER EVC % OF TOTAL
1	0.9764E-06	0.2568E-01	0.2001E-03	5.262
2	0.1508E-05	0.3942E-01	0.2149E-03	5.617
3	0.9136E-08	0.2351E-03	0.2107E-03	5.421
4	0.1595E-06	0.4169E-02	0.1974E-03	5.160
5	0.4283E-05	0.1130	0.2167E-03	5.717
6	0.8981E-06	0.2332E-01	0.2121E-03	5.507

ENGINE INTAKE VALVE BACKFLOW

CYL	VAL	BEFORE EVC AMOUNT(KG)	BEFORE EVC % OF TOTAL	AFTER EVC AMOUNT(KG)	AFTER EVC % OF TOTAL	REVERSE ANGLE
1	1	0.1607E-06	0.8729E-02	0.1394E-03	7.572	539.4
1	1	0.8157E-06	0.4159E-01	0.6068E-04	3.093	551.3
2	1	0.4102E-08	0.2215E-03	0.1396E-03	7.536	540.4
2	1	0.1504E-05	0.7621E-01	0.7529E-04	3.816	549.1
3	1	0.4493E-08	0.2374E-03	0.1392E-03	7.355	541.3
3	1	0.4643E-08	0.2329E-03	0.7149E-04	3.586	549.5
4	1	0.1498E-06	0.7590E-02	0.5941E-04	3.010	552.0
4	1	0.9670E-08	0.5223E-03	0.1380E-03	7.452	539.3
5	1	0.3124E-05	0.1598	0.7662E-04	3.919	549.0
5	1	0.1159E-05	0.6316E-01	0.1401E-03	7.631	541.0
6	1	0.4105E-07	0.2080E-02	0.7508E-04	3.804	550.4
6	1	0.8571E-06	0.4565E-01	0.1370E-03	7.298	543.5

CYCLE AVERAGED ENGINE CYLINDER EXHAUST INDICATED SPECIFIC EMISSIONS

CYL	NO (g/kW/hr)	NO (g/hp/hr)	NO2 (g/kW/hr)	NO2 (g/hp/hr)	CO (g/kW/hr)	CO (g/hp/hr)	HC (g/kW/hr)	HC (g/hp/hr)
1	5.978	4.458	0.000	0.000	1.901	1.418	0.9578E-01	0.7142E-01
2	6.019	4.488	0.000	0.000	1.837	1.370	0.9565E-01	0.7132E-01
3	6.213	4.633	0.000	0.000	1.620	1.208	0.9544E-01	0.7117E-01
4	5.983	4.461	0.000	0.000	1.854	1.383	0.9566E-01	0.7134E-01
5	5.963	4.447	0.000	0.000	1.915	1.428	0.9581E-01	0.7145E-01
6	6.164	4.597	0.000	0.000	1.667	1.243	0.9558E-01	0.7127E-01

CYCLE AVERAGED AMBIENT EMISSIONS

AMBIENT	NO (g/hr)	NO2 (g/hr)	CO (g/hr)	HC (g/hr)
amb1	0.000	0.000	0.000	0.000
amb2	0.000	0.000	0.000	0.000
amb3	1666.	0.000	497.7	26.39

Appendix D – Deutz Wave Simulation Results

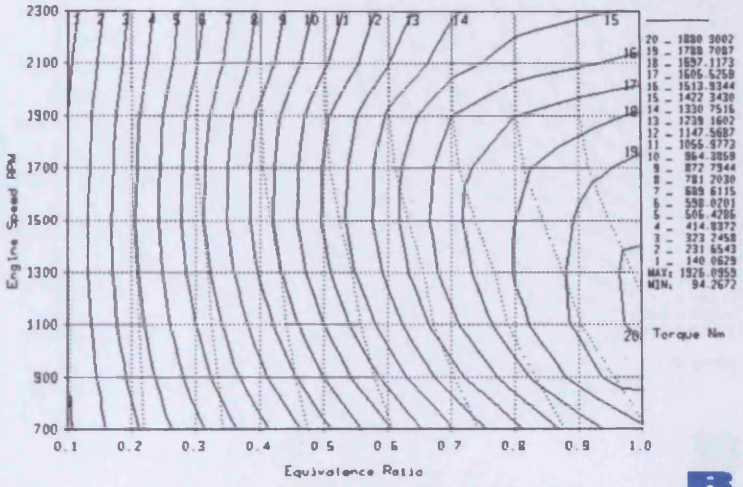

Deutz 1015 torque predictions

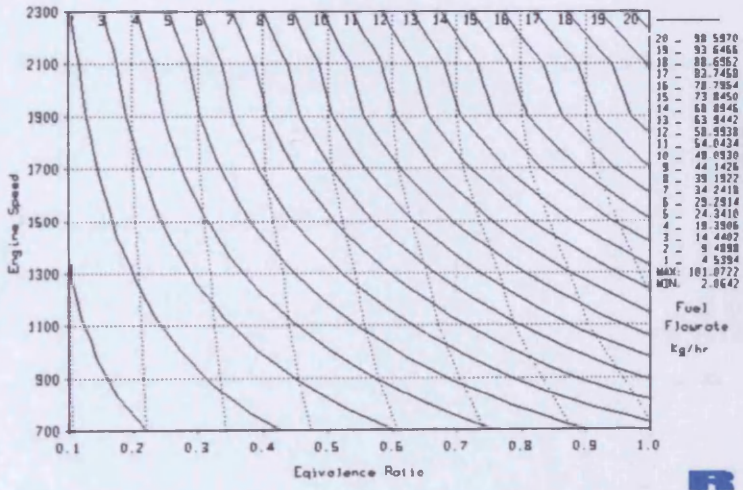

Deutz 1015 fuel flow predictions

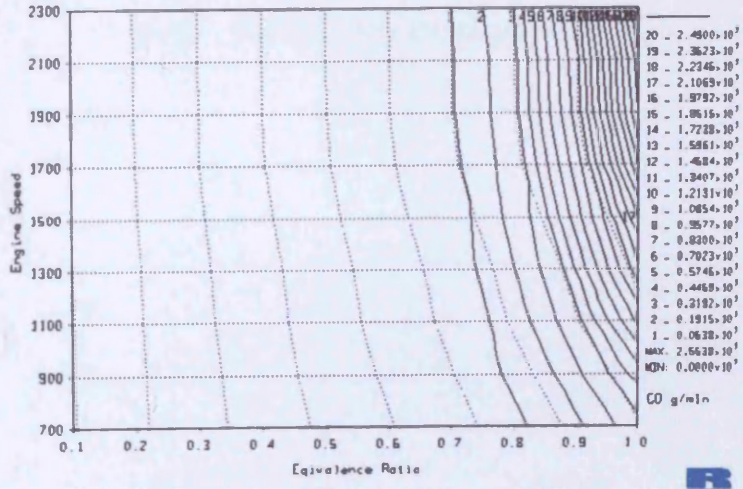

Deutz 1015 CO emission predictions

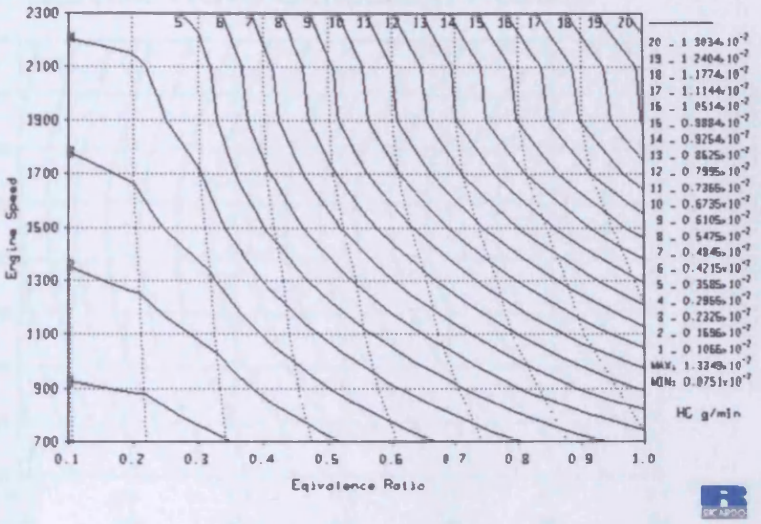

Deutz 1015 HC emission predictions

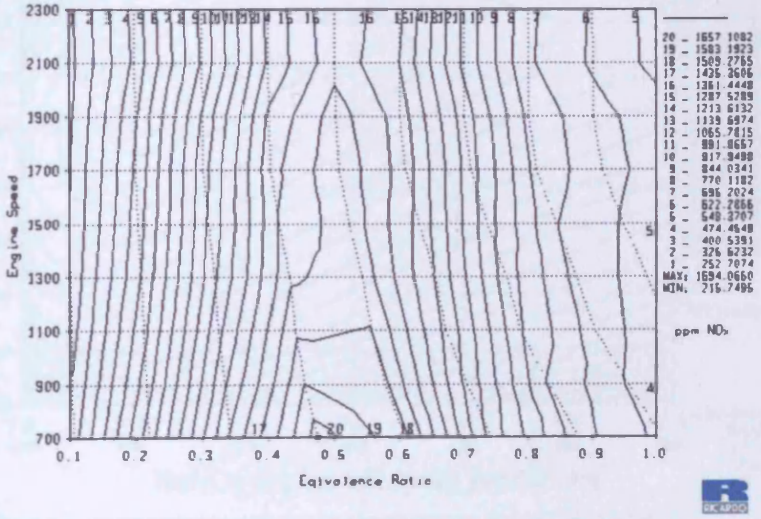

Deutz 1015 NO_X emission predictions

Appendix E – NoNOx Wave Simulation Results

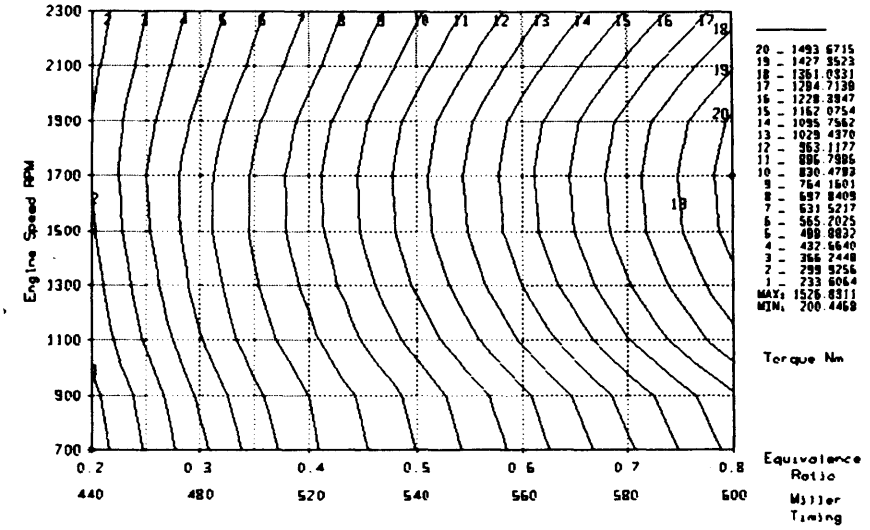

NoNOx engine torque predictions

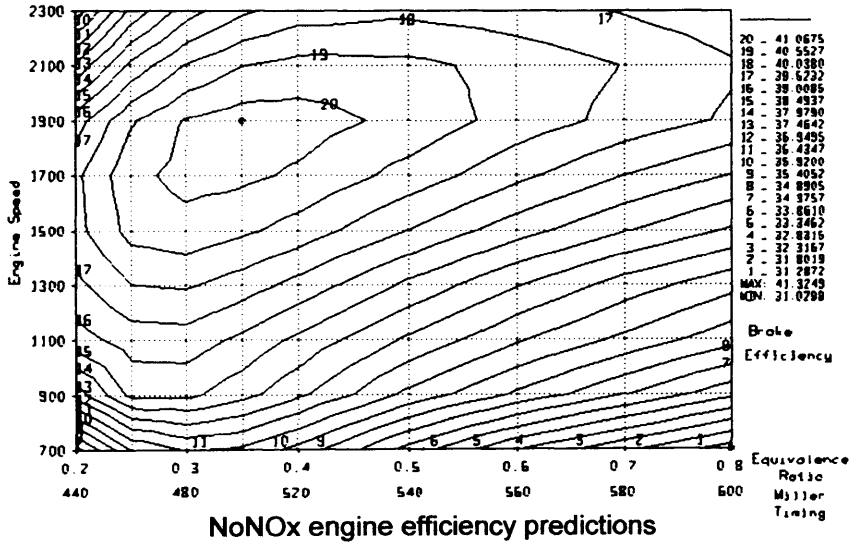

NoNOx engine efficiency predictions

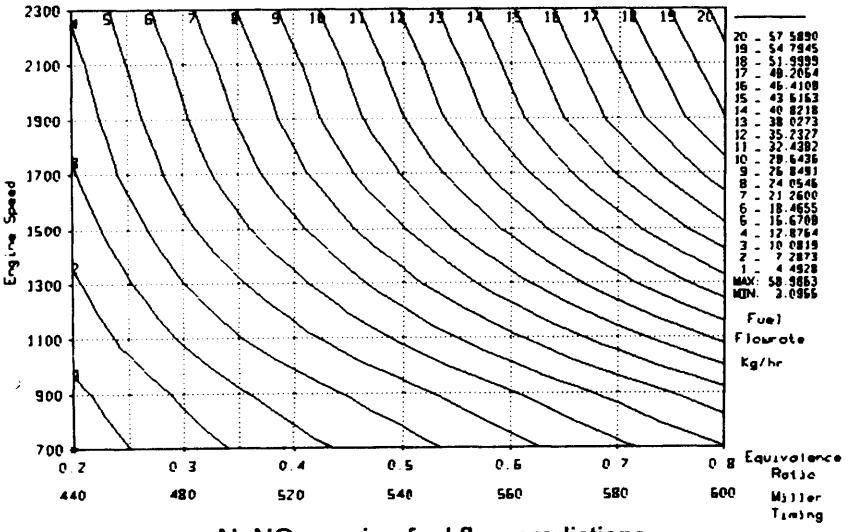

NoNOx engine fuel flow predictions

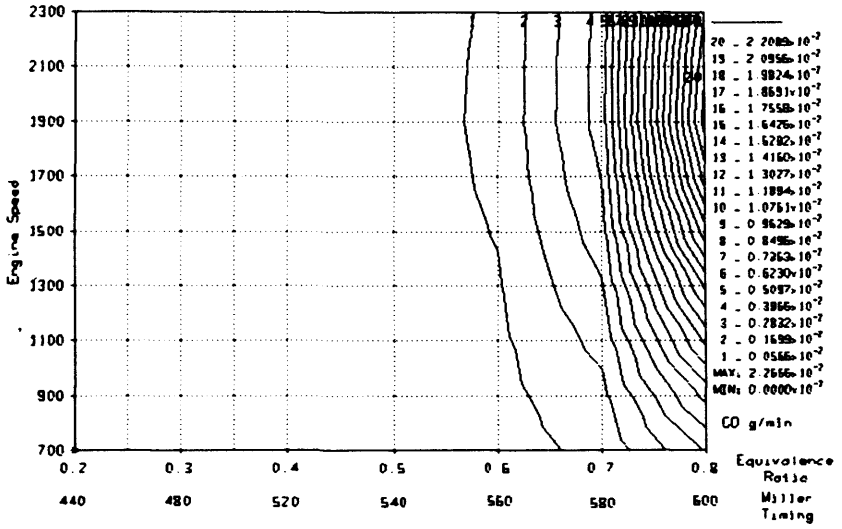

NoNOx engine CO emission predictions

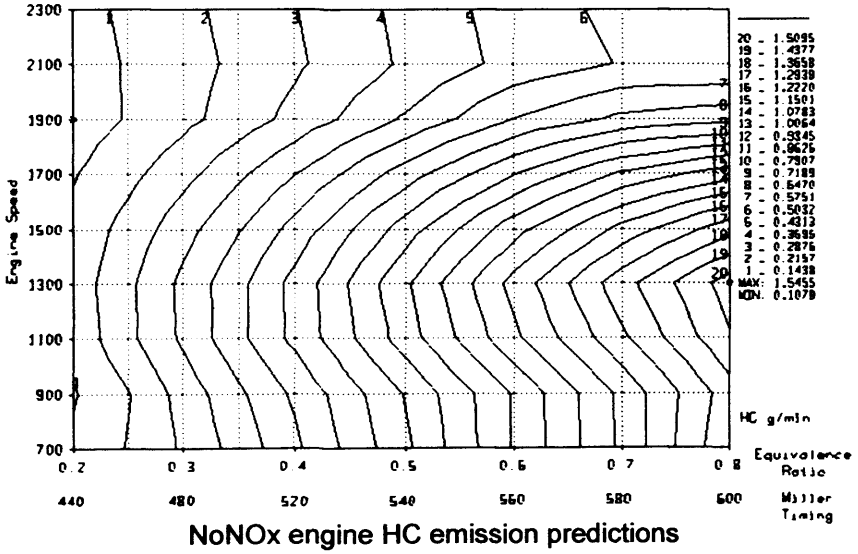

NoNOx engine HC emission predictions

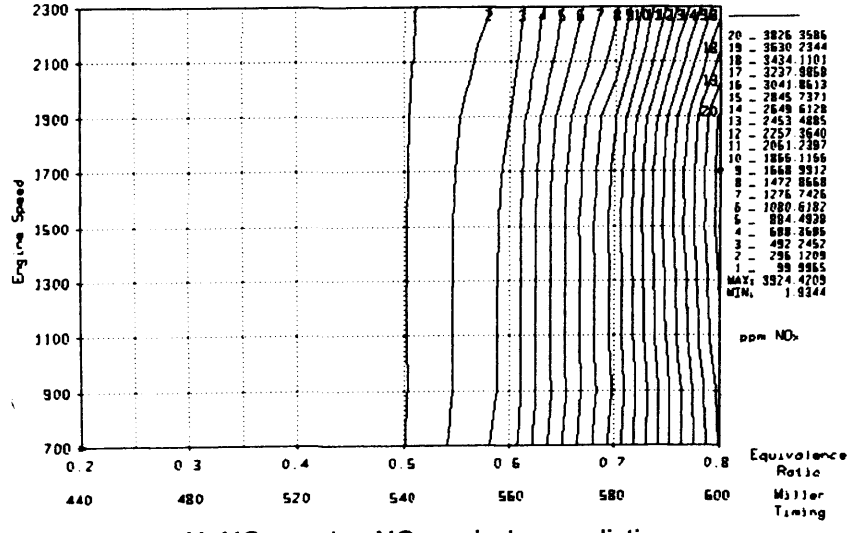

NoNOx engine NO_X emission predictions

Appendix F – Sample Vectis Input File

```
!VECTIS_MAIN_INPUT MODULAR VERSION 3.400
OUTPUT_DIRECTORY
H:\G3 comparison
#=============================================================================
INPUT_DIRECTORY
H:\G3 comparison
#=============================================================================
EQUATIONS
EQN_U_MOMENTUM
EQN_V_MOMENTUM
EQN_W_MOMENTUM
EQN_PRESSURE
EQN_TURBULENCE_ENERGY
EQN_TURBULENCE_DISSIPATION
EQN_PASSIVE_SCALAR
#=============================================================================
U_MOMENTUM
 5 2 0 2 -6
 1.0000e-001 1.0000e+000 1.0000e+000 1.0000e+000 1.0000e+000 1.0000e+000 1.0000e+000
#=============================================================================
V_MOMENTUM
 5 2 0 2 -6
 1.0000e-001 1.0000e+000 1.0000e+000 1.0000e+000 1.0000e+000 1.0000e+000 1.0000e+000
#=============================================================================
W_MOMENTUM
 5 2 0 2 -6
 1.0000e-001 1.0000e+000 1.0000e+000 1.0000e+000 1.0000e+000 1.0000e+000 1.0000e+000
#=============================================================================
PRESSURE
 10 1 3 2 -8
 1.0000e-001 1.0000e+000 1.0000e+000 1.0000e+000 1.0000e+000 1.0000e+000 1.0000e+000
#=============================================================================
TURBULENCE_ENERGY
 10 1 0 2 -6
 1.0000e-001 1.0000e+000 1.0000e+000 1.0000e+000 1.0000e+000 1.0000e+000 1.0000e+000
#=============================================================================
TURBULENCE_DISSIPATION
 10 1 0 2 -6
 1.0000e-001 1.0000e+000 1.0000e+000 1.0000e+000 1.0000e+000 1.0000e+000 1.0000e+000
#=============================================================================
PASSIVE_SCALAR
 10 1 0 2 -6
 1.0000e-001 1.0000e+000 1.0000e+000 1.0000e+000 1.0000e+000 1.0000e+000 1.0000e+000
#=============================================================================
SOLUTION_CONTROL_2
F
-1 1.000000e-008
0.000000e+000 1.200000e-002 1.000000e+000
2 5.000000e-005 1.000000e-004
#=============================================================================
ALGORITHM
PISO
#=============================================================================
SOLVER_SCHEME
 1
#=============================================================================
CORRECTION_STEP_NUMBER
 5
#=============================================================================
REFERENCE_POINT
 19 41 15
#=============================================================================
MONITORING_POINT_IJK
17 21 21
MON
#=============================================================================

CHECKPOINT
F F F 10 F F
T
#=============================================================================
LINK_FILE
0100.dat
CROSS_LINK_TIMEREGION
 1 0.000000e+000
#
LINK_FILE
0500.dat
CROSS_LINK_TIMEREGION
 2 1.700000e-004
#
LINK_FILE
0750.dat
CROSS_LINK_TIMEREGION
 3 4.100000e-004
#
LINK_FILE
1000.dat
CROSS_LINK_TIMEREGION
 4 6.000000e-004
#
LINK_FILE
1500.dat
CROSS_LINK_TIMEREGION
 5 7.900000e-004
#
LINK_FILE
1903.dat
CROSS_LINK_TIMEREGION
 6 1.110000e-003
#
LINK_FILE
2000.dat
CROSS_LINK_TIMEREGION
 7 1.260000e-003
#
```

```
LINK_FILE
2500.dat
CROSS_LINK_TIMEREGION
 8 1.430000e-003
#
LINK_FILE
3000.dat
CROSS_LINK_TIMEREGION
 9 1.750000e-003
#
LINK_FILE
3500.dat
CROSS_LINK_TIMEREGION
 10 2.090000e-003
#
LINK_FILE
4000.dat
CROSS_LINK_TIMEREGION
 11 2.460000e-003
#
LINK_FILE
4235.dat
CROSS_LINK_TIMEREGION
 12 2.780000e-003
#
LINK_FILE
4500.dat
CROSS_LINK_TIMEREGION
 13 2.950000e-003
#
LINK_FILE
5000.dat
CROSS_LINK_TIMEREGION
 14 3.340000e-003
#
LINK_FILE
5500.dat
CROSS_LINK_TIMEREGION
 15 3.940000e-003
#
LINK_FILE
6000.dat
CROSS_LINK_TIMEREGION
 16 5.270000e-003
#
#=============================================================================
CROSSLINK_DROPLET_RELOCATION
 F
#=============================================================================
BOUNDARY_MOTION
 4 1 3 1 1
 0.000000e+000 0.000000e+000 1.000000e+000
 0.000000e+000 1.000000e-004
 7.000000e-005 0.000000e+000
 1.700000e-004 -1.432300e-004
BOUNDARY_MOTION
 4 1 4 2 2
 0.000000e+000 0.000000e+000 1.000000e+000
 1.699999e-004 2.567700e-004
 2.500000e-004 1.429500e-004
 3.400000e-004 4.200000e-007
 4.100000e-004 -9.983000e-005
BOUNDARY_MOTION
 4 1 3 3 3
 0.000000e+000 0.000000e+000 1.000000e+000
 4.099990e-004 1.501700e-004
 5.100000e-004 -3.000000e-007
 6.000000e-004 -1.493000e-004
BOUNDARY_MOTION
 4 1 3 4 4
 0.000000e+000 0.000000e+000 1.000000e+000
 5.999990e-004 1.007000e-004
 6.700000e-004 6.400000e-007
 7.900000e-004 -2.008400e-004
BOUNDARY_MOTION
 4 1 4 5 5
 0.000000e+000 0.000000e+000 1.000000e+000
 7.899999e-004 2.991600e-004
 9.800000e-004 1.260000e-006
 1.050000e-003 -1.003600e-004
 1.110000e-003 -1.987700e-004
BOUNDARY_MOTION
 4 1 2 6 6
 0.000000e+000 0.000000e+000 1.000000e+000
 1.109999e-003 2.042300e-004
 1.240000e-003 1.490000e-006
BOUNDARY_MOTION
 4 1 3 7 7
 0.000000e+000 0.000000e+000 1.000000e+000
 1.239999e-003 9.800000e-005
 1.300000e-003 6.650000e-007
 1.430000e-003 -2.001900e-004
BOUNDARY_MOTION
 4 1 3 8 8
 0.000000e+000 0.000000e+000 1.000000e+000
 1.430000e-003 2.998100e-004
 1.620000e-003 -5.200000e-007
 1.750000e-003 -2.011600e-004
BOUNDARY_MOTION
 4 1 3 9 9
 0.000000e+000 0.000000e+000 1.000000e+000
 1.749999e-003 2.988400e-004
 1.950000e-003 -8.700000e-007
 2.090000e-003 -1.996600e-004
BOUNDARY_MOTION
 4 1 3 10 10
 0.000000e+000 0.000000e+000 1.000000e+000
 2.089990e-003 3.003400e-004
 2.310000e-003 3.800000e-007
 2.460000e-003 -1.990400e-004
BOUNDARY_MOTION
 4 1 2 11 11
 0.000000e+000 0.000000e+000 1.000000e+000
 2.459999e-003 3.009600e-004
 2.700000e-003 9.300000e-006
```

```
BOUNDARY_MOTION
 4 1 3 12 12
 0.000000e+000 0.000000e+000 1.000000e+000
 2.699999e-003 2.359300e-004
 2.900000e-003 4.200000e-007
 2.950000e-003 -6.492000e-005
BOUNDARY_MOTION
 4 1 3 13 13
 0.000000e+000 0.000000e+000 1.000000e+000
 2.949999e-003 2.000800e-004
 3.140000e-003 -2.000000e-007
 3.340000e-003 -1.995600e-004
BOUNDARY_MOTION
 4 1 3 14 14
 0.000000e+000 0.000000e+000 1.000000e+000
 3.340000e-003 3.004400e-004
 3.690000e-003 1.100000e-007
 3.940000e-003 -1.997400e-004
BOUNDARY_MOTION
 4 1 3 15 15
 0.000000e+000 0.000000e+000 1.000000e+000
 3.939999e-003 3.002600e-004
 4.440000e-003 -2.700000e-007
 5.270000e-003 -2.996700e-004
BOUNDARY_MOTION
 4 1 4 16 16
 0.000000e+000 0.000000e+000 1.000000e+000
 5.269999e-003 6.000000e-005
 6.250000e-003 1.300900e-004
 6.790000e-003 2.343400e-004
 1.200000e-002 2.343400e-004
#==============================================================================
INLET_OUTLET_BOUNDARY
 2 0 1 1 4
INLET_OUTLET_BOUNDARY
 3 0 2 2 4
#==============================================================================
ZERO_DIMENSIONAL_DATA
1
1 5
0.000e+000 5.000e-002 1.000e+000 2.935e+002 1.022370e+005 1.000e-001 5.000e-004 0.000e+000
0.000000e+000 1.000000e+000 0.000000e+000 0.000000e+000
ZERO_DIMENSIONAL_DATA
2
1 5
0.000e+000 -5.000e-002 1.000e+000 2.935e+002 1.004130e+005 1.000e-001 5.000e-004 0.000e+000
0.000000e+000 1.000000e+000 0.000000e+000 0.000000e+000
#==============================================================================
WALL_BOUNDARY
 1
 3.000000e+002 5.000000e-005
WALL_BOUNDARY
 4
 3.000000e+002 5.000000e-005
#==============================================================================

INITIAL_CONDITION
0.000000e+000 0.000000e+000 0.000000e+000
1.000e+000 0.000e+000 0.000e+000 0.000e+000 0.000e+000 0.000e+000 0.000e+000
1.000e-001 5.000e-004 1.004150e+005 2.935e+002 0.000e+000
0.000e+000 1.000e+000 0.000e+000 0.000e+000
#==============================================================================
PRANDTL_NUMBER
7.000e-001
#==============================================================================
SPECIES_DATA
 1.604e+001
 1.7450e+003 1.5900e-001 0.0000e+000 0.0000e+000 0.0000e+000
 6.7055e-006 4.5297e-008 -1.2064e-011 1.6092e-015 0.0000e+000
#==============================================================================
SPECIES_DATA
 2.897e+001
 1.0470e+003 -1.3417e-001 2.7578e-004 -1.5304e-007 3.8210e-011
 6.7055e-006 4.5297e-008 -1.2064e-011 1.6092e-015 0.0000e+000
#==============================================================================
SPECIES_DATA
 2.918e+001
 1.0470e+003 -1.3417e-001 2.7578e-004 -1.5304e-007 3.8210e-011
 6.7055e-006 4.5297e-008 -1.2064e-011 1.6092e-015 0.0000e+000
#==============================================================================
SPECIES_DATA
 2.800e+001
 1.0470e+003 -1.3417e-001 2.7578e-004 -1.5304e-007 3.8210e-011
 6.7055e-006 4.5297e-008 -1.2064e-011 1.6092e-015 0.0000e+000
#==============================================================================
SPRAY_CALCULATION
 F
#==============================================================================
TURBULENCE_MODEL
 2
#==============================================================================
SCALE_RESTART
 1.000e+000
#==============================================================================
```

Appendix G - NoNOx Wave Simulation Results (10% H_2, 90% CH_4)

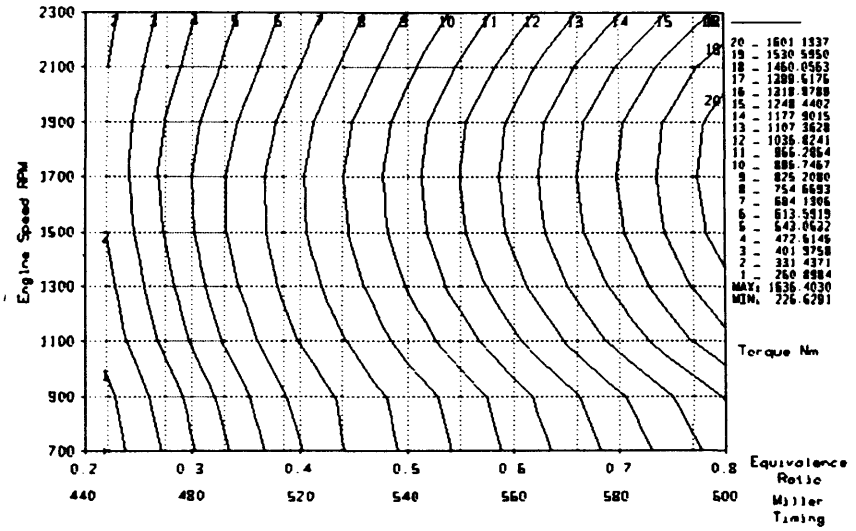

NoNOx engine torque predictions

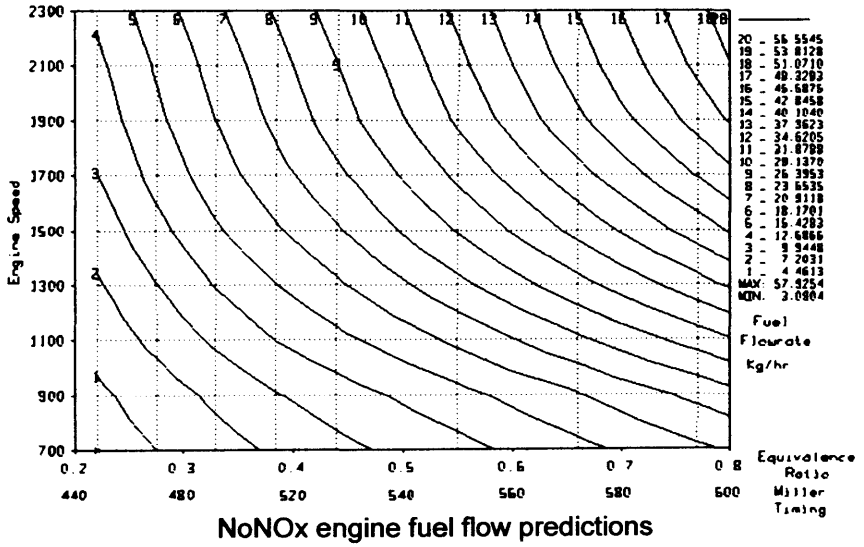

NoNOx engine fuel flow predictions

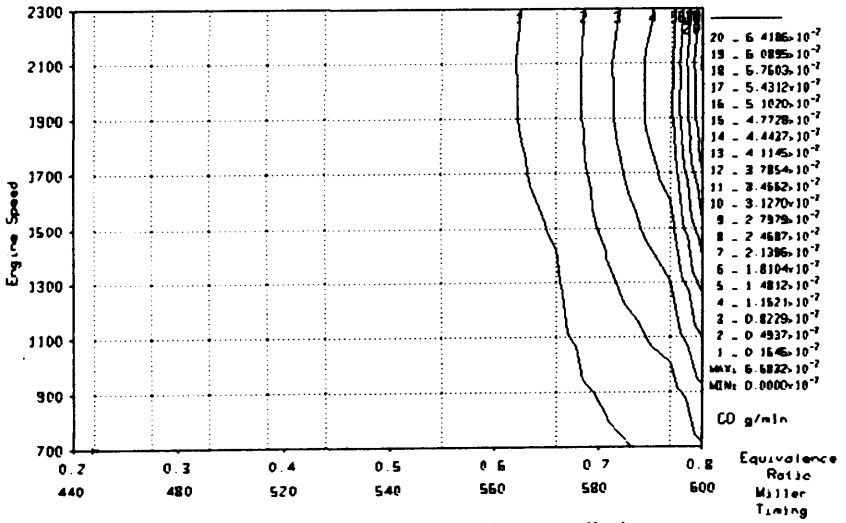

NoNOx engine CO emission predictions

Appendix H – NoNOx Engine Specifications

NONOX

Natural Gas Engines for Heavy-Duty Vehicles

The development of the NONOX engine started in 1995 with the formation of the NONOX company. The company developed and built its own engine test bench facility and is therefore independent to develop and adapt new technologies. NONOX employs a powerful team of highly skilled and experienced engineers with expertise in the field of engine- and micro-electronic-technology.

One of the innovative NONOX-developed technologies is the Electromagnetic Operated Control Valve [EOCV] system, a system which substantially improves the efficiency of SI Natural Gas engines up to diesel like values.

The EOCV system was first applied and tested on a single cylinder test bench where the concept proved its validity. Following those results, a second and third generation of the valve was developed and finally applied to a 300 kW DEUTZ V6 engine.

The EOCV system replaces the throttle plate of a conventional SI Natural Gas engine it avoids pumping losses and it enables the application of significant higher compression ratios.

A very important feature of the EOCV valve as used in the NONOX engine is that it operates completely electronically controlled without mechanical drive from the engine. The EOCV valve uses its own actuator which is controlled by its own valve control system. This means that the operation of the valve can be controlled independently. No structural mechanical redesign of the original engine is necessary.

Of course the NONOX engine also has its own engine management system in which total control of all engine functions are co-ordinated. The valve control electronics are interfaced with the overall engine management system by means of a CAN J1939 based interface.

The advantages of the NONOX engine:

- Fuel cost benefits compared to HDDE
- Same power as HDDE
- Specific fuel consumption within scatter of 0-5% compared to HDDE over entire map
- Reduction in CO2 emission of 25% compared to HDDE
- Emission legislation level EURO 4 and EURO5 / EEV
- Air-Fuel-ratio control
- Anti knock control
- Misfire detection control
- Diagnostics

Power range 12.000 ccm NONOX engine

NONOX NG 230 - A	
Engine specifications	
No. of cylinders	V6
max. Torque [Nm]	1300
Output [kW]	230
Cylinder bore [mm]	132
Piston stroke [mm]	145
Displacement [l]	11.906
CR	13.5:1
Weight dry [kg]	830
Emission levels	EEV

NONOX NG 270 - A	
Engine specifications	
No. of cylinders	V6
max. Torque [Nm]	1500
Output [kW]	270
Cylinder bore [mm]	132
Piston stroke [mm]	145
Displacement [l]	11.906
CR	13.5:1
Weight dry [kg]	830
Emission levels	EEV

NONOX NG 300 - A	
Engine specifications	
No. of cylinders	V6
max. Torque [Nm]	1780
Output [kW]	300
Cylinder bore [mm]	132
Piston stroke [mm]	145
Displacement [l]	11.906
CR	13.5:1
Weight dry [kg]	830
Emission levels	EEV

Same power as HDDE and high torque at low engine speeds

Diesel like specific fuel cosumption even at low loads due to throttle free load control valve

NONOX BV is a joint venture between GET Gas Engine Technologie BV and RDM Technology BV

Natural Gas Engines for Heavy-Duty Vehicles

The NONOX NG application

The NONOX NG engine has been developed using a 1015 DEUTZ base engine.

The NONOX engine is a dedicated Natural Gas Engine. A LPG version can be made available on demand.

This NONOX/DEUTZ engine has been fully tested and qualified and is now ready for series production.

Although the NONOX technology has been developed on a DEUTZ engine, the technology as such can be applied as an add-on system to any series production engine.

NONOX

NONOX BV
Economiestraat 39
NL - 6433 KC Hoensbroek

Tel. +31 (0) 45 56 30 584
Fax +31 (0) 45 56 30 287
E-mail: info@nonox-bv.com
Internet www.nonox-bv.com

Your contact persons

Paul Uitenbroek
Technical Director

Jan Olierook
Sales Manager

Appendix I – Miller Cycle CFD Results

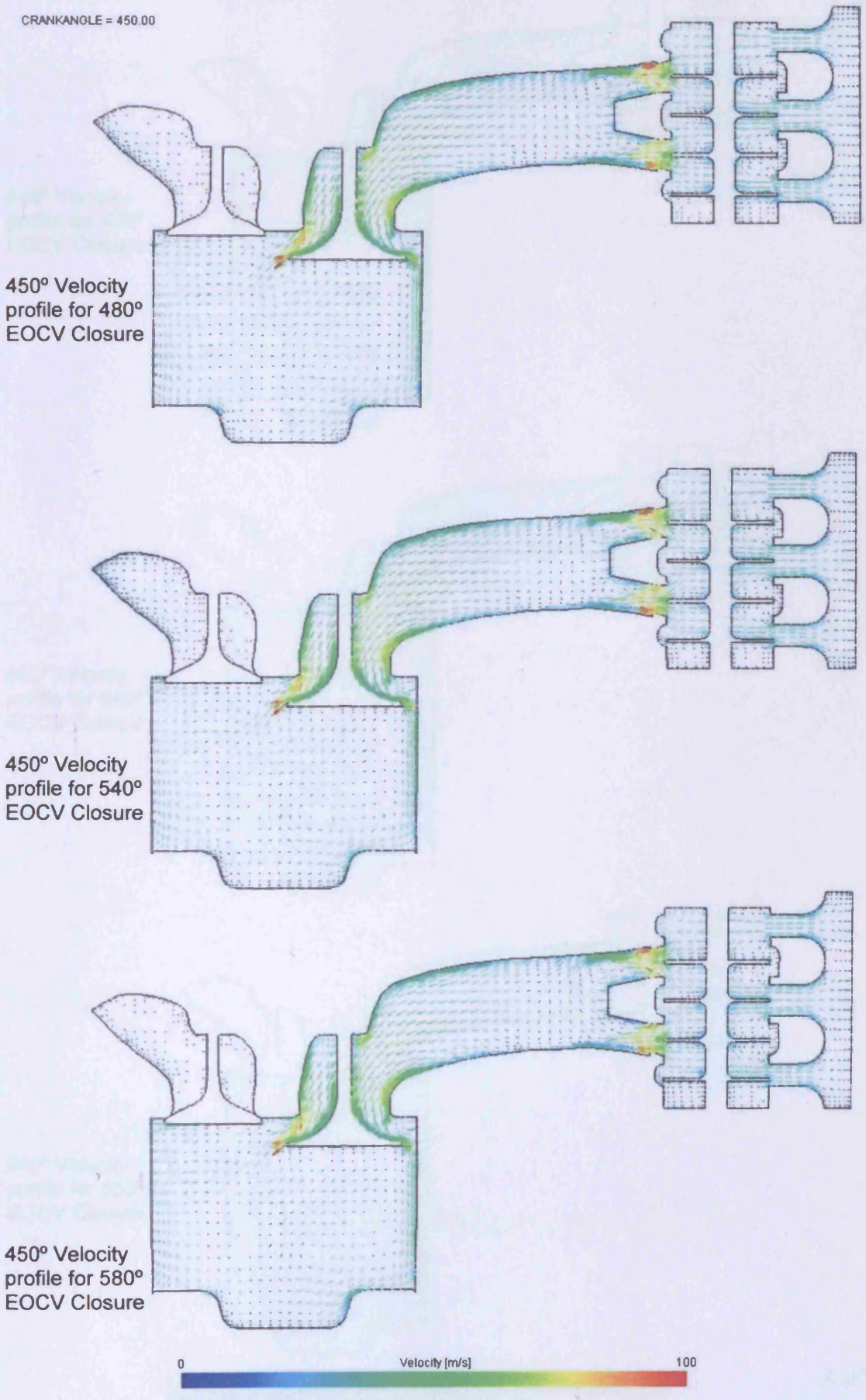

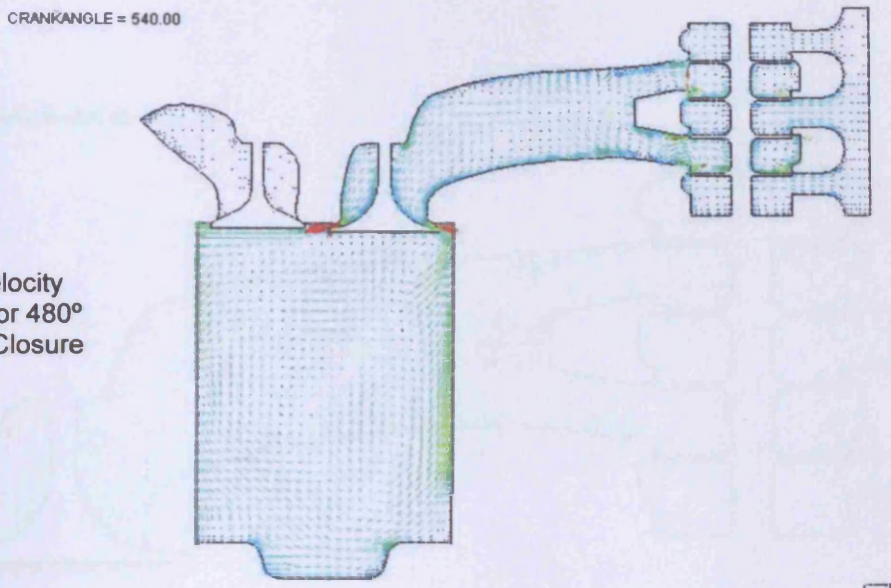

540° Velocity profile for 480° EOCV Closure

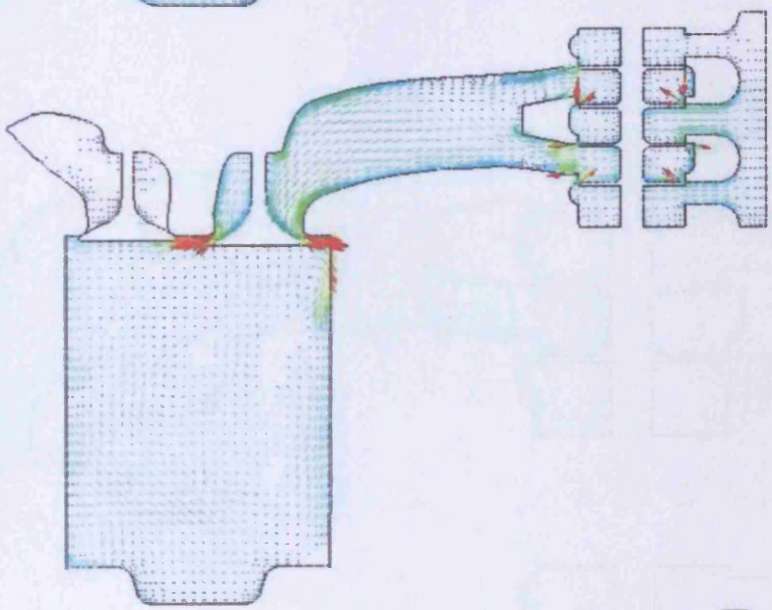

540° Velocity profile for 540° EOCV Closure

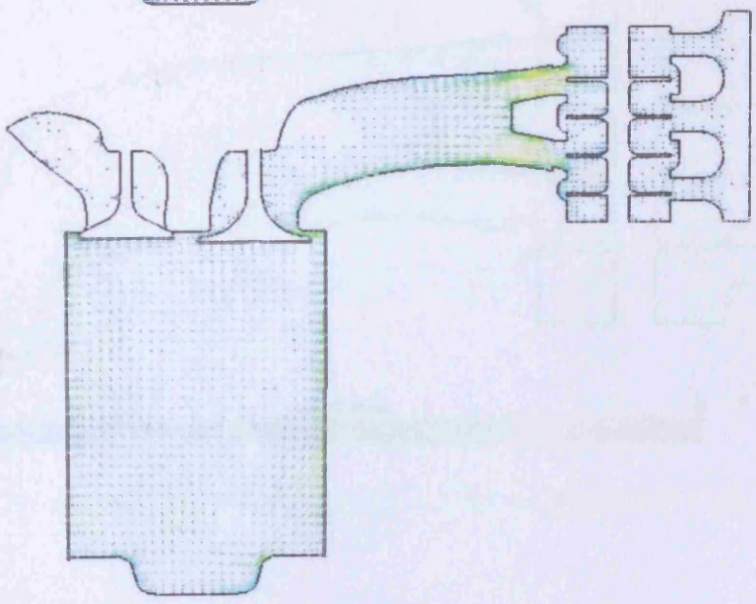

540° Velocity profile for 580° EOCV Closure

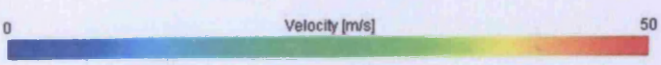

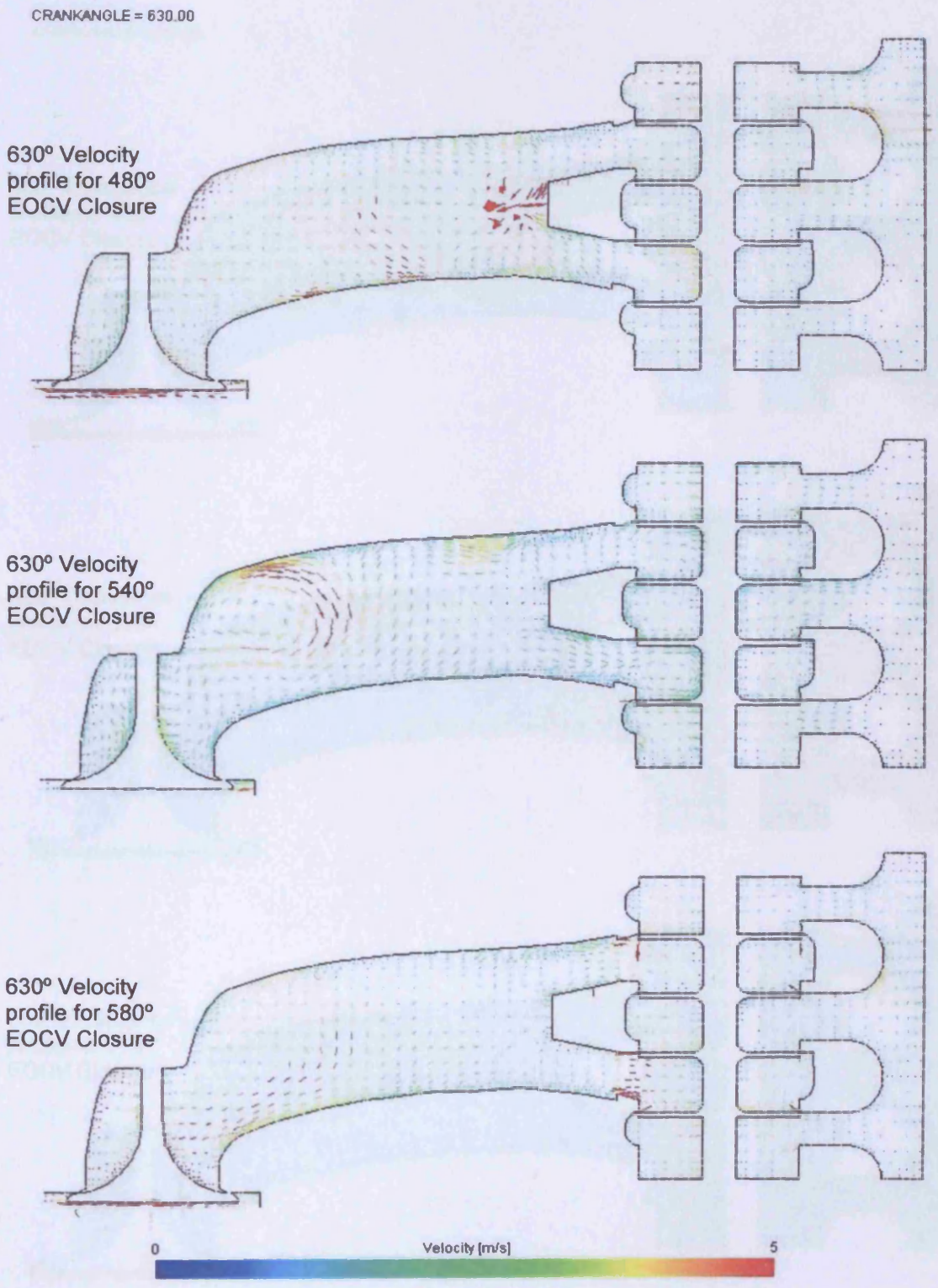
CRANKANGLE = 630.00
630° Velocity profile for 480° EOCV Closure
630° Velocity profile for 540° EOCV Closure
630° Velocity profile for 580° EOCV Closure
0
Velocity [m/s]
5

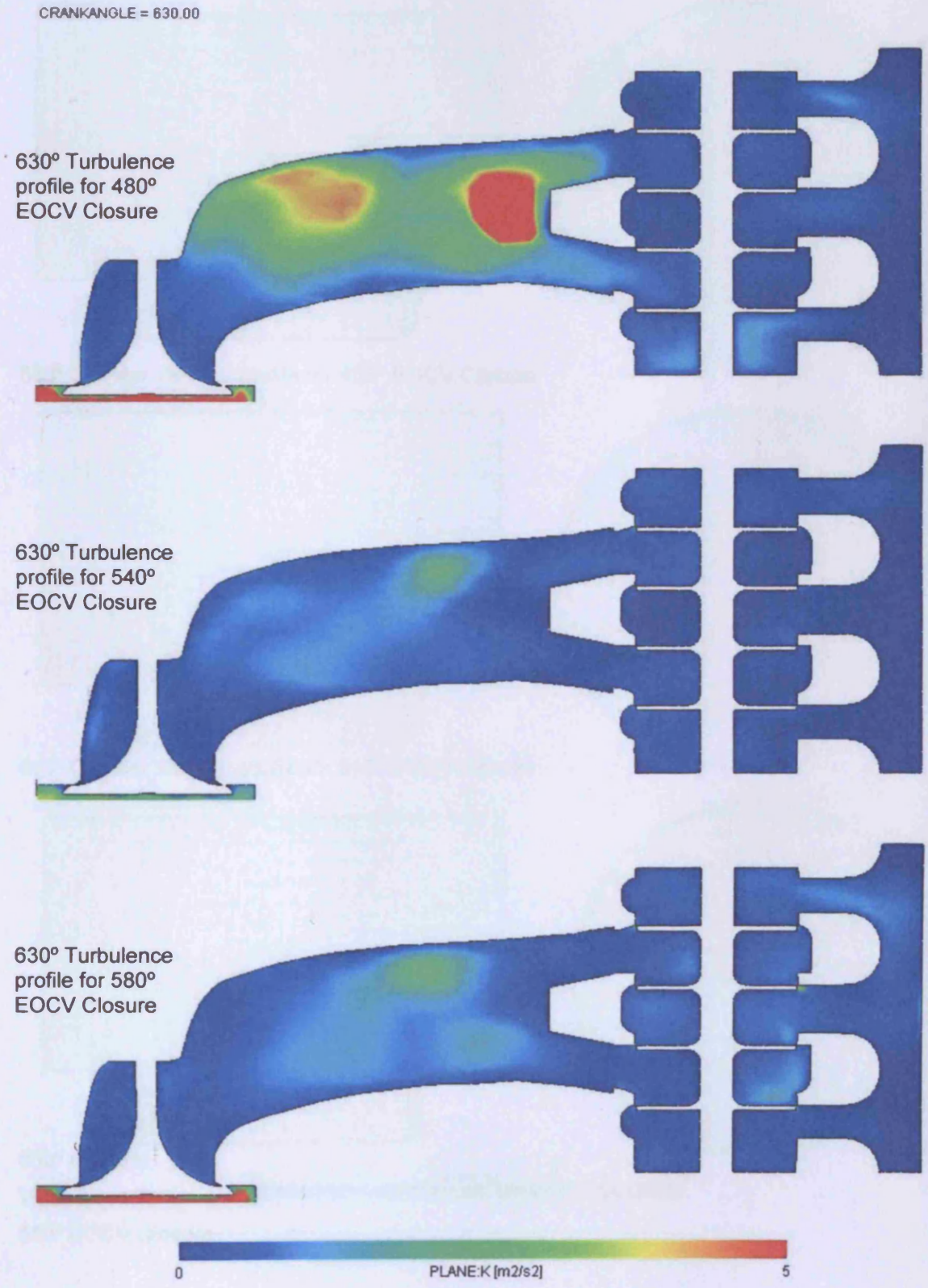
CRANKANGLE = 630.00
630° Turbulence profile for 480° EOCV Closure
630° Turbulence profile for 540° EOCV Closure
630° Turbulence profile for 580° EOCV Closure
0
PLANE:K [m2/s2]
5

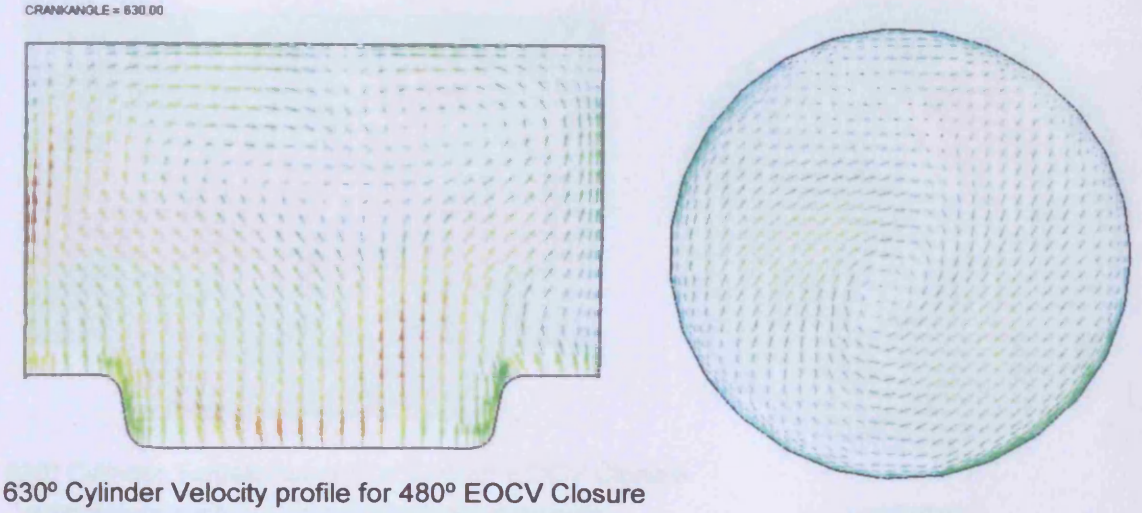

630° Cylinder Velocity profile for 480° EOCV Closure

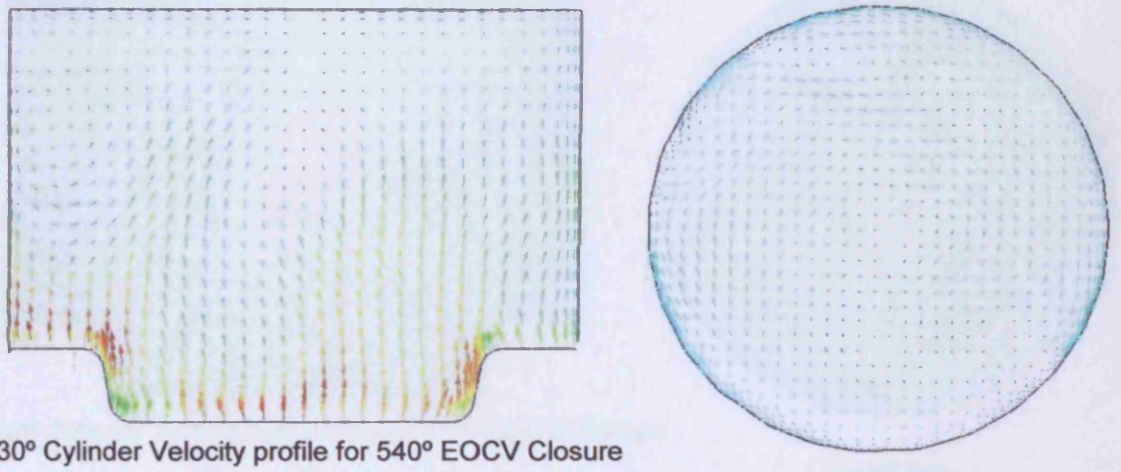

630° Cylinder Velocity profile for 540° EOCV Closure

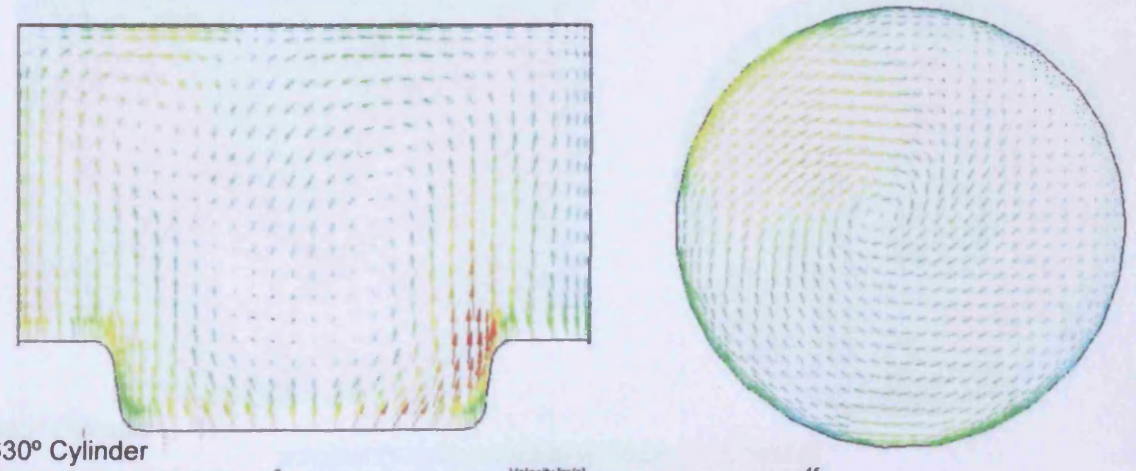

630° Cylinder
Velocity profile for
580° EOCV Closure

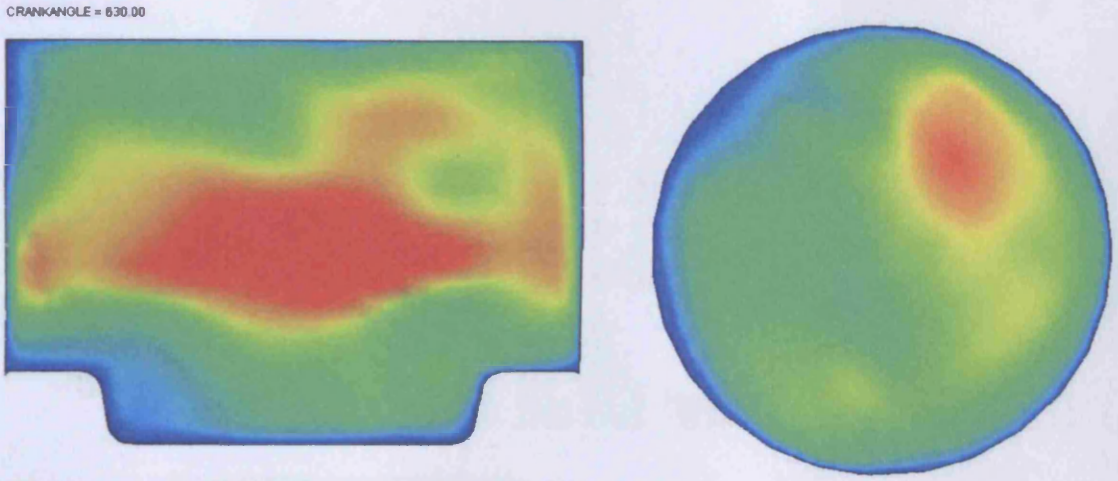

630° Cylinder Turbulence profile for 480° EOCV Closure

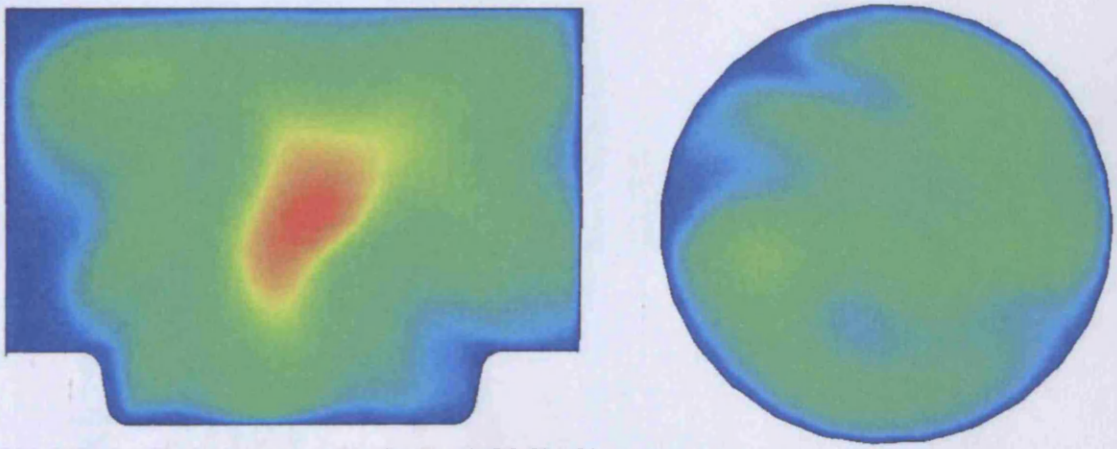

630° Cylinder Turbulence profile for 540° EOCV Closure

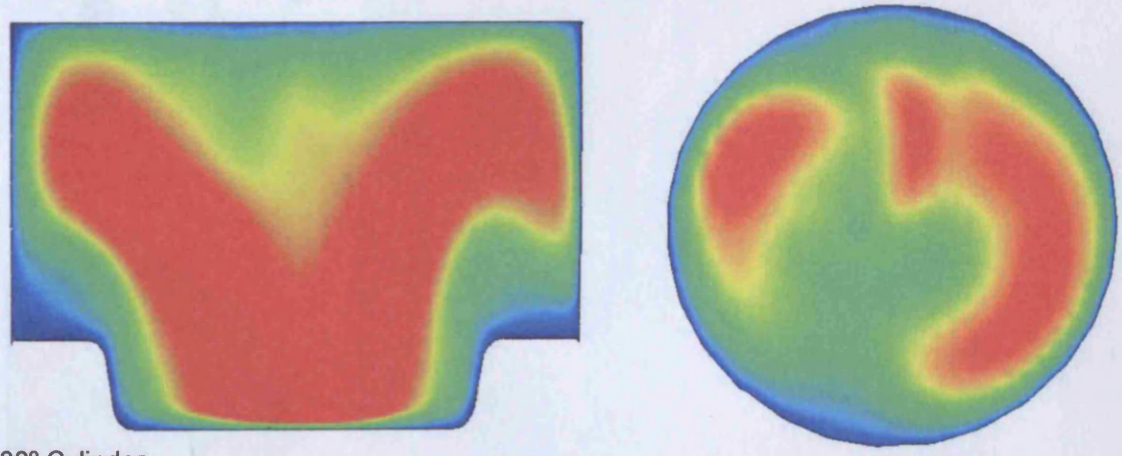

630° Cylinder Turbulence profile for 580° EOCV Closure

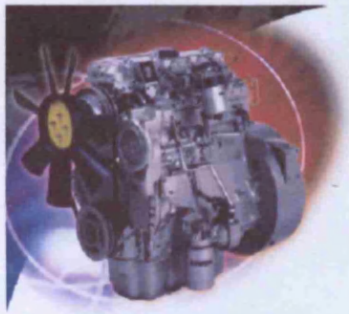

Perkins

1000 Series

Agricultural/Industrial Power Units

1004-4T

83 kW/111 bhp

A tough 4-cylinder turbocharged diesel for compressors, telescopic handlers, backhoe loaders, fork lift trucks, agricultural and construction equipment.

Based on Perkins' 60 years' experience in the development and production of diesel engines, this quality product will give trouble free operation and high performance over a long engine life.

Reliable power

Perkins' high manufacturing standards are approved to ISO 9000.
Maximum cooling efficiency is provided by the gear driven water pump and independent fan drive. Leak free operation is ensured by Viton crankshaft seals and sophisticated controlled swell joints, giving protection in the toughest conditions.

Durable power

A long, trouble free life is assured by the use of the highest quality components throughout the engine, from the deep skirted cylinder block, designed with the aid of computer technology, to premium quality, 3-ring controlled expansion pistons.

High performance, productive power

Good power to weight with high torque and 22% torque back up, made possible by the Quadram direct injection combustion system matched to a high specification turbocharger.

Economical power

Excellent fuel economy – a direct result of the unique Quadram combustion system.

Easy low cost maintenance

Service intervals of 400 hours for oil and filters.
Quick, easy maintenance is made possible by the convenient positioning of service points, for easy accessibility.
Improved parts availability and reduced inventory costs are achieved by the true family concept of the 1000 Series, giving parts commonality across the engine range.

Quiet, clean power

Operator and environmentally friendly with low noise, rapid startability low emissions, achieved with the Quadram, and high specification fuel injection equipment. At 96 dBA the 1004-4T is probably the quietest engine in its class.

Performance Data	Gross Intermittent*	Speed rev/min	Net Intermittent	Speed rev/min
Power Output (kW)	83	2600	74.5	2600
Power Output (bhp)	111	2600	99	2600
Peak Torque (Nm)	368	1600	333	1600
Peak Torque (lbf ft)	271	1600	245	1600

Power output for a run-in engine, after 60 hours.
*Rating Standard ISO 3046 / 4 Mar.

The graphs are for illustrative purposes only and may not reflect final specifications.

1000 Series
1004-4T

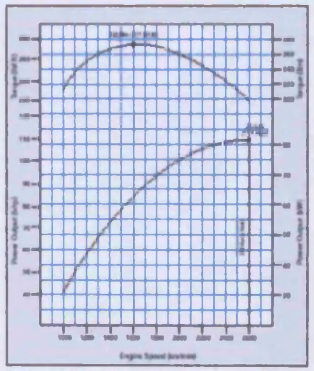

Note: Lower speed ratings may not be read from this curve.
Other ratings are available, please consult your Perkins representative.

Engine Specification

Cast iron engine block
Flywheel and flywheel housing
Rotary fuel injection pump
Fuel filter and prefilter
All-speed mechanical governor
Low inertia injectors
Turbocharger
Inlet manifold
Cast iron exhaust manifold – centre outlet
Lub. oil sump
Spin on oil filter and oil cooler
12V/24V starter and alternator
Choice of cooling fans belt driven
Gear driven coolant pump
Lub. oil pressure switch
Cold start aid

Perkins

Perkins Engines Company Limited
Peterborough PE1 5NA
United Kingdom
Telephone +44 (0)1733 583000
Fax +44 (0)1733 582240
www.perkins.com

Option Groups

A selection of optional items is available to enable the customer to make up a specification precisely matched to his needs. These include alternative ratings, inlet manifolds, exhaust outlets, a range of flywheels and flywheel housings to suit various clutches and transmissions and a selection of power take-offs.

General Data

Bore and stroke	100 mm x 127 mm (3.937 in x 5.00 in)
Number of cylinders	4 in-line
Cubic capacity	4.0 litres (243.0 cu.in.)
Cycle	4 stroke
Aspiration	Turbocharged
Combustion system	Quadram direct injection
Compression ratio	16:1
Firing order	1.3.4.2
Rotation	Anti-clockwise, viewed on flywheel
Cooling	Liquid
Length	651.5 mm (25.65 in)
Width	612 mm (24.1 in)
Height	779.8 mm (30.7 in)
Dry weight	279 Kg

Overall dimensions and weight will depend on final specification

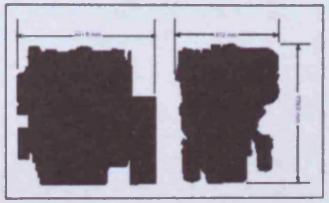

Appendix K – Low Sulphur Diesel TEM Images

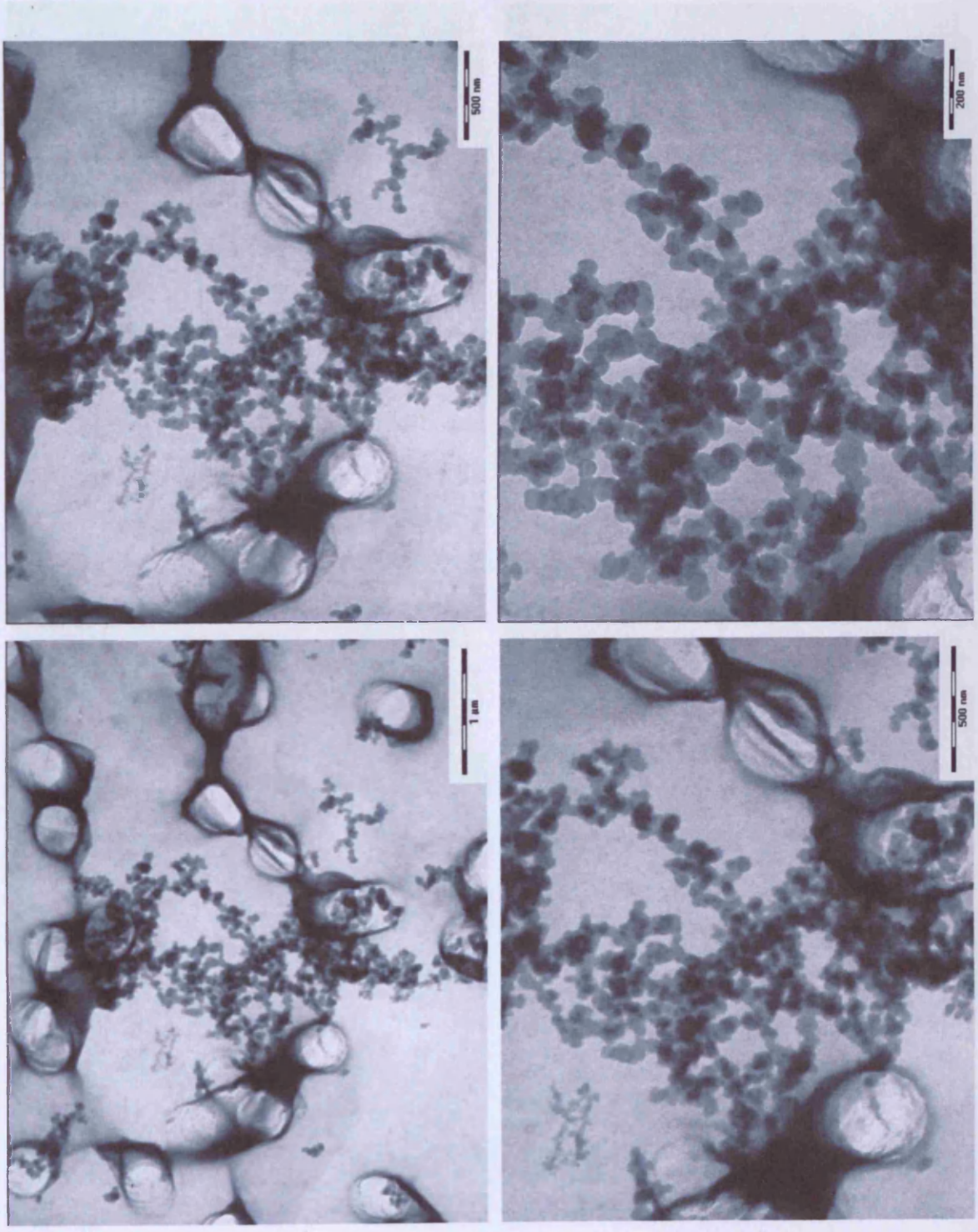

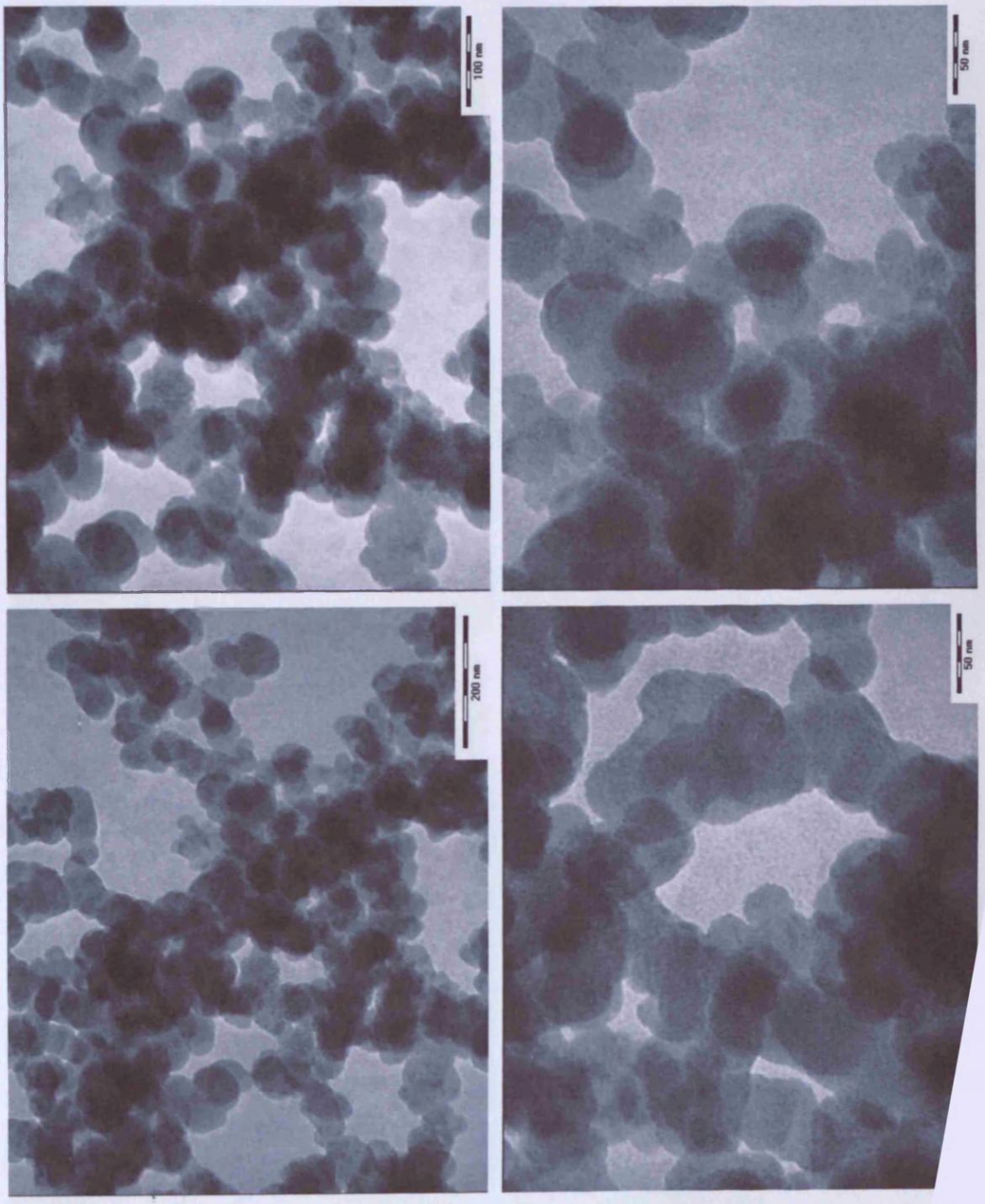
100 nm
50 nm
200 nm
50 nm

Appendix L – Red Diesel TEM Images

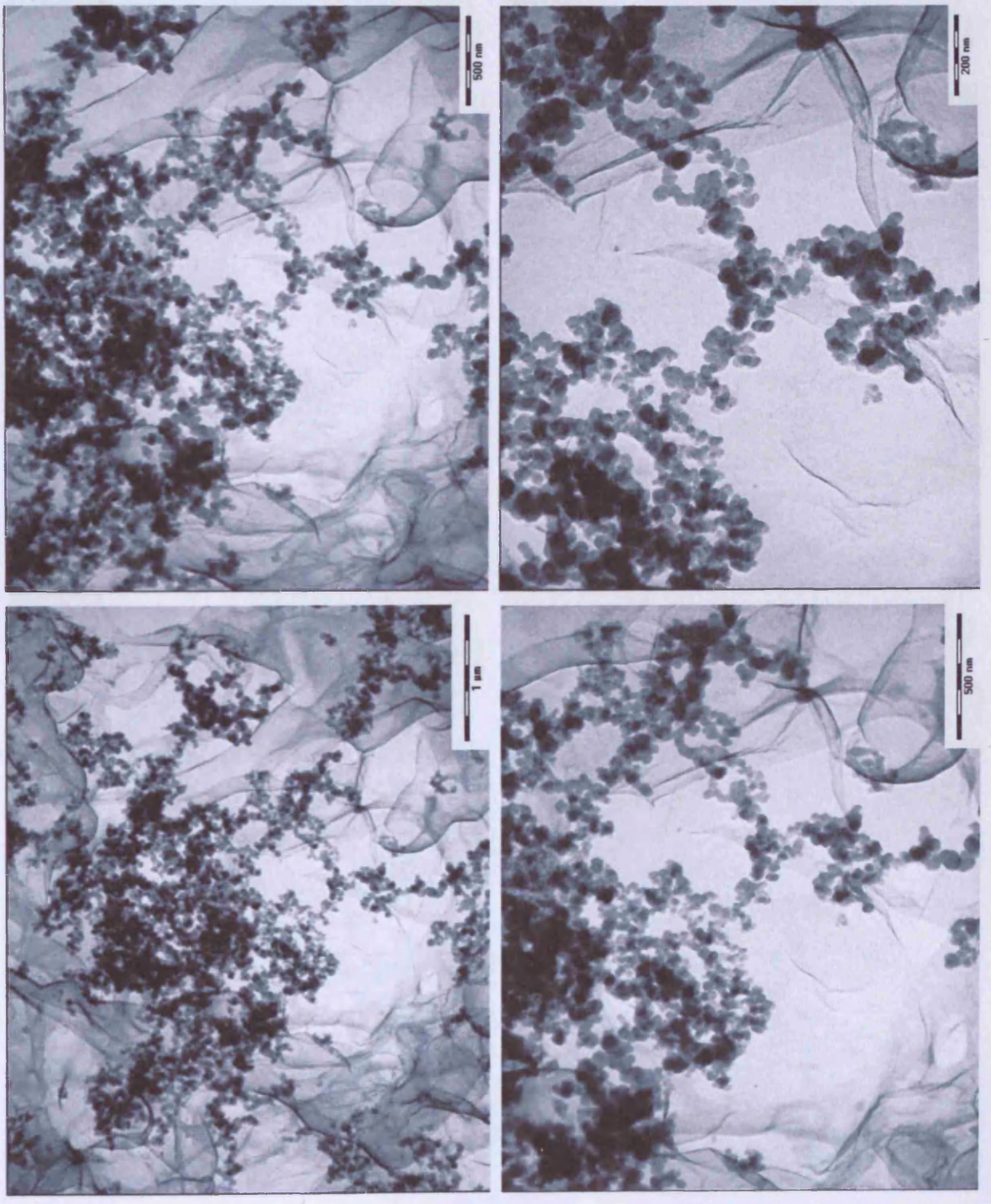

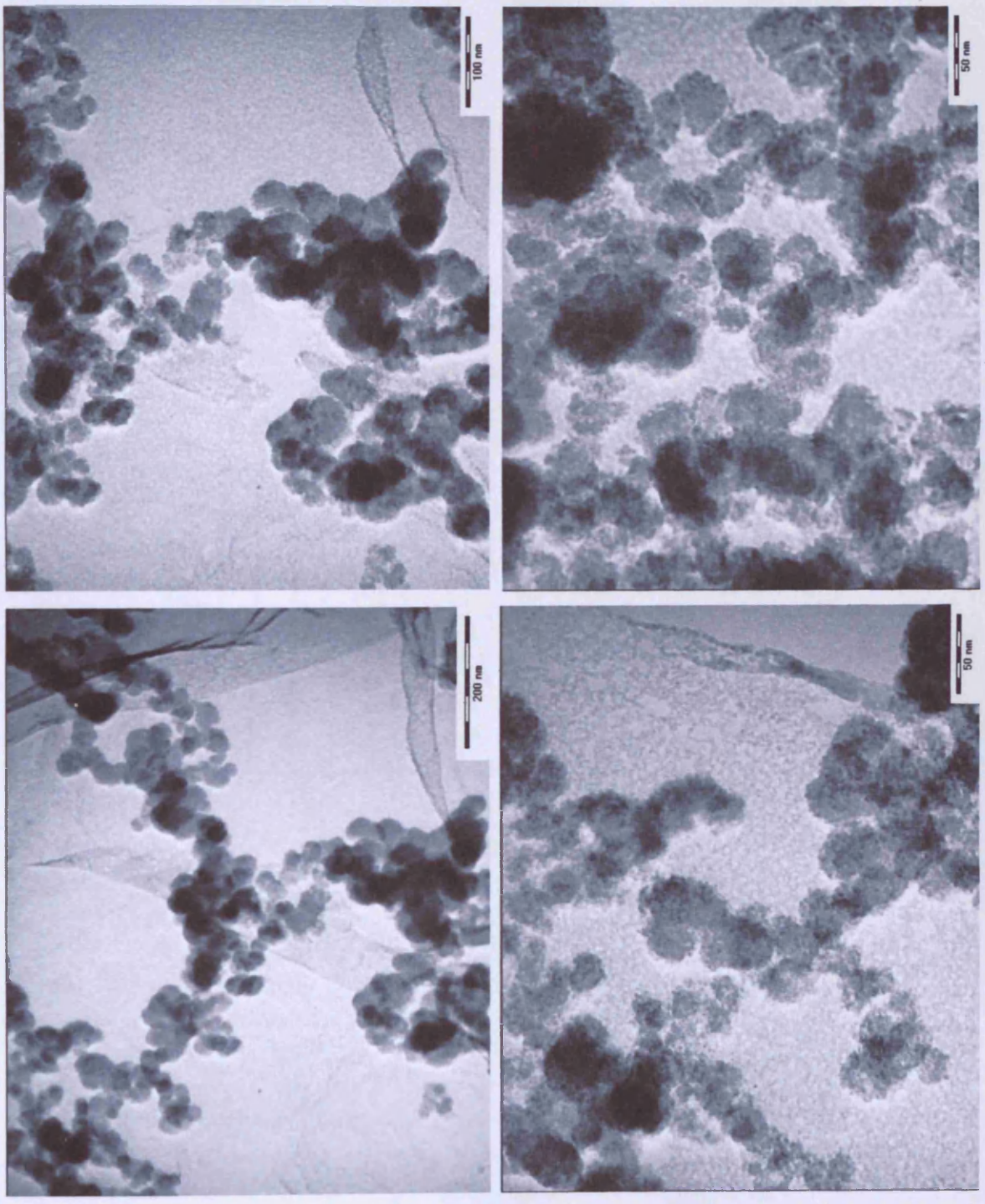
100 nm
50 nm
200 nm
50 nm

Appendix M – Perkins Wave Simulation Results

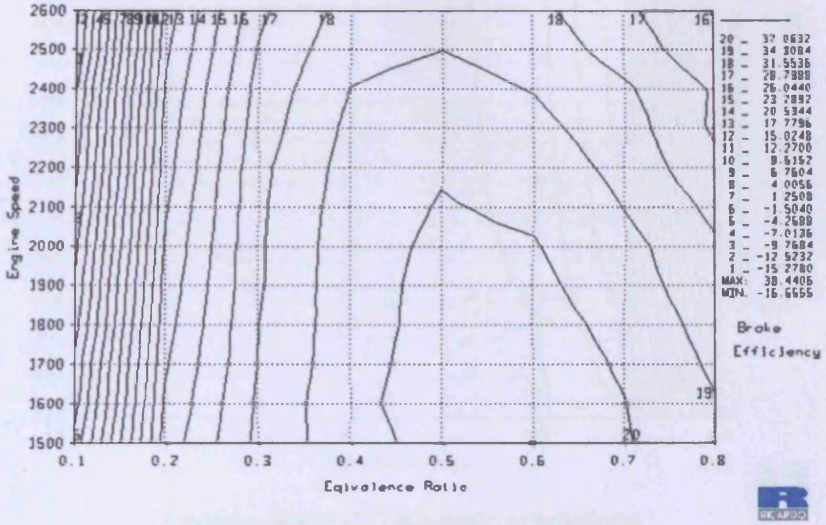

Perkins diesel efficiency predictions

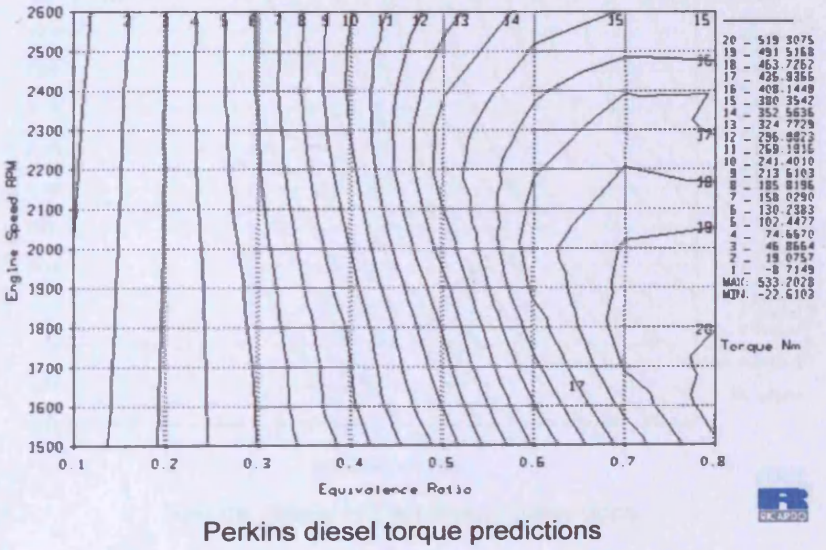

Perkins diesel torque predictions

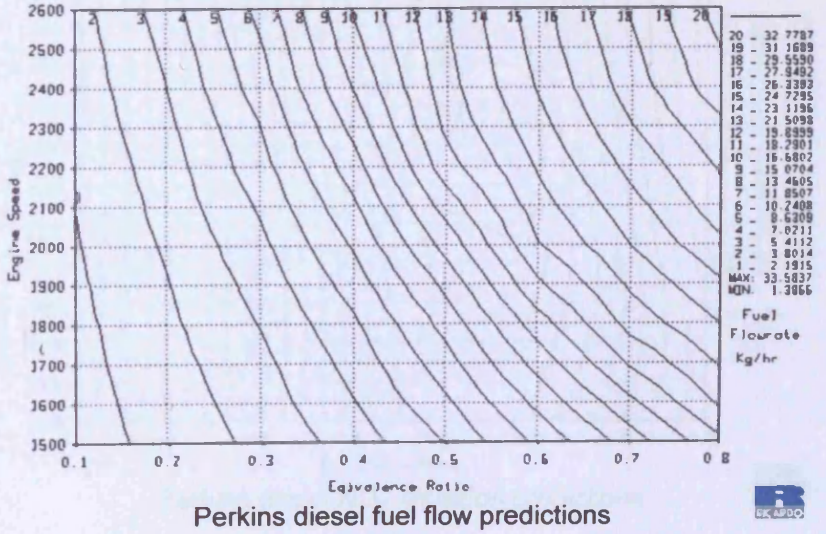

Perkins diesel fuel flow predictions

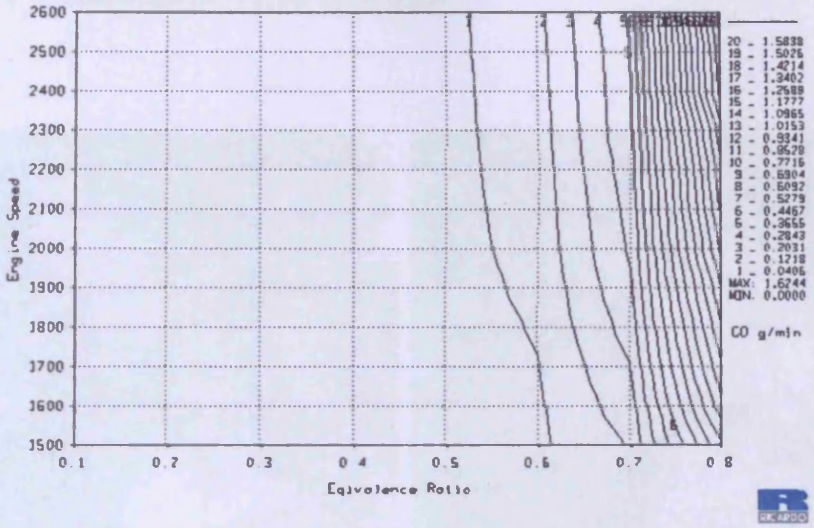

Perkins diesel CO emission predictions

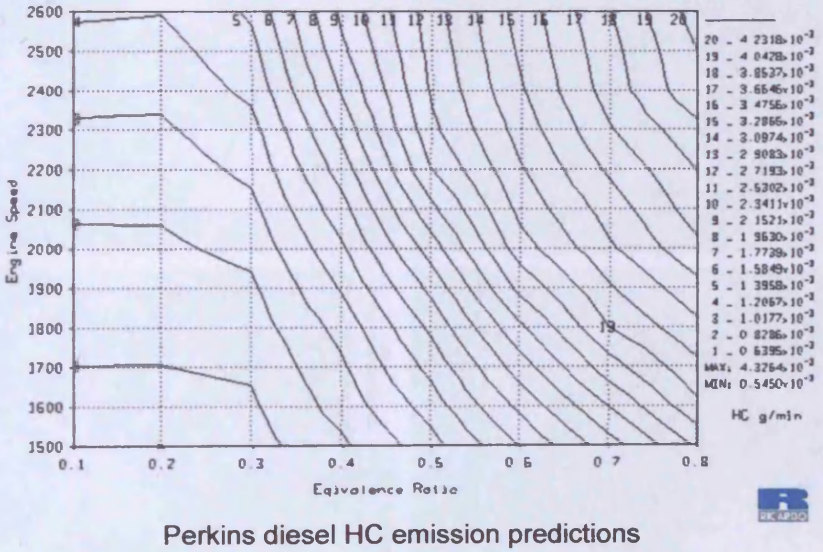

Perkins diesel HC emission predictions

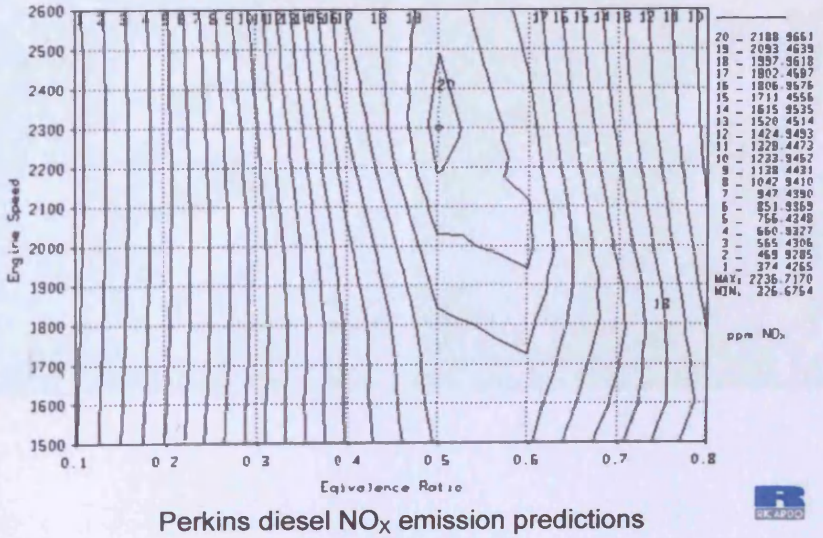

Perkins diesel NO_X emission predictions

Appendix N – Biodiesel TEM Images